Effect of Addition Flowrates of Grafted Polymers on the Flocculation of Kaolinite Suspensions and Oil Sands Mature Fine Tailings

by

Kilian Slöetjes

A thesis submitted in partial fulfillment of the requirements for the degree of

Master of Science

in

Chemical Engineering

Department of Chemical and Materials Engineering
University of Alberta

Abstract

Bitumen extracted from oil sands has been a major source of wealth for Canada, but it comes at a high price because the Clark hot water process generates large volumes of tailings which must be stored in ponds that threaten the environment. These tailing ponds must be treated to meet the land reclamation targets implemented by the government of Alberta.

Tailings are mixtures of clays and sands (~ 30 %), water (~ 70 %) and residual bitumen. Mature fine tailings (MFT) are hard to treat because colloidal interactions stabilize the suspended fine clay particles. The efficiency of the several methods used to treat tailings is low, limiting soil recovery and industry sustainability. One method used for tailings treatment is flocculation. Its aims are to gather tailing particles into large flocs that settle fast (by gravity or helped by mechanical means), recover the process water, and reduce the volume of tailing ponds. Flocculants, such as neutral or negatively-charged polyacrylamides, are typically added to tailings, but the flocs they generate break under shear, retain water, and leave fine solids behind in the supernatant water.

This thesis is dedicated to enhancing oil sands tailings treatment by changing hydrophobicity and cationic charge of natural polymers. Specifically, I grafted cationic polymers onto amylopectin backbones via free radical graft polymerization and tested the performance of the new amylopectin-*graft*-poly[(vinylbenzyl)trimethylammonium chloride] (AP-*g*-PVBTMAC) by flocculating MFT (diluted to 10 wt.%) and measuring the initial settling rate, supernatant turbidity, capillary suction time (CST), and sediment solids content. I also compared different AP-*g*-PVBTMAC microstructures to find the optimum graft length and frequency, and combined the best AP-*g*-PVBTMAC with a commercial high molecular weight anionic polyacrylamide

(Magnafloc ® 1011, MF1011) to investigate how polymer addition flowrates affected kaolinite suspensions.

Unlike the dosage, the polymer microstructure parameters (graft length and frequency) did not influence much the flocculation, but AP-*g*-PVBTMAC outperformed the homopolymer PVBTMAC, and the blend of pure AP and PVBTMAC in all flocculation metrics, proving that the amylopectin backbone plays an important role in the flocculation and dewatering. When combined with MF1011, focused beam reflectance measurements (FBRM) showed that addition flowrates determined the size and structure of the flocs as well as fines capture. A minimum addition flowrate of AP-*g*-PVBTMAC was required to destabilize the suspension and to form primary flocs, which could then grow through combined charge neutralization and bridging mechanism with MF1011. While the addition flowrate of the cationic flocculant affected CST and turbidity, the addition flowrate of the anionic flocculant mattered for flocs solids content based on the central composite design results.

Preface

The thesis is an original work by Kilian Slöetjes with some guidance by Daniel D.V. Dixon and João B.P. Soares.

Kilian Slöetjes was responsible for the statistical design of experiments, data collection, analysis and manuscript preparation. Daniel D.V. Dixon provided occasional guidance regarding some experimental procedures. Professor João B.P. Soares was involved in revisions of the thesis and provided insightful inputs throughout this research work.

Acknowledgments

I am very grateful for the experience I have acquired and the time I have spent at the University of Alberta pursuing this degree. I would like to thank all the people that contributed to this project for supporting me.

To begin with, I would like to express my gratitude to my supervisor, Professor João B.P. Soares, who guided and provided me with insightful feedback throughout this project. I am not only thankful for his expert knowledge and creativity but also for his trust, positivity and availability all over of my work. This relationship was key to my happiness and fulfillment carrying out this project. Furthermore, I would like to express my sincere appreciation to all the members of our research group who maintain a friendly and stimulating work environment.

As regards my project, I wish to thank Daniel Dixon for his help on polymer synthesis, molecular weight measurements and flocculation tests discussions. I also appreciate the help of the Institute for Oil Sands Innovation (IOSI) labs for the use of some of their equipment. I particularly thank Lisa Brandt and Brittany Mackinnon for helping me with equipment training and for facilitating lab access for experiments.

Finally, I would like to thank all my friends and family, especially Remy Samson and my parents who encouraged me and participated in this work with active listening.

Thank you for your unwavering support, care and love.

Table of Contents

List of Tables

List of Figures

Nomenclature

AAS	Atomic absorption spectrophotometry
AER	Alberta Energy Regulator
AGU	Anhydroglucose unit
ANOVA	Analysis of variance
AP	Amylopectin
AP-*g*-HPAM	Amylopectin-*graft*-hydrolyzed polyacrylamide
AP-*g*-PAA	Amylopectin-*graft*-poly(acrylic acid)
AP-*g*-PAM	Amylopectin-*graft*-polyacrylamide
AP-*g*-PVBTMAC	Amylopectin-*graft*-poly[(vinylbenzyl)trimethylammonium chloride]
AP-*g*-PVBTMAC-co-	Amylopectin-*graft*-poly[(vinylbenzyl)trimethylammonium chloride]-*co*-polyacrylamide
AS	Amylose
bpd	Barrels per day
CAN	Ceric ammonium nitrate
CCD	Central composite design
CH4	Methane
CLD	Chord length distribution
CO2	Carbon Dioxide
Copo-P~	Polymer samples with co-grafts PVBTMAC and PAM
CST	Capillary suction time
DI	Deionized
DLVO	Derjaguin-Landau-Verwey-Overbeek
EDL	Electrical double layer
FxLy	Label of polymer sample with graft frequency Fx and length Ly
FBRM	Focused beam reflectance measurement
FCF	Flocculation-coagulation-flocculation
FTIR	Fourier Transform Infrared Spectroscopy
GF	Graft frequency
GL	Graft length
GPC	Gel permeation chromatography
ICP-OES	Inductively coupled plasma-optical emission spectroscopy
ISR	Initial settling rate
KPS	Potassium persulfate
LOD	Limit of detection
LOQ	Limit of quantification
MF / MF1011	Magnafloc 1011 ®
MFT	Mature fine tailings
NaOH	Sodium hydroxide
NTU	Nephelometric Turbidity Units
PAM / HPAM	Polyacrylamide / Hydrolyzed polyacrylamide
PDADMAC	Polydiallyldimethylammonium chloride
PNIPAM	Poly(N-isopropylacrylamide)
PSD	Particle size distribution
ppm	Parts per million
RiR	Reference intensity ratio
rpm	Rounds per minute
SAGD	Steam assisted gravity drainage
SFR	Sand-to-Fine ratio
VDW	Van der Waals
XRD	X-ray diffraction

1- Introduction

The oil sands industry has been a major source of wealth for Alberta and Canada over the past century. The production of usable crude bitumen needs different steps: extraction, upgrading (to facilitate its transport in pipelines), and tailored refining (to match end-use applications). Each stage produces by-products that threaten the environment. The waste streams from oil sands upstream exploration are called oil sands tailings. They are a mixture of water, solids (sand and clays) and residual bitumen. Because the solids in this mixture are small, the suspension remains stable after settling in large tailings ponds for a few years. This suspension is known as mature fine tailings (MFT).

Breakthroughs in dewatering and consolidation technologies led to the use of very high molecular weight anionic polyacrylamides (HPAM) as the current industrial standard. Unfortunately, these flocculants do not capture the smallest particles (fines < 44 μm) in the MFT efficiently, and form shear-sensitive flocs that entrap water by hydrogen bonding and hydrophilic interactions. They also need inorganic coagulants, such as multivalent cations to destabilize the suspension which ideally should be removed later before the water can be recycled to the process.

Since the goal is environment remediation, natural polymers have attracted interest. Natural polymers are cost-effective, but they do not flocculate tailings well, despite the shear resistance provided by their rigid carbon backbone. These natural polymers can be modified by grafting copolymers on their backbones to increase their flocculation performance and water solubility. It is especially interesting to graft cationic polymers onto their backbones to eliminate the need for cationic coagulants.

One of the objectives of this thesis was to treat MFT with new cationic-grafted natural flocculants. Since we know that flocculation results depend on the flocculation conditions, the second objective of this thesis was to study the effect of polymer addition flowrate on the flocculation results.

In this thesis, I made amylopectin-*graft*-poly[(vinylbenzyl)trimethylammonium chloride] (AP-*g*-PVBTMAC) flocculants with varying graft lengths and frequencies, and used them to treat MFT and kaolinite suspensions. I used a simple synthesis procedure to make it easy to scale up the flocculant production to industrial applications: macroradicals were formed on the amylopectin

backbone and then poly[(vinylbenzyl)trimethylammonium chloride] (PVBTMAC) chains were grafted from these sites.

I assessed how well AP-*g*-PVBTMAC flocculated and dewatered a 10 wt. % MFT suspension by measuring initial settling rate (ISR), the initial and sediment (after 24 hours of consolidation) capillary suction time (CST), the supernatant turbidity and the sediment solids content. The second aspect of my thesis was to find out whether the cationic AP-*g*-PVBTMAC could improve the performance of a commercial anionic polyacrylamide, Magnafloc 1011 ® for the flocculation of a kaolinite suspension. This system allowed me to study the impact of addition flowrates of both polymers on the flocculation of kaolinite suspensions, thus, revealing new insights on the flocculation mechanism with anionic and cationic charges.

Chapter 2 of this thesis reviews the background of oil sands processing in Alberta, the environmental problems caused by tailings ponds, and current treatment methods. *Chapter 3* explains the materials and methods used in the experiments, measurements and analysis. This chapter also covers characterization methods for flocculants and suspensions, and the flocculation metrics used to quantify the performance of each polymer. *Chapter 4* discusses the main results of the research work: characterization of the polymer and suspension, statistical analysis and comparison between different flocculation systems. It also discusses a new method I developed to estimate the size of the flocs using image processing. Finally, *Chapter 5* summarizes the key findings of this thesis and suggests future studies to improve the current understanding of the field.

2- Background and Literature Review

2.1 Alberta's Oil Reserve and Exploration Process

Canada has the third largest oil reserve in the world, after Venezuela and Saudi Arabia. Approximately 97 % of it is in the Alberta oil sands, comprising about 165.4 billion barrels [1]. These reserves cover approximately 142 200 km^2 [2], divided in three main oil sands areas: the Athabasca Basin, the Cold Lake Basin and the Peace River Basin (Figure 2.1).

Figure 2.1 – Oil sands deposits in Alberta (redrawn from [3-5]).

The current production of crude bitumen today is 2.8 million barrels per day (bpd). The production rate is expected to reach 4 million bpd by 2025 [2]. The bitumen must be extracted

from the oil sands ore through several processes, depending on its location and composition. Table 2.1 lists the typical composition of an oil sands ore.

Table 2.1 – Oil sands ore composition [6].

Component	Percentage
Water	3-5 %
Bitumen	8-12 %
Sands / Clays	~10 %
Inorganic Materials	~75 %

The ore composition may vary depending on its location and depth, which impacts the extraction process used to extract the raw bitumen. Figure 2.2 highlights the two main processes used to extract bitumen: surface mining for shallow deposits (< 75 m) [7] and thermal in-situ extraction for deep deposits (> 200 m) [8-9].

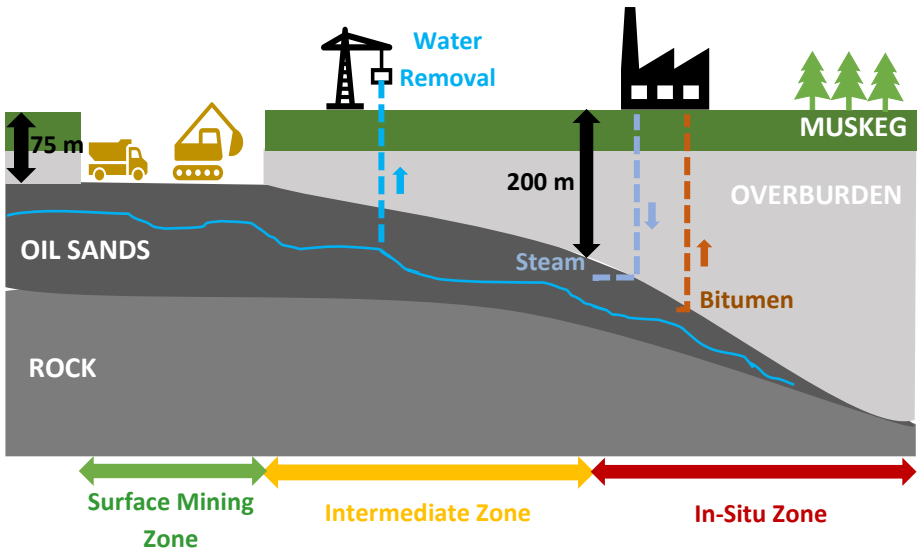

Figure 2.2 – Surface mining and in-situ bitumen extraction (redrawn from [12]).

Surface mining can be used to extract bitumen from a small percentage of Alberta's reserve, since only 20 % of the total deposits (4800 km^2 in the Athabasca region) are shallow enough to use this process [7,10,11]. Surface mining is straightforward: after removing the muskeg (wet peatland), the overburden (low-bitumen sand and clay layer), and the groundwater to depressurize the basal aquifers, the ore is shoveled out of the mine, loaded into trucks, and transported to the processing plant [12]. At the plant, the ore is dumped into a crusher to break down oversized materials before being treated in the Clark Hot Water Extraction Process (patented in 1929) [13]. In this process, a sodium hydroxide solution (NaOH, pH ~ 9) and hot water (80-85 °C) disperse sand and clay particles and extract the bitumen. Surface mining extracts about 90 % of recoverable oil [13,14], but it also produces undesirable oil sands tailings. Oil sands tailings are made of water, coarse sand, clays (kaolinite and illite) and residual bitumen. Contrarily, in-situ extraction recovers only 60 % of the oil but consumes far less fresh water than surface mining: about 0.4 barrels of fresh water are required to produce a barrel of synthetic crude oil against 2.5 to 4 for surface mining [15]. Neither in-situ or surface mining are economically viable in the intermediate zone [14].

The in-situ technique is adequate for most deposits in Canada [14]. In this process, steam or solvent is injected into deep deposits to heat and separate the bitumen from the ore, which is then pumped to the surface (Figure 2.2). Because this energy-sensitive process is widely used, new techniques such as steam assisted gravity drainage (SAGD) [8] or cyclic steam stimulation (CSS) [9], have been developed to limit greenhouse gas emissions. SAGD uses two wells of different depths. The upper well guides the injected steam to the deposit, while bitumen and condensed steam are recovered in the lower well (Figure 2.2) [8]. CSS only needs one well and is divided in three steps: high-pressure steam injection, soaking period, and oil production [16]. The first step reduces the oil viscosity after a few weeks of injection, while the second step allows the steam to diffuse through the reservoir [16].

The newly extracted raw bitumen is viscous, dense, and contains contaminants such as asphaltenes or sulfur [5]. It must be upgraded by eliminating (with physical or chemical means) these contaminants to form synthetic crude oil [17]. Diluent might also be added to make it easier to flow in pipelines [18].

Both extraction methods consume significant amounts of fresh water; recycling water to the process and dewatering the oil sands ore and tailings are key for the sustainability of the industry.

2.2 Environmental Tailings Problem and Management

The wastes generated by extraction, froth treatment, and bitumen upgrading threaten the environment because they may contain polycyclic aromatic hydrocarbons, heavy metals, and other toxic substances [19]. Therefore, oil sands tailings are collected in large tailings ponds (Figure 2.3), where the solids are left to settle to recover the water remaining in the suspension.

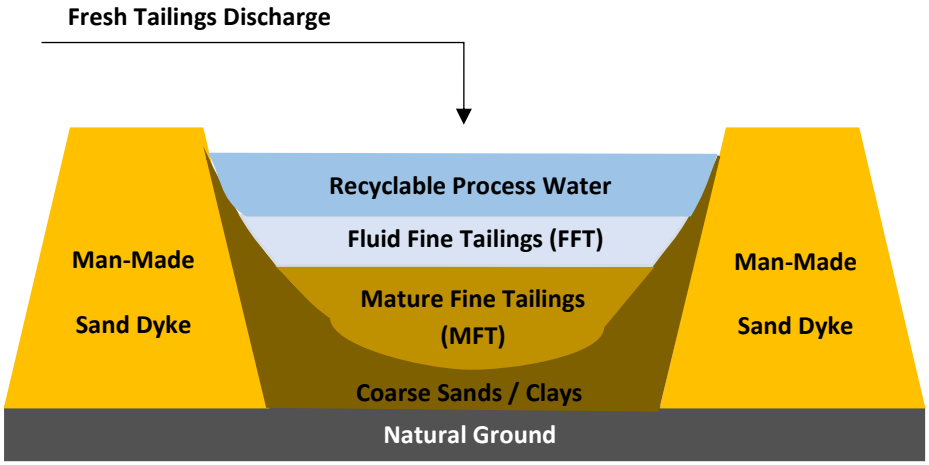

Figure 2.3 – Theoretical tailings pond cross-section (adapted from [20]).

Tailings ponds cover an area of about 176 km^2, with a corresponding volume of 766×10^6 m^3 in the Athabasca oil sands region [21,22]. The land occupied by tailing ponds threatens wildlife and vegetation because they emit CO_2, CH_4, volatile organic compounds (VOCs) and reduced sulfur compounds (due to volatilization and biogenic activity) [22]. The ponds also disrupt the natural land surface and ground water [11,23]. To make matters worse, the volume of tailings continues to grow due to increasing production, which is not compensated *yet* by better tailings treatment. Even though, the Alberta Energy Regulator (AER) has implemented the *Directive 085: Fluid Tailings Management for Oil Sands Mining Projects* in 2016 to ensure land reclamation within ten years after of the end of the mine lifetime [24], land reclamation will still require large scale reconstruction of whole ecosystems [25].

As shown in Figure 2.3, when fresh tailings are discharged into a tailings pond, the coarser particles settle quickly allowing for the recovery of large volumes of supernatant water, but a substantial amount of water remains trapped in the heterogenous mixture even after a few years of consolidation. This mixture, called mature fine tailings (MFT), is stable due to colloidal interactions (mainly Van der Walls attraction forces and electrostatic repulsion) between fine clay particles (< 44 μm). MFT is usually made up of about 70 wt. % of water, 30 wt. % of solids (negatively charged clays) and up to approximately 3 wt. % of residual bitumen. The composition and MFT properties may change depending on the ore locations and extraction method [22], complicating the development of general MFT treatment methods because clay surface areas, charges, and particle size distributions may differ significantly among ore samples.

A few types of MFT treatment can be used to recover trapped water and obtain trafficable solid cakes, ranging from mechanical (centrifugation or deep deposits) to chemical (flocculation, chemically modified tailings). Composite (or consolidated) tailings (CT) and paste technology (PT) (also known as thickened tailings, TT) are two techniques used for large-scale industrial operations to obtain shear-resistant and transportable solid cakes [26,27].

Consolidated tailing forms dense sediments thanks to the aggregation of coarse sand from fresh tailings, MFT (4:1 ratio) and chemical additives such as gypsum [22,26]. Unfortunately, the additive adds ions to the recycled water [28] that can reduce bitumen recovery and foul the extraction process equipment [26]. These drawbacks are absent from paste technology, which adds flocculants (typically polymers) to tailings to make large flocs that settle fast. This method accelerates the timeline to about half an hour [26], but its economic viability can be questioned since it requires high start-up and operational costs, and also requires periodical cleaning because of bitumen build-up [26].

2.3 Mature Fine Tailings (MFT) Flocculation

2.3.1 MFT Stability and DLVO Theory

Coarse particles (often sand or silt) in tailings ponds can settle quickly, which is not the case for fine clay particles (< ~ 44 μm) [29]. One may think that this is related to the sedimentation time governed by Stokes' Law, but the real reasons are colloidal interactions due to the high surface area of these small particles [26,29]. This is confirmed in Table 2.2, from Suez Water handbook [30]. Fine clays will not settle naturally because they have high surface areas; suspension stability is likely to be governed by surface interactions.

Table 2.2 – Settling time and surface area order of magnitude for coarse particles and fine (colloidal) particles according to the Suez water handbook [30].

Type of Particle	Nature of particles and diameter (μm)	Settling time for 1m of water	Surface Area (m-2/m-3)
Coarse particles	Gravel ~10^4 Coarse Sand~10^3 Fine Sand~10^2	1 s 10 s 2 min	6.10^2 6.10^3 6.10^4
Fine particles (colloidal)	Clay~10^0 Fine Clay (colloidal particles) ~10^{-1} or 10^{-2}	2 days 2 to 20 years	6.10^6 6.10^7-10^8

As the particles become smaller, the surface charge density increases, raising the repulsion among them and, consequently, the energy required to flocculate them [31]. The Derjaguin-Landau-Verwey-Overbeek (DLVO) theory significantly helps understand the destabilization mechanism of colloidal suspensions [21]. This theory combines repulsive electrical double layer forces and attractive Van der Waals forces to describe interactions between two particles [32], as shown in Figure 2.4 for two interacting spheres of different radii. Van Der Waals (VDW) forces (Keesom, Debye and London) are attractive at close range and proportional to the surface area and mass of the particles. The VDW forces depend on the properties of the medium through the Hamaker constant (A_{CWC}) and promote aggregation. However, they weaken and rapidly become negligible over few hundreds of nanometers [33]. Therefore, they are not prevailing in MFT, which

is governed by repulsive electrical double layer interactions (EDL). These repulsive forces contribute to the stabilization of the suspension. In other words, they contribute to the energy barrier that needs to be overcome if coagulation is targeted for applications where floc strength matters (flocculation leads to fragile/reversible flocs). This repulsive term relies on the double layer theory completed by the Stern theory, which combines the Gouy-Chapman (diffuse layer) and the Helmholtz theories [32].

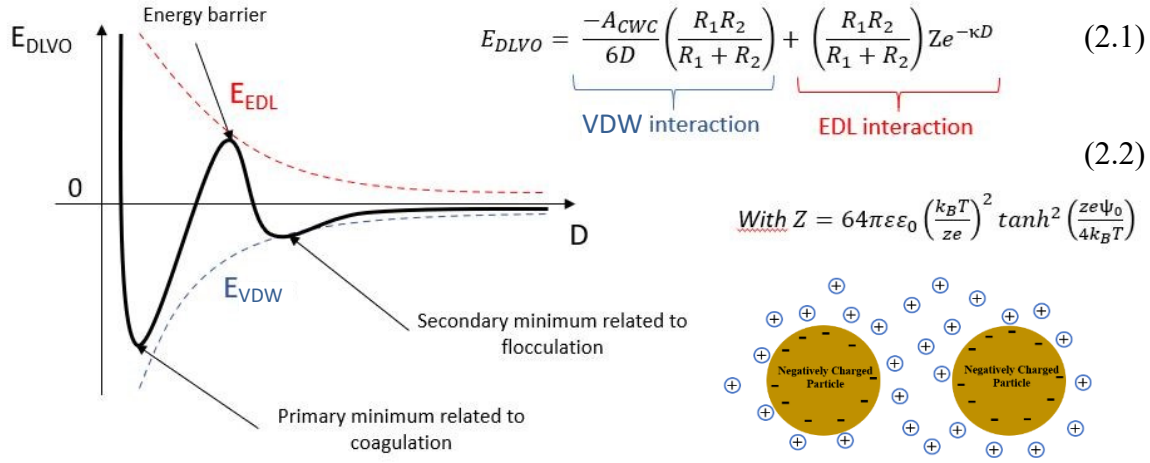

$$E_{DLVO} = \underbrace{\frac{-A_{CWC}}{6D}\left(\frac{R_1R_2}{R_1+R_2}\right)}_{\text{VDW interaction}} + \underbrace{\left(\frac{R_1R_2}{R_1+R_2}\right)Ze^{-\kappa D}}_{\text{EDL interaction}} \quad (2.1)$$

$$\text{With } Z = 64\pi\varepsilon\varepsilon_0\left(\frac{k_BT}{ze}\right)^2 tanh^2\left(\frac{ze\psi_0}{4k_BT}\right) \quad (2.2)$$

Figure 2.4 – Brief summary of the DLVO theory (expressions adapted from H. Zeng's book [32]).

The Stern theory states that positive ions cover the surface of the particles but do not fully neutralize their charge, hence the presence of a diffuse layer farther away from the particle surface (Figure 2.5). The interaction constant Z (Figure 2.4) depends on multiple variables, among which are the valency of the ions (z) and the surface potential (ψ_0), directly related to the surface charge [32]. The counterion concentration is high close to the particle surface and decreases when we move away from it. A moving particle carries charges present in the diffuse layer in the so-called shear plane. The potential at this plane can be measured and is called the zeta-potential (ζ) [32,34]. Therefore, the zeta potential is related to the movement of the particle and indirectly to the surface charge.

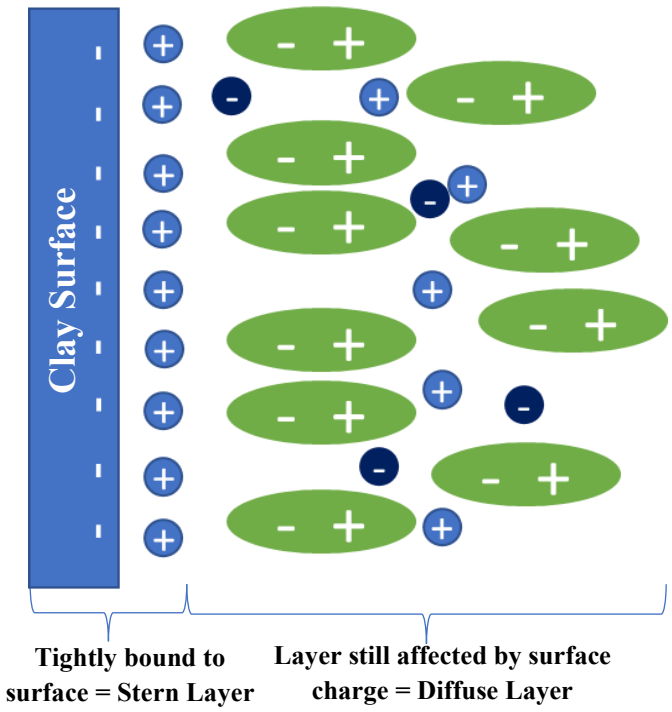

Figure 2.5 – Simplified diagram representing the electrical double layer for a clay surface (adapted from [35]).

2.3.2 Flocculation and Coagulation

Clays are the most important particles in MFT treatment methods. The surface of clays is negatively charged (Figure 2.5) because of imperfections in the crystal lattice [30] and ionization of pendant alumina or silica groups. When counter-ions are added to allow for coagulation (Figure 2.6), they form a layer around the clay particles (Figure 2.5).

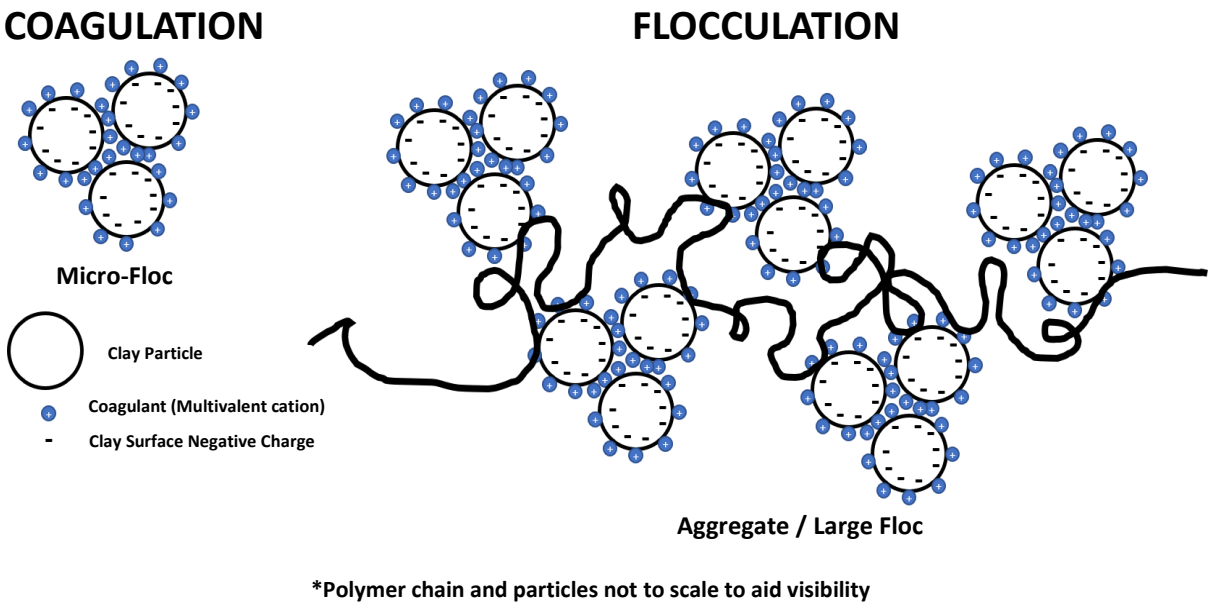

Figure 2.6 – Coagulation and flocculation principles.

Gypsum, $CaSO_4$-$2H_2O$, is a coagulant typically used to treat tailings [13,22,26]. Like other coagulants, the multivalent cation (Ca^{2+}) is attracted to the negatively-charged clays and compresses the EDL, reducing the energy barrier so that VDW forces prevail over electrostatic repulsive forces, forming micro-flocs (also called primary flocs) [36]. The main drawback of inorganic coagulants is the change of water salinity, which hinders bitumen recovery. Inorganic coagulants can also generate scaling in process units, so the water needs to be treated to be reused in the process [28]. Polymer flocculants have been introduced to address this limitation [37].

Flocculation is a two-step process in which the suspension is first destabilized and then the flocculant (in black, Figure 2.6) bridges the micro-flocs together, forming larger flocs as part of a three-dimensional network [26,38]. Flocculation efficiency relies on the adsorption of the flocculant on the surfaces of the clay particles (Figure 2.7) to promote chemical or physical bonding between them, forming aggregates (Figure 2.6) [37,39].

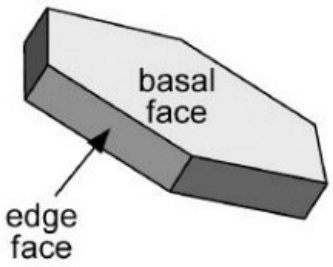

Figure 2.7 – Clay particle surface from [40].

Figure 2.7 shows a schematic of a clay particle, such as kaolinite. The particle is composed by the basal face and the edge face. Most of the flocculants used to treat MFT have amide functionalities that can adsorb on neutral sites by H-bonding with silica groups [26]. Cationic and anionic polymers are likely to adsorb mainly via electrostatic interactions or salt linkages, even if hydrogen bonding may contribute to this process.

Silica groups predominate on the basal face, accounting for most of the particle surface, while a mixture of alumina and silica groups exist on the edge surface [40]. Since the adsorption of neutral polymers depends on the availability of neutral adsorption sites, it is easy to understand why pH influences the adsorption of polymers on MFT particles. The zeta potential for both faces as a function of pH (Figure 2.8) explains which face dominates adsorption of neutral polymer for a given pH [41].

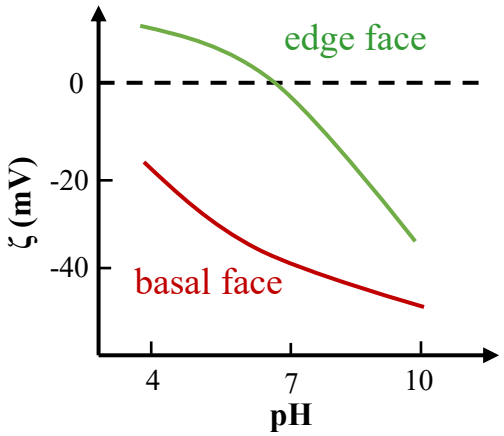

Figure 2.8 – Dependency of zeta potential with pH for basal and edge faces. Redrawn from [41].

Particle charge is dominated by the silica groups on the basal face, as shown in Figure 2.8, but polymer adsorption is governed by edge faces, especially for pH near 7. Other studies confirmed that at higher pH values, the negative charges on the silica surface increase, increasing

the electrostatic attraction between flocculant and silica of opposite sign (measured with single molecule force spectroscopy and dissipative quartz crystal microbalance), ultimately leading to higher polymer deposition on particles [42].

Anionic flocculants can also adsorb on clay particles through salt linkages or electrostatic interactions with cationic local patches, since the overall negative charge is not homogenously distributed along the clay surface [26,43].

The conformation of the polymer also plays a major role on its efficiency as a flocculant [26]. The conformation adopted by a polymer chain in solution depends on its charge density and solution ionic strength. For example, the commercial anionic polyacrylamide Magnafloc 1011 ® (MF1011) tends to develop electrical repulsion between its negatively charged segments, and will adopt a more extended conformation (Figure 2.10) than a neutral polymer such as PAM (Structures in Figure 2.9) [44].

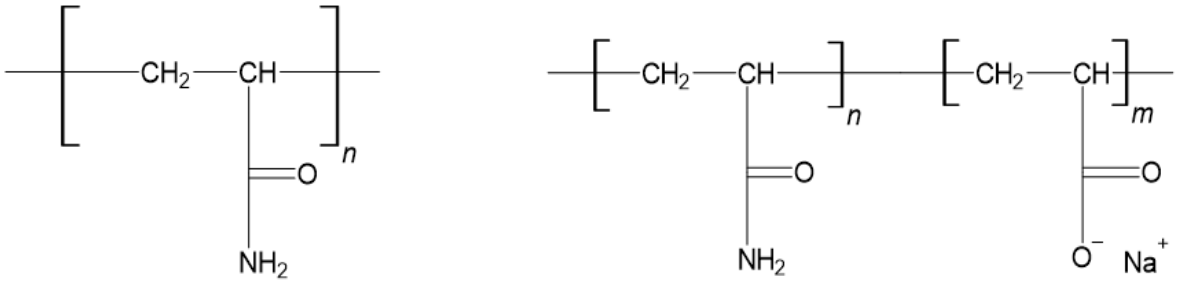

Polyacrylamide (PAM) Magnafloc 1011 (MF 1011)

Figure 2.9 – Two examples of polymer flocculants and their structures.

If the salinity is increased, the polymer conformation changes and the hydrodynamic radius decreases along with repulsions (Figure 2.10). Dynamic light scattering studies showed that Magnafloc molecules tend to be more condensed in saline solutions (Figure 2.10.a), which leads to a denser adsorption layer than in freshwater [26,44]. This is coherent with molecular dynamics simulations of HPAM adsorption on quartz [45]. High ionic strength promotes adsorption and contributes to the formation of a denser adsorbed layer of polymer, whereas pH has a minor influence in this case [45].

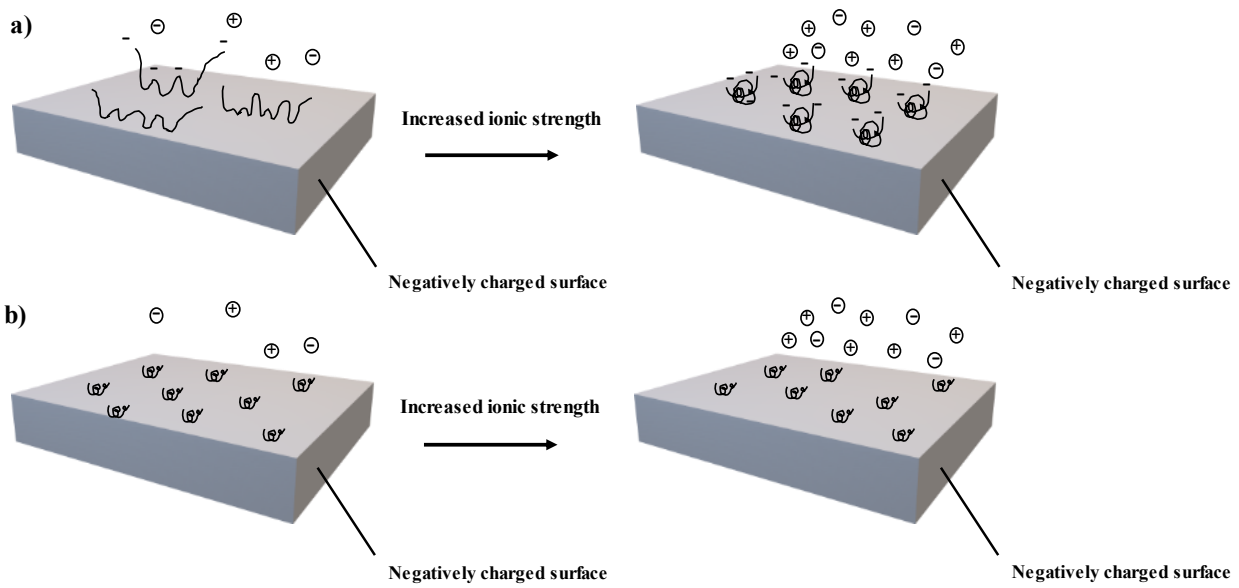

Figure 2.10 – Impact of ionic strength on the adsorbed conformation of polymers on negatively charged surfaces: a) Magnafloc 1011, b) PAM (redrawn from [44]).

In addition to its charge density, the very high molecular weight of Magnafloc is a key parameter for the flocculation performance [31] as longer polymer chains can adsorb onto the surfaces of several particles [26].

Another parameter to consider is the polymer dosage. If it is too high, there will be few sites available at the particle surfaces to allow for effective bridging and steric repulsion among polymer chains may occur. If ionic polymers are used, the polymer-covered particle surfaces may repel each other after complete coverage (surface charge reversal) [39,46]. On the other hand, if the polymer dosage is too low, fewer bridging interactions will take place [47]. At low concentration, the initial polymer layer adsorbed on the particle acts as a barrier for further polymer deposition due to electrostatic repulsion and fewer chains are available to bridge particles together [48].

Therefore, it is important to find the optimum flocculant dosage that maximizes bridging interactions. This is particularly true for anionic polymers, such as Magnafloc or partially hydrolyzed polyacrylamide (HPAM) in saline solution, since the attractive interactions are stronger but occur at shorter range than in freshwater, requiring higher polymer dosages to bridge the particles effectively [44,49]. Nevertheless, while the individual adsorption forces are weak, the large number of adsorbed segments makes the process irreversible. Other parameters may also

influence polymer adsorption on clay, such as mixing energy that should be optimized to maximize the efficient collisions between flocculant macromolecules and clay particles [50].

Even though the DLVO theory – in its simplified version in Eq. (2.1) – helps understand the interparticle interactions in complex suspensions such as MFT, it does not account for other non-negligible interactions. For instance, Eq. (2.1) could be augmented as shown below,

$$E_{tot}(D) = \underbrace{\overbrace{E_{VDW} + E_{EDL}}^{\text{DLVO}} + E_{bridge}}_{\text{Ji et al. [44]}} + \underbrace{E_{ster} + E_{dep} + E_{hydroph} + E_{hydro} + E_{hydra}}_{\text{Additional interactions to consider}} \quad (2.3)$$

New models have been tested, assuming that the major driving force affecting flocculation is the competition between repulsive interactions (EDL potential) and attractive interactions (VDW and bridging interactions) [44]. Ji et al.'s model modified the DLVO theory to include bridging interactions between functional groups of the polymer and the adsorption sites of the particles (Figure 2.11).

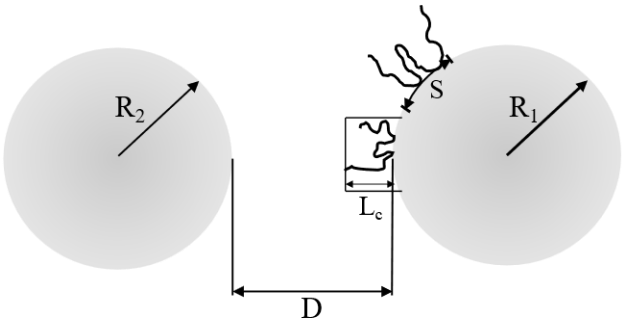

$$E_{bridge}(D) = \beta \frac{4\pi R_1 R_2 \varepsilon}{(R_1 + R_2)s^2} \frac{(L_C D - D^2/2 - L_C^2/2)}{l}$$

Figure 2.11 – Ji et al.'s model to describe polymer-particle and particle-particle interactions. Redrawn from [44].

The novelty of this model lies in the four parameters in the expression of the bridging energy [44]:

- L_C: (Figure 2.11) takes into account the conformation of the adsorbed polymer, which is related to the thickness of polymer's adsorbed layer.
- l: for the segment length, which equals two times the C-C bond length.

- ε: is the bonding energy per segment.
- β: is the percentage of polymer molecules that form effective bridges among all adsorbed polymer molecules.

This model described well the effect of salinity on the flocculation of SiO_2 particles [44] with neutral and ionic polymers [38], accounting for charge neutralization *and* polymer adsorption and conformation.

This model could be supplemented as in Eq. 2.3 with other non-DLVO interactions [51,52]. Since steric interactions (E_{ster}, Eq. 2.3) have to be taken into account when the surfaces of the particles are saturated (optimum concentration for maximum adhesion force). Attractive depletion (E_{dep}, Eq. 2.3) forces that arise from the osmotic pressure between the bulk solution that contains the polymer and the zone free of polymer [53], could also be added to the model. Similarly, hydrophobic interactions ($E_{hydroph}$, Eq. 2.3) affect the polymer dewaterability for MFT treatment [54]. For a representative study, hydrodynamic forces (E_{hydro}, Eq. 2.3) should also be taken into account because they may affect polymer-particle interactions by modifying the probability of collision between them, they may also change the structure of the flocs formed with shear.

Finally, because of the varying mineralogy and age of clay particles in MFT, hydration forces (E_{hydra}, Eq. 2.3) could also be integrated in the model. Clay crystal surface can adsorb water molecules (especially if the solution salinity is high) [35], which can form ordered structures within the solution (hydrate complex) with multiple layers of water molecules adsorbed. Because of the energy required to create a perturbation, a repulsive force (hydration) can be generated [55]. This force should vary from a mineralogy type to another.

Identifying the order of magnitude of each contribution separately with experiments is challenging, which explains the state of the current knowledge. In order to optimize the flocculation, one must understand its mechanism. This is the purpose of the following sections 2.3.3, 2.3.4 and 2.3.5.

2.3.3 Bridging Mechanism

Bridging is the most frequent flocculation mechanism (Figure 2.12.a). It occurs through the simultaneous adsorption of high molecular weight (usually non-ionic) polymers onto multiple particles simultaneously [37,44,56,57]. This is possible because when high molecular weight polymers adsorb on surfaces, they form long tails and loops that extend beyond the electrical double layer of the particles [37,44]. Unfortunately, these same high molecular weight polymers may retain higher water contents in the sediments [58]. As mentioned above, amide functionalities can adsorb on the particle neutral sites through H-bonding – typically aluminol groups. Therefore, the conformation of the polymer on the particle surface – also a function of polymer dosage and solution salinity – affects the overall efficiency of the bridging mechanism.

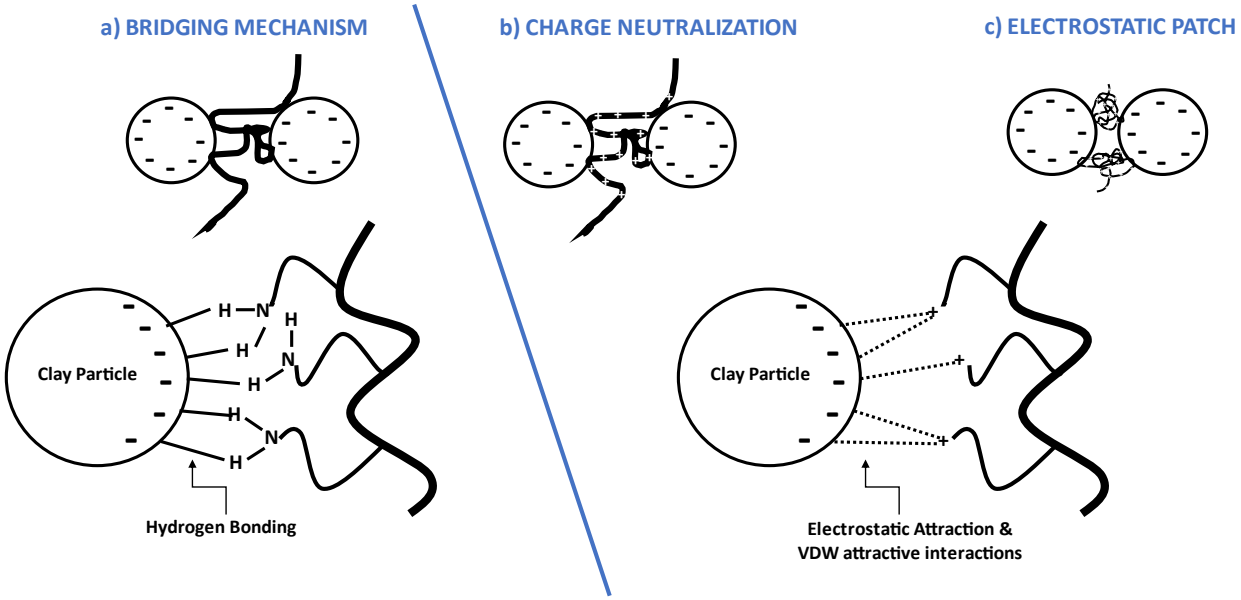

Figure 2.12 – Three main flocculation mechanisms: a) bridging, b) charge neutralization and c) electrostatic patch (redrawn from [37]).

2.3.4 Charge Neutralization

This mechanism can be observed when flocculating negatively-charged particles with a cationic polymer (Figure 2.12.b). The positive charges in the flocculant are attracted to the negative charges of the clay particles (Van Der Walls interactions may also play a lesser role), prevailing over the repulsive interactions. Maximum aggregation happens once the surface potential is zero,

at the isoelectric point, but too much polymer may reverse the surface charges and stabilize the suspension [39,46].

2.3.5 Electrostatic Patch

Low molecular weight cationic polyelectrolytes interact with clay surfaces through the charge neutralization mechanism, but the flocculant cannot cover the surface of the particle because of its low molecular weight (Figure 2.12.c), forming small, localized charge neutralization patches. This mechanism is rarer than the two previous ones, especially since it creates weak interactions that makes fragile flocs [37].

2.3.6 Multiple-Step Flocculation / Coagulation

Since mixing affects the adsorption of flocculants on clay particles, several multiple-step tailings treatment methods have been investigated. It has been shown that sequential coagulation / flocculation processes can outperform a single flocculation step. For instance, a flocculation-coagulation-flocculation sequence can lower the concentration of solids in the recovered water from 1-4 wt. % to 0.13 wt. % [59]. The first addition of an anionic polymer, flocculates the largest particles, while the cationic coagulant destabilizes the fines and forms small flocs. Finally, the second addition of a small amount of anionic polymer flocculant gathers the two types of flocs into larger ones [59]. This addition sequence is particularly efficient in the case of high amounts of suspended solids, for which it is hard to reach mixing conditions that help form large flocs in one flocculation steps. Similarly, adding the same dose of polymer in two separate stages increased settling rate and reduced the total solids content in the supernatant water [60]. As mixing is likely to break shear-sensitive flocs, the second addition is supposed to help re-flocculate them into larger flocs [26,50,60].

2.3.7 Dual Polymer Flocculation

Since the chemical structure and sequences of addition of flocculants affect tailings treatment [59], several researchers investigated the combination of cationic and anionic polymers [61,62,63,64,65]. For example, the cationic polymer polydiallyldimethylammonium chloride (polyDADMAC) was used sequentially with the anionic partially hydrolyzed polyacrylamide (HPAM) to treat mature fine tailings, leading to lower CSTs and higher final filtrate volumes than those made with a single polymer [61]. The cationic flocculant brings fine particles together and forms small flocs, while the anionic polymer further aggregates the fine particles and the small flocs into larger porous flocs [62] that are easier to dewater since the pores act as water channels during filtration [61,62]. Dual polymer treatment on pure kaolinite suspensions also led to shorter CSTs filter cake with higher solids contents, and faster and higher net water releases [63].

Residual bitumen complicates the treatment of MFT because it might coat the clay particles surfaces, modifying the properties and number of polymer adsorption sites. When bitumen is added to kaolinite suspensions (used to model MFT), higher flocculant dosages are needed for the same performance [63]. The sequential use of lignosulfonate and an anionic polymer is a solution to this problem because lignosulfonate interacts with bitumen, allowing for better fines removal at fast settling rates [64].

Some recent studies suggest that the behavior observed with MFT at high solids contents is not only due to different mixing conditions. Zhou et al. introduced the notion of sand to fine ratio (SFR) [65]. Once again, they observed a synergy between dual polymers wherein the loose and extended flocs made with the high molecular weight anionic polymer and suspended fines were consolidated by the small cationic polymer through strong electrostatic attraction with fines and the large anionic polymer. They also showed that increasing the SFR from 0.1 to 1.5 reduced the required polymer dosage [65]. They proposed that coarse sands acted as *"cores"* carrying and increasing the density of the loose flocs, while reducing the amount of entrapped water. Usually, the maximum achievable solids content is limited because fine clays gel in *"house-of-cards"* structures [40]. But with this approach, the positively-charged cores weaken the repulsion among the neighboring segments and fine solids. The short cationic chains capture the fines and their interaction with the long anionic chains allows for the formation of denser flocs [65].

2.4 Polymeric Flocculants

2.4.1 Synthetic and Natural Copolymer Flocculants

Flocculation performance improved greatly since the early ages of synthetic flocculants in the 50s [40]. Their microstructures have been tailored (molecular weight, ionic charge and charge density, configuration, hydrophobicity etc.) to meet the requirements of a specific application. Anionic polyacrylamide is the most used flocculant [66], but the flocs formed with this polymer are shear sensitive, which may cause problems when they are pumped through pipelines; the flocs may break irreversibly, seriously decreasing the efficiency of this flocculant. Anionic PAMs also do not dewater the sediments well and capture the fines efficiently [26].

Some cationic polymers, such as poly[(vinylbenzyl)trimethyl ammonium chloride] (PVBTMAC) [67,68] or polydiallyl dimethyl ammonium chloride (PDADMAC) [69], have been developed to capture fines better than anionic flocculants. They dewater undiluted MFTs faster and form sediments with higher shear strength than commercial anionic PAMs [69], but they also must be used at significantly higher dosages than anionic PAMs of similar molecular weights [69].

Hybrid polymers have also been produced to capture more fines and make denser sediments that retain less water than PAM [26]. Inorganic-organic hybrid polymers can improve the flocculation of fines due to interactions between microparticles and polyelectrolytes [70]. Temperature sensitive polymers such as poly(N-isopropylacrylamide) (PNIPAM) induce polymer bridging or hydrophobic attractions, depending on the flocculation temperature: the polymer conformation changes from extended coils (hydrophilic) to globular (hydrophobic) above the LCST [26].

Due to environmental concerns, there is also an emerging interest in bio-based flocculants such as cellulose, chitosan or starch derivatives [66]. These natural polymers have a more rigid structure and cost less than synthetic polymers. Starch derivatives can be modified with vinyl monomers grafts [71], but they are biodegradable, which limits their shelf lives and require high dosages [66]. Their backbones can be modified by attaching branches to change their chemical or physical properties [72].

2.4.2 Graft Copolymers

Comb-like structures help polymer adsorption on clay particles and, consequently, improve the flocculation performance [48]. Natural polymers can be used as backbones onto or from which synthetic polymer grafts can grow by three methods: 1) *grafting from* active sites on the backbone, 2) *grafting to* the backbone chains that contain terminal active sites, or 3) *grafting through* [73]. The simplest synthesis method is grafting from via free radical. In this case the synthetic polymer chains grow from active sites previously generated on the natural polymer backbone (Figure 2.13) [73,74].

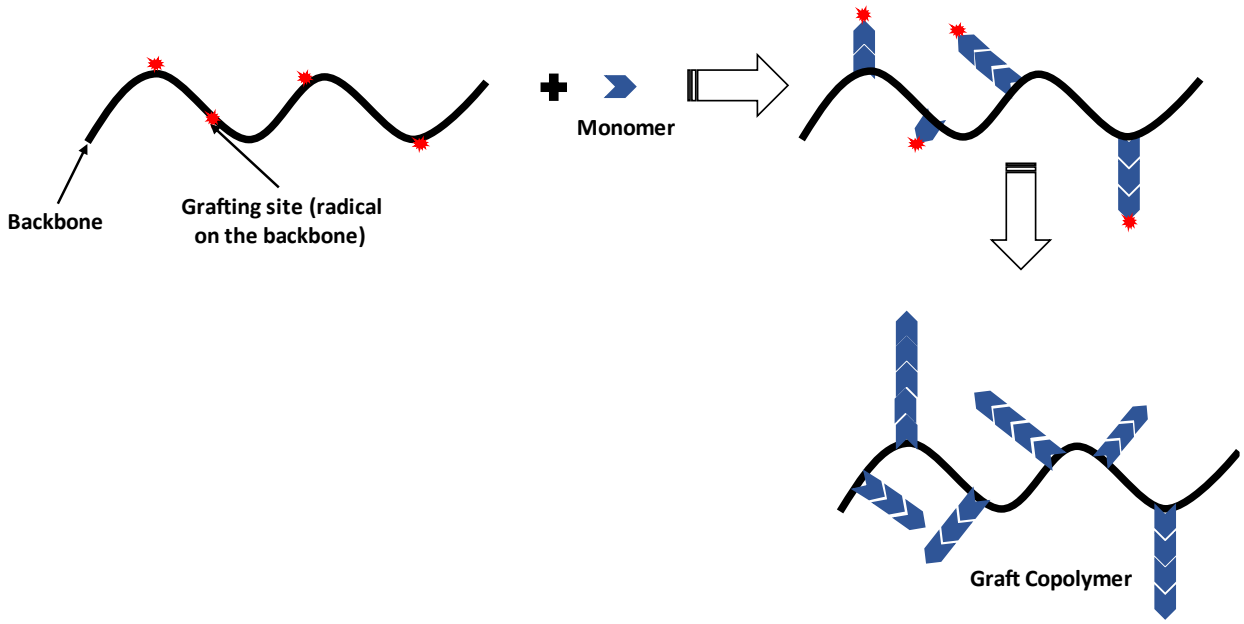

Figure 2.13 – Grafting from mechanism (redrawn from [74]).

The backbone active sites can be generated with free radical initiators, redox systems, enzymes, or radiation [75,76]. The better flocculation performance of these natural grafted polymers – compared to synthetic polymers – is attributed to their ability to form shear resistant flocs and to expel water thanks to their rigid and hydrophobic backbones [77]. The advantage of high molecular weight polymers lies on their ability to adsorb onto multiple particles through their extended long chains. The backbones of grafted polymers do the same, while the dangling grafts approach colloidal particles easily (Figure 2.14), thus forming a strongly bridged 3D network [78]. This can be interpreted in terms of extended radius of gyration and hydrodynamic volume available for the flocculation in the case of grafted polymers [79].

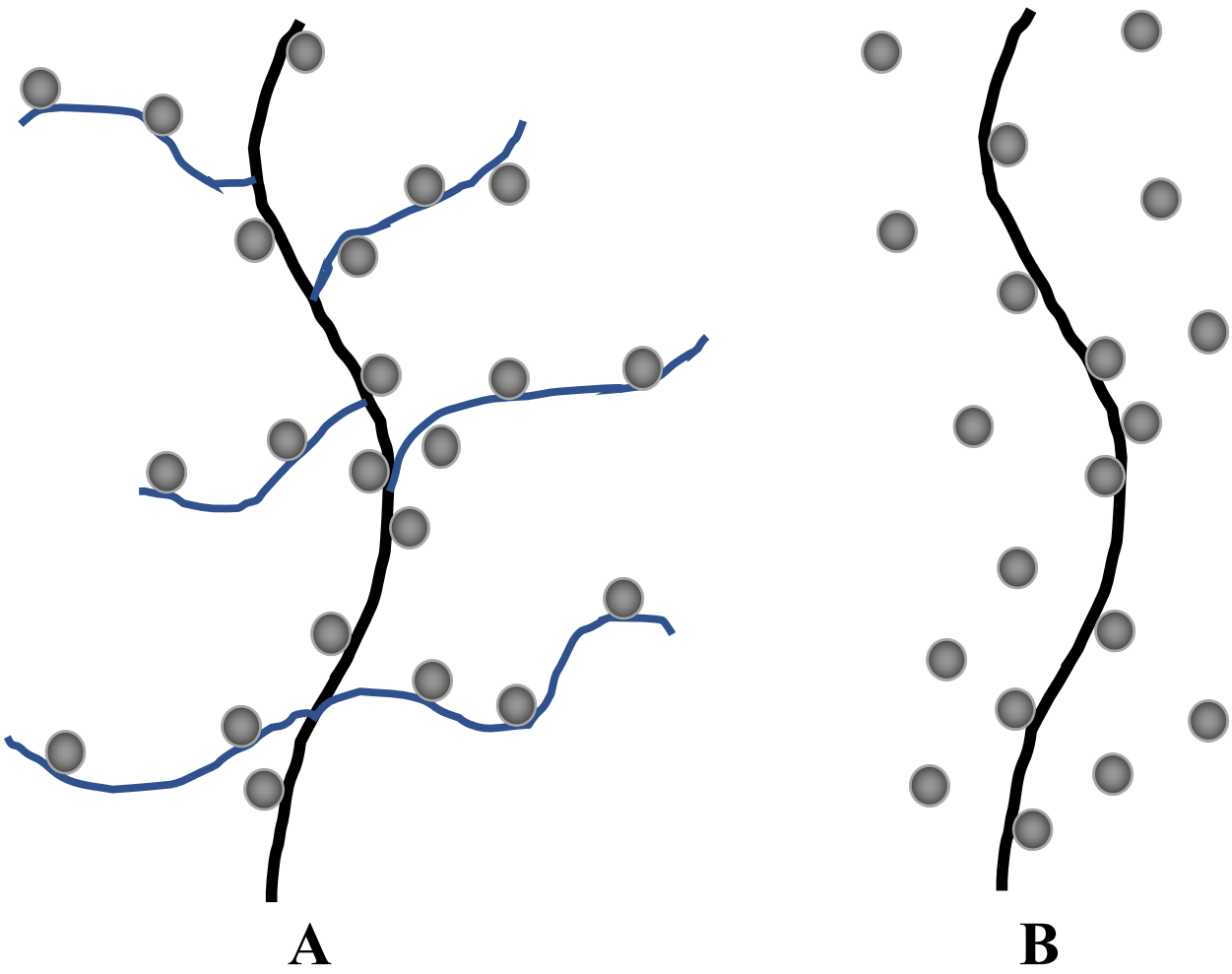

Figure 2.14 – Flocculation approach for graft (A) and linear (B) polymers (redrawn from [78]).

2.4.3 Amylopectin Graft Copolymers

Among the polysaccharides, starch shows key advantages such as easy modifications using vinyl monomers and superior flocculation performance [71]. Starch is abundant in nature (found in roots, fruits or stems [80]) and is usually composed by ~ 25 % amylose and ~ 75 % amylopectin depending on the source [81]. These two polymers are made of anhydroglucose units (AGU) [71]. Amylose (AS, Figure 2.15.A) is a linear and amorphous polymer composed by repeating glucose units with α-1,4 glycosidic linkages while amylopectin (AP, Figure 2.15.B) is a crystalline and branched polymer made of repeating glucose units with α-1,4 glycosidic and α-1,6 glycosidic linkages for every ~ 30 glucose units [81].

Because of the hydrophobic backbone of amylopectin (AP), it loses water more easily than polyacrylamide (PAM) [72]. It has also been reported that amylopectin graft copolymers (AP-g-PAM), substantially outperformed amylose graft copolymers thanks to the higher molecular weight of amylopectin (50-1000 kg/mol) when compared to amylose (10-60 kg/mol) [72]. Amylose is not water soluble, unlike AP which is water soluble above 90 °C. However, AP was reported to be retrograded if left for a long time in solution [83].

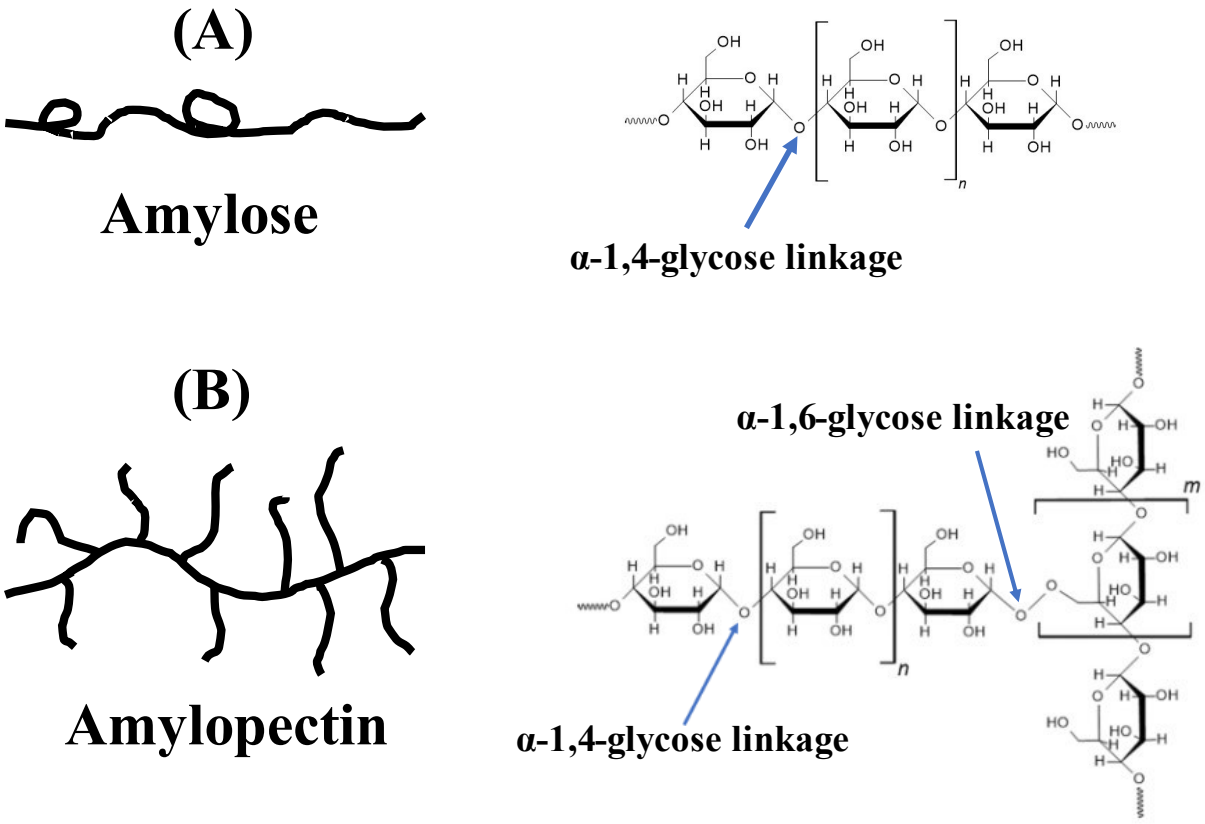

Figure 2.15 – Amylose (A) and amylopectin (B) [82].

Several investigations studied the effect of grafting different monomers to amylopectin. One of the first goes back to 1997: Rath and Singh compared how different grades of amylopectin-graft-polyacrylamide (AP-*g*-PAM) flocculated clay suspensions [72]. They performed jar tests on kaolin suspensions with varying monomer and catalyst amounts. The initiator used was the redox ceric ammonium nitrate (CAN). They concluded that the optimum flocculant had the lowest graft frequency and the longer grafted PAM chains [72]. Sarkar et al. investigated the use of amylopectin-graft-poly (acrylic acid) (AP-*g*-PAA) for Fe-ore, kaolin and mining industry

wastewater [84]. They synthesized AP-*g*-PAA using potassium persulfate (KPS) as initiator. They found that the flocculant with the highest hydrodynamic radius was the best, corroborating other studies on flocculation mechanism [79].

Years later, amphoteric amylopectin graft polymers were produced by partial base hydrolysis of AP-*g*-PAM followed by a cationization with microwave-assisted method [85]. This amphoteric polymer flocculated kaolin and iron ore suspensions efficiently [85], suggesting that cationic charges on the grafts helped flocculate negatively charged colloidal suspensions. Kumar et al. [86], synthesized cationic and amphoteric flocculants (AP-*g*-C and AP-AT-C) with acrylamide and (3-acrylamidopropyl) triethylammonium chloride (ATMAC) grafts onto amylopectin using ammonium persulfate as free radical initiator. They concluded from their flocculation tests on kaolin suspension at neutral pH that cationic polymers favored the bridging mechanism while amphoteric polymers favored electrostatic interactions, which contradicted other studies on kaolin suspension flocculation with cationic flocculants. For instance, Chen et al. [87] showed that electrostatic interaction is the dominant mechanism for the adsorption of cationic starch on kaolin, with a temperature dependent adsorption on the kaolin surface following Langmuir isotherm ($R^2 > 0.99$) [87], which also confirmed the previous studies showing that surface coverage was dependent on polymer's conformation and so its hydrodynamic volume [79]. They concluded that higher concentration of cationic units improved the approachability of the flocculants because of longer grafts, thus forming bigger flocs that settle faster. They also mentioned that a high charge density could be detrimental to the flocculation performance because of the repulsive interactions among the polymer chains [87].

Our group focused on the application of this graft flocculants for MFT treatment, Bazoubandi et al. [88] showed that AP-*g*-PAM formed sediments with higher solids content than commercial polyacrylamides and attributed this enhancement to the amylopectin hydrophobic core, since the hydrophilicity of PAM grafts is one of the known weaknesses of commercial polyacrylamides. Unfortunately, these polymers could not achieve complete fines capture (hence poor supernatant water quality) and they form large shear sensitive flocs [26,83]. Moreover, clay particles may be coated with bitumen which will significantly decrease the interactions of PAM with MFT clays [89]. More recently, Davey et al. [83] synthesized amylopectin-graft-hydrolyzed-poly (methyl acrylate) (AP-*g*-H-PMA). Polymers with longer chains and lower grafting densities were found to have superior performance. AP-*g*-H-PMA outperformed commercial anionic

polyacrylamide and AP, HPMA homopolymers. Interestingly, no negative effects of overdosing were observed in the dosage range tested [77]. However, this work still required the addition of multivalent cations as coagulant for the subsequent flocculation to happen.

Based on these previous works, amylopectin can be used as an effective backbone for graft copolymerization since some of its graft derivatives are more efficient than some commercial flocculants. However, few publications dealt with the grafting of cationic synthetic polymers to avoid the undesired addition of multivalent cations as coagulant, and to address the uncomplete fines capture of currently used polymers. It has also been observed that flocculants hydrophobicity was a key parameter for water expulsion within the flocs [69]. Consequently, (vinylbenzyl)trimethylammonium chloride (VBTMAC) is a great cationic graft candidate because of its hydrophobic pendant benzene ring. This monomer is water soluble and can easily be polymerized until high molecular weight by free radical polymerization. Moreover, it polymerizes faster than the commonly used diallyl dimethyl ammonium chloride [69].

Therefore, this work will focus on the synthesis and the application to MFT treatment of the cationic and partially hydrophobic natural graft polymer: amylopectin-graft-poly((vinylbenzyl)trimethylammonium chloride)).

However, previous publications also showed that operating conditions were key to the flocculation process as well as the use of the synergy effect of a simultaneous use of cationic and anionic polymers.

Consequently, the second part of this project is dedicated to the systematic study of addition flowrates impact on the dual flocculation of kaolin suspensions with amylopectin-graft-poly((vinylbenzyl)trimethylammonium chloride)) and the commercial anionic and high molecular weight polyacrylamide MAGNAFLOC ® 1011.

3. Materials and Methods

3.1 Materials

Powdered amylopectin (AP) from maize, (vinylbenzyl)trimethylammonium chloride (VBTMAC) (99 %) and acrylamide (≥ 99 %), potassium persulfate (KPS) free radical initiator (≥ 99 %), toluene (99.9 %), acetone (99.9 %), and kaolinite were purchased from Sigma-Aldrich. Dilute MFT and kaolinite suspensions were prepared with deionized (DI) water. A commercial anionic polyacrylamide (HPAM), MAGNAFLOC® 1011 (MW ~ 10^7 g/mol) from BASF was used in some of the flocculations.

3.2 MFT Sample Characterization

3.2.1 Dean-Stark Extraction

A Dean-Stark apparatus was used to measure the water, solids and residual bitumen contents of the MFT sample (Figure 3.1). The apparatus includes: an electric heater, a long neck round bottom flask, a 100 mL Dean-Stark trap and a water-cooled condenser. A mass of about 125 g of MFT was weighed into a 123 mm (length) × 43 mm (internal diameter) extraction thimble. Approximately 350 mL of toluene was added into the round bottom flask to evaporate all the water in the MFT sample with boiling toluene. After adding toluene, the extraction thimble containing the MFT sample was placed in a metallic basket located at the long neck portion of the apparatus. The rest of the apparatus was then assembled with grease to ensure thermal insulation. The temperature of the electric heater was set above the boiling point of toluene (T > 111°C). Under these conditions, the toluene evaporated and diffused through the extraction thimble where it evaporated the water in the MFT sample. Water and toluene vapors rose to the condenser and dropped into the trap after being cooled and condensed.

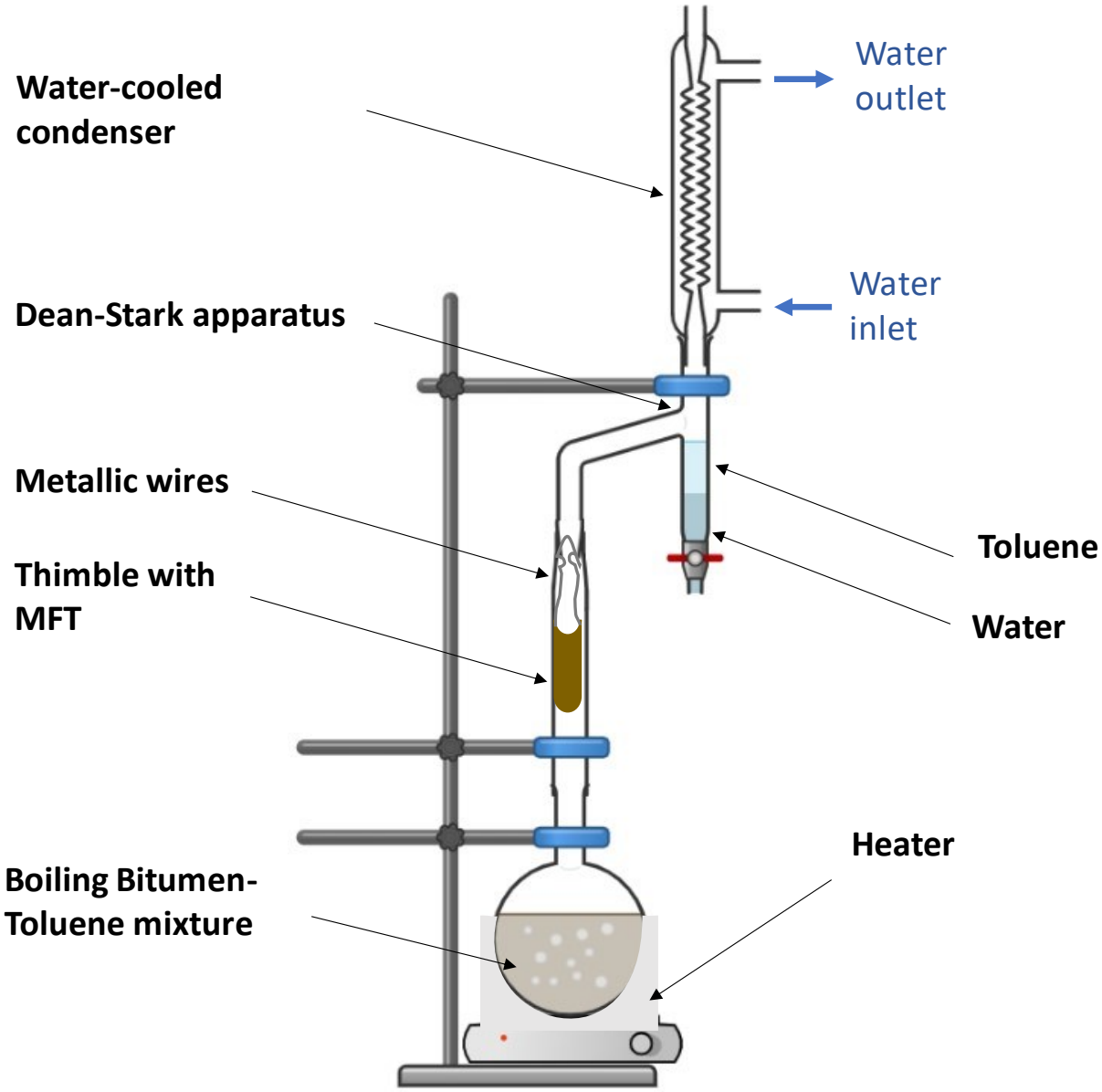

Figure 3.1 - Dean-Stark apparatus diagram.

Water and toluene are immiscible. Water is denser and reaches the bottom while toluene remains on the top of the trap. Thanks to this difference, water can be drained while toluene remains in the system, eventually overflowing and dropping back to the round bottom flask. Toluene also dissolves bitumen from the MFT sample.

The apparatus was operated until the water level stabilized with the toluene in the trap becoming colorless and having a distinct interface with the water phase. The water phase was then drained from the trap and weighed. The extraction thimble was placed in a vacuum oven and left

to dry for 24 hours at 50 °C. The brown toluene-bitumen mixture in the round bottom flask remained under heating (without the condenser) to fully evaporate the toluene in the fume-hood. Finally, the dry solids in the extraction thimble and the residual bitumen in the round bottom flask were weighed. This extraction procedure was repeated three times.

3.2.2 Inductively Coupled Plasma-Optical Emission Spectroscopy (ICP-OES)

Inductively coupled plasma-optical emission spectroscopy (ICP-OES) was used to measure the concentration of the major cations (Na^+, K^+, Mg^{2+} and Ca^{2+}) in the MFT sample. We chose ICP-OES over atomic absorption spectrophotometry (AAS) because we needed to analyze several elements simultaneously. ICP-OES is more sensitive than AAS in the concentration range (1 to 1000 ppm) of ions found in MFT process water [90,91].

The MFT sample was centrifuged at 4200 rpm for 20 min and then filtered with a press filter at 10 psig for 30 minutes with a grade 5 (2.5 - 5 μm pore size) Whatman filter paper to collect the MFT process water. Multi-element certified standard solutions purchased from SCP Scientific were used for calibration, and separate certified multi-element solutions were used as external reference standards. A Thermo iCAP6300 Duo ICP-OES unit from Thermo Fisher was used to measure the cations in the process water from the MFT sample used in this project.

3.2.3 Particle Size Distribution (PSD)

The particle size distribution (PSD) was estimated with a Malvern Mastersizer 3000, using Mie scattering theory to compute the volume and number PSDs. Three runs were carried out before and after sonication – with five measurements per run – to ensure that the results were statistically valid. The sonication step helps achieve a stable PSD by breaking up weak particle agglomerates that may exist in heterogeneous systems such as MFT.

3.2.4 X-Ray Diffraction (XRD)

X-Ray powder diffraction (XRD) analysis was done with a Rigaku Ultima IV diffractometer to identify the crystalline phases in the MFT sample. The reference intensity ratio (RiR) provided an estimation of the semi-quantitative phase analysis. As a reference, the same analysis was done on the kaolinite purchased from Sigma-Aldrich.

3.3 Polymeric Flocculant Characterization

3.3.1 Synthesis of Amylopectin-*graft*-poly[(vinylbenzyl)trimethylammonium chloride] (AP-*g*-PVBTMAC)

The synthesis of AP-*g*-PVBTMAC followed the (slightly modified) procedure proposed by Bazoubandi and Soares [88]. The reaction scheme is presented in Figure 3.2.

Knowing that the molecular mass of amylopectin (AP) is determined based on the molar mass of anhydroglucose (AGU, 162.15 g/mol), the required amount of AP was dissolved in DI water under constant stirring (300 rpm, magnetic stir bar) in a 250 mL round bottom flask under reflux at 90°C in an oil bath for 20 minutes. This high temperature step dissolved the AP in the reacting medium, which could be observed once the solution became transparent. The system was then sealed with a rubber septum and purged with N_2 at 70°C under continuous mixing for 40 minutes to eliminate dissolved O_2, which acts as a radical poison. During the AP purge step, the desired mass of VBTMAC was dissolved in DI water in a 250 mL Erlenmeyer flask under continuous mixing at room temperature. The KPS (free radical initiator) solution was also prepared in DI water. The KPS and VBTMAC solutions were purged with N_2 for 20 minutes at room temperature. The KPS solution was then injected into the AP solution through a needle and allowed to react for 20 minutes.

As KPS decomposed in the range of 50-60 °C [83,84,88], its primary radicals abstracted hydrogen atoms from the AP backbones, forming active grafting sites (macroradicals) [92]. After the 20 minutes pre-contact time, the purged VBTMAC solution was added to the flask to react with the newly formed macroradicals. The N_2 purge was then stopped. This reaction proceeded overnight at 70 °C and at a constant mixing rate of 300 rpm to reach maximum conversion.

The mixture was then cooled and the reaction stopped by exposing it to air. The resulting viscous mixture was precipitated and washed with acetone (3:1 acetone by volume) to remove unreacted monomer. No further product purification was carried out to separate the PVBTMAC homopolymer from the grafted AP-g-PVBTMAC, since this step would make the synthesis too complex for commercial application. The product was placed in a vacuum oven to evaporate the excess of acetone and then left to dry in a freeze-dryer overnight.

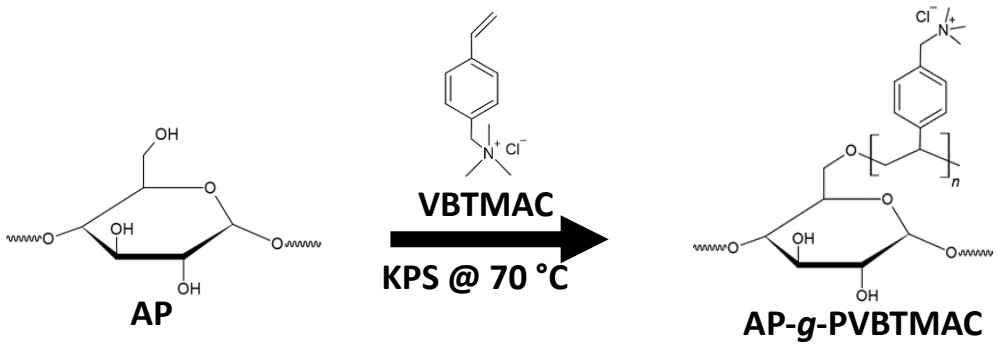

Figure 3.2 – Overall chemical reaction involved in the synthesis of AP-*g*-PVBTMAC.

Since we did not measure conversion and did not purify the product, the grafting parameters were defined based on the work of Bazoubandi and Soares [88]:

- The average length of the grafts is proportional to the ratio of the monomer concentration (VBTMAC) to the square root of the initiator (KPS):

$$< Graft\ Length > \propto \frac{[VBTMAC]}{\sqrt{[KPS]}} \tag{3.2}$$

- The average graft frequency is related to the ratio of the initiator concentration to the amylopectin (AP) concentration:

$$< Graft\ Frequency > \propto \frac{[KPS]}{[AP]} \tag{3.1}$$

3.3.2 Fourier-Transform Infrared Spectroscopy (FTIR)

We used Fourier-transform infrared spectroscopy (FTIR) to find out if VBTMAC chains were grafted to the AP backbones. The main absorption peaks of both VBTMAC and AP were identified and then compared to the FTIR spectrum of AP-g-PVBTMAC using an Agilent Technologies Cary 600 Series FTIR in the mid-IR region from about 4000-400 cm^{-1}. The attenuated total reflectance technique was used for the spectral analysis and each sample was scanned with 30 runs.

3.3.3 Gel Permeation Chromatography (GPC)

The molecular weight distributions of the polymers were measured with an Agilent Technologies 1260 Infinity gel permeation chromatography (GPC) unit equipped with in-line triple detection: a differential refractometer, a viscometer, and a two angle (15 and 90°) light scattering detector. GPC is widely used to measure the molecular weight distributions of polymers and was chosen for its speed of analysis and its high replicability [93].

GPC fractionates polymers according to their hydrodynamic volumes. This separation mechanism may be problematic for branched polymers, since they might elute at the same retention volume (same hydrodynamic volume) with linear polymers of lower molecular weights [93,94,95,96], but in-line triple detection ensures that the measurements are relevant. Ten PEO standards from 21,000 g/mol to 1,000,000 g/mol were used to make the universal calibration curve. A solution of 1 mg/mL of polymer was then prepared and injected (100 μL) in the GPC apparatus. The mobile phase used for all the analyses was a solution of 0.3 M sodium sulfate, 0.05 M acetic acid and 0.002 M sodium acetate. The measurements were set to run for 40 minutes with sampling every second.

3.4 MFT Flocculation with AP-*g*-PVBTMAC

3.4.1 Sample Preparation

All flocculations followed the same procedure. The original MFT sample was mixed with an anchor-type agitator (900 rpm, 4 min) linked to a RW 20 overhead stirrer from IKA. This type of mixing agitator minimizes dead zones and increases recirculation at the walls of the MFT bucket [97]. The desired weight of MFT was then sampled at the bottom of the bucket and diluted with deionized (DI) water to 10 wt.% solids in a 250 mL glass beaker. The diluted MFT was mixed at 600 rpm for 1 minute and then 300 rpm for another 1 minute with a Heidolph Hei-Torque Precision 200 Overhead Stirrer and a four-blade impeller (Figure 3.3). The flocculant was then injected into the mixture with a 25 mL syringe (Figure 3.3) and the sample was stirred for a minute at 300 rpm. Flocculation metrics (discussed in sections 3.4.3 to 3.4.6) were done immediately after this step.

Flocculations were done with different polymer dosages: 666, 1333, 2666, 4000, 5333, 6666, 8000 and 10000 ppm on a weight basis relative to the MFT solids (mg of polymer per kg of MFT solids). The concentration of the polymer solution was 2 mg/mL. The total mass of each experiment was 150 g. Therefore, the higher the polymer dosage, the less DI water was added to the MFT to reach a same dilution target of 10 wt. %.

The same sample preparation process was followed to flocculate kaolinite suspensions. In this case, the pH was adjusted to 7.9 (measured pH of the given MFT sample) and the solids content was adjusted to match that of the MFT sample.

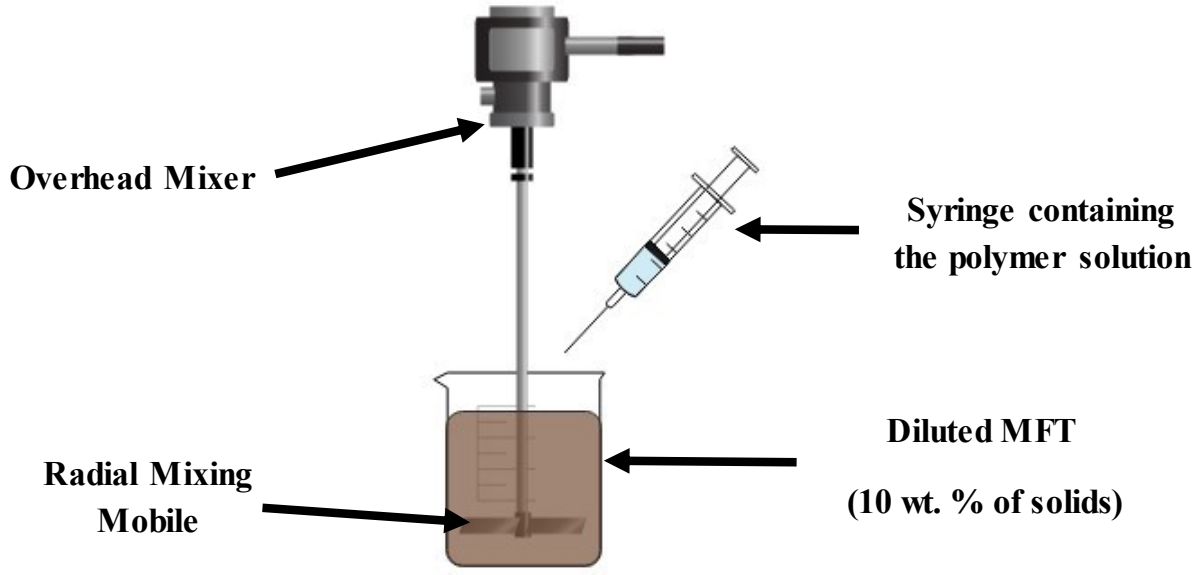

Figure 3.3 – Typical benchtop setup used for flocculation.

3.4.2 Screening Tests Design

Screening tests were performed to identify the impact of graft length, graft density, and polymer concentration on the flocculation of 10 wt. % MFT with AP-*g*-PVBTMAC. Table 3.1 lists the polymers synthesized for this screening test design (Figure 3.4). We tested eight dosages (666, 1333, 2666, 4000, 5333, 6666, 8000 and 10000 ppm) for each polymer and compared the initial settling rate (Section 3.4.4), initial capillary suction time and sediment capillary suction time (Section 3.4.3), supernatant turbidity (Section 3.4.5), and solids content (Section 3.4.6). The homopolymer PVBTMAC and AP-PVBTMAC blend were also tested under the same conditions

as references, to assess the influence of the grafting onto the amylopectin backbone on the flocculation.

Table 3.1 – Polymers flocculants synthesized for the screening tests.

No.	AP-g-PVBTMAC	AP (mol AGU /L)	KPS (mol/L)	VBTMAC (mol/L)	AP* (wt.%)	[I]/[AP]	Graft Frequency	[VBTMAC]/[I]$^{0.5}$	Graft Length
1	F_4L_1	*0.04*	4×10^{-4}	*0.3*	*9.27*	*0.010*	F_4	*15*	L_1
2	F_4L_2	*0.04*	4×10^{-4}	*0.5*	*5.77*	*0.010*	F_4	*25*	L_2
3	F_4L_3	*0.04*	4×10^{-4}	*0.7*	*4.19*	*0.010*	F_4	*35*	L_3
4	F_4L_4	*0.04*	4×10^{-4}	*0.9*	*3.29*	*0.010*	F_4	*45*	L_4
5	F_4L_5	*0.02*	2×10^{-4}	*0.7*	*2.16*	*0.010*	F_4	*49.5*	L_5
6	F_1L_3	*0.2*	4×10^{-4}	*0.7*	*17.9*	*0.002*	F_1	*35*	L_3
7	F_2L_3	*0.09*	4×10^{-4}	*0.7*	*8.96*	*0.004*	F_2	*35*	L_3
8	F_3L_3	*0.06*	4×10^{-4}	*0.7*	*6.16*	*0.007*	F_3	*35*	L_3
Homo PVB+	*X*	*/*	4×10^{-4}	*0.7*	*/*	*/*	*/*	*/*	*/*

** Weight Percent of Amylopectin with respect to the total mass of AP and VB+ used in the polymerization*

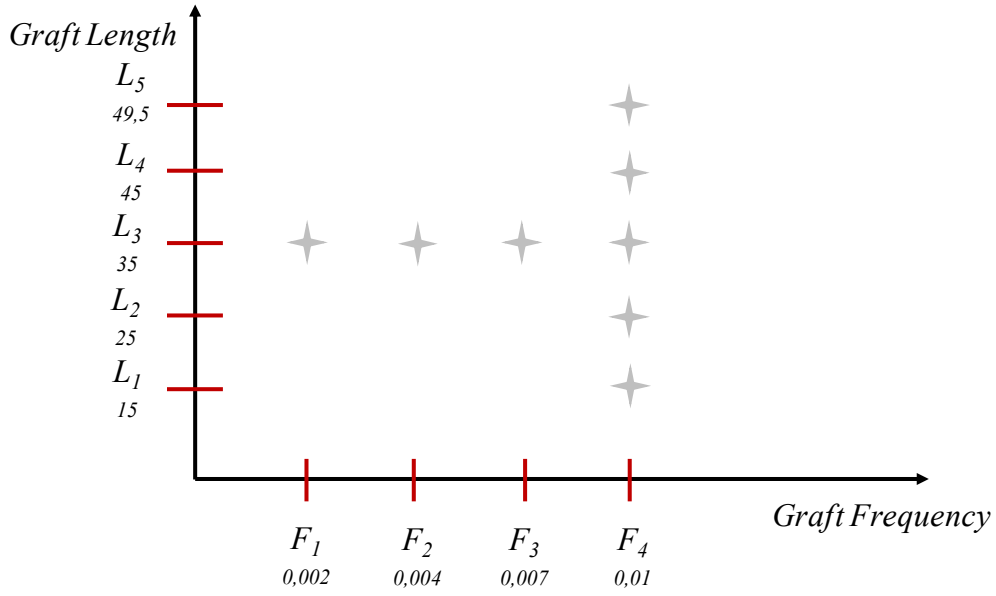

Figure 3.4 – Screening test design: F_x is the graft frequency, and L_y is the graft length.

3.4.3 Initial and Sediment Capillary Suction Time (CST)

Capillary suction time (CST) was used to measure the dewatering ability of the flocculant by measuring the time required for the water expelled from the sediments to flow (via capillary action) from one electrode to another (Figure 3.5). Cylinders ensure the concentrical flow (same path in all 2-D directions) on the filter paper. A Triton Electronics Meter Type 319 multipurpose CST instrument, 7 cm x 9 cm Triton filter paper and small metallic cylinders were used. The test was repeated four times for two different runs of the same polymer dosage on initial flocs and consolidated solids (sediments) after 24 hours of settling.

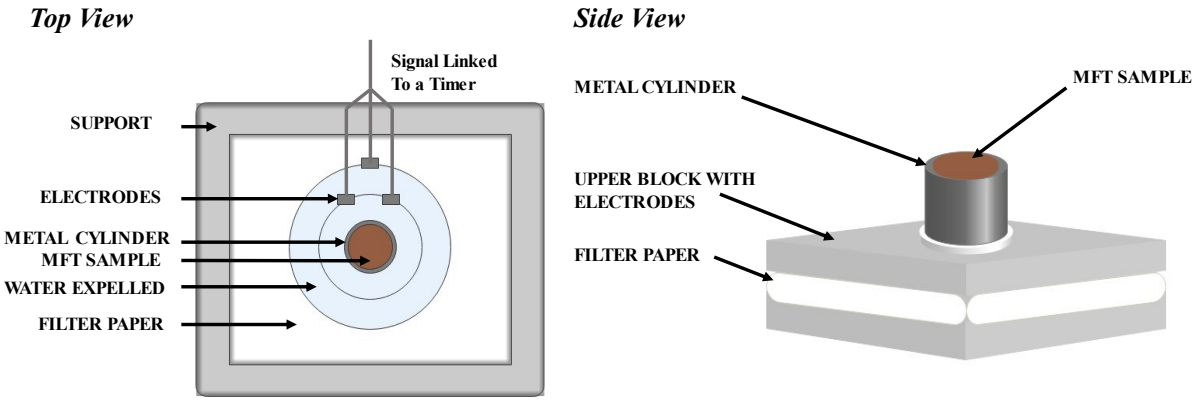

Figure 3.5 – CST apparatus (redrawn from [83]).

3.4.4 Initial Settling Rate (ISR)

The initial settling rate (ISR) was measured by transferring about 100 mL of flocculated slurry into a graduated cylinder. The cylinder was sealed with parafilm and inverted twice to ensure that the beginning of the settling was measured as the chronometer started. Flocs where then allowed to settle under gravity for one hour. The height of the descending mudline (Figure 3.6) was measured each 2 minutes for the first 10 minutes, then each 5 minutes from 10 to 30 minutes, and finally each 10 minutes until one hour. The ISR was calculated from the initial slope of the mudline height versus time curve. After one hour, the sample was left to consolidate for 24 hours.

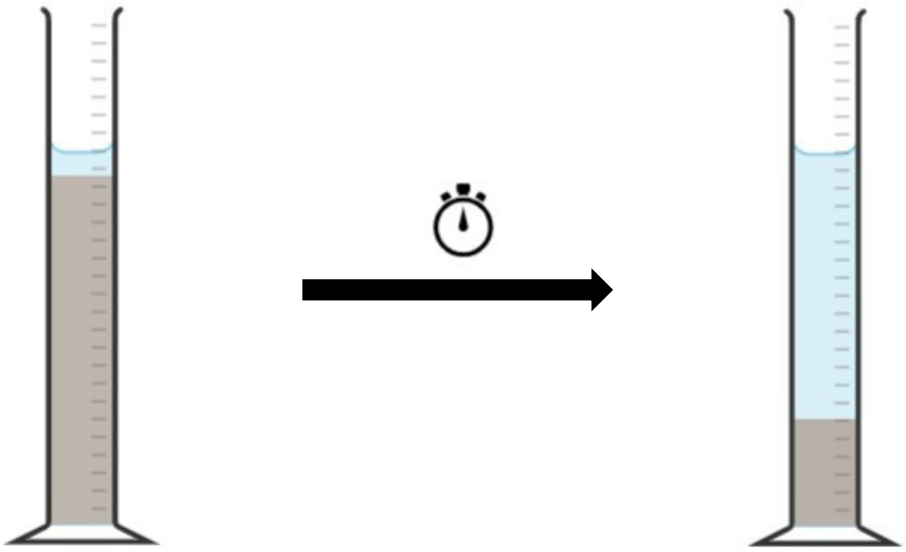

Figure 3.6 – Representation of the descending mudline with time.

3.4.5 Supernatant Turbidity

Supernatant turbidity was used to quantify the quality of the water released from the flocs and the ability of the polymer to capture fines. It is measured in nephelometric turbidity units (NTU). The higher the transparency of the sample, the lower the turbidity (Figure 3.7). Low supernatant turbidity is required for efficient water recovery and recycling. Supernatant turbidity was measured immediately after flocculant addition, after 24 hours or one week of settling.

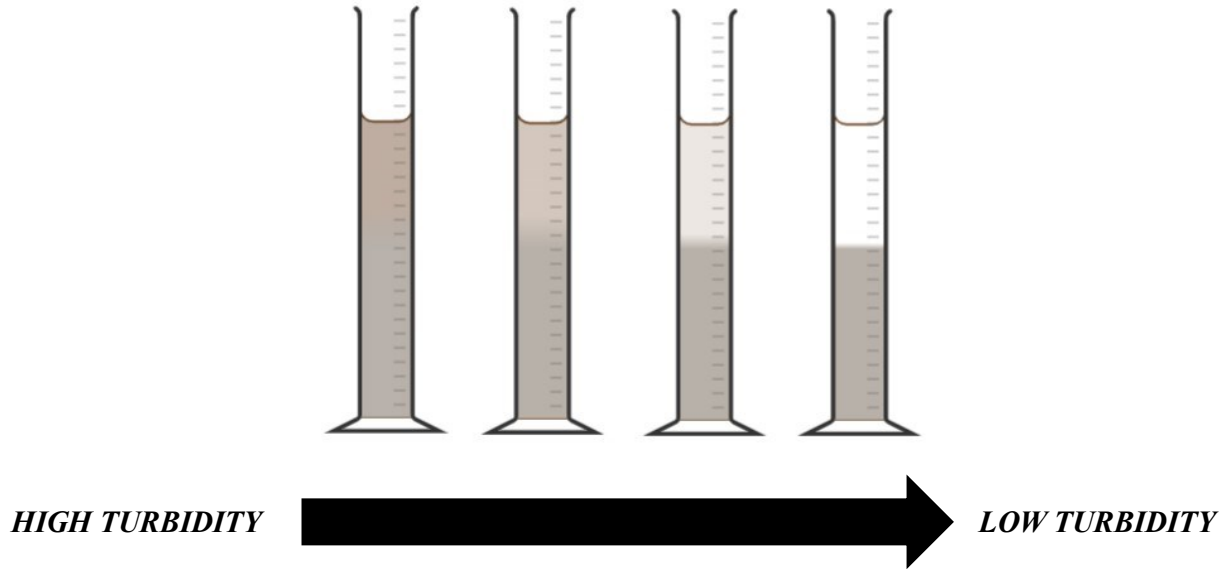

Figure 3.7 – Graphic image of supernatant turbidity evolution.

The turbidity was measured with a HACH 2100N laboratory turbidimeter. Since the instrument is calibrated for 50 mL vials, but the volume recovered in most of the experiments was lower than 50mL, we established a calibration curve for 15 mL vials (Figure 3.8). The measurements were repeated three times for each point to estimate the standard error on one measurement (for detailed measurements see Table A1).

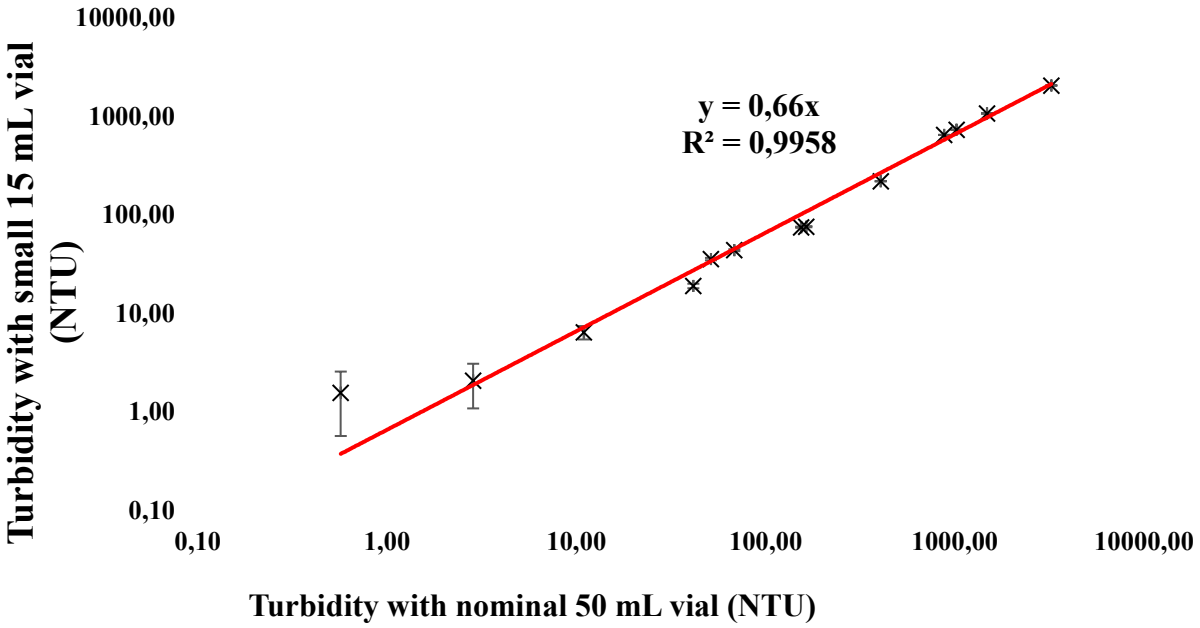

Figure 3.8 – Calibration curve: supernatant turbidity measurement with nominal 50 mL vial versus small 15 mL vial in log scale.

3.4.6 Sediment Solids Content

Once the supernatant had been removed, the sediment CST and the solids content were measured.

To measure the solids content, approximately 5 mL of wet sediment was sampled from the graduate cylinder and placed into aluminium foil container (previously weighed) and weighed before being dried for 24 hours in a vacuum oven at 50°C. The dry solids (plus the container) were then weighed, so that the solids content could be estimated according to the following equation,

$$Solids\ Content\ (\%) = \frac{dry\ weight - container\ weight}{wet\ weight - container\ weight} \times 100 \quad (3.3)$$

This process was repeated three times for each sample (total of six measurements per dosage for the solids content of a given sample).

3.5 Dual Polymer Flocculation

3.5.1 Synthesis and Testing of Amylopectin-*graft*-poly[(vinylbenzyl)trimethylammonium chloride]-co-polyacrylamide (AP-*g*-PVBTMAC-co-PAM)

The synthesis followed the procedure described in Section 3.3.1, with acrylamide (Am) following the same steps as the other monomer VBTMAC. The following reactivity ratios were taken for PVBTMAC-co-PAM: r_{VBTMAC} = 2.48, r_{Am} = 0.46 (Vajihinejad, [98]). The monomer fractions in the reactor were determined based on the copolymer fractions predicted with the Mayo-Lewis equation (Eq. 3.4), assuming low conversions to neglect composition drift.

$$F_{VBTMAC} = \frac{r_{VBTMAC} f_{VBTMAC}^2 + f_{VBTMAC} f_{Am}}{r_{VBTMAC} f_{VBTMAC}^2 + 2 f_{VBTMAC} f_{Am} + r_{Am} f_{Am}^2} \quad (3.4)$$

To simplify the approach, the average graft length was considered as proportional to the ratio of the sum of Am and VBTMAC concentrations to the square root of the concentration of the initiator. The graft frequency definition remained the same (Eq. 3.1).

$$< Graft\ Length > \propto \frac{[VBTMAC] + [Am]}{\sqrt{[KPS]}} \quad (3.5)$$

Table 3.2 summarizes the properties of all graft copolymers. They were tested under the same conditions described in Section 3.4.2.

Table 3.2 – Random copolymers grafts test design.

No.	AP-g-PVBTMAC-co-PAM	AP (mol AGU / L)	KPS (mol/L)	VBTMAC (mol/L)	Am (mol/L	F_{VBTMAC}	[I]/[AP]	Graft Frequency	[Total Monomers]/[I]$^{0.5}$	Graft Length
1	F_1L_1	0.04	4×10^{-4}	0.2	2	0.4	0.010	F_1	110	L_1
2	F_1L_2	0.04	4×10^{-4}	0.1	0.38	0.6	0.010	F_1	24	L_2
3	F_1L_3	0.04	4×10^{-4}	0.1	2.88	0.2	0.010	F_1	149	L_3
4	F_1L_4	0.04	4×10^{-4}	0.8	1.72	0.7	0.010	F_1	126	L_4
5	F_1L_5	0.04	4×10^{-4}	0.4	0.86	0.7	0.010	F_1	63	L_5
6	F_2L_1	0.08	4×10^{-4}	0.2	2	0.4	0.005	F_2	110	L_1
7	F_3L_2	0.036	3.6×10^{-4}	0.64	3.98	0.5	0.010	F_1	242	L_6

3.5.2 Comparison of Commercial Flocculants Combined with AP-*g*-PVBTMAC

Two commercial anionic flocculants (KemSep® A-8353, Magnafloc 1011) were compared with calcium ions and AP-*g*-PVBTMAC. The best one was then tested with different dosages of cationic and anionic species. One test used only calcium ions as a reference.

In a typical procedure, 150 g of diluted (5 or 10 wt.%) tailings was flocculated and mixed at 300 rpm for 2 mins. After mixing, the supernatant was recovered for turbidity measurements. The flocculated sediments were transferred to a filter press (OFI Testing Equipment, Inc.) consisting of four 0.2-L stainless-steel cylindrical filtering units and grade 4 Whatman filter papers. The pressure was adjusted to 10 psig. The treated MFT was filtered for 1 h. The filter cake was dried for 24 h in an oven at 60 °C to calculate the final solids content, as discussed in Section 3.2.6. Some flocculation tests were performed with undiluted MFT.

3.6 Dual Polymer Flocculation with Controlled Addition

3.6.1 Central Composite Design and Response Surface Methodology

Central composite designs (CCD) were first introduced by Box and Wilson [99] to assess the non-linearity of responses for a number of factors with a minimum number of experiments. They can be performed in stages, if the data acquired show that two factor interactions are required to describe the system [99]. The first stage usually consists of a center point and a fractional or full factorial design, which can then be completed with star experimental points located at a distance α from the center point. Different levels (Figure 3.9) can be used for the factors but three levels are usually used (-1, 0, +1) [100,101].

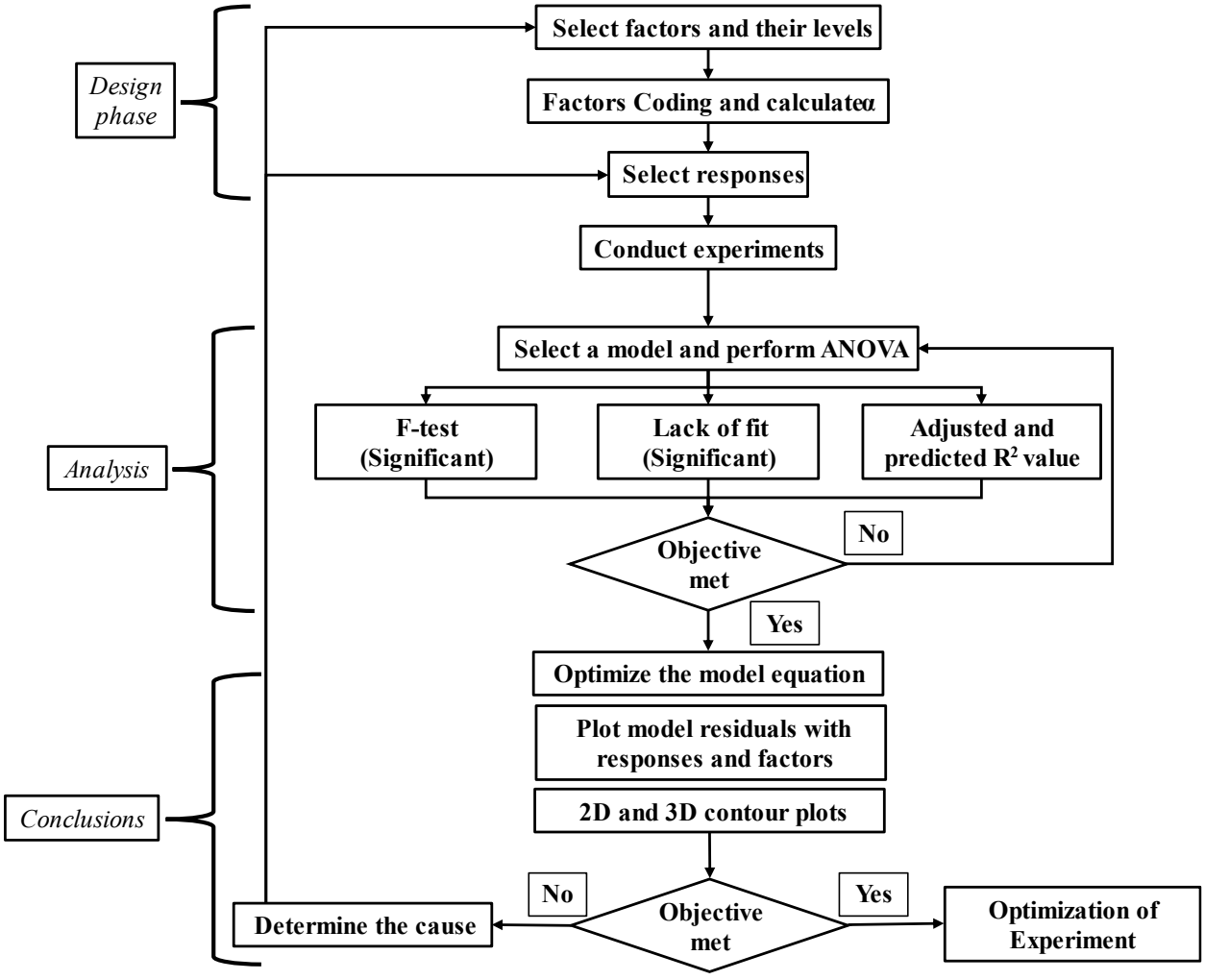

Figure 3.9 – Central composite design flow diagram (adapted from [99]).

Box and Wilson also explained why designs with spherical or nearly spherical variance functions (called rotatable) are better: the estimated response has a constant variance at all points equidistant from the center [99,102]. We chose a spherical over a rotatable design, to respect the nearly rotatability while covering the largest range possible for each factor. For this type of design, including a full factorial design, the location of star points can be calculated with Eq. (3.6), where k is the number of factors,

$$\alpha = \sqrt{k} \tag{3.6}$$

In this project, the effects of five factors (Table 3.3) on the flocculation of kaolinite suspensions were studied:

- Cationic polymer (AP-*g*-PVBTMAC) dosage in kilo parts per million (kppm)
- Anionic polymer (MF 1011) dosage in kppm
- Cationic polymer (AP-*g*-PVBTMAC) addition flowrate in mL/min
- Anionic polymer (MF 1011) addition flowrate in mL/min
- Kaolinite suspension solids content in wt.% of solids

The α value was 2.236 (with $k = 5$) and the levels were symmetrical for both polymer dosages.

Table 3.3 – Independent factors and their levels used in the CCD.

Factors	**Factors levels**				
	-2.236 (-α)	-1	0	+1	+2.236 (+α)
$\boldsymbol{X_1}$: AP-g-PVBTMAC dosage (kppm)	0.528	3	5	7	9.472
$\boldsymbol{X_2}$: MF 1011 dosage (kppm)	0.528	3	5	7	9.472
$\boldsymbol{X_3}$: AP-g-PVBTMAC addition flowrate (mL/min)	16.46	35.00	50.00	65.00	83.54
$\boldsymbol{X_4}$: MF 1011 addition flowrate (mL/min)	3.82	10.00	15.00	20.00	26.18
$\boldsymbol{X_5}$: Suspension solids content (wt.%)	1.1	6.0	10.0	14.0	18.9

Kaolinite suspensions were chosen to model the flocculation behavior of MFT because kaolinite is one of the most common types of clays in MFT. It is also easier to control the

suspension properties and uniformity of kaolinite suspensions, since there is no residual bitumen that could affect the results [62].

(Eq. 3.7) changes the actual values of the parameters into dimensionless values that are proportional to their coordinates in the experimental space [103] to ensure that their estimated impact on the responses is defined on the same basis, regardless of their orders of magnitude.

$$X_i = \left(\frac{A_i - A_i^0}{1/2 \times (A_i^{+1} - A_i^{-1})} \right) \tag{3.7}$$

where A_i is the actual value, A_i^0 the actual value at the central point, $A_i^{+1}$and A_i^{-1} the actual values at +1 and -1 levels, respectively.

With the coded variables, multiple predictive responses (Y) can be estimated with a second order model for k factors with coded levels, $X_i$and X_j. This model comprises the intercept (β_0), first order terms (β_i coefficients), second order terms (β_{ii} coefficients), first order interaction terms (β_{ij} coefficients), and an error term (ε) (Eq. 3.8) [103],

$$Y = \beta_0 + \sum_{i=1}^{k} \beta_i X_i + \sum_{1 \le i < j}^{k} \beta_{ij} X_i X_j + \sum_{i=1}^{k} \beta_{ii} X_i^2 + \varepsilon \tag{3.8}$$

As shown in Figure 3.7, the next step is to conduct the experiments. First, we need to calculate the number of experiments, N (Eq. 3.9).

$$N = 2^k + 2k + c_p \tag{3.9}$$

with k independent factors and c_p number of replicates of the center point. The 2^k term corresponds to the number of runs required to complete the full factorial design with k factors, and $2k$ is the number of alpha points.

The center point was repeated six times ($c_p = 6$) and five factors were studied ($k = 5$), adding up to $N = 48$ runs. Eq (3.8) predicts that 21 coefficients are needed in the model; therefore, the design had enough degrees of freedom to estimate the internal error.

The different treatments were conducted randomly to avoid biasing the experimental results. Table 3.4 presents the full CCD design (the design of the screening experiments is shown in Appendix A2). Based on the screening results, the sample F_4L_2 (graft frequency and length proportional to 0.01 and 25, respectively, see Table 3.1) was chosen for these 48 runs. Flocculations were performed on fresh kaolinite suspensions (see ageing issues in Section 4.6.4) at a pH 7.9 and the same solids content as the MFT sample, 33.3 wt. %.

The results were analyzed using R-Studio features for model regression analysis, residual plots and contour plots with the response surface methods (rsm) package.

Table 3.4 – Full CCD design for the 5 factors under investigation.

Run	C* dosage (kppm)	A** dosage (kppm)	C* addition flowrate (mL/min)	A** addition flowrate (mL/min)	Solids content (wt.%)
1	3 *(-1)*	7 *(+1)*	65 *(+1)*	10 *(-1)*	14 *(+1)*
2	3 *(-1)*	7 *(+1)*	35 *(-1)*	20 *(+1)*	6 *(-1)*
3	3 *(-1)*	3 *(-1)*	35 *(-1)*	20 *(+1)*	6 *(-1)*
4	7 *(+1)*	3 *(-1)*	65 *(+1)*	10 *(-1)*	14 *(+1)*
5	3 *(-1)*	3 *(-1)*	35 *(-1)*	10 *(-1)*	6 *(-1)*
6	7 *(+1)*	7 *(+1)*	35 *(-1)*	20 *(+1)*	14 *(+1)*
7	7 *(+1)*	7 *(+1)*	65 *(+1)*	10 *(-1)*	6 *(-1)*
8	3 *(-1)*	3 *(-1)*	65 *(+1)*	20 *(+1)*	14 *(+1)*
9	7 *(+1)*	7 *(+1)*	65 *(+1)*	20 *(+1)*	14 *(+1)*
10	3 *(-1)*	7 *(+1)*	35 *(-1)*	10 *(-1)*	6 *(-1)*
11	7 *(+1)*	7 *(+1)*	35 *(-1)*	10 *(-1)*	14 *(+1)*
12	5 *(0)*	5 *(0)*	50 *(0)*	15 *(0)*	10 *(0)*
13	3 *(-1)*	7 *(+1)*	65 *(+1)*	20 *(+1)*	14 *(+1)*
14	3 *(-1)*	3 *(-1)*	65 *(+1)*	10 *(-1)*	6 *(-1)*
15	3 *(-1)*	3 *(-1)*	65 *(+1)*	10 *(-1)*	14 *(+1)*
16	3 *(-1)*	7 *(+1)*	35 *(-1)*	20 *(+1)*	14 *(+1)*
17	5 *(0)*	5 *(0)*	50 *(0)*	15 *(0)*	10 *(0)*
18	7 *(+1)*	3 *(-1)*	65 *(+1)*	20 *(+1)*	14 *(+1)*
19	7 *(+1)*	3 *(-1)*	65 *(+1)*	10 *(-1)*	6 *(-1)*
20	7 *(+1)*	3 *(-1)*	35 *(-1)*	20 *(+1)*	6 *(-1)*
21	7 *(+1)*	7 *(+1)*	65 *(+1)*	20 *(+1)*	6 *(-1)*
22	7 *(+1)*	3 *(-1)*	35 *(-1)*	10 *(-1)*	14 *(+1)*
23	7 *(+1)*	7 *(+1)*	35 *(-1)*	20 *(+1)*	6 *(-1)*
24	7 *(+1)*	7 *(+1)*	35 *(-1)*	10 *(-1)*	6 *(-1)*
25	7 *(+1)*	3 *(-1)*	35 *(-1)*	10 *(-1)*	6 *(-1)*
26	5 *(0)*	5 *(0)*	50 *(0)*	15 *(0)*	10 *(0)*
27	3 *(-1)*	3 *(-1)*	35 *(-1)*	20 *(+1)*	14 *(+1)*
28	7 *(+1)*	7 *(+1)*	65 *(+1)*	10 *(-1)*	14 *(+1)*
29	7 *(+1)*	3 *(-1)*	65 *(+1)*	20 *(+1)*	6 *(-1)*
30	3 *(-1)*	3 *(-1)*	35 *(-1)*	10 *(-1)*	14 *(+1)*
31	7 *(+1)*	3 *(-1)*	35 *(-1)*	20 *(+1)*	14 *(+1)*
32	3 *(-1)*	7 *(+1)*	35 *(-1)*	10 *(-1)*	14 *(+1)*
33	3 *(-1)*	3 *(-1)*	65 *(+1)*	20 *(+1)*	6 *(-1)*
34	3 *(-1)*	7 *(+1)*	65 *(+1)*	20 *(+1)*	6 *(-1)*
35	3 *(-1)*	7 *(+1)*	65 *(+1)*	10 *(-1)*	6 *(-1)*
36	0.528 *(-α)*	5 *(0)*	50 *(0)*	15 *(0)*	10 *(0)*
37	5 *(0)*	5 *(0)*	50 *(0)*	15 *(0)*	18.9 *(+α)*
38	5 *(0)*	5 *(0)*	50 *(0)*	15 *(0)*	10 *(0)*
39	5 *(0)*	5 *(0)*	50 *(0)*	26.2 *(+α)*	10 *(0)*
40	5 *(0)*	5 *(0)*	83.54 *(+α)*	15 *(0)*	10 *(0)*
41	5 *(0)*	5 *(0)*	50 *(0)*	15 *(0)*	1.1 *(-α)*
42	5 *(0)*	5 *(0)*	16.46 *(-α)*	15 *(0)*	10 *(0)*
43	5 *(0)*	5 *(0)*	50 *(0)*	15 *(0)*	10 *(0)*
44	5 *(0)*	5 *(0)*	50 *(0)*	3.82 *(-α)*	10 *(0)*
45	5 *(0)*	0.528 *(-α)*	50 *(0)*	15 *(0)*	10 *(0)*
46	5 *(0)*	9.472 *(+α)*	50 *(0)*	15 *(0)*	10 *(0)*
47	9.472 *(+α)*	5 *(0)*	50 *(0)*	15 *(0)*	10 *(0)*
48	5 *(0)*	5 *(0)*	50 *(0)*	15 *(0)*	10 *(0)*

*C refers to the cationic polymer specie, here AP-g-PVBTMAC F_4L_2
**A refers to the anionic polymer specie, here MF 1011

3.6.2 Control of Volumes and Addition Flowrates

Cationic and anionic polymer addition flowrates (and volume for the desired dosage) were controlled with syringe pumps. A standard single syringe infuse Pump 11 Elite from Harvard Apparatus (max flowrate of 88.29 mL/min) was used to add cationic polymer solution (it needed higher flowrates, according to the screening tests), while the anionic polymer pump was an older version of the syringe infuse Pump 11 Plus from Harvard Apparatus (maximum flowrate of 26.55 mL/min) (presented in Figure 3.10). For both additions, 50 mL BD plastic syringes with internal diameters of 26.7 mm were used. Stainless steel needles were used to keep a constant zone of addition throughout the runs required for the full design (Figure 3.9).

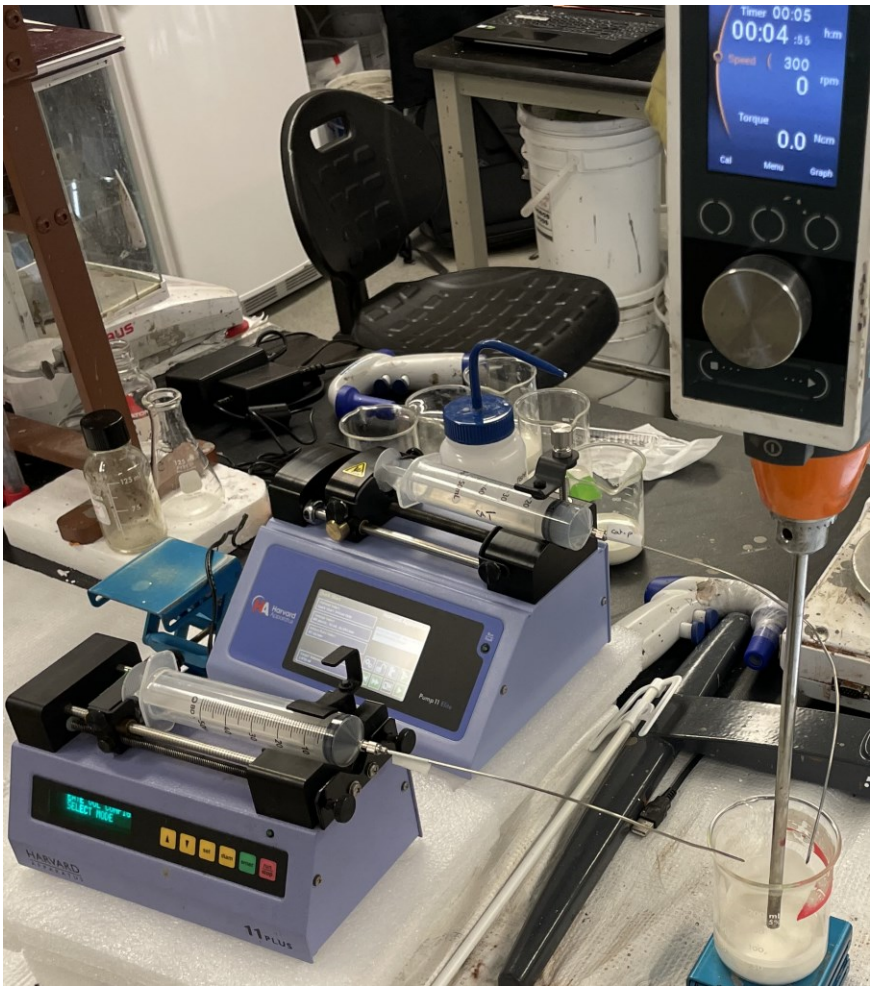

Figure 3.10 – Flocculation setup with both syringe pumps and the mechanical mixer.

3.7 Floc Size Estimation

3.7.1 Flocs Segmentation with Image Processing

Experimental observations showed that the flocs sizes depended on the addition conditions. Top-view pictures of the flocs formed right after flocculation were taken with a fixed tripod, a commercial phone (12 Mpx, 3024 × 4032), and a ruler (used as a scale) for each run, as shown in Figure 3.11.

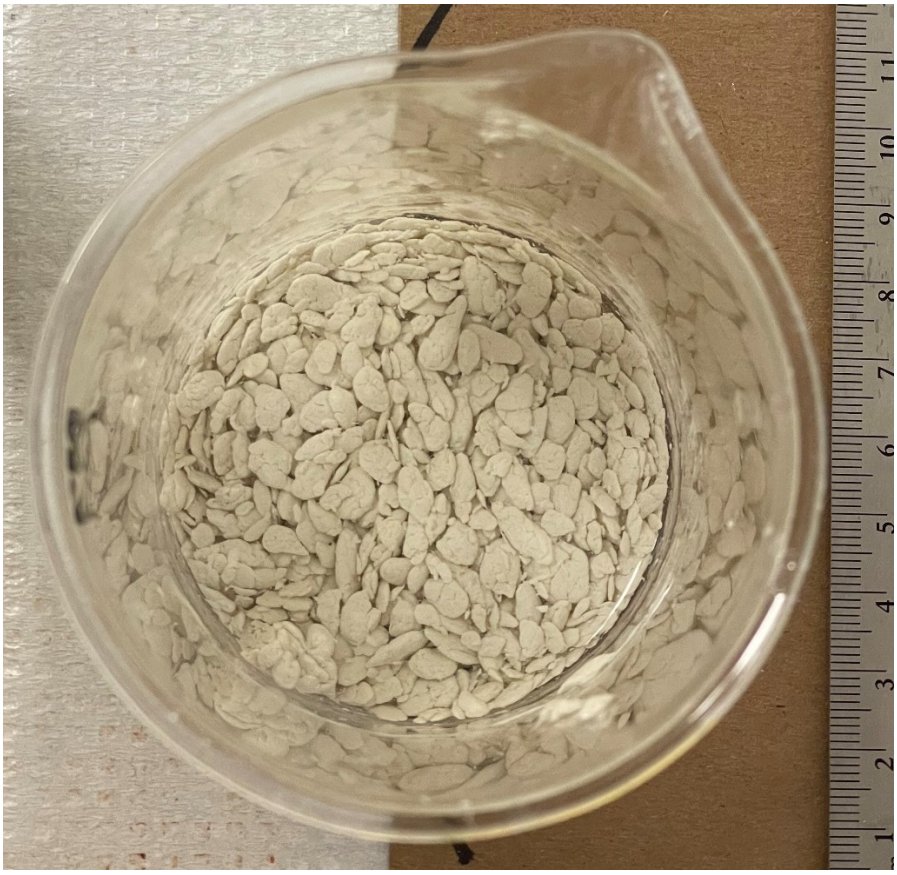

Figure 3.11 – Example of a raw picture taken immediately after flocculation (CCD Run 1).

Since the camera setup (angle and distance to object) change the perceived length (in pixels), the internal diameter of the beaker (6.8 cm) was checked each time with the ruler. Before treating the image, we needed to circle crop (MATLAB® code adapted from [104]) the raw picture to extract only the zone containing the flocs. The program prompts the user to draw a circle for the region to be cropped (with @drawcircle, Figure 3.12.a) and creates a circle mask to blacken all the pixels outside of the drawn circle (Figure 3.12.b). The results are the circle-cropped image (Figure

3.12.c), the position of the circle, and its radius. The latter was used to convert the mean size of the flocs in pixels into centimeters. The code for this circle cropping algorithm is in Appendix A3 (Figure A3.1).

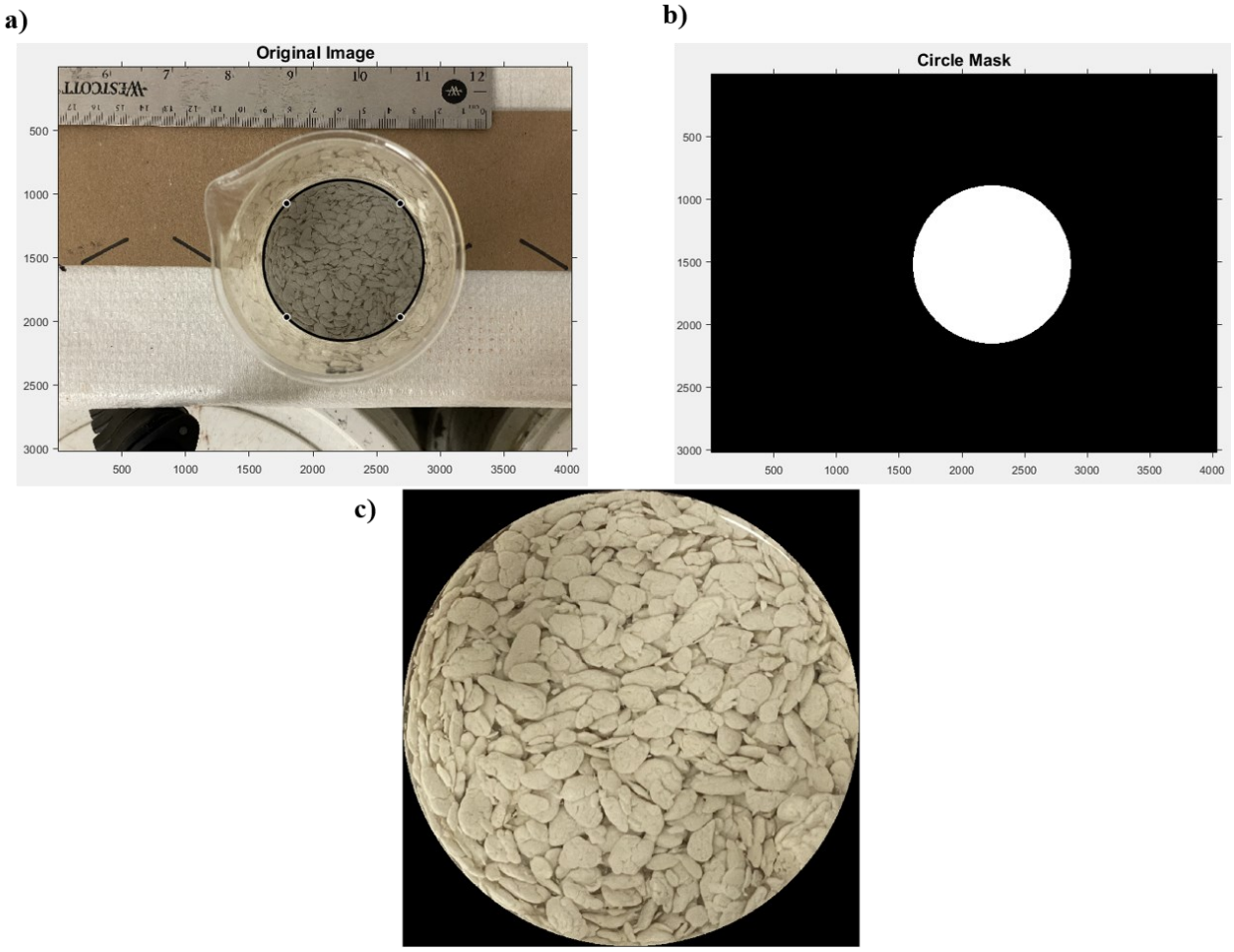

Figure 3.12 – Detail of the circle-crop method: a) user-drawn circle on the original image; b) circle mask to blacken pixels outside the circle; c) circle-cropped image.

The next step is to isolate each floc numerically using the MATLAB image processing toolbox. The circle-cropped image was first converted into a grayscale image with enhanced contrast using @adapthisteq (Figure 3.13.a). At this point, a new binary image is created with @im2bw, based on a gray threshold. From this binary image, two methods were compared: a simplified method used in this study and the more sophisticated marker-based watershed segmentation [105,106].

In the latter, the intensity of a pixel in the image represents the elevation of the corresponding position [107]. The topography of the image is then flooded from the bottom to surround each regional minimum by defining watershed lines. Regional maxima are obtained with @imextendedmax to mark the foreground objects for the watershed segmentation. Then the image is cleaned using a cycle of morphological open closing. The image holes are first filled with @imfill and the image is then opened (erosion followed by dilation) with a matrix that identifies the pixel being processed and its neighborhood (structuring element) using @imopen. The opened image is used to remove all small objects from the binary image with @bwareaopen. Then, the identified peaks are turned into valleys since the watershed transform identifies low points not high points [105,107]. Finally, the watershed transform is applied. The performance of the watershed segmentation is discussed in Section 4.6.5, and the computer code used for this analysis is in Appendix A3 (Figure A3.2).

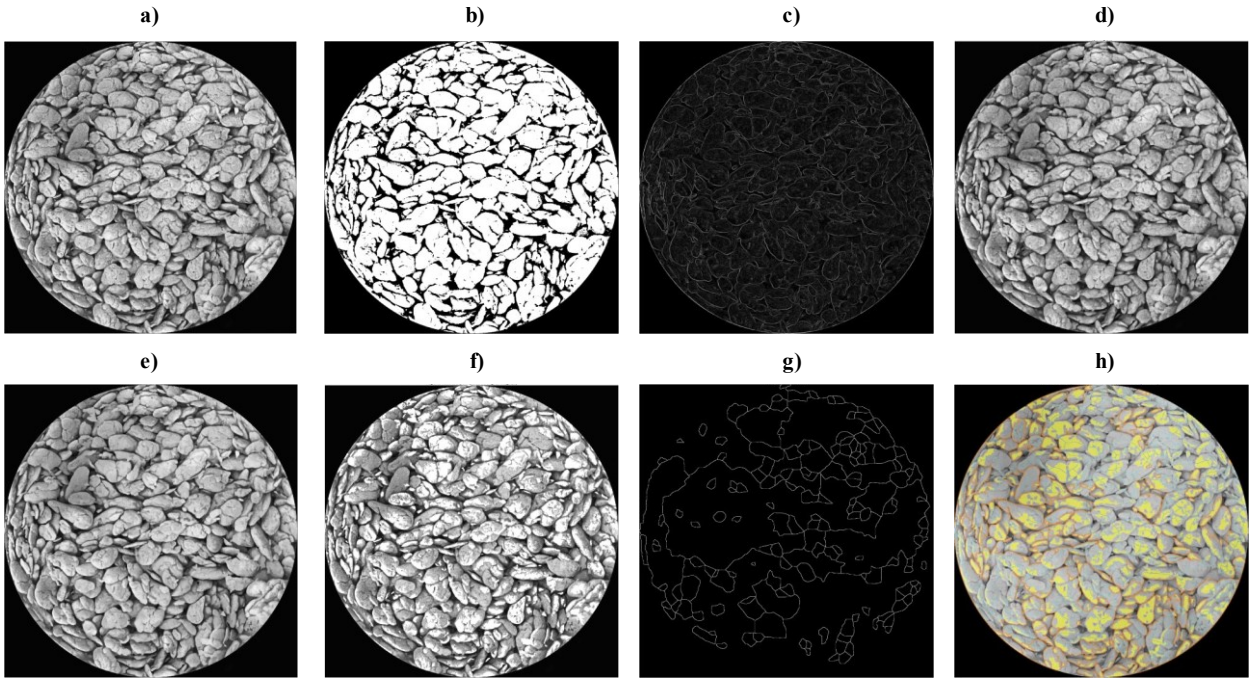

Figure 3.13 – Marker-based watershed segmentation steps: a) grayscale image, b) binary image, c) gradient magnitude image, d) opening image, e) opening-closing by reconstruction image, f) regional maxima overlaid with the original image, g) watershed ridge lines, h) markers and objects superimposed on the original image.

The other method relies on the estimation of the perimeter of each floc (same group of pixels) with @bwperim (Figure 3.14). Because of its simplicity, overlapping is likely to happen as

it is not a proper segmentation as the watershed method. The results of both methods are discussed in Section 4.6.6. The computer code for this process is in Appendix A3 (Figure A3.2).

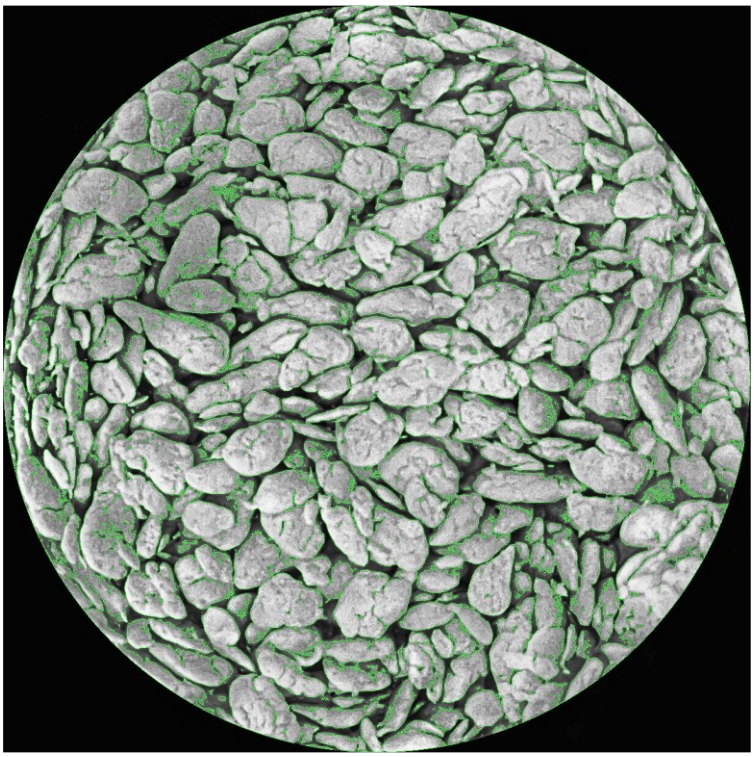

Figure 3.14 – Perimeter "segmentation" superimposed with original grayscale image.

3.7.2 Floc Size Estimation and Distribution

Floc size (in pixels) was estimated once they were isolated with the segmentation. To obtain a floc size distribution, the computer program [108] (Figure A3.3 in Appendix A3) asks the user to enter one integer number to define the number of classes for the PSD. The next step was to extract all the sizes of the isolated flocs in a vector.

To use in this approach, we must define the size basis. Because of the shape of the flocs, the minimum Feret diameter (minimum distance between a pair of parallel lines tangent to the projected outline of the particle [109]) (Figure 3.15) was used for the perimeter method and the information was extracted from the processed image with @bwferet. For the watershed method, the equivalent diameter of a circle with the same projected area as the given floc was used with @regionprops.

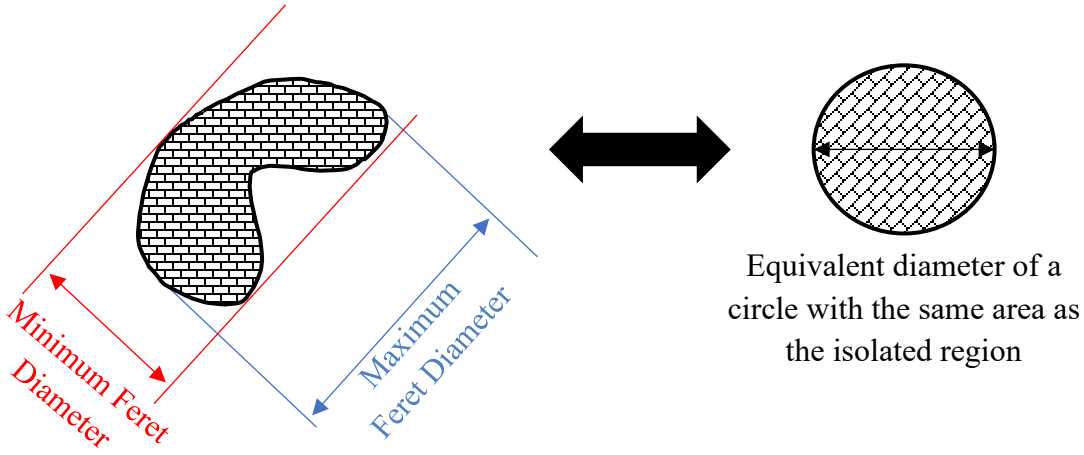

Figure 3.15 – Schematic representation of the Feret diameters and the equivalent diameter used for floc size estimation.

The floc size distribution was fitted with a lognormal distribution. The perimeter fractal dimension was also calculated using the Lee and Kramer correlation [110] (Eq. 3.10) in complement of the mean size.

$$A \; \alpha \; P^{\frac{2}{d_{PF}}} \tag{3.10}$$

The computer code used for both methods is in Figure A4.4 and Figure A4.5 respectively.

A focused beam reflectance measurement (FBRM) apparatus (detailed in Section 3.7.3) was used to confirm the size of the flocs estimated with image processing. Since FBRM gives results in chord length, we converted the sizes given by FBRM in volume sphere-equivalent diameter (D(4,3)) in cm with the calibration proposed by Vajihinejad [98],

$$FBRM\ Chord\ Length = 1.04 \times D(4,3) + 44.84\ ;\ Rsq = 0.99 \tag{3.11}$$

The calibration shown in Eq. (3.11) is only valid for FBRM set in coarse mode and flocs chord lengths between 0 and 500 µm.

3.7.3 Flocculation Dynamic Study with Focused Beam Reflectance Measurement (FBRM)

We studied the temporal evolution of floc size, of a mixed (300 rpm in 250 mL beakers) kaolinite suspension (7.9 pH, 5 wt. %) with fixed polymer dosage and solids content at varying addition flowrates (Table 3.5), using a focused beam reflectance measurement (FBRM) ParticleTrack G400 apparatus from METTLER TOLEDO.

Table 3.5 – Experiment design used to study the evolution of floc size with polymer addition flowrate using FBRM.

Run	C* Dosage (kppm)	A** Dosage (kppm)	C* Addition flowrate (mL/min)	A** Addition flowrate (mL/min)	Solids Content (wt. %)
1	1.5***	1.5	80	10	5
2	1.5	1.5	10	25	5
3	1.5	1.5	55	15	5
4	1.5	1.5	10	80	5
5	1.5	1.5	25	10	5
6	1.5	1.5	15	55	5

*C refers to the cationic polymer specie, here AP-g-PVBTMAC F_4L_2.
**A refers to the anionic polymer specie, here MF 1011.
***Another set of experiment was conducted with 3 kppm dosages.

Two replicates were conducted for each flocculation to ensure the reproducibility of the results. The weighted chord length distribution and the square weighted mean chord length versus time were measured. The evolution of floc sizes with flocculation time was followed with particles counts ordered in size classes (< 10, 10-50, 50-150, 150-300, 300-1000 μm) from the addition of polymers to a steady-state value after 3 min of flocculation.

4. Results and Discussion

4.1 MFT and Kaolinite Suspension Characterization

4.1.1 Dean-Stark Extraction

Table 4.1 lists the percentages of water, solids and bitumen in the MFT sample measured with Dean-Stark extraction. These results are within the expected range for MFT [6].

Table 4.1 - MFT composition measured by Dean-Stark extraction.

Constituent	Run 1 (wt.%)	Run 2 (wt.%)	Run 3 (wt.%)	Average (wt.%)	Standard Error (%)
Water	65.5	65.7	66.1	65.8	0.19
Solids	31.6	31.5	30.9	31.3	0.22
Bitumen	2.90	2.83	2.97	2.89	0.04

It is hard to achieve better reproducibility since water can be lost in the system, especially when combining Soxhlet and Dean-Stark extraction with a 20 mL volume trap.

4.1.2 ICP-OES Analysis

Table 4.2 shows the ICP-OES results for the three undiluted MFT subsamples. Quantifying the major cations in the process water is important because they may affect the flocculation [21] by deactivating adsorption sites [44] or compressing the electrical double layer [40].

Table 4.2 – Major cations concentrations in the undiluted MFT sample.

Sample ID	Al^{3+} (mg/L)	Ca^{2+} (mg/L)	K^{+} (mg/L)	Mg^{2+} (mg/L)	Na^{+} (mg/L)
MFT Water 1	1.381	13.74	14.91	7.265	806.7
MFT Water 2	5.799	12.72	17.54	9.047	809.7
MFT Water 3	12.24	23.66	16.34	11.87	747.0
Average	6.480	16.71	16.26	9.394	787.8
Std Error	2.58	2.85	0.619	1.09	16.7
LOD*	0.040	0.040	0.830	0.050	0.120
LOQ**	0.130	0.120	2.640	0.180	0.360

*LOD: Limit of detection / **LOQ: Limit of quantification

4.1.3 PSD Analysis of MFT sample and kaolinite suspension

Table 4.3 and 4.4 show the particle size distribution (PSD) (volume basis) of the MFT and the kaolinite suspension, respectively, including the mean Sauter diameter (surface area-to-volume, D[3,2]), volume mean diameter (D[3,4]), median, D_{10}, and D_{90} (details and additional comments presented in Appendix B1). Since MFT suspensions are stable, the values did not decrease significantly after sonication, except for D_{90} (Table 4.3), which may be attributed to the breakage of large aggregates because of sonication.

Table 4.3 – PSD results in volume basis for the MFT sample.

VOLUME		D[3,2] (µm)	D[4,3] (µm)	D_{10} (µm)	D_{50} (µm)	D_{90} (µm)	Weighted Residual* (%)	Specific Surface Area (m^2/kg)
MEANS	Pre-Sonication	3.76	19.8	1.42	10.0	48.3	0.30	1595
	Post-Sonication	3.66	18.5	1.37	9.61	45.5	0.31	1642
GLOBAL MEANS		3.71	19.2	1.40	9.80	46.9	0.30	1618

* Weighted residual is calculated by the Mastersizer 3000 software based on the data fit.

The volume and number PSDs of the MFT (Figure 4.1) are monomodal. Both distributions are relatively symmetrical, except for small deviations in the range from 0.1 to 1 µm for the volume PSD. This is confirmed by the calculation of the span,

$$Span = \frac{D_{90} - D_{10}}{D_{50}} \tag{4.1}$$

For instance, the Span for the number distribution (see Table B1.3 for D_{10}, D_{50} and D_{90}) is equal to 1.16, which shows a low degree of dispersion around the mean value.

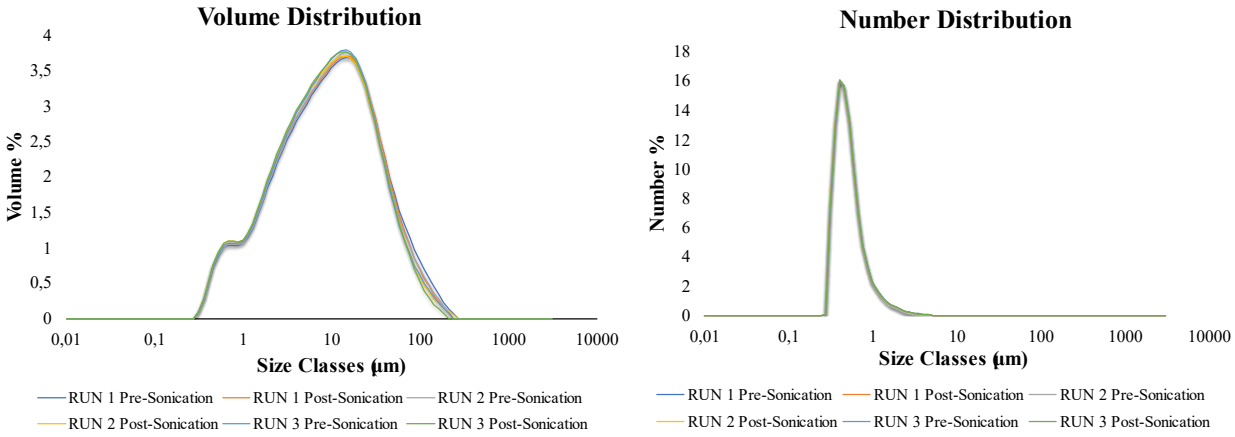

Figure 4.1 – Volume (left) and number frequency (right) distributions for the MFT sample.

The volume and number frequency distributions (Figure 4.2) of the kaolinite suspension show a similar profile (Span = 1.12 for the number distribution), but the volume distribution is narrower (Span of 2.22 versus 4.64 for MFT).

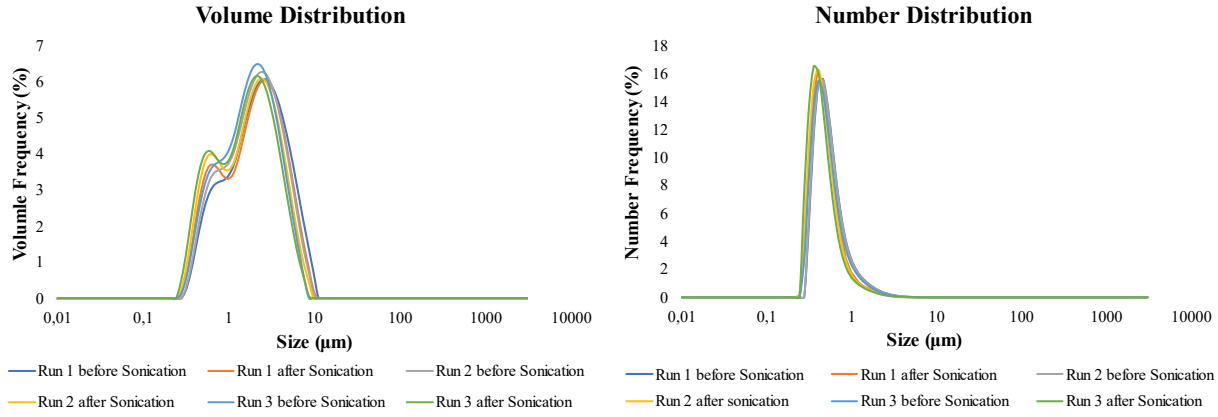

Figure 4.2 – Volume (left) and number frequency (right) distributions for the kaolinite suspension.

The specific surface area of the kaolinite particles in the kaolinite suspension (Table 4.4) is about 2.5 smaller than those for the clay particles in the MFT sample (Table 4.3).

Assuming that the clays in MFT and kaolinite suspension have the same density and type of adsorption sites, a higher specific surface area should make it easier for the polymer to adsorb and flocculate the particles, but this assumption is simplistic because the MFT clays can be coated with asphaltenes and other functional groups [111], [112]. This is important to keep in mind when using kaolinite to model MFT behavior. Contrarily, one may hypothesize that smaller particle sizes may stabilize the suspension via competing Van der Waals / electrical double layer interactions, but the effect of sonication on the mean sizes (Table 4.4) suggests otherwise.

Table 4.4 – PSD results in volume basis for the kaolinite suspension.

VOLUME		D[3,2] (µm)	D[4,3] (µm)	D_{10} (µm)	D_{50} (µm)	D_{90} (µm)	Weighted Residual* (%)	Specific Surface Area (m^2/kg)
MEANS	Pre-Sonication	1.47	2.60	0.65	2.12	5.30	0.86	4098
	Post-Sonication	1.28	2.38	0.56	1.94	4.92	0.97	4691
GLOBAL MEANS		1.38	2.49	0.60	2.03	5.11	0.91	4395

* Weighted residual is calculated by the Mastersizer 3000 software based on the data fit.

4.1.4 XRD Analysis

The XRD results with reference intensity ratio (RiR) performed on the MFT sample are presented in Figure 4.3 and Table 4.5.

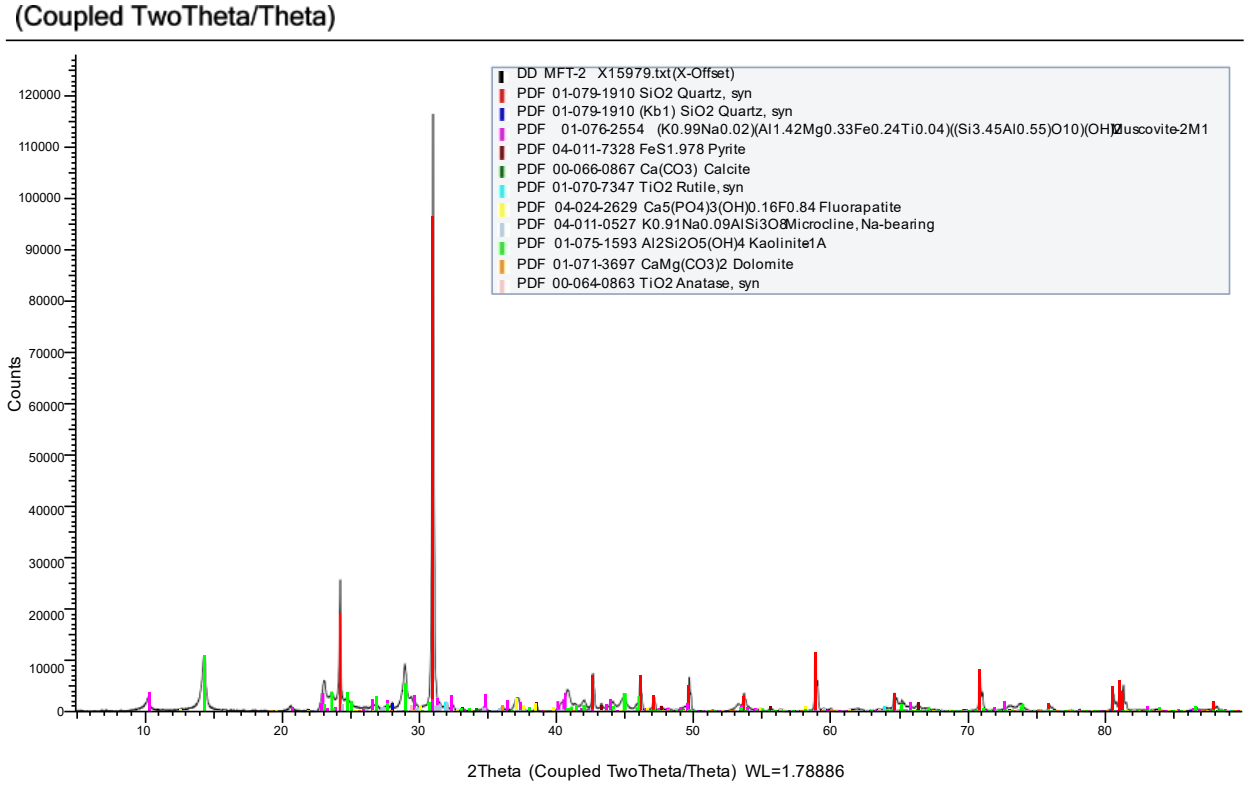

Figure 4.3 – XRD spectrum of the MFT sample with peak identification.

The semi-quantitative RiR measurements [113,114] confirm the presence of quartz (55.9 %) as the major compound in the dried MFT sample, followed by muscovite-2M1 (16.4 %) and kaolinite-1A (15.9 %). Muscovite and kaolinite are present in about the same amounts in this sample. Since kaolinite is often chosen to model MFT behavior [29,64,136,137], we chose it to represent MFT in some of the flocculation tests.

The kaolinite sample was also analyzed by XRD to determine its composition (Figure 4.4, Table 4.6).

Table 4.5 – XRD RiR Summary for the MFT sample.

Compound Name	Formula	Y-Scale* (%)	I/Ic**	S-Q*** (%)	Concentration Level
Quartz, syn	SiO_2	82.95	3.070	55.9	Major
Muscovite-2M1	$K_{0.99}Na_{0.02})(Al_{1.42}Mg_{0.33}Fe_{0.24}Ti_{0.04})((Si_{3.45}Al_{0.55})O_{10})(OH)_2$	3.10	0.390	16.4	Major
Pyrite	$FeS_{1.978}$	1.35	2.860	1.0	Trace
Calcite	$Ca(CO_3)$	0.39	3.220	0.3	Trace
Rutile, syn	TiO_2	1.32	3.620	0.8	Trace
Fluorapatite	$Ca_5(PO_4)_3(OH)_{0.16}F_{0.84}$	2.12	1.070	4.1	Minor
Microcline	$K0.91Na0.09AlSi_3O_8$	1.35	0.590	4.7	Minor
Kaolinite-1A	$Al_2Si_2O_5(OH)_4$	9.21	1.200	15.9	Major
Dolomite	$CaMg(CO_3)_2$	0.83	2.540	0.7	Trace
Anatase, syn	TiO_2	0.95	5.010	0.4	Trace

* Height of strongest line divided by the highest point of the parent scan multiplied by 100.
** Ratio of the intensities of the strongest line of the compound of interest and the strongest line of the corundum both measured from a scan of a 50-50 mixture as stored in the PDF database.
*** Semi-quantitative weight percentage of the phase corresponding to the selected pattern [115].

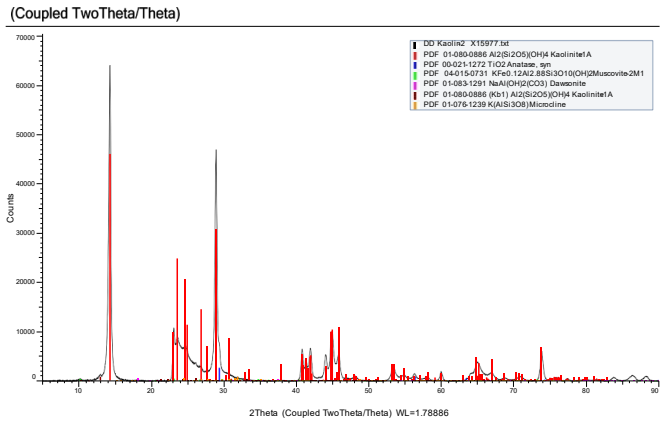

Figure 4.4 – XRD spectrum of the kaolinite stock with peak identification.

Table 4.6 – XRD RiR Summary for the kaolinite stock sample.

Compound Name	Formula	Y-Scale* (%)	I/Ic**	S-Q*** (%)	Concentration Level
Anatase, syn	TiO_2	4.32	3.300	1.8	Minor
Dawsonite	$NaAl(OH)_2(CO_3)$	0.62	1.940	0.4	Trace
Kaolinite	$Al_2(Si_2O_5)(OH)_4$	72.00	1.100	91.2	Major
Microline	$K(AlSi_3O_8)$	1.07	0.620	2.4	Minor
Muscovite-2M1	$KFe_{0.12}Al_{2.88}Si_3O_{10}(OH)_2$	1.22	0.410	4.1	Minor

4.2 Polymeric Flocculants Characterization

4.2.1 Proposed Graft Copolymerization Mechanism

Table 4.7 suggests a possible mechanism for the free radical graft copolymerization of AP and VBTMAC with KPS [83,84]. The primary radicals formed by KPS decomposition abstract protons from the AP backbones to produce the macroradicals needed for grafting. Based on previous publications, an interaction time of 20 minutes between the primary radicals and the AP backbones is needed to form the macroradicals [83,88]. Unfortunately, the simultaneous homo-propagation of VBTMAC to PVBTMAC cannot be avoided. Without post-polymerization purification, the reaction makes a blend of PVBTMAC and AP-*g*-PVBTMAC.

Table 4.7 – Graft copolymerization reaction scheme.

Initiation	$K_2S_2O_8 \xrightarrow{\Delta} 2K^+ + 2SO_4^{\cdot-}$
	$AP-OH + SO_4^{\cdot-} \rightarrow AP-O^{\cdot} + HSO_4^-$
	$M + SO_4^{\cdot-} \rightarrow M^{\cdot}$
Propagation	$AP-O^{\cdot} + M \rightarrow AP-O-M^{\cdot}$
	$AP-O-M^{\cdot} + nM \rightarrow AP-O-(M)_n-M^{\cdot}$
	$M^{\cdot} + pM \rightarrow (M)_p-M^{\cdot}$
Termination	*Combination*
	$AP-O-(M)_n-M^{\cdot} + AP-O-(M)_m-M^{\cdot} \rightarrow \mathbf{AP-O-(M)_{n+m}-O-AP}$
	$(M)_p-M^{\cdot} + (M)_q-M^{\cdot} \rightarrow (M)_{p+q}$
	OR
	$AP-O-(M)_n-M^{\cdot} + (M)_p-M^{\cdot} \rightarrow \mathbf{AP-O-(M)_{n+p}}$
	Disproportionation
	$AP-O-(M)_n-M^{\cdot} + AP-O-(M)_m-M^{\cdot} \rightarrow \mathbf{AP-O-(M)_n} + \mathbf{AP-O-(M)_m}$
	OR
	$(M)_p-M^{\cdot} + (M)_q-M^{\cdot} \rightarrow (M)_p + (M)_q$
	OR
	$AP-O-(M)_n-M^{\cdot} + (M)_p-M^{\cdot} \rightarrow \mathbf{AP-O-(M)_n} + (M)_p$
	Undesired coupling with initiator
	↓
	Grafted Polymer $\mathbf{AP-g-PVBTMAC}$ + *PVBTMAC homopolymer*

**Long chain approximation has been assumed, therefore* $n+1 \sim n$

AP-OH = reactive hydroxyl group of the AP backbone; M = VBTMAC monomer, AP-O-$(M)_n$-$M^{\cdot}$ and $(M)_n^{\cdot}$ = macroradicals (living chains), where the subscript specifies the length of the macroradical.

4.2.2 FTIR Analysis of AP-*g*-PVBTMAC

Fourier-transform infrared spectroscopy (FTIR) can tentatively confirm whether grafting took place if the spectrum of the grafted material comprises the main absorption peaks of both AP and PVBTMAC [83,88]. Figure 4.5 identifies the main peaks for AP [116,117]. Similarly, Figure 4.6 identifies the main peaks for VBTMAC [118,119,120]. Finally, Figure 4.7 compares AP, VBTMAC and AP-g-PVBTMAC (for the polymer sample F_4L_5, see Table 3.1) spectra.

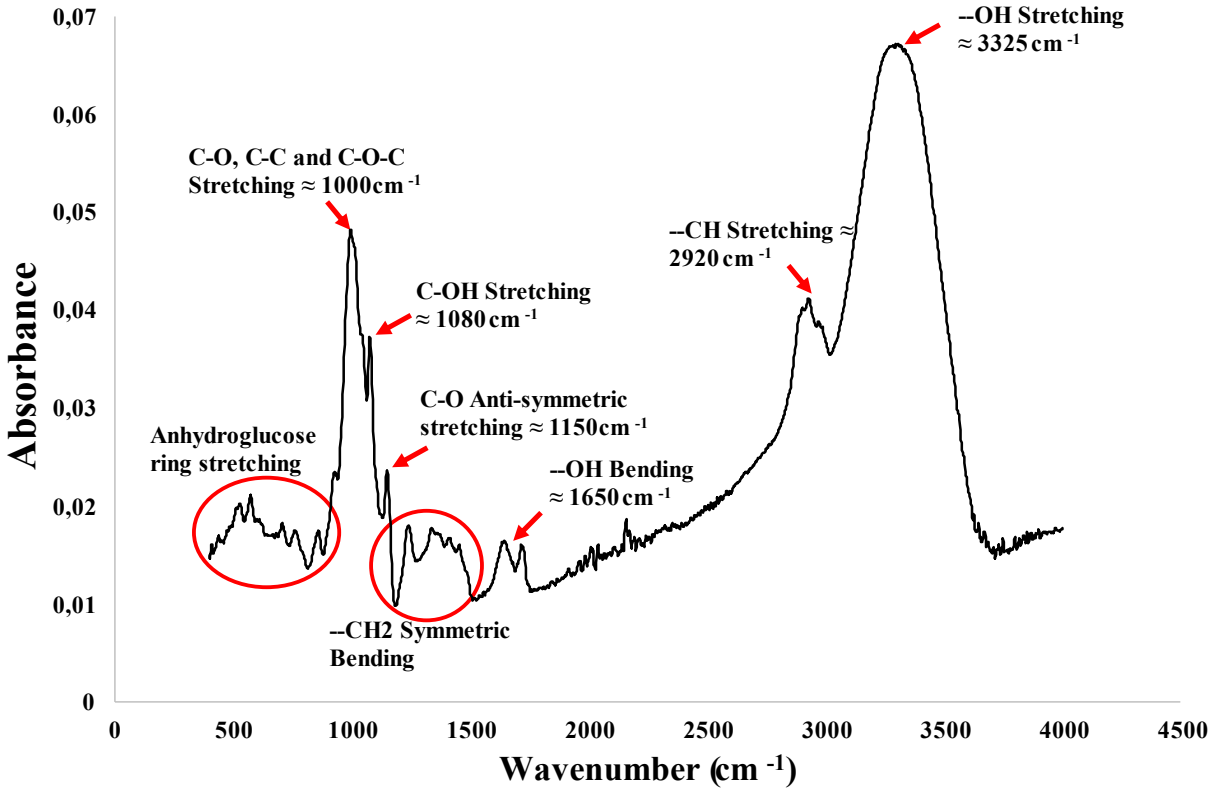

Figure 4.5 – FTIR absorbance spectrum of amylopectin (AP).

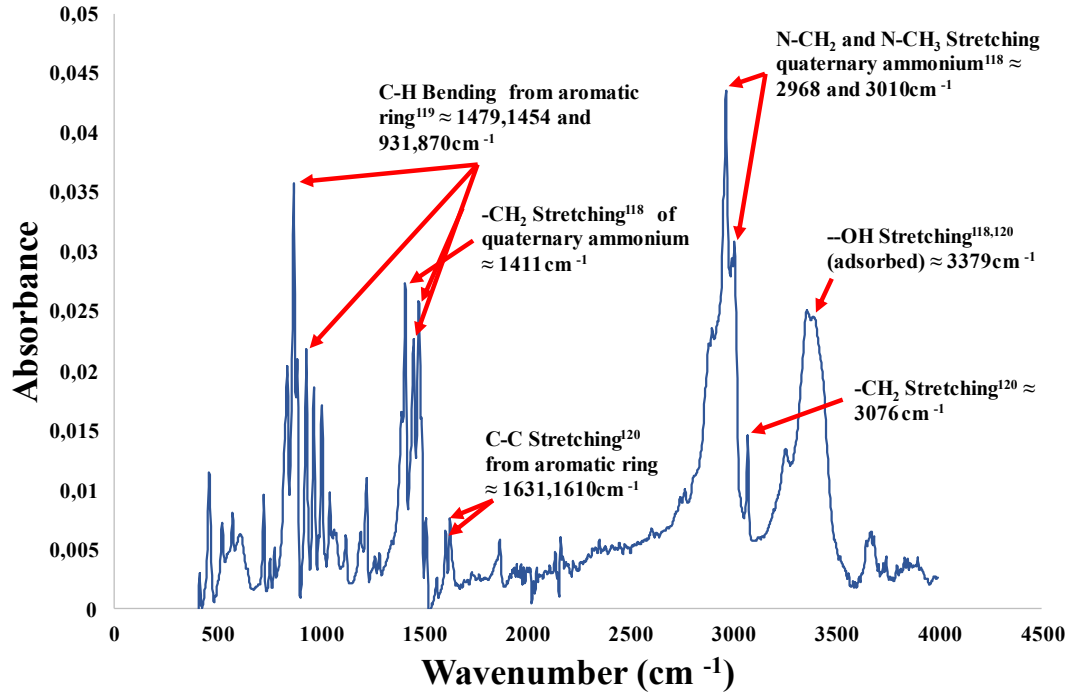

Figure 4.6 – FTIR absorbance spectrum of (vinyl benzyl) trimethylammonium chloride (VBTMAC).

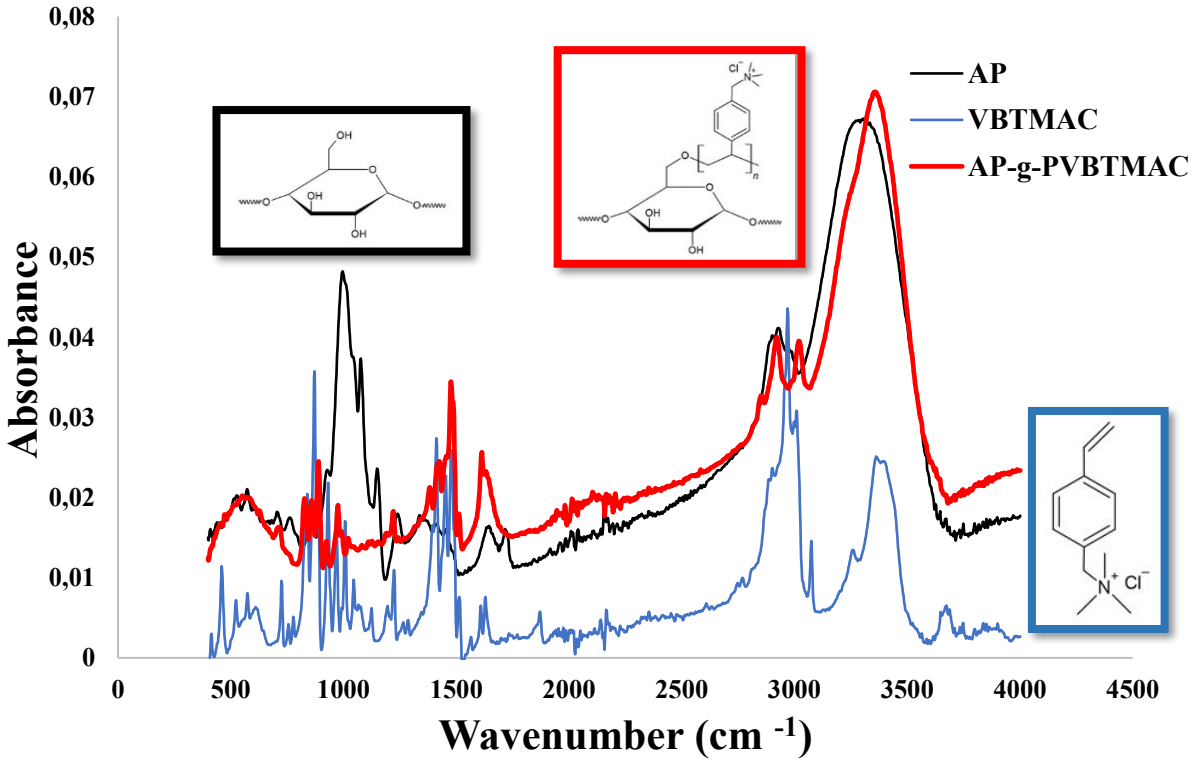

Figure 4.7 – Comparison of the FTIR absorbance spectra of AP, VBTMAC and AP-*g*-VBTMAC (sample F_4L_5).

The FTIR spectrum of the grafted polymer AP-*g*-VBTMAC (represented in red in Figure 4.7) show that the -OH bonding peak (at 3425 cm^{-1}) falls beyond those for AP (3370 cm^{-1}) and VBTMAC (3379 cm^{-1}). The main absorption peaks of AP and VBTMAC are still present in the spectrum of the grafted polymer except for the peak characteristic of -C-OH stretching at 1080 cm^{-1} (and C-O, C-C and C-O-C peak at 1000 cm^{-1}). This could be due to successful grafting of PVBTMAC chains in place of the hydroxyl groups on AP backbones, but this spectrum alone does not prove grafting.

Therefore, NMR spectroscopy is often combined with FTIR to compare the spectra of AP-PVBTMAC blend to AP-g-PVBTMAC [83,88,121]. Grafting occurs by abstracting hydroxyl protons in the ~ 4 to 6 ppm region of ^{1}H NMR. A difference in signal intensity in this region (proportional to the molar concentration) could confirm if PVBTMAC chains were grafted onto amylopectin backbones with the proton NMR [88], while the ^{13}C NMR could identify the grafting site [83]. But results presented in the literature compare signal intensities of overlapping peaks [83,121] and the height of a peak depends on broadening and data processing. Besides, we did not try to separate the grafted fraction of AP-g-PVBTMAC from the homopolymer PVBTMAC. For these reasons, we did not use NMR in this study.

4.2.3 Molecular Weight Analysis of AP-*g*-PVBTMAC (GPC)

Table 4.8 summarizes the polymer properties measured with GPC. Some polymers were not fully soluble in the mobile phase and could not be analyzed by GPC. The upper limit of the GPC calibration curve was 10^6 Da. The molecular weight of sample MF1011 was expected to be in the order of 10^7 Da, which is too high for GPC analysis.

Table 4.8 – Properties measured by GPC for the polymers analyzed.

Sample	M_w	M_n	Đ	R_g(nm)	R_h(nm)	R_h/R_g
F_4L_5	6.29×10^6	3.88×10^6	1.62	33.7	30.2	0.89
F_4L_3	9.30×10^6	7.27×10^6	1.28	57.4	61.3	1.07
F_4L_2	1.97×10^6	1.26×10^6	1.56	35.9	34.1	0.95
F_4L_4	3.31×10^6	2.28×10^6	1.45	56.2	51.2	0.91
F_3L_3	2.99×10^6	1.87×10^6	1.59	53.8	44.9	0.83
PVBTMAC	3.11×10^6	1.98×10^6	1.57	47.4	41.9	0.88
F_4L_1-70°C	7.38×10^5	4.45×10^5	1.66	17.3	18.3	1.06
F_4L_4-70°C	1.24×10^6	7.87×10^5	1.58	30.0	31.6	1.05
F_3L_3-70°C	2.37×10^6	1.49×10^6	1.59	37.4	34.3	0.92
F_1L_3-70°C	2.55×10^6	1.34×10^6	1.90	40.8	36.2	0.89
PVBTMAC-70°C	1.36×10^6	8.47×10^5	1.60	27.2	32.4	1.19

**Polymers not listed in this table were not soluble in the mobile phase.*
**70 °C refers to the temperature of the synthesis, 50 °C is the default polymerization temperature.*

The molecular weights of all polymers analyzed by GPC were in the range of a few million Daltons. This is good for flocculation. High molecular weight polymers have long tails and loops that extend beyond the electrical double layer, which favour charge neutralization with cationic flocculants. The radius of gyration (R_g) was also measured with the GPC light scattering detector, and the hydrodynamic radius (R_h) was calculated by the GPC software based on the value of the molecular weight,

$$Log(R_h) = 0.60 \times Log(M_w) - 2.63 \quad (4.1)$$

It is interesting to compare the R_g values – the average distance to the center of mass – to the R_h values – size of the solvated molecule in solution – since the R_h/R_g ratio indicates the polymer conformation in solution [93]. For instance, for sample F_3L_3, $R_h/R_g = 0.83 < 1$, indicating a compact conformation (for hard spheres in an ideal solvent, $R_h/R_g = 0.77$) [123,124,125]. Since the hydrophobic backbone represents the major portion of the molecule, the grafted polymer adopts a compact comb-like structure when placed in water.

The R_h/R_g ratio approaches 1 (more extended conformations) for polymers with the highest graft frequency (0.01) and short graft lengths (15, 25 and 35 for F_4L_1, F_4L_2, and F_4L_3 respectively) (Table 4.8). This is likely due to two effects:

1) High graft frequencies can increase R_h since the hydrophilic (polar) grafts expand in water, while the radius of gyration – related to the center of mass, which is concentrated in the backbone – remains unchanged.

2) Short graft lengths favor extended conformations since the grafts contain cationic charges that repel each other.

Table 4.8 also shows that most of the grafted polymers have: higher M_w and M_n than the PVBTMAC homopolymer, and narrow PDI (between 1.28 and 1.90), which indicates that grafting was successful. Figure 4.8 provides additional confirmation of grafting since the molecular weight distribution of the polymer sample F_4L_4 is unimodal and with a narrow PDI (1.45, Table 4.8) (the molecular weight distributions of the other samples are in Appendix B2). A blend of two polymers would tend to be broad and even bimodal if some unreacted amylopectin was still in the system.

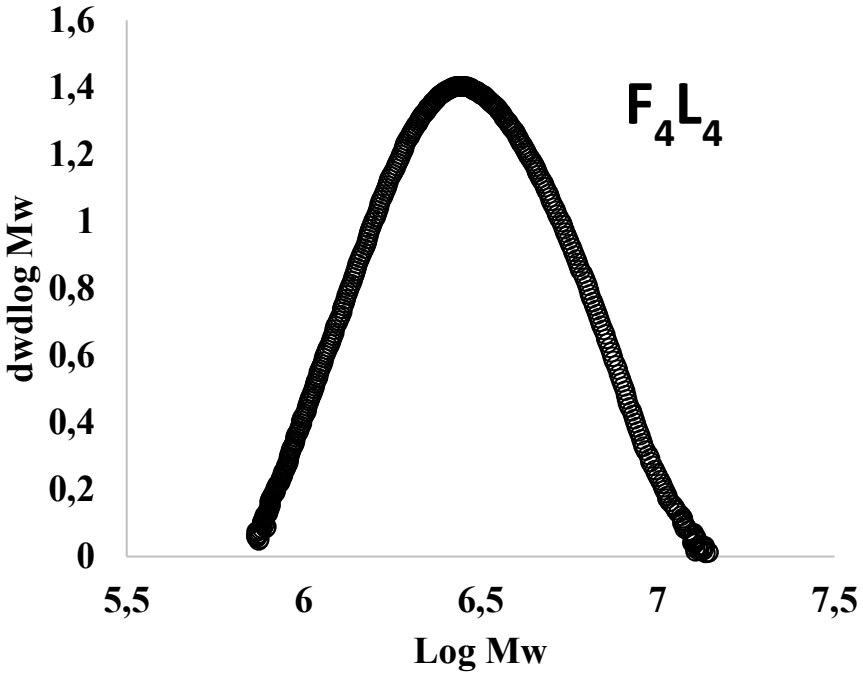

Figure 4.8 – Molecular weight distribution of sample F_4L_4.

4.3 Parameters Affecting the Flocculation of MFT with AP-*g*-PVBTMAC

4.3.1 Polymer Dosage

Different grades of AP-*g*-VBTMAC (Table 3.1) were used to flocculate MFT. The results were compared with PVBTMAC homopolymer to reveal the effect of amylopectin on the flocculation. The effect of polymer dosage on flocculation of 10 wt.% MFT is presented in Figures 4.9 - 4.13.

The ISR (Figure 4.9) decreases from 0.6 to 4 kpmm, and then increases sharply at higher dosages for all flocculants. Even though the trends are similar, the ISR values depend on polymer microstructure: ISR reaches up to 15 and 12 cm/h for samples F_4L_1 and F_4L_5 (defined in Table 3.1), but only to 9 cm/h for F_1L_3 and F_2L_3, suggesting that GF influences ISR (discussed in Section 4.3.3). Most grafted polymers outperformed the homopolymer and the physical blend AP – PVBTMAC with higher ISR.

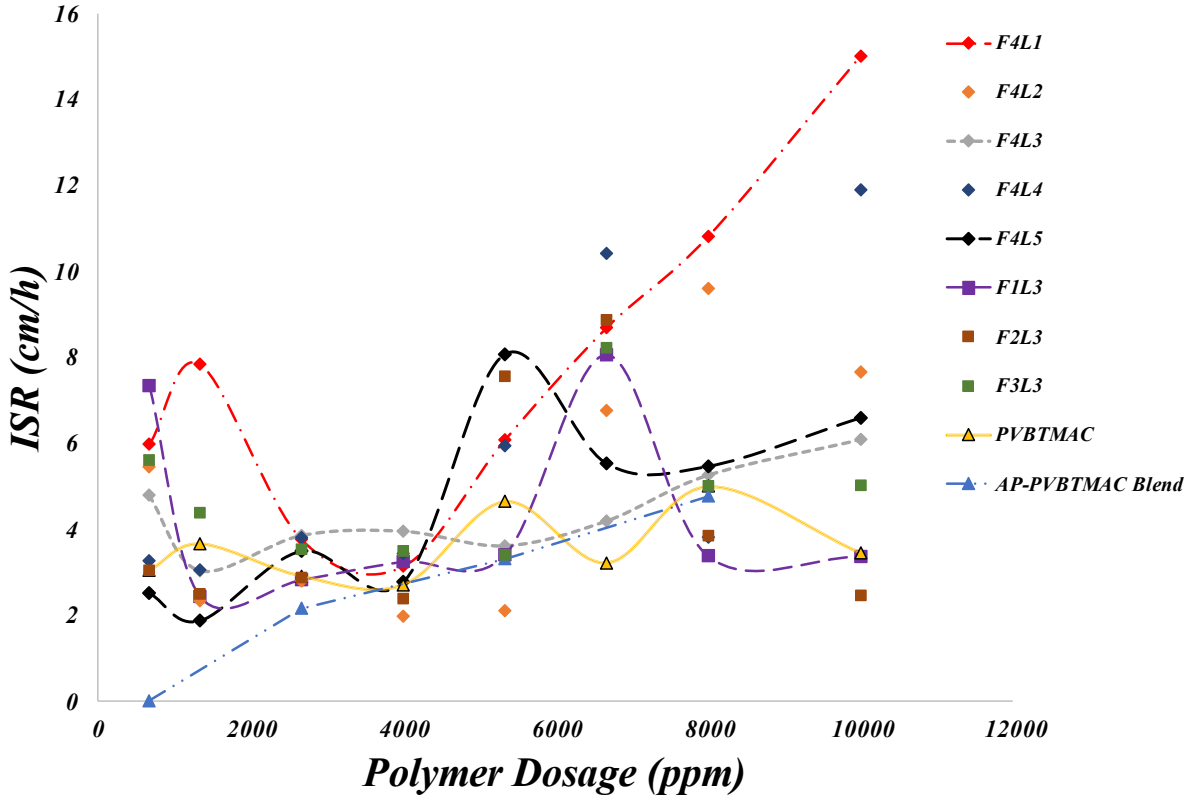

Figure 4.9 – Effect of polymer dosage on ISR.

Figure 4.10 shows how the solids content varies with flocculant dosage. Sample F_4L_1 leads to the highest solids content (14 - 26 wt. %), while F_4L_4 to the lowest (10 - 16 wt. %). It is expected that the graft length GL influences the amount of water entrapped in the flocs (discussed in Section 4.3.2). For instance, sample F_4L_4, with longer grafts, forms less dense flocs than sample F_4L_1. All of the grafted polymers outperformed PVBTMAC, solids content was higher by 2 to 10 wt. %. It can be speculated that the hydrophobic amylopectin backbone form flocs that entrap less water than pure PVBTMAC. The small increase in solids content observed when using a blend of homopolymer PVBTMAC and pure AP supports this hypothesis, even the blend is also outperformed by grafted polymers.

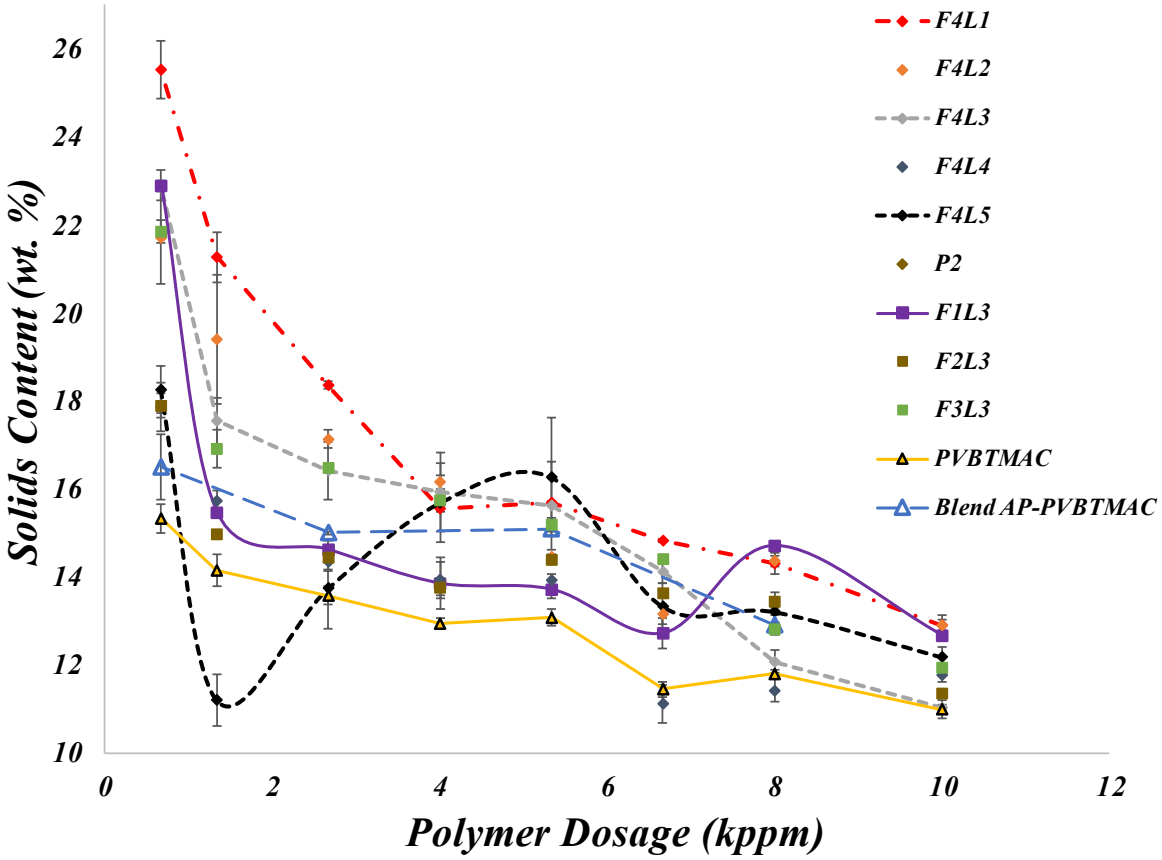

Figure 4.10 – Effect of polymer dosage on solids content.

Figure 4.10 also shows that the sediment solids content decreases with increasing polymer dosage. The linear correlation between the mudline height and the sediment solids content (Figure 4.11) confirms that more water is entrapped in the sediments as more fines are captured. Therefore,

the polymer that captures the most fines (lowest supernatant turbidity), such as sample F_4L_4, also makes sediments with the lowest solids content.

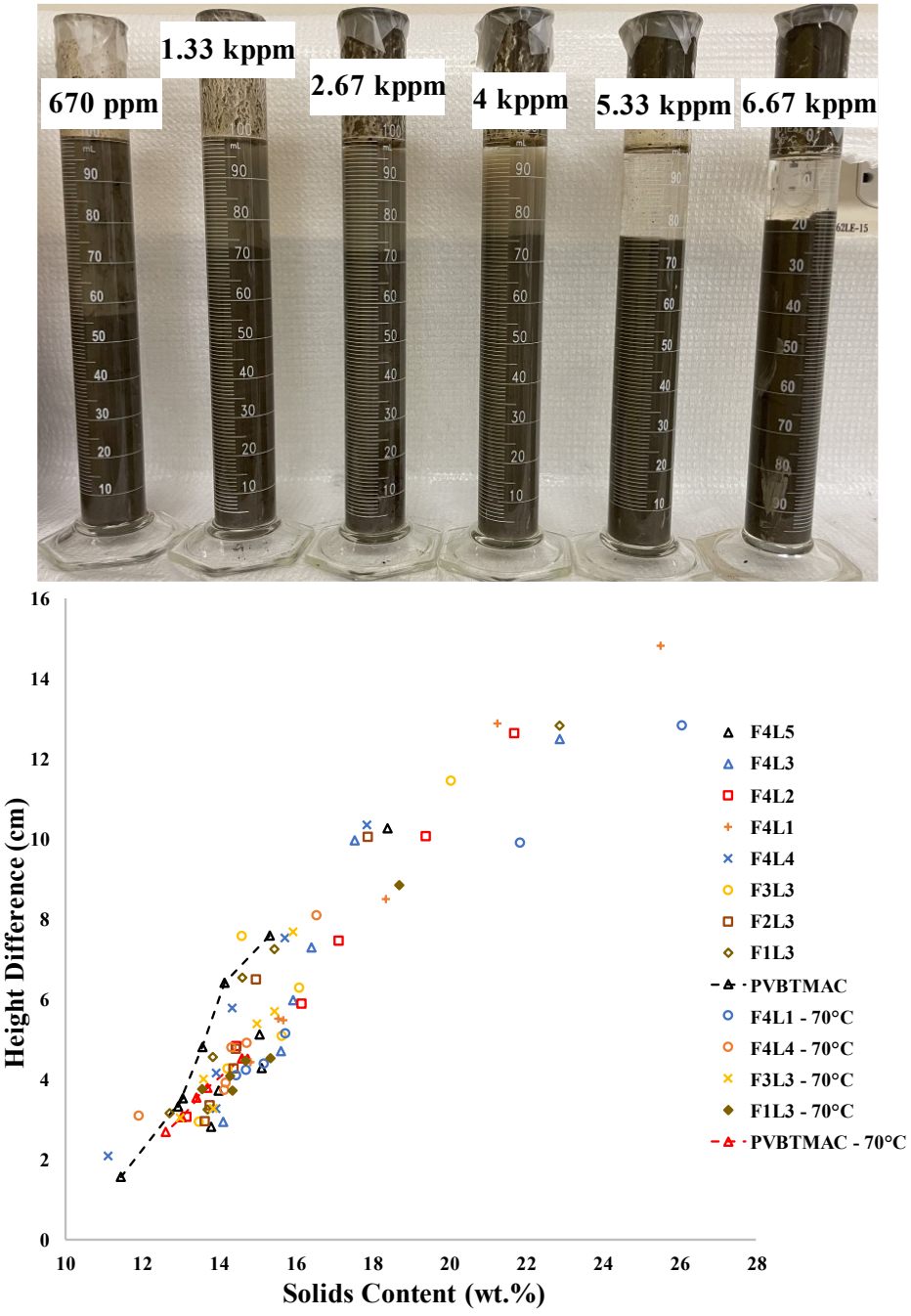

$$Height\ difference = Height\ of\ the\ mudline\ at\ t = 0 - Height\ of\ the\ mudline\ at\ t = 24\ hours$$

Figure 4.11 – Height difference in function of sediment solids content with the visual example of the sample F_4L_5, first run.

The supernatant turbidity (Figure 4.12) is two orders of magnitude lower with grafted polymers at low dosages (< 4 kppm) than with PVBTMAC, but it decreases with polymer dosage for PVBTMAC and grafted polymers, indicating that the fines are captured through the same mechanism. The high supernatant turbidity (100-1000 NTU) at dosages below 4 kppm indicates incomplete fines capture. The supernatant turbidity then declines with increasing polymer dosage until it reaches a minimum (< 1 NTU at 5.33-8 kppm, depending on the flocculant). This corresponds to the charge neutralization mechanism observed [26,39] for this type of cationic polymer. The turbidity increases at higher dosages, likely because of polymer overdosing (charge reversal) [39,46]. The optimum dosage for PVBTMAC is 5.3 kppm, lower than for the grafted polymers, suggesting that less PVBTMAC is needed for the optimum coverage on clay particle surfaces. The shorter PVBTMAC chains may approach the particle surface more easily than the grafted polymers with lower (effective) charge density.

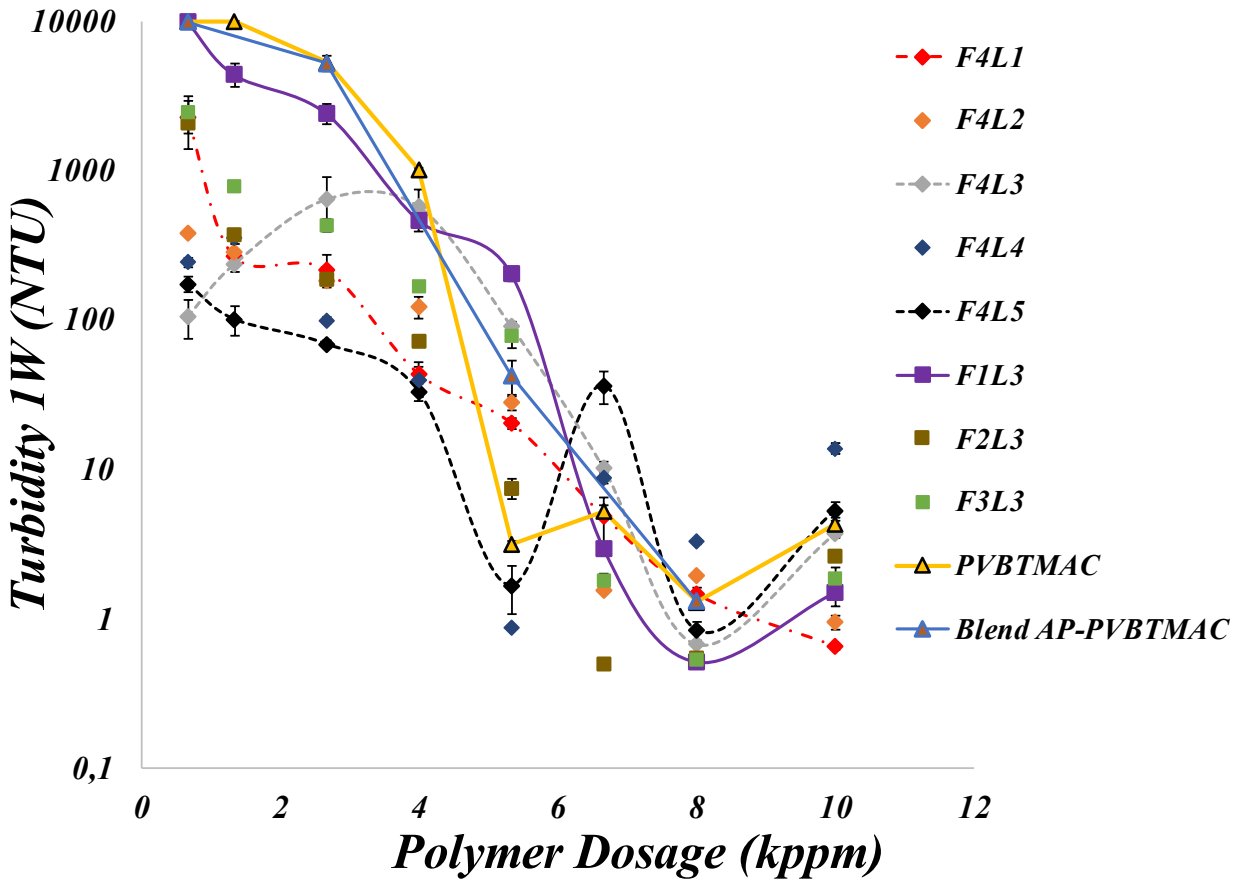

Figure 4.12 – Effect of polymer dosage on Turbidity after one week.

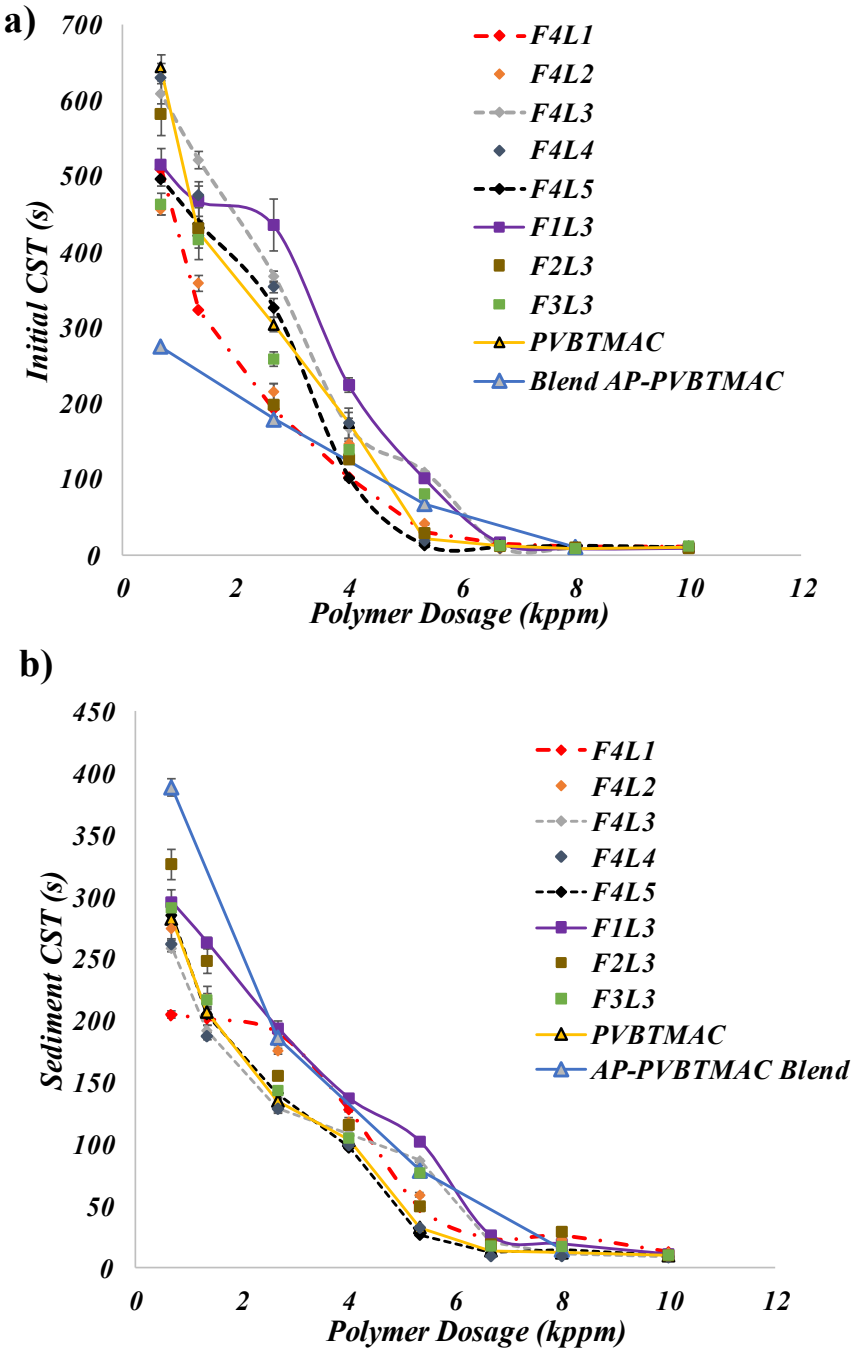

Figure 4.13 – Effect of polymer dosage on: a) initial, and b) sediment CSTs.

Initial and sediment (after 24 hours consolidation) CSTs (Figure 4.13) show the same trend with polymer dosage. CST declines steeply with increasing polymer dosage until 5.3 kppm, then keeps decreasing at a slower rate after 6.7 kppm. CST is lower for PVBTMAC than for some of the grafted polymers.

The higher solids content obtained with grafted polymers indicates that hydrophobicity is key for water expulsion during the consolidation phase, during which the repulsion between the polymer backbone and water molecules creates dryer sediments. Porous flocs are likely to entrap water and have large channels for water to go through, which could explain the high dewaterability (low CSTs) of the flocs formed with PVBTMAC, compared to the densely packed sediments formed with grafted polymers.

Most grafted polymers outperformed PVBTMAC for ISR, sediment solids content, and supernatant turbidity over the range of dosages studied. The ISR results can be explained by the higher molecular weight of the grafted material compared to PVBTMAC, as observed in previous studies [126]. But it is also possible that the shear strength provided by the amylopectin backbone allows for a higher ISR because grafted polymers form flocs that do not break easily. As for solids content, the hydrophobicity of the amylopectin backbone allows for the formation of denser flocs.

These results pinpoint some of the advantages and disadvantages of amylopectin-grafted polymers. The CSTs for all flocculants are satisfactory when compared to polyacrylamides or hydrolyzed polymethyl acrylate (~10 for polymers tested versus 200 to 300 seconds for PAM) with no overdosing effects in this regard [83,88,127]. Supernatant turbidity with these new flocculants is two orders of magnitude smaller than with commercial PAM without the addition of multivalent cations. But, the ISR obtained with AP-*g*-PVBTMAC is 10 times lower than those observed with anionic grafts onto amylopectin or commercial anionic polyacrylamides [83]. More importantly, solids content is decreasing with increasing polymer dosage for all the cationic polymers tested (in the dosage range tested), suggesting that more and more water remains trapped within the sediments as the dosage increases. The set of curves of ISR, solids content, supernatant turbidity, and CSTs versus polymer dosage for polymer synthesized at 70 °C, is presented in Appendix B3 and confirms the observations above.

4.3.2 Graft Length

Five polymers with the same graft frequency (GF = 0.01) and graft lengths from GL = 15 to 49.5 were synthesized to quantify the effect of cationic graft length on flocculation (Figures 4.14 - 4.17).

The ISR decreases for longer grafts at all dosages (Figure 4.14). This behavior is unexpected, as longer grafts should form larger flocs that would settle faster, as shown in Figure 4.15. Flocs produced with cationic flocculants are significantly smaller than those formed with neutral or anionic polymers. It is possible that flocs grow larger as the grafts become longer, but at the same time they become less dense. Therefore, the increase in size is not significant compared to the decrease in density.

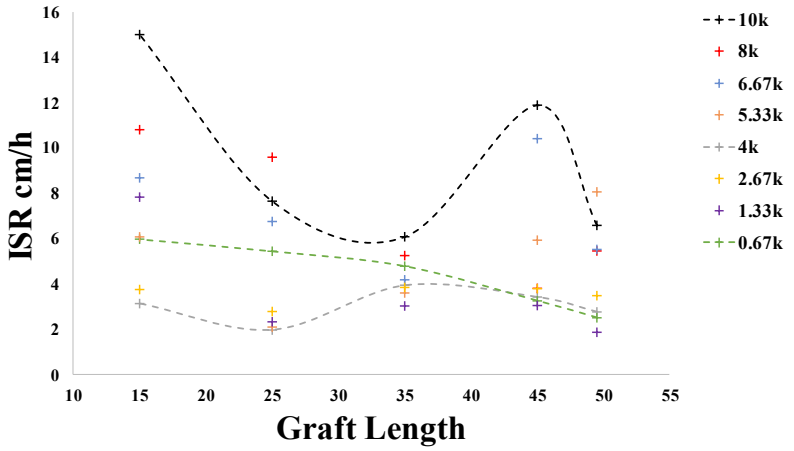

Figure 4.14 – Effect of graft length on ISR with polymer dosages in ppm.

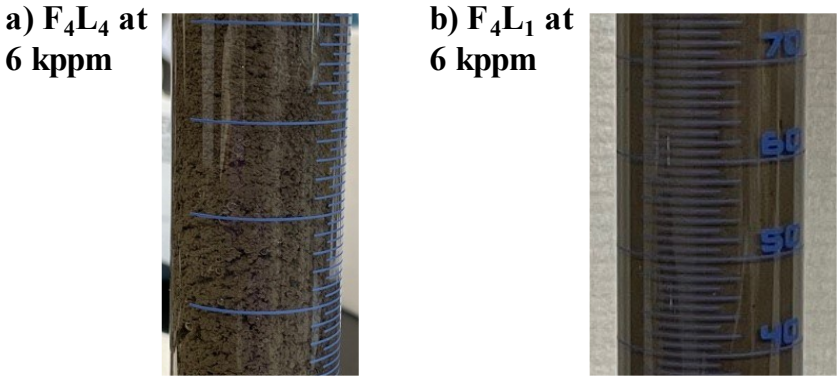

Figure 4.15 – Comparison of flocs sizes depending on the graft length: a) F_4L_4; b) F_4L_1.

The sediment solids content (Figure 4.16) also declines with increasing graft length, supporting this hypothesis. Thus, as longer grafts form larger but loosely packed flocs (clearly visible in Figure 4.15), the solids content decreases.

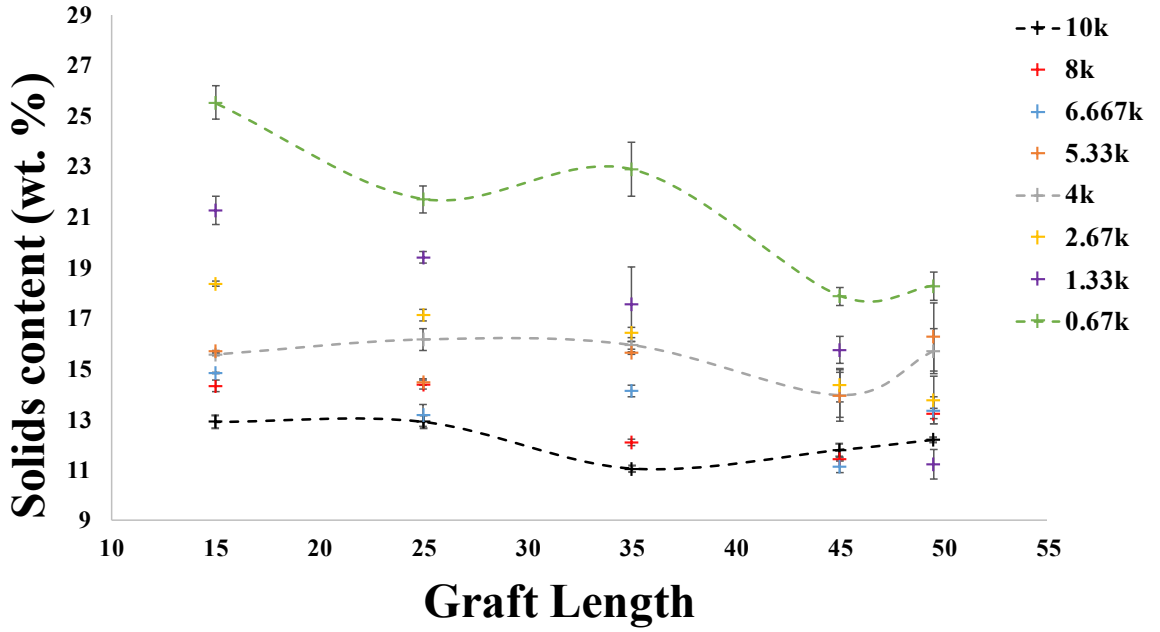

Figure 4.16 – Effect of graft length on solids content with dosages in ppm.

The supernatant turbidity (measured after one week of settling) does not show any clear trend (Figure 4.17.a). Increasing graft length increases fines capture at dosages below 4 kppm, but it increases fines capture above 5.33 kppm. The supernatant turbidity remains low < ~ 10 NTU regardless of graft length.

Graft length has also no significant impact on initial sediment CSTs (Figure 4.17.b and c). The hydrophobic character of PVBTMAC is given by its benzene rings, but it is likely that the hydrophobicity of the grafts is negligible compared to the hydrophobicity of the amylopectin backbone, which could explain why changing the structure of the grafts does not affect the dewaterability. The results presented here are consistent with polymers synthesized at 70 °C as shown in Appendix B4.

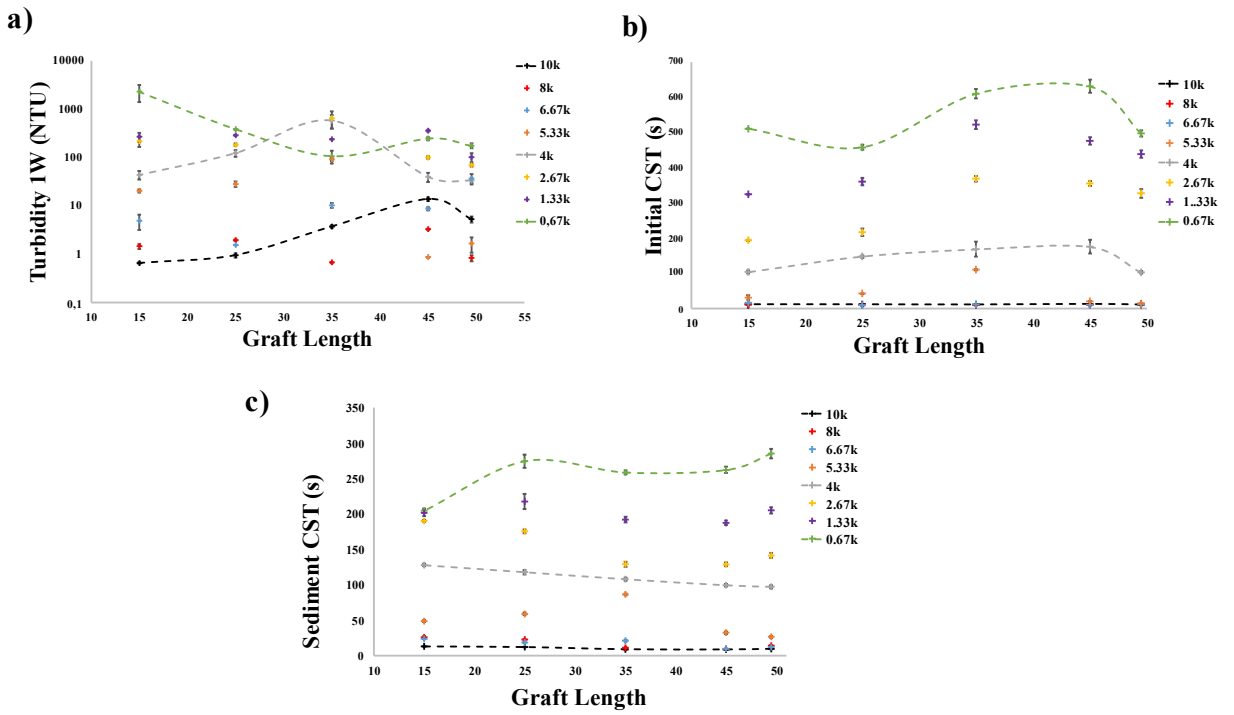

Figure 4.17 – Effect of graft length on flocculation: a) supernatant turbidity after one week, b) initial CST, and c) sediment CST, with polymer dosages in ppm.

4.3.3 Graft Frequency

Four polymers with the same graft length (GL = 35) and graft frequencies from GF = 0.002 to 0.01 were synthesized to quantify the effect of cationic graft frequency on flocculation (Figure 4.18).

The ISR (Figure 4.18.a) does not depend on graft frequency: it decreases with increasing graft frequency at 6.67 kppm and 0.67 kppm but increases at 8 kppm and 10 kppm. A high graft frequency is favorable for the compaction of the flocs as the solids content (Figure 4.18.b) increases for all dosages, except for 8 kppm and 10 kppm, for which the solids content remained stable and low (below 14 wt. %). This may be caused by overdosing, which created undesired repulsions, leading to interstitial gap within the flocs.

The supernatant turbidity (Figure 4.18.c) falls from few hundreds NTU to tens of NTU with greater graft frequencies at low dosages but rises for dosages above 6 kppm. Once again, the

repulsion created by the increased charge density due to the higher frequency of cationic grafts are detrimental to polymers adsorption and ultimately fines capture.

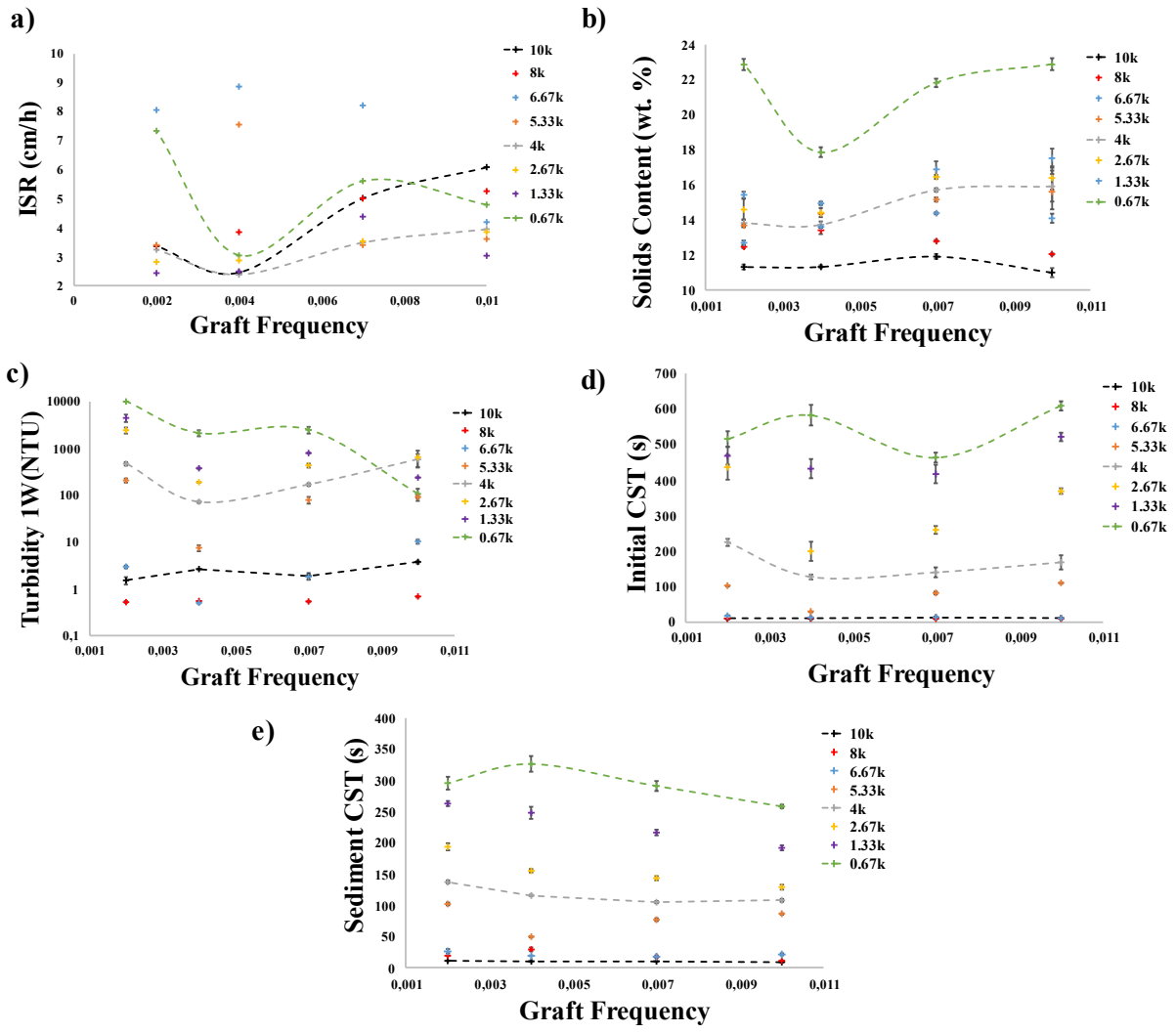

Figure 4.18 - Effect of graft frequency on flocculation: a) ISR, b) sediment solids content, c) supernatant turbidity after one week, d) initial CST and e) sediment CST, with dosages in ppm.

The initial CST (Figure 4.18.d) does not show a clear trend for all dosages, but the sediment CST (Figure 4.18.e) decreases slowly with increasing graft frequency, especially at low dosages. No CSTs lower than 10s were achieved. Similar results for polymers synthesized at 70°C are showed in Appendix B5.

Appendix B6 presents the ISR, sediment solids content, supernatant turbidity, initial and sediment CSTs trends with molecular weight for all polymers tested. Surprisingly, a greater

molecular weight did not seem to favor flocculation (as shown in Figure B6), contrary to previous studies [68,77,88,129]. Since ISR is not directly related to the polymer molecular weight, as known for polyacrylamides, the flocculation mechanism for this system is likely to be different. Bridging depends on the polymer molecular weight to bind clay particles together [130], but charge neutralization could behave differently in the presence of the amylopectin backbone.

4.3.4 Effect of Synthesis Temperature on MFT Flocculation

All graphs presented in Figures 4.9 - 4.13 show polymers synthesized at 50°C, since KPS was used as free-radical initiator and start decomposing above 50 °C [128]. The mild impact of polymer structure variations (discussed in sections 4.3.2 and 4.3.3) on the flocculation performance suggested that the low conversion achieved after 24 hours of synthesis at 50 °C could be the cause. The half-life time of KPS is close to 130 hours at this temperature and the reaction was left for 24 hours. Therefore, polymers were synthesized at 70 °C to reduce the half-life time to 21 hours (with ~ 55 % of the initiator consumed) [129].

The flocculation performance of the polymers was hardly impacted by the change in polymerization temperature (Figures 4.9 – 4.13 and Figures B3.1- B3.4 show the same trends and similar values for F_4L_1, F_4L_4, F_3L_3, F_1L_3 and PVBTMAC). For instance, the flocculation results for polymer F_4L_4 for both synthesis temperatures, have no significant impact (Figure 4.19, same results presented in Appendix B3, Figure B3.5 for F_3L_3). The molecular weight measurements obtained with the triple-detection GPC (Table 4.8) show a factor of 4 times between the polymers synthesized at 50 and 70 °C, with the polymers synthesized at 50 °C being larger.

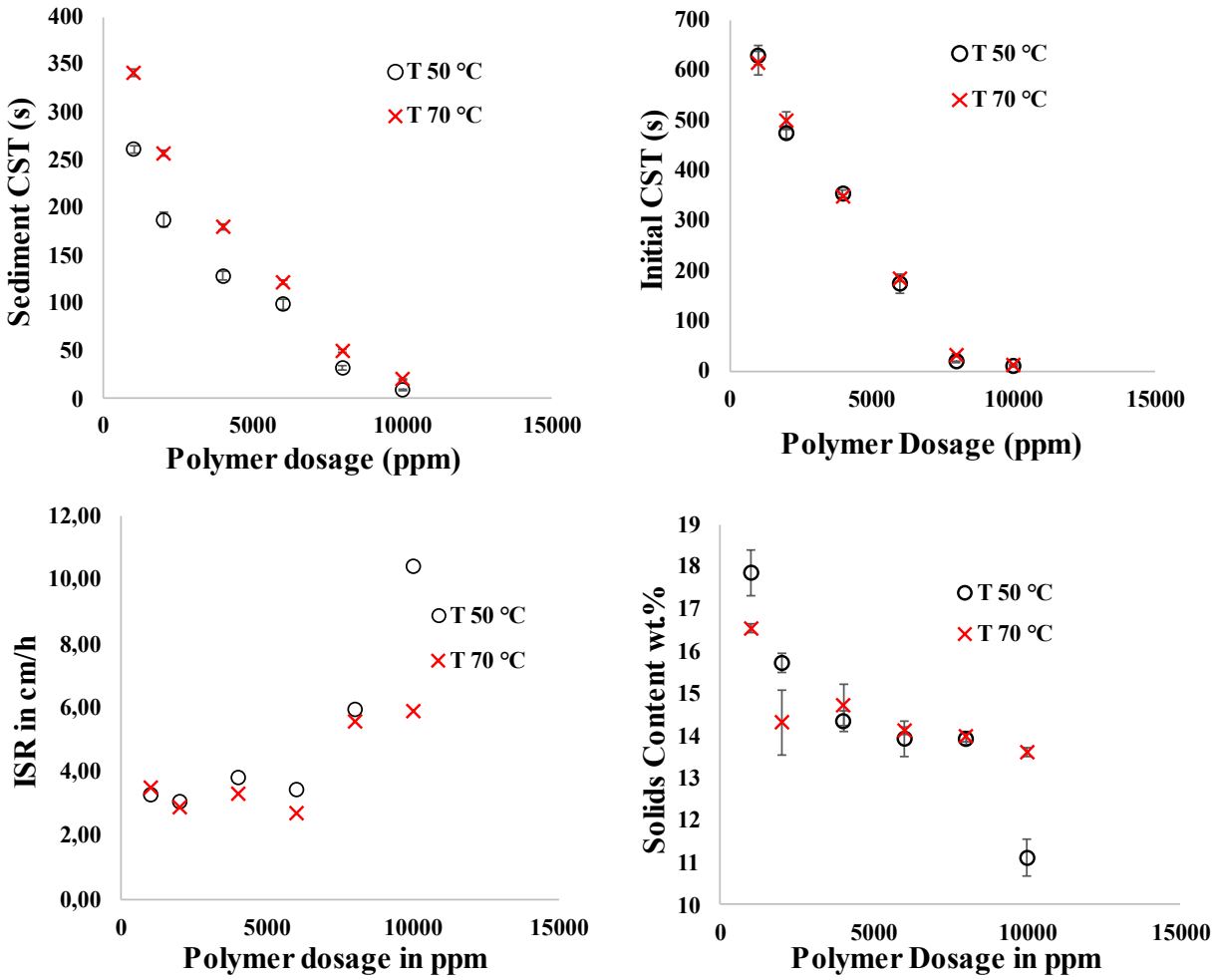

Figure 4.19 – Comparison of flocculation performance for two different polymerization temperatures 50 °C and 70 °C for F_4L_4.

4.4 Characterization and Flocculation Tests of AP-*g*-PVBTMAC-co-PAM

The flocs made with AP-*g*-PVBTMAC have lower ISR than those made with anionic polymers, and they also make sediments with decreasing solids content with increasing dosage. To better investigate these observations, random copolymer grafts with acrylamide and VBTMAC were produced (Figure 4.20) with different VBTMAC/acrylamide ratios. The hypothesis here was that acrylamide could favor the bridging mechanism and the formation of larger flocs, while keeping the advantage of VBTMAC units to compress the electrical double layer for the polymer

to adsorb on clay particles (leading to enhanced fines capture in comparison with pure PAM grafts).

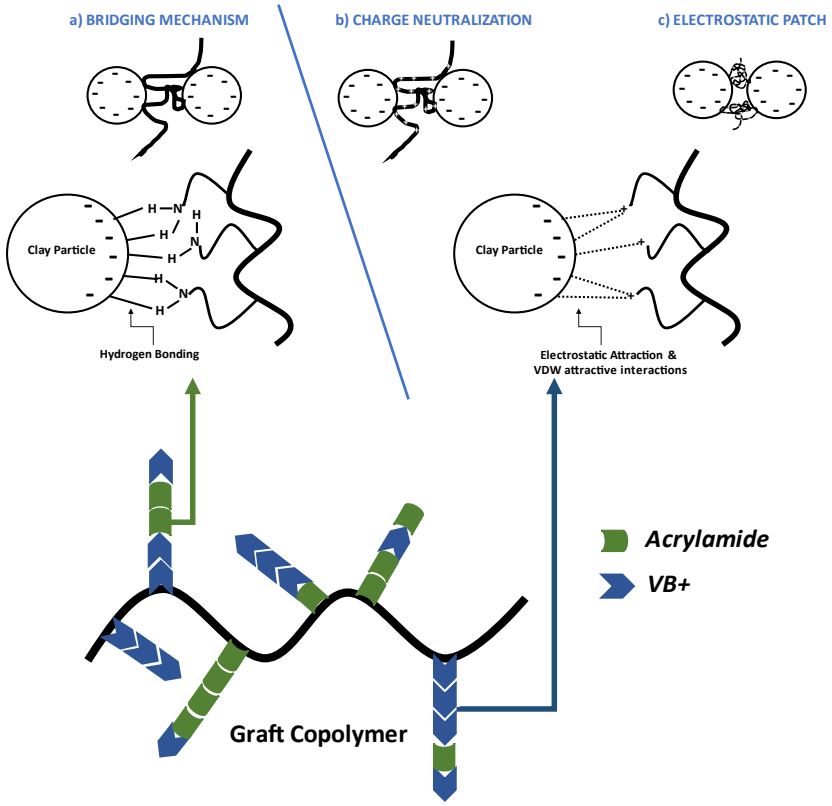

Figure 4.20 – Schematic of the double type of grafts copolymer on amylopectin backbone (in black).

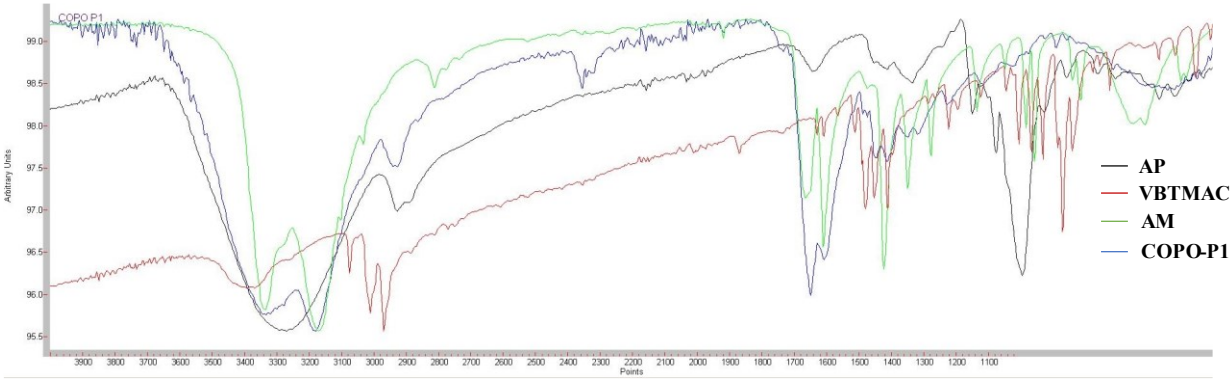

Figure 4.21 - FTIR spectrum of AP-*g*-(PVBTMAC-*co*-PAM) (example of sample Copo-P1).

Figure 4.21 presents the FTIR spectrum of the co-graft polymer P1 (Copo-P1, AP-*g*-(PVBTMAC-*co*-PAM)). The Copo-P1 spectrum presents the characteristic peaks related to AP as discussed in Figures 4.5 - 4.7. The clear double peak characteristic of primary amides at 3250-3350 cm^{-1}, and two strong peaks at 1600 and 1650 cm^{-1} corresponding to N-H bonding and C=O

amide stretch, respectively [74]. The theoretical copolymer fraction of VBTMAC in Copo-P1 was 0.4. The peaks characteristic of VBTMAC are less visible in the grafted product and probably overlap with some of the acrylamide peaks. Also, the unexpected peak at ~ 2350 cm^{-1} is likely due to CO_2 surrounding the sample during the run, it is probably not contained in Copo-P1. The FTIR analysis confirms the presence of characteristic peaks for both AP, PAM, and less clearly, VBTMAC in the AP-*g*-(PVBTMAC-*co*-PAM) sample, but it is unconclusive as regards to grafting.

Some of the copolymers synthesized were not fully soluble in water soluble and were not used in the flocculations. Only Copo-P1, Copo-P5, and Copo-P6 were used for the results presented in Figure 4.22.

Supernatant turbidity (after one week of settling, Figure 4.22.a) surprisingly increases from 23 to 180 NTU with polymer dosage for Copo-P1 showing a unique behavior, which corroborates the previous observations on ISR and solids content. The PAM-clays interactions may screen the attractive interactions between PVBTMAC grafts and fines required to obtain low supernatant turbidity.

Sediment solids content (Figure 4.22.b) decreases with polymer dosage for all flocculants because of the presence of PVBTMAC grafts. Therefore, all polymers have a similar performance except for Copo-P1, for which the decline is more marked likely because of its reduced cationic charge density since theoretically about 60% of the grafts are acrylamide.

Shorter grafts lead to the lowest initial CST for a given dosage based on the results presented in Figure 4.22.c, probably because shorter grafts produce more compact flocs initially. However, the opposite performance is seen after consolidation (Sediment CST, Figure 4.22.d) since longer grafts generate larger channels for water to go through. The behavior of Copo-P1 differs from the other polymers tested as the sediment CST remains high near 200 s regardless of the polymer dosage, which shows no efficient water release after consolidation with a majority of PAM grafts despite the presence of the amylopectin backbone. Water may be retained within the flocs because of hydrogen bonding between PAM's amide and water molecules, which balances the hydrophobic interactions with amylopectin.

The ISR (Figure 4.22.e) decreases fast from 33 to 4 cm/h for dosages of 2 kppm and 10 k ppm respectively, for Copo-P1, which theoretically contains a majority of acrylamide (Table 3.2).

But the ISR for Copo-P5 and Copo-P6 increases with dosage. It is likely that a majority of acrylamide incorporated in the graft copolymer leads to bridging forming larger flocs that settle faster, hence the larger ISR obtained with Copo-P1, but as the content of VBTMAC in the grafts increases, the ISR decreases because of the relative increase in cationic graft dosage, which may form smaller flocs that exhibit smaller settling rates. Once again, the change in graft length (from 63: Copo-P6 to 126: Copo-P5, Table 3.2) does not impact the ISR.

PVBTMAC remains at very low ISR regardless of the dosage in comparison with Copo-P5 and Copo-P6. The comparison with AP-g-PVBTMAC F_4L_4 (the best performing grafted structure as regards ISR) shows that the ISR increase is clearer with amylopectin and PVBTMAC alone without acrylamide. Therefore, the higher ISR of Copo-P5 and F_4L_4 compared to PVBTMAC is likely due to the presence of the AP backbone.

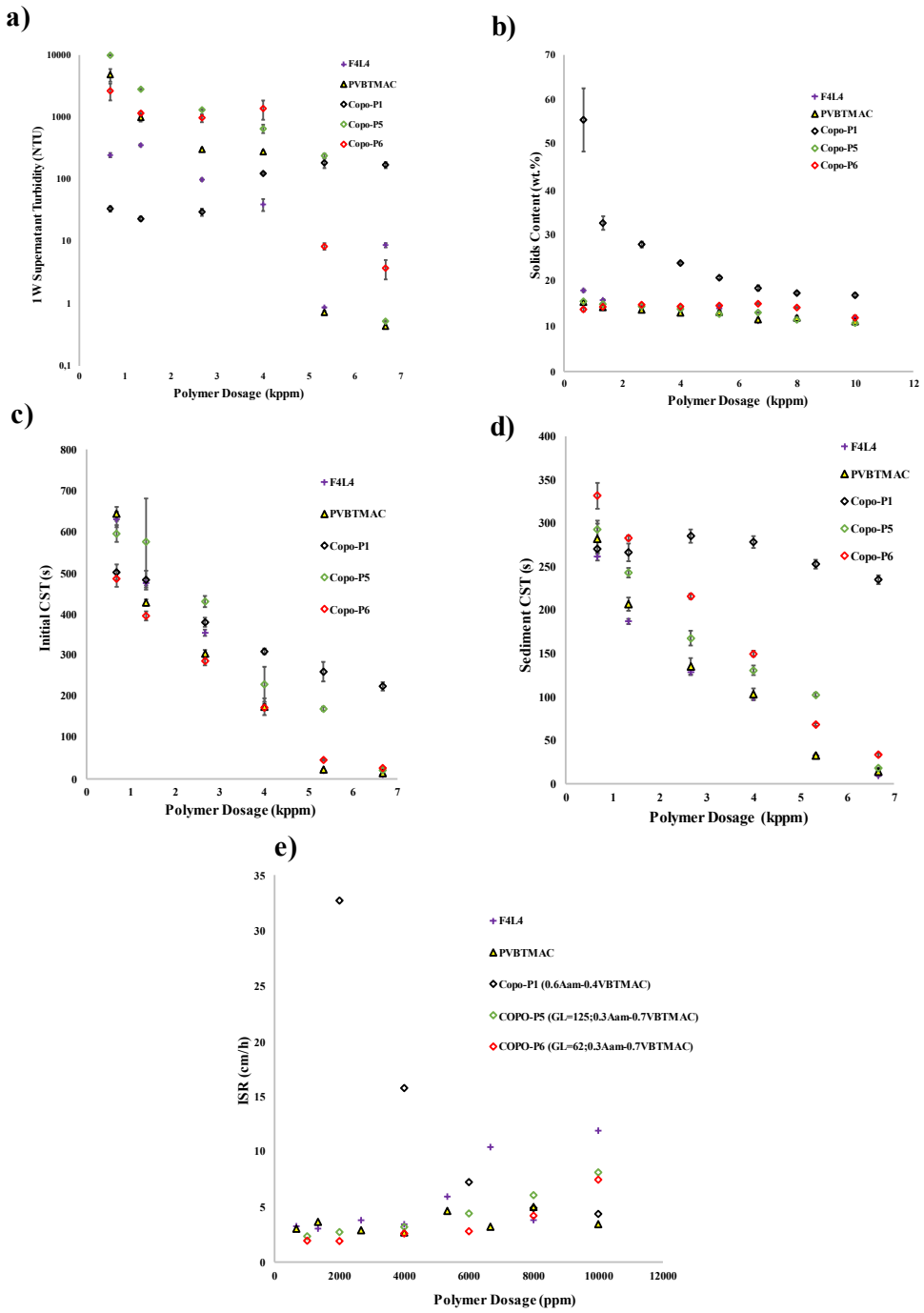

Figure 4.22 – Flocculation results of AP-*g*-(PVBTMAC-*co*-PAM) polymers at different dosages: a) ISR, b) sediment solids content, c) supernatant turbidity, and d/e) initial/sediment CST.

4.5 Addition of Two Polymers for MFT Flocculation – Preliminary Results

The results of the flocculation of 5 wt. % MFT with several flocculants are compared in Figure 4.23 and Figure 4.24.

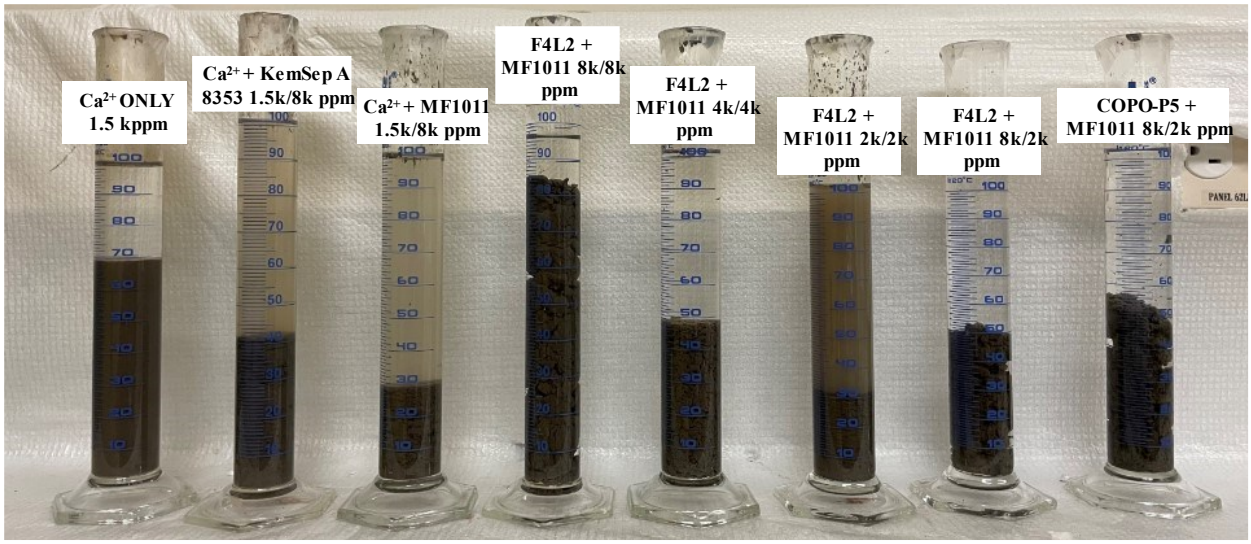

Figure 4.23 – Comparison of different dual polymer systems and commercial flocculants (KemSep A8353 and MF 1011) after 24 hours of settling.

Two commercial anionic flocculants were compared (in combination with 1.5 kppm Ca^{2+}, also used as a reference). As expected, when Ca^{2+} is used alone, no flocculation takes place. The ISR could not be measured since particles settled too slowly, but the coagulated solids released approximately 30 mL of clear supernatant water after 24 hours (Figure 4.23). Magnafloc 1011 (MF 1011) outperformed KemSep A 8353 in all metrics (Figure 4.24).

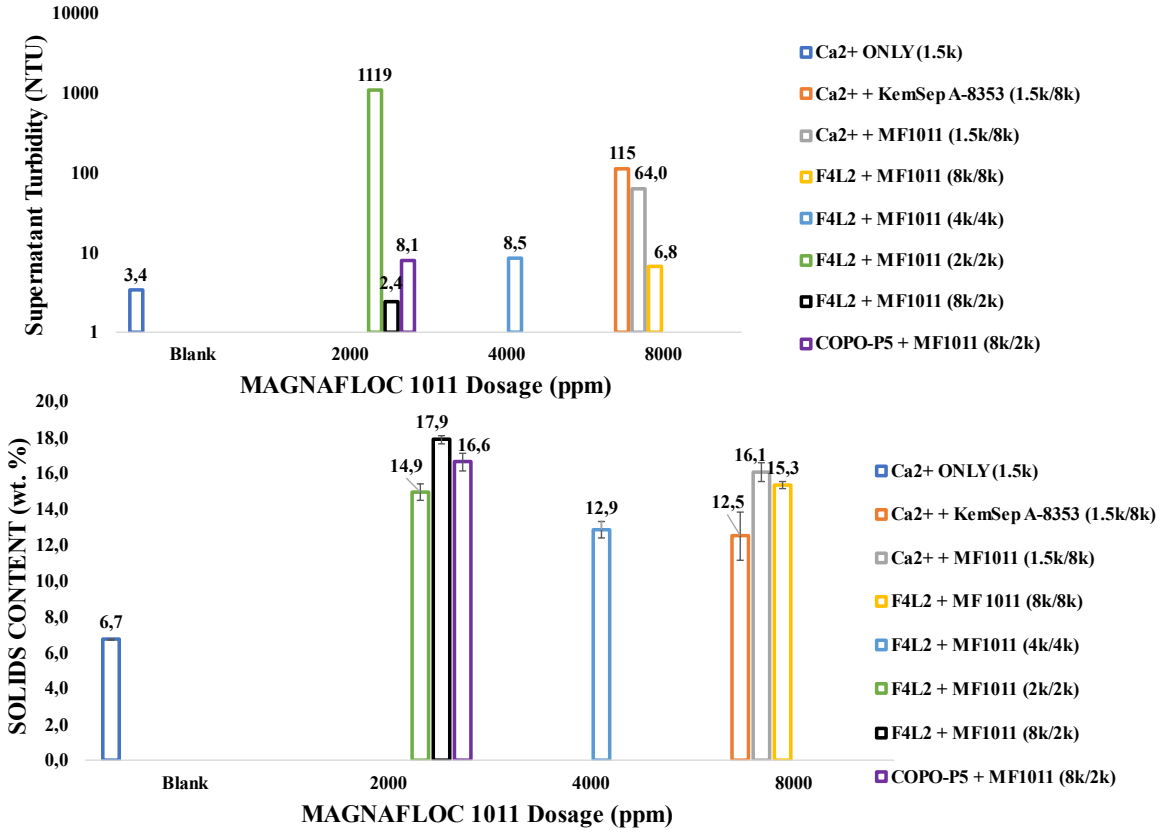

Figure 4.24 – Solids content and supernatant turbidity results of the comparison study.

The newly synthesized AP-*g*-PVBTMAC (F_4L_2), combined with MF1011, quickly formed shear-resistant large flocs (Figure 4.23) and produced a clear supernatant (< 10 NTU). The ISR could not be measured because the large flocs settled too fast. Interestingly, the large size of the flocs did not reduce the solids content, which remained close to that of MF1011 combined with Ca^{2+} (about 15 wt. %).

When the dosages of MF1011 and F_4L_2 were halved, the size of the flocs decreased linearly with the dosage; because less flocculant was used, fewer fines were captured and the supernatant turbidity increased, but it remained lower than with MF1011 and Ca^{2+} (Figure 4.24). The advantage of reducing the dosage of MF1011 is the decrease in the medium viscosity: while the large flocs formed with 8k (F_4L_2)/8k (MF1011) ppm settled almost instantaneously, despite the high medium viscosity, with 4k/4k ppm the viscosity is still high and hinders the settling of the smaller flocs, as shown in Figure 4.25. This issue was not observed for dosages below 4 kppm.

Figure 4.25 – Settling of the smallest flocs formed by F_4L_2 + MF1011 (4k/4k ppm).

At 2k/2k ppm, the cationic polymer dosage is not enough to capture all the fines. The turbidity increased dramatically to 1120 NTU, while the solids content remained unchanged at 14.9 wt. %. Using 1.5 kppm of Ca^{2+} neutralizes charges more effectively than 2 kppm of F_4L_2, as shown by the low supernatant turbidity (3.4 NTU) reached at a smaller dosage, likely because Ca^{2+} adsorb more effectively on the clay surface than F_4L_2, and also because the charge density of 1.5 kppm of calcium ions is higher than 2 kppm of F_4L_2.

Adding 8 kppm of F_4L_2 and 2 kppm of MF1011 produces large flocs with clear supernatant (2.4 NTU), likely because of the reduced viscosity that allowed for the settling of small particles. The solids content also increases to 17.9 wt. %, thus outperforming all the other systems.

Finally, the copolymer grafts Copo-P5 forms seemingly weaker flocs than pure VBTMAC grafted to AP when added with MF1011 and the turbidity measurements confirm that it captures fines less effectively (8.1 NTU for Copo-P5 versus 2.4 NTU for F_4L_2 with the same dosage). Some repulsive interactions may arise from the grafted polyacrylamide chains and the very high molecular weight anionic polyacrylamide (MF1011), similar to the overdosing phenomenon mentioned in previous studies [77].

In order to reproduce realistic conditions for the industry, higher MFT concentration flocculation – at 10 wt. % solids suspensions and undiluted – were conducted. Some measurements were also carried out instantaneously (Figure 4.26).

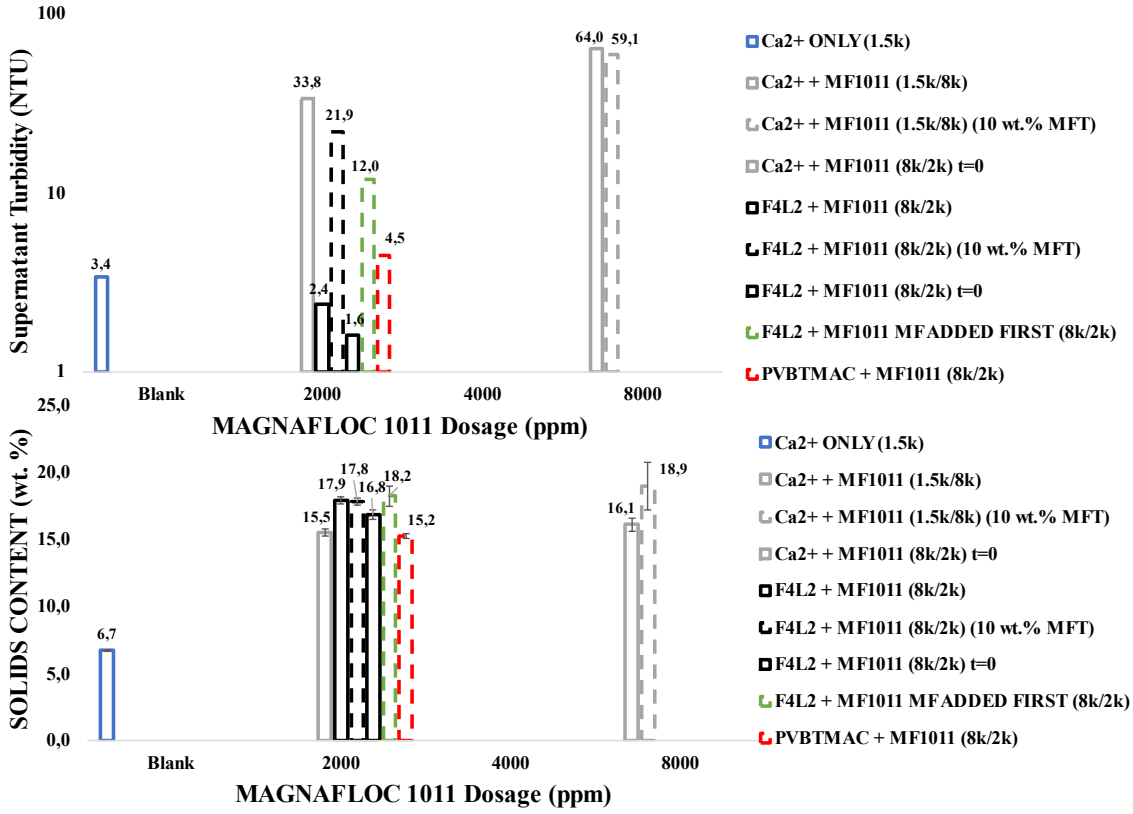

Figure 4.26 – Solids content and supernatant turbidity results in various conditions.

The performance of the commercial system (8k/8k of Ca^{2+} and MF1011) improved with an increase in suspension solids concentration from 5 to 10 wt. %: solids content increases to 18.9 wt. %, and the supernatant turbidity decreases to 59 NTU (Figure 4.26). Contrarily, F_4L_2/MF1011 is more sensitive to the suspension solids concentration (factor 10 increase on the supernatant turbidity). This confirms the previous observation that the cationic graft polymer is not as efficient as calcium ions to neutralize clay particles surface charges. The instantaneous measurements at 5 wt. % (instead of sampling after 24 hours of settling) do not show a significant difference in terms of solids content, but the turbidity decreases by a factor 2 for both systems with direct measurement (Figure 4.26).

The effect of amylopectin on flocculation of 5 wt. % MFT was also investigated by comparing AP-*g*-PVBTMAC results to the dual system PVBTMAC/MF1011 at the same dosage (8k/2k ppm). Amylopectin helps forming denser flocs (17.9 wt. % with F_4L_2 versus 15.2 wt. % with PVBTMAC).

The structure of the flocs visually differs depending on the sequence of addition of both polymers (Figure 4.27), which is confirmed with solids content results (Figure 4.28) after press filtration (10 psig, 20 min) on undiluted MFT.

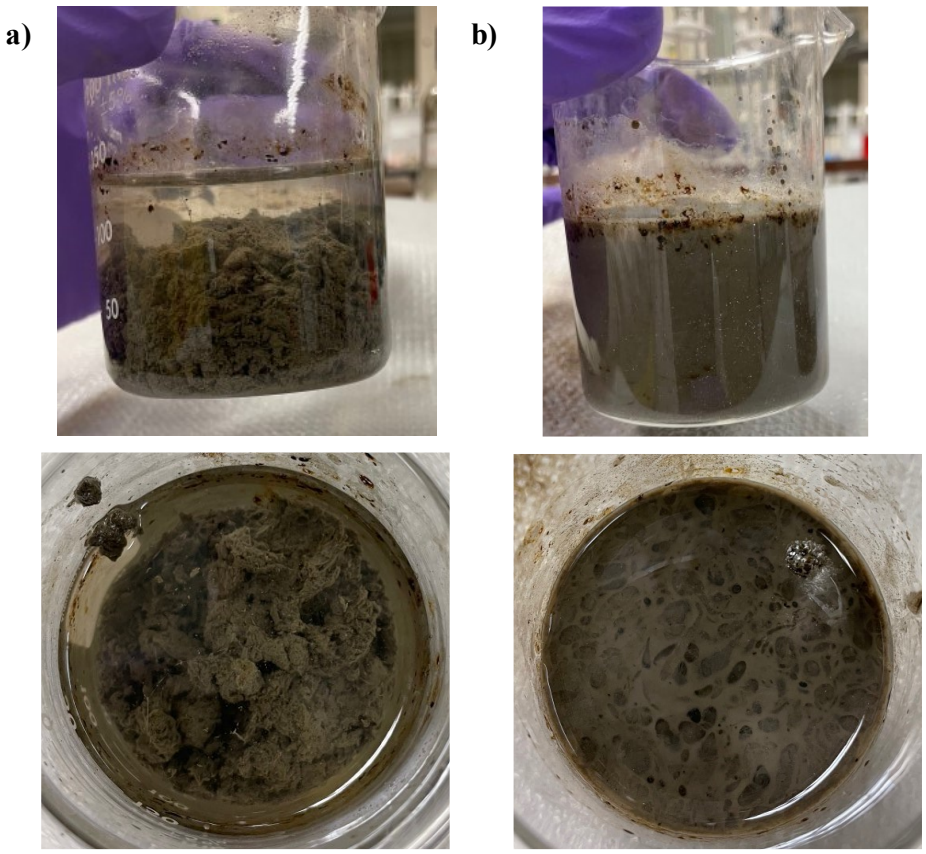

Figure 4.27 – Instantaneous flocculation results of AP-*g*-PVBTMAC (F_4L_2) and MF1011 on 5 wt. % MFT: a) F_4L_2 added first, b) MF1011 added first.

Flocculations of undiluted MFT (Figure 4.28) reveal that PVBTMAC combined with MF1011 is once again outperformed by the combination of MF1011 with amylopectin cationic graft polymers. F_4L_4 leads to higher solids content after press filtration compared to F_4L_2 when used with MF1011 (54.3 wt. % compared to 47.8 wt. %). Since F_4L_2 and F_4L_4 have the same graft frequency, the greater graft length of F_4L_4 likely produces less dense flocs that allow for a better water release during the press filtration because of the larger channels within the flocs. For both F_4L_4/MF1011 and Ca^{2+}/MF1011, slow addition of the polymers decreases the solids content (from 54.3 to 50.3 wt. % and from 61.2 to 58 wt. % respectively). Therefore, the effect of the mode of addition is investigated in Section 4.6.

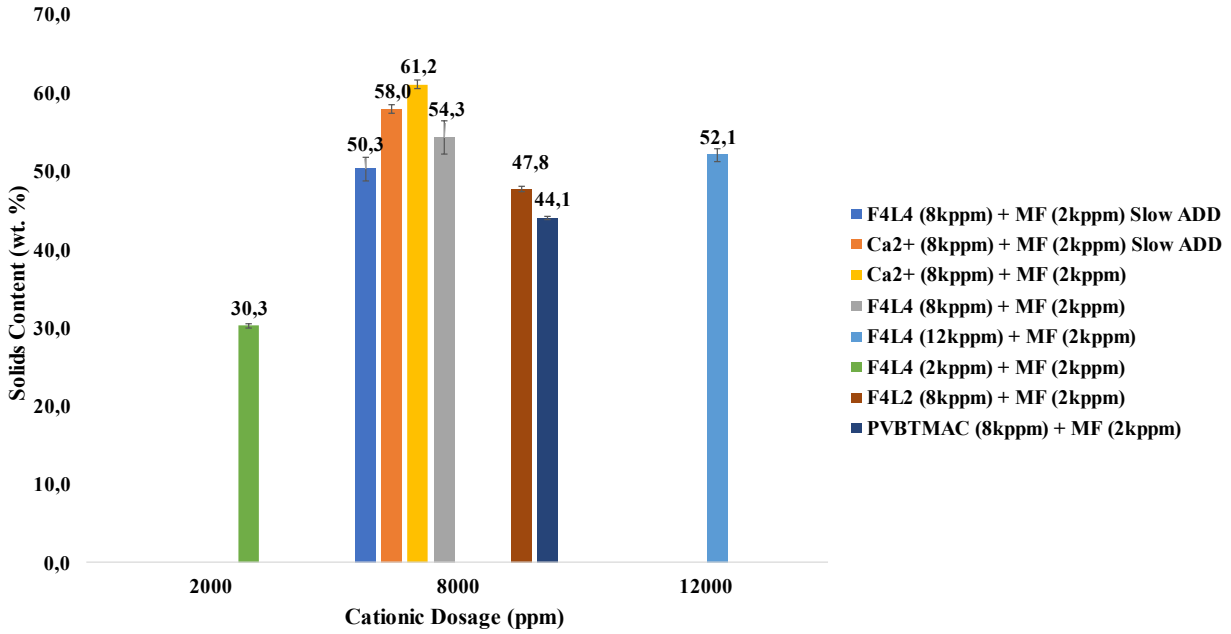

Figure 4.28 – Solids content results of undiluted MFT flocculation.

The type of impeller also impacted the flocculation results for a same mixing speed of 300 rpm, as mentioned in previous studies [131]. Polymers were not uniformly dispersed in the medium and remained unsheared in the dead zone – where flocs were immediately settling – under the blades of a typical radial mixer. Therefore, a new impeller has been designed and 3D printed to correct this issue (Figure 4.29).

Figure 4.29 – 3D printed radial impeller.

The new impeller (Figure 4.30.A) prevents the flocs from settling at the bottom of the beaker in the dead zone like with the usual radial mixer (Figure 4.30.B). Mixing conditions affected flocculation (of 6 and 14 wt. % kaolinite suspension), as shown by the comparison of: this new impeller, the usual radial mobile, and an helicoidal mixer (presented in Appendix B7).

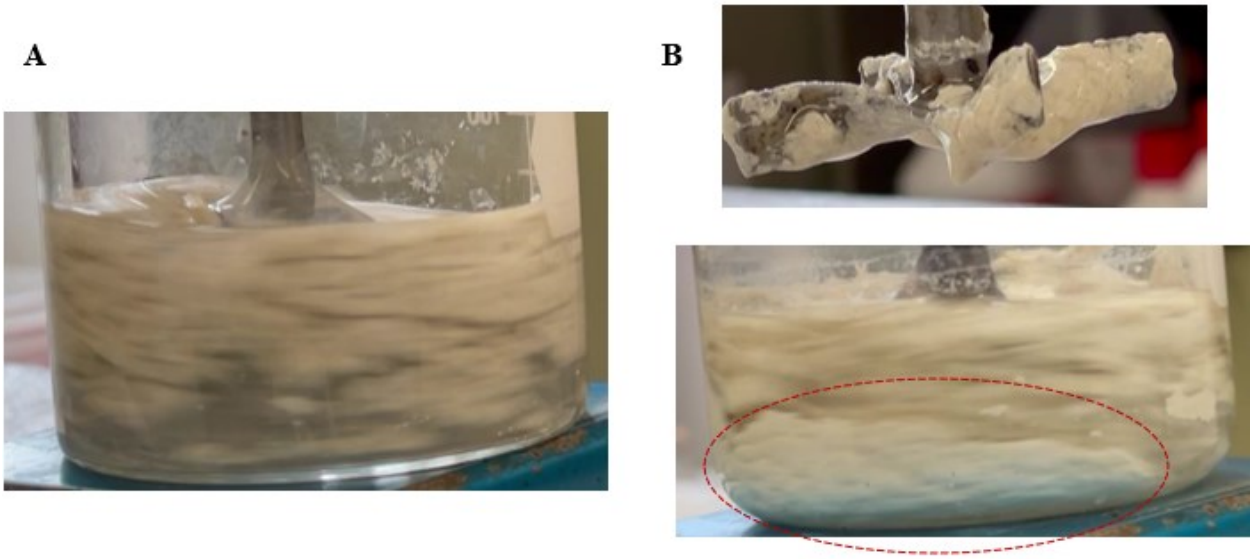

Figure 4.30 – Comparison between impeller mixing efficiency: A) 3D printed impeller and B) usual radial impeller.

4.6 Effect of AP-*g*-PVBTMAC and MF1011 dosages, addition flowrates and kaolinite suspension solids content on flocculation

4.6.1 Five Factors CCD Flocculation Results

Table 4.9 summarizes the result of the central composite design of experiments used to quantify the effects of AP-*g*-PVBTMAC and MF1011 dosages, addition flowrates, and kaolinite suspensions solids content (Table 3.4) on the responses: initial CST, supernatant turbidity at $t = 0$ and sediment solids content. Second order regressions were obtained using ANOVA and the response surface methods (*rsm)* package from the software R-Studio [132]. Statistically significant predictors – the coefficient of determination (R^2), the adjusted determination coefficient (R^2_{adj}), the significant p-value with a 95 % confidence interval ($p < 0.05$) and a non-significant lack of it (LOF) (by making sure that LOF p-value > 0.1, while F-value > LOF p-value) [133] – were used to develop the empirical models for the response variables. Residual plots were also generated to ensure the accuracy of the model. The number of degrees of freedom required to estimate the internal error was guaranteed because the number of runs carried out (48) was much higher than the maximum number of terms required to describe a second order model with interactions (a maximum of 21 coefficients were required for the regression).

Table 4.9 – Summary of the CCD flocculation results.

RUN N°	*Initial CST (s)*	*Supernatant Turbidity at t=0 (NTU)*	*Sediment Solids Content (wt.%)*
1	670 ± 12	235 ± 1	42.4 ± 0.3
2	316 ± 8	39.9 ± 0.0	49.9 ± 0.5
3	186 ± 1	30.1 ± 0.1	50.9 ± 0.4
4	63.1 ± 3.9	14.2 ± 0.1	45.5 ± 0.2
5	171 ± 3	33.8 ± 0.1	47.4 ± 0.4
6	279 ± 6	35.3 ± 0.2	41.3 ± 0.3
7	59.8 ± 2.9	53.0 ± 0.1	46.9 ± 0.7
8	497 ± 10	91.4 ± 0.2	45.9 ± 0.1
9	308 ± 6	57.7 ± 0.1	43.2 ± 0.2
10	408 ± 5	55.9 ± 0.1	51.7 ± 0.7
11	224 ± 4	106 ± 0	41.6 ± 0.2
12	251 ± 5	28.1 ± 0.1	45.4 ± 0.2
13	630 ± 11	189 ± 0	46.8 ± 0.2
14	244 ± 10	49.7 ± 0.1	50.5 ± 0.1
15	288 ± 5	144 ± 0	48.1 ± 0.1
16	386 ± 4	46.1 ± 0.3	46.6 ± 0.2
17	257 ± 6	43.0 ± 0	48.6 ± 0.1
18	15.5 ± 0.2	147 ± 1	48.3 ± 0.1
19	13.4 ± 0.4	424 ± 0	49.3 ± 0.4
20	14.4 ± 0.9	385 ± 0	50.9 ± 0.1
21	174 ± 5	30.4 ± 0.2	46.8 ± 0.2
22	15.8 ± 1.5	324 ± 1	46.9 ± 0.3
23	325 ± 1	20.4 ± 0.0	45.7 ± 0.2
24	275 ± 9	14.4 ± 0.1	45.1 ± 0.2
25	13.3 ± 0.3	241 ± 0	51.3 ± 0.2
26	263 ± 10	35.6 ± 0.1	46.8 ± 0.3
27	475 ± 11	63.6 ± 0.1	49.2 ± 0.2
28	313 ± 13	121 ± 1	41.7 ± 0.1
29	14.9 ± 1.1	60.5 ± 0.1	51.7 ± 0.0
30	344 ± 7	108 ± 0	46.6 ± 0.1
31	23.7 ± 3.7	626 ± 2	52.7 ± 0.2
32	275 ± 7	99.7 ± 0.0	41.8 ± 0.7
33	281 ± 9	53.1 ± 0.0	52.5 ± 0.6
34	372 ± 13	73.0 ± 0.1	52.6 ± 0.3
35	436 ± 18	67.0 ± 0.1	47.5 ± 0.4
36	609 ± 14	1450 ± 2	59.6 ± 0.3
37	375 ± 8	164 ± 1	44.5 ± 0.1
38	128 ± 10	47.6 ± 0.3	44.6 ± 0.3
39	54.7 ± 7.1	34.1 ± 0.2	46.9 ± 0.4
40	291 ± 4	90.7 ± 0.1	45.3 ± 0.3
41	158 ± 1	42.9 ± 0.2	53.1 ± 0.8
42	457 ± 7	66.0 ± 0.1	48.6 ± 0.2
43	235 ± 6	36.7 ± 0.3	43.8 ± 0.3
44	401 ± 8	32.1 ± 0.1	41.6 ± 0.3
45	13.6 ± 2.0	67.6 ± 0.1	52.9 ± 0.6
46	599 ± 5	97.4 ± 0.4	44.5 ± 0.2
47	12.4 ± 0.2	198 ± 1	51.1 ± 2.2
48	269 ± 17	43.0 ± 0.1	43.8 ± 0.3

4.6.2 Initial CST Regression Model

The CST model (Eq. 4.2) was obtained after dropping out insignificant predictors through the ANOVA study integrated to the *rsm* package. To eliminate the non-normality in the residuals, the square root of the initial CST was used in the model. This type of transformation – to find a function that meets the assumptions of the regression model – is common in regression analysis [134]. The factors X_1-X_5 are defined in Table 3.3.

$$\sqrt{CST} = 14.06 - 4.60X_1 + 3.81X_2 + 0.12X_3 + 1.47X_5 + 1.88X_1X_2 - 0.89X_1X_3 + 0.81X_3X_5 + 0.78{X_3}^2$$

(Eq. 4.2)

Table 4.10 – Statistical results of the initial CST model.

Statistical descriptor	
R^2	0.86
R^2_{adj}	0.84
p-value	1.4×10^{-14}
F-value vs. LOF p-value	1.13 > 0.39 (>0.1)

Table 4.10 confirms that the criteria imposed for model validation were satisfied, with a good agreement between predicted and observed CST values, as shown in Figure 4.31.b. The residual plots for all the predictors and the experimental values (Figure 4.31.a) are randomly distributed around 0 over the range covered in the CCD, showing that the model is not biased.

Terms containing the cationic polymer dosage (X_1) reduce the initial CST because of the hydrophobicity provided by amylopectin backbones and PVBTMAC grafts. This observation also agrees with the results from screening tests. Terms containing the anionic polymer dosage (X_2) increase the initial CST, likely because of the high affinity of PAM with water (Figure 4.32.a). The solids content of the kaolinite suspension (X_5) also increases the CST. As the preliminary results showed, the dual polymer system does not perform well with concentrated suspensions because of mixing issues that hinder the effective collisions between polymer and clay particles.

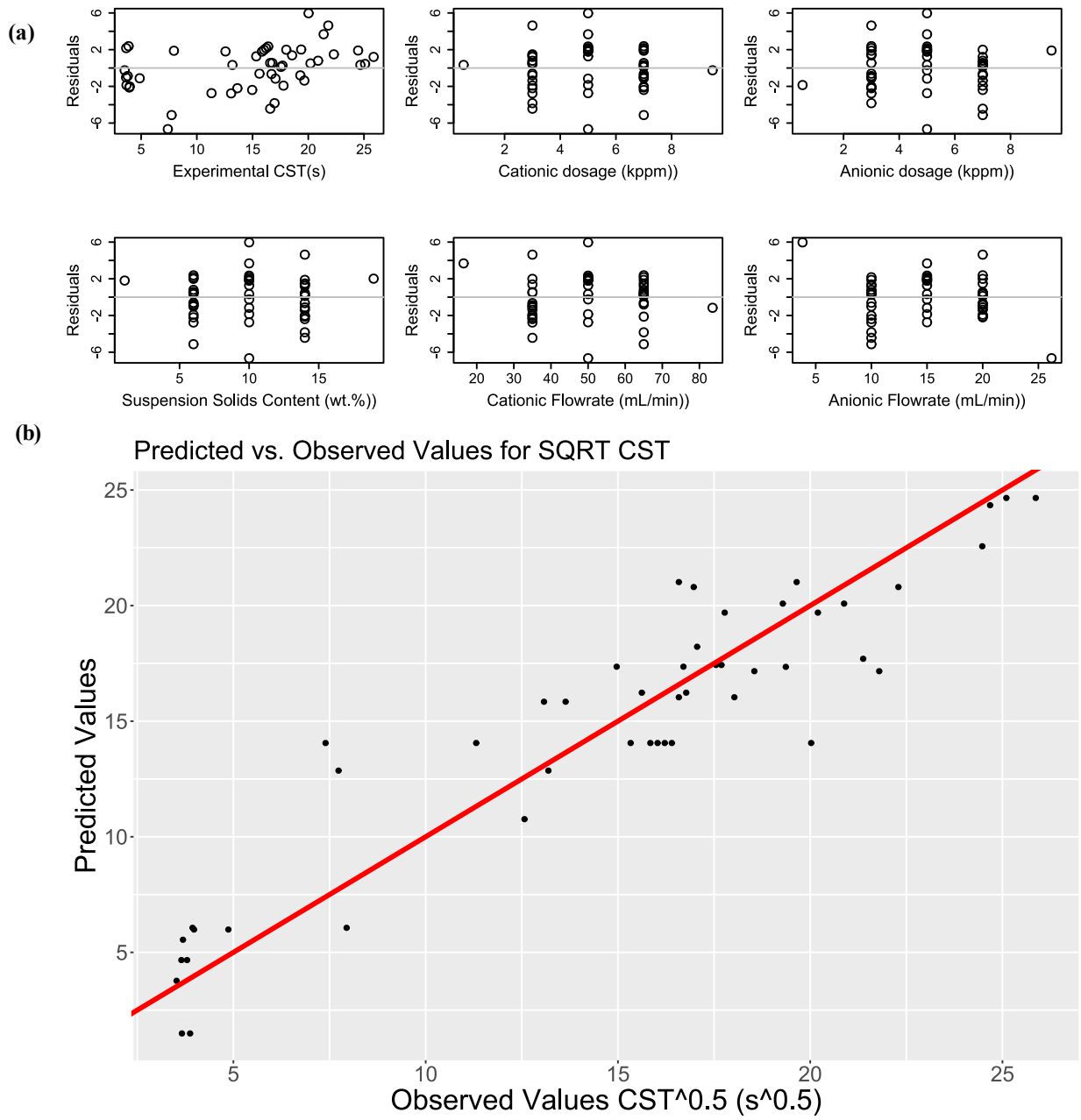

Figure 4.31 – a) Residual plots, b) Predicted versus observed values for the initial CST model.

Interestingly, the initial CST is not affected by the anionic polymer flowrate (X_4) (it is only significantly impacted by its dosage, see Figure 4.32.a), but it decreases with a fast addition of the cationic polymer (X_5) (see the quadratic term in Eq. 4.2 and Figure 4.32.c). This could be attributed to the major role of the cationic polymer, which first destabilizes the suspension and starts forming

small dense flocs that are then bridged together with the addition of the anionic polymer. The flowrates studied in this CCD are not symmetrical because the results found from the half-factorial screening design (Appendix B8) suggested that a higher cationic flowrate favoured flocculation (since the suspended solids have to be first destabilized before flocculation can take place).

The contour plots of the interaction terms presented in Figure 4.32.a and Figure 4.32.b show that aiming at the highest cationic addition flowrate with diluted suspensions (decreasing the suspension solids content) and high dosage minimizes the initial CST.

Because of the transformation operated on the CST response, the model is not applicable for cationic dosages higher than 6k ppm, where it would predict an unacceptable negative square root. Nevertheless, it has been chosen to model the system since most polymers will never be used at dosages above 6k ppm in the industry. The summary of the statistical analysis of the model is presented in Appendix B9.

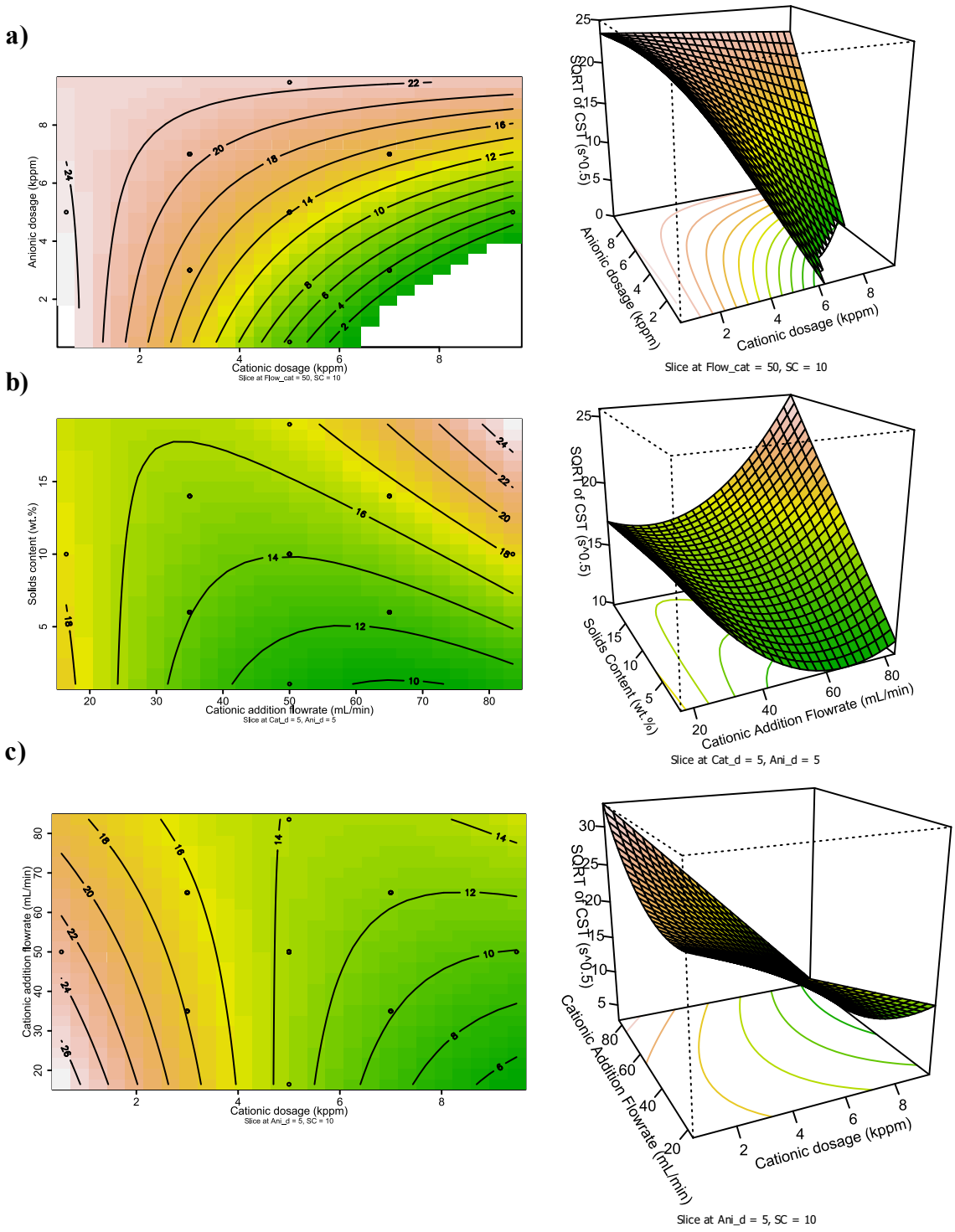

Figure 4.32 – Surface response of initial $\sqrt{\mathbf{CST}}$ as a function of: a) anionic and cationic dosages, b) suspension solids content and cationic addition flowrate, c) cationic addition flowrate and dosage.

4.6.3 Supernatant Turbidity Regression Model

The supernatant turbidity model as a function of the statistically significant coded factors is presented in Eq. 4.3 and Table 4.11. The anionic addition flowrate was found to be insignificant and was rejected from the model.

$$\boldsymbol{LOG(Turbidity) = 4.47 - 0.02X_1 - 0.17X_2 + 0.04X_3 + 0.25X_5 - 0.37X_1X_2 + 0.26X_2X_3 - 0.23X_1X_3 + 0.14X_2X_5 - 0.12X_1X_5 + 0.44{X_1}^2 + 0.09{X_2}^2 + 0.11{X_5}^2}$$

(Eq. 4.3)

Table 4.11 – Statistical results of the supernatant turbidity (t = 0) model

Statistical descriptor	
R^2	0.63
R^2_{adj}	0.52
p-value	3.2×10^{-5}
F-value vs. LOF p-value	2.41 > 0.03 (<0.1)

The model fails to describe the system accurately for supernatant turbidity (Table 4.11, summary in Appendix B8), even though, it still describes the observed trends (Figure 4.33.b). Since the turbidity response is noisy, the lack of fit is significant and the adjusted coefficient of determination is low. The unexplained variance may be caused by the viscosity of the supernatant because of MF1011. Since turbidity measurements were conducted immediately after the flocculants were added, some primary flocs may not have had time to settle when MF1011 dosage was high, which introduces a bias related to MF1011 dosage (faster settling at low dosage, bias visible on residual plots Figure 4.33.a). Supernatant turbidity is also sensitive to the hydrodynamic conditions when measured directly after flocculation and the reproducibility is a challenge, which could also explain the outliers underestimated by the model at the highest turbidity (Figure 4.33.a).

With these model limitations in mind, contour plots (Figure 4.34) show that the optimum would be to keep dosages close to ~ 5 – 6 kppm for both polymers (Figure 4.34.a, c, d). With these dosages, a wide range of cationic addition flowrate (from 20 to 80 mL/min) can be covered without impacting the supernatant turbidity. Contrarily, increasing the suspension solids content will inevitably increase the supernatant turbidity (Figure 4.34.b).

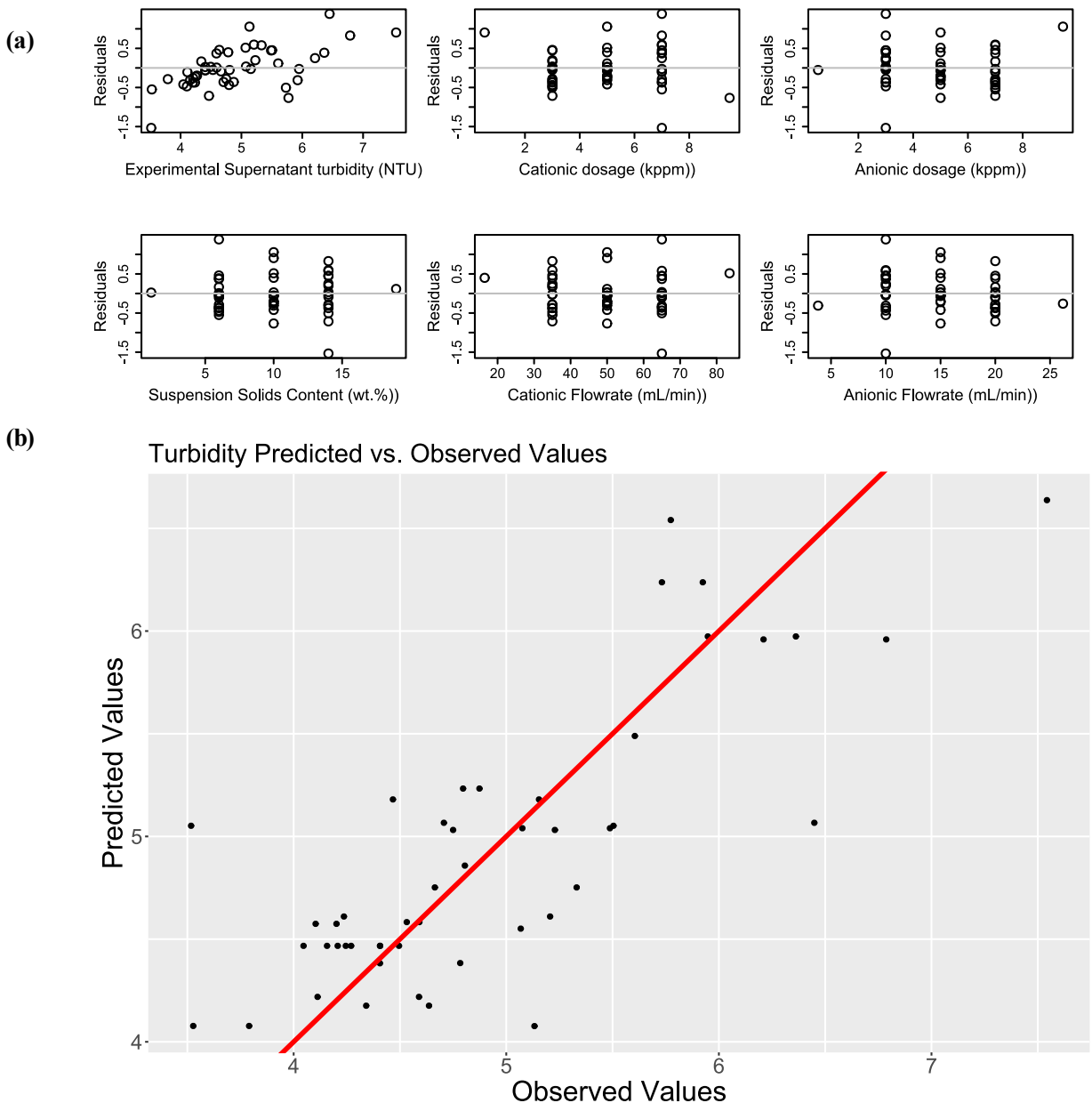

Figure 4.33 – a) Residual plots, b) Predicted versus observed values for the initial supernatant turbidity model.

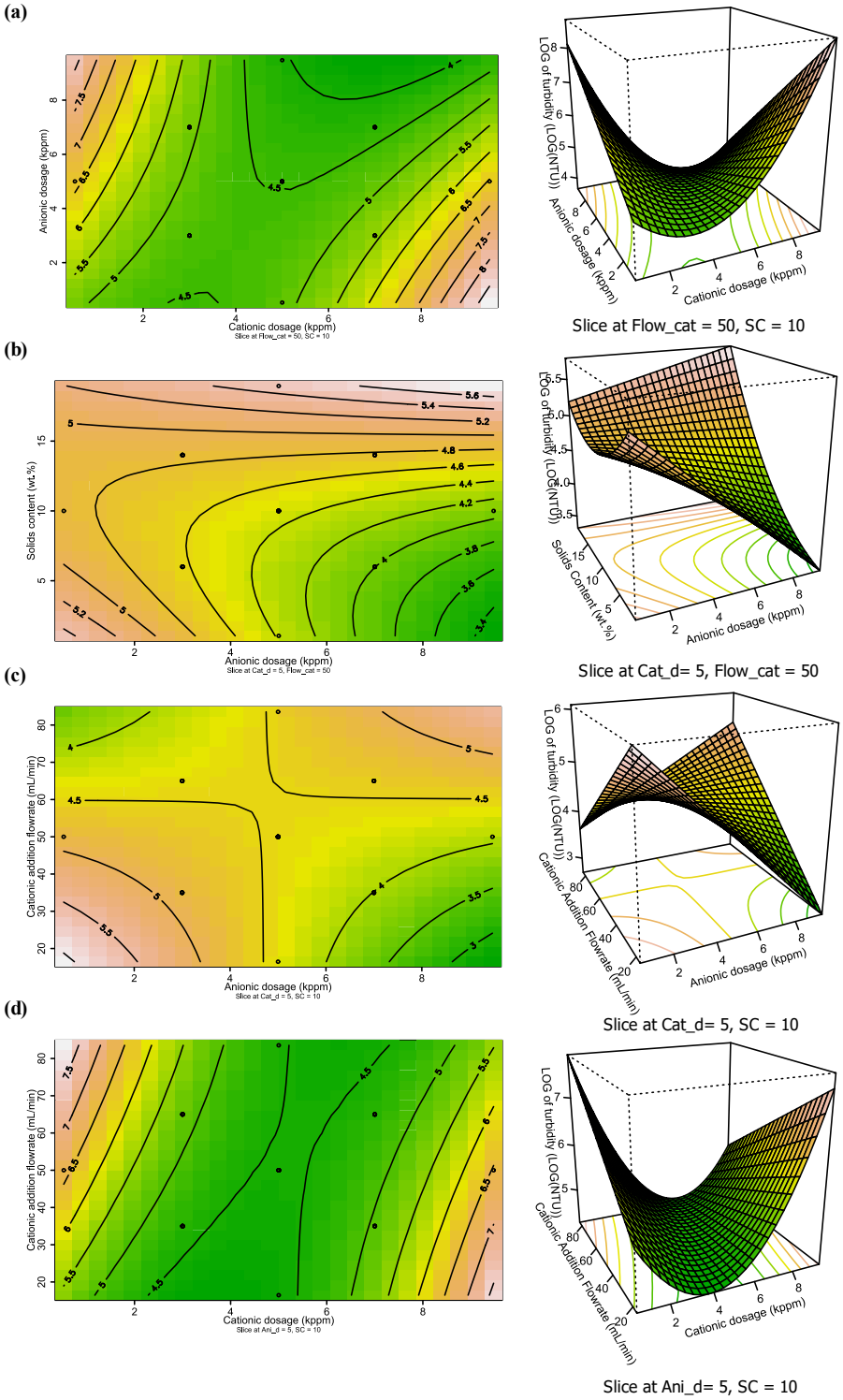

Figure 4.34 – Surface response of initial $\boldsymbol{LOG(Turbidity)}$ as a function of: a) anionic and cationic polymers dosages, b) suspension solids content and anionic polymer dosage, c) cationic addition flowrate and anionic dosage and d) cationic dosage.

4.6.4 Flocs Solids Content Regression Model

Solids content measurement needed to be modeled as $\sqrt{SC}$ to obtain the best statistical results (Table 4.12). This time the analysis of p-values for each predictors showed that the cationic addition flowrate was not significant. After rearranging the model, the solids content depends on cationic and anionic polymers dosages (X_1 and X_2 respectively), anionic flowrate (X_4) and kaolinite suspension solids content (X_5) as shown in (Eq. 4.4).

$$\sqrt{SC} = 6.754 - 0.07X_1 - 0.13X_2 - 0.08X_4 - 0.14X_5 - 0.07X_1X_2 - 0.05X_2X_5 + 0.12{X_1}^2 + 0.03{X_2}^2 - 0.03{X_4}^2 + 0.03{X_5}^2$$

(Eq. 4.4)

Table 4.12 – Statistical results of the solids content model

Statistical descriptor	
R^2	0.84
R^2_{adj}	0.79
p-value	1.19×10^{-11}
F-value vs. LOF p-value	1.07 > 0.43 (>0.1)

The statistical results (Table 4.12) and the residual plots (Figure 4.35.a) are satisfactory and the model fits well the experimental trends (Figure 4.35.b). The most important contributions to flocs solids content are the suspension solids content, the anionic dosage, and the cationic dosage. Suspension solids content decreases the solids content of the flocs as expected (Eq. 4.4 and Figure 4.36.c). Even if there might be more particles available for adsorption, the probability of effective collisions between the polymer and clay may be decreased because of the poor mixing. Clay particles may form small clusters at high concentration (not house of cards gelation because the clay content remain smaller than 30 wt. % and the pH of 7.9 is not favorable [40]), which could also hinder the ability of the polymers to flocculate the particles as some adsorption sites become unavailable.

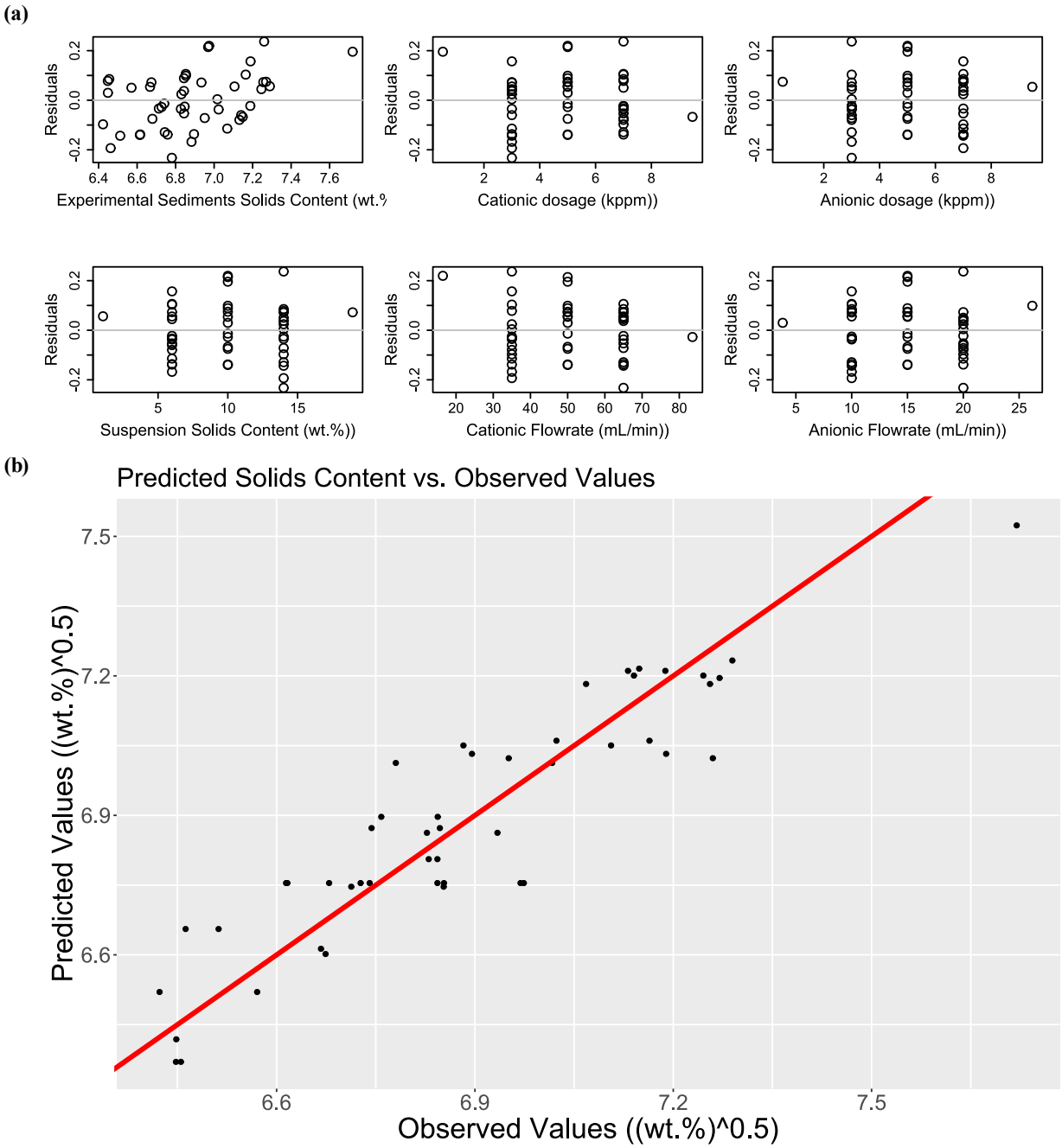

Figure 4.35 – a) Residual plots, b) Predicted versus observed values for the initial supernatant turbidity model.

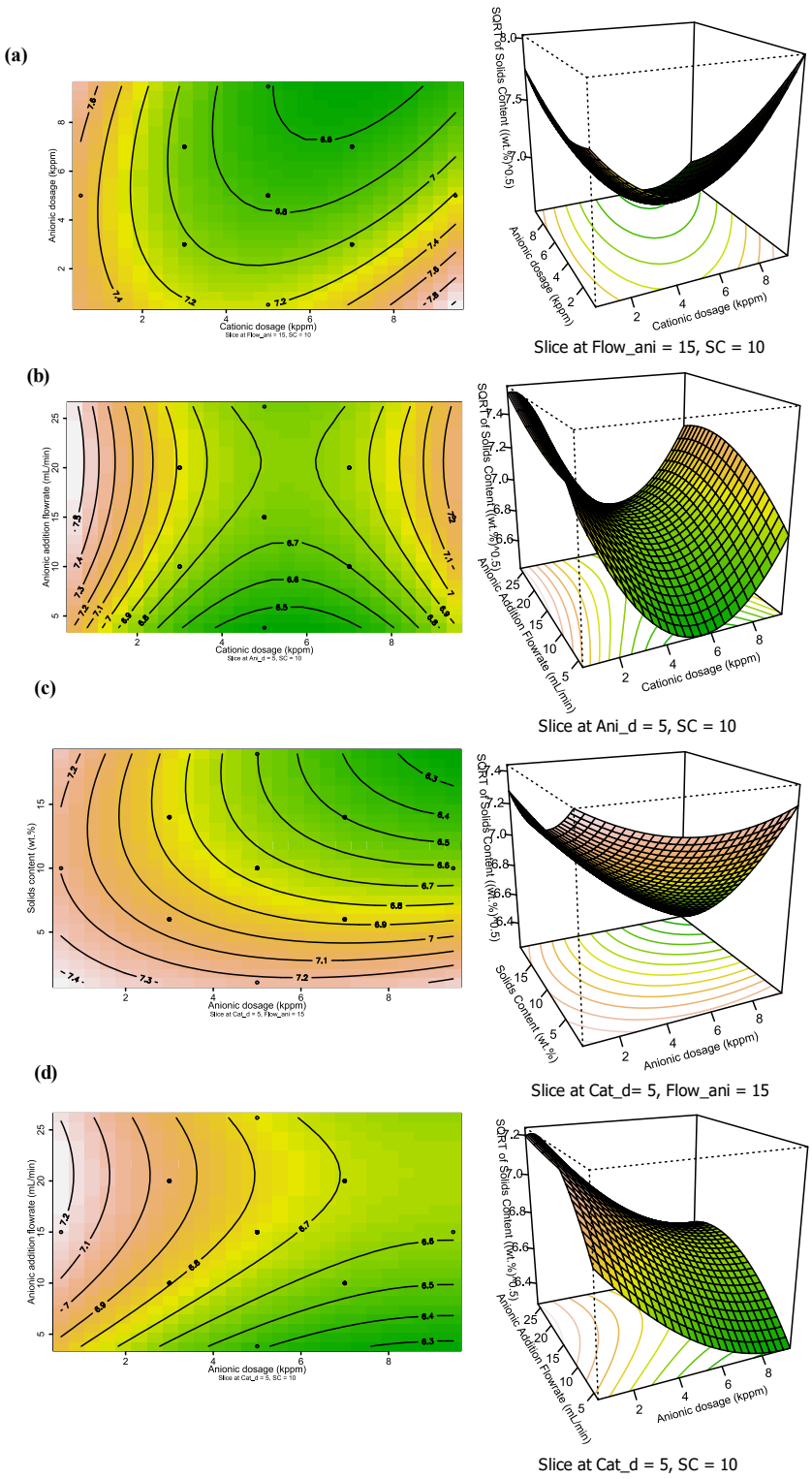

Figure 4.36 – Surface response of initial $\sqrt{SC}$ as a function of: a) anionic and cationic dosages, b) anionic addition flowrate and cationic dosage, c) suspension solids content and anionic dosage, d) anionic addition flowrate and dosage.

Increasing the MF1011 dosage is also detrimental to the solids content of the flocs, as the large flocs it produces are more likely to retain water than the dense flocs obtained with AP-*g*-PVBTMAC (Figure 4.36.a). Contour plots show that a low anionic dosage (< 2 kppm) (Figure 4.36.a, c, d) and low suspension solids content (Figure 4.36.c) favor high flocs solids content. Contrarily, high anionic addition flowrate (20 mL/min) yields the highest solids content (Figure 4.36.b), while extremes in cationic dosage (< 2 kppm, > 7 kppm) achieve high solids content. Since a cationic dosage inferior to 2k ppm does not capture fines efficiently (see preliminary results in Section 4.5), a high cationic dosage (> 7 kppm) is advised. This is still a problem for the large-scale application of this type of dual system, the dosage required for effective flocculation may be reduced by improving the control of the cationic polymer's structure and its charge density.

Obtaining the optimum conditions for each response is hard because of the number of factors, but using desirability functions (defined in Appendix B10) helps obtain them. Because of the poor modelling of the supernatant turbidity response, it was excluded from the objective function. The two following conditions were defined for a satisfactory flocculation:

- Need a minimum sediment solids content of 53 wt. %
- Need a maximum CST of 20 s

A portion of the code used to achieve this work is presented in Appendix B10.

In good agreement with the previous results, the desirability functions predict that the two criteria defined are met for a cationic dosage superior to 7 kppm (Figure 4.37.a). Contrarily, the anionic dosage needs to be lower than 2 kppm if its addition flowrate remains low (< 10 mL/min) (Figure 4.37.b, c and d). But no conditions are found on the cationic addition flowrate (Figure 4.37c), which may be due to the objectives defined being too restrictive.

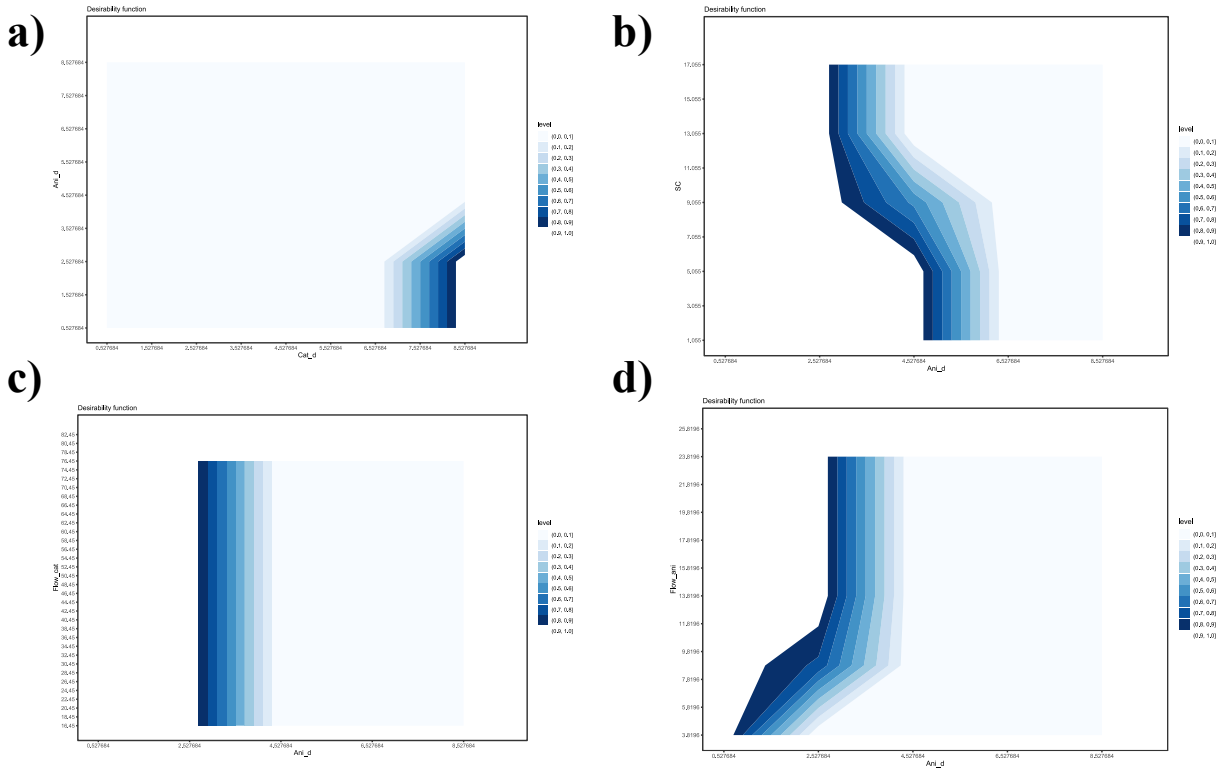

Figure 4.37 – Results of the optimization study to reach a minimum 53.1 wt. % solids content and a maximum 20 s CST.

4.6.5 Kaolinite Suspension Ageing

Over the course of the 48 runs required for the full CCD design, the kaolinite suspension aged, which modified its properties. The first observation of suspension ageing is presented in Figure 4.38.

Figure 4.38 – One week old kaolinite suspension.

Some clay or impurities clusters were formed, despite the constant mixing and the parafilm sealing. Therefore, a PSD analysis has been carried out on the aged suspension to compare it with the fresh PSD presented in Section 4.1.3, the results are presented in Table 4.13.

Table 4.13 – PSD results in volume basis of the one-week-old kaolinite suspension.

VOLUME		D[3,2] (µm)	D[4,3] (µm)	D_{10} (µm)	D_{50} (µm)	D_{90} (µm)	Weighted Residual (%)	Specific Surface Area (m^2/kg)
RUN 1	Pre-Sonication	1.28	2.48	0.551	1.94	5.28	0.98	4694
	Post-Sonication	1.26	2.59	0.527	2.07	5.52	0.98	4748
RUN 2	Pre-Sonication	1.26	2.45	0.543	1.91	5.23	1.03	4764
	Post-Sonication	1.24	2.54	0.520	2.03	5.44	1.05	4824
RUN 3	Pre-Sonication	1.23	2.40	0.533	1.85	5.14	1.03	4881
	Post-Sonication	1.22	2.51	0.511	1.97	5.41	1.02	4933
MEANS	Pre-Sonication	1.26	2.44	0.540	1.90	5.22	1.01	4780
	Post-Sonication	1.24	2.55	0.520	2.02	5.46	1.02	4835
GLOBAL MEANS		1.25	2.50	0.530	1.96	5.34	1.02	4807

When comparing the PSD from the one-week-old suspension (Table 4.13) to the fresh suspension (Table 4.4), all descriptors of the distribution are surprisingly smaller for the old suspension (Figure 4.39). If clay aggregation occurred because of ageing, the mean Sauter diameter should have been larger (old: 1.25 µm versus fresh: 1.51 µm) and the specific surface area should have been reduced, but it increased to 4807 m^2/kg. We measured the pH of both fresh and one-week-old suspension with a Fischer Probe Orion 81725 Ross Sure-Flow Comp. The pH shifted from 7.9 ± 0.2 (fresh suspension) to 6.3 ± 0.1 after one week of ageing. Since flocculation and dewatering performance are known to be dependent on pH for kaolinite suspensions [136], few test runs were performed with the same MF1011 (3k ppm, 20 mL/min)/ AP-*g*-PVBTMAC (F_4L_2) (7k ppm, 65 mL/min) dual system at 14 wt. % solids kaolinite suspension.

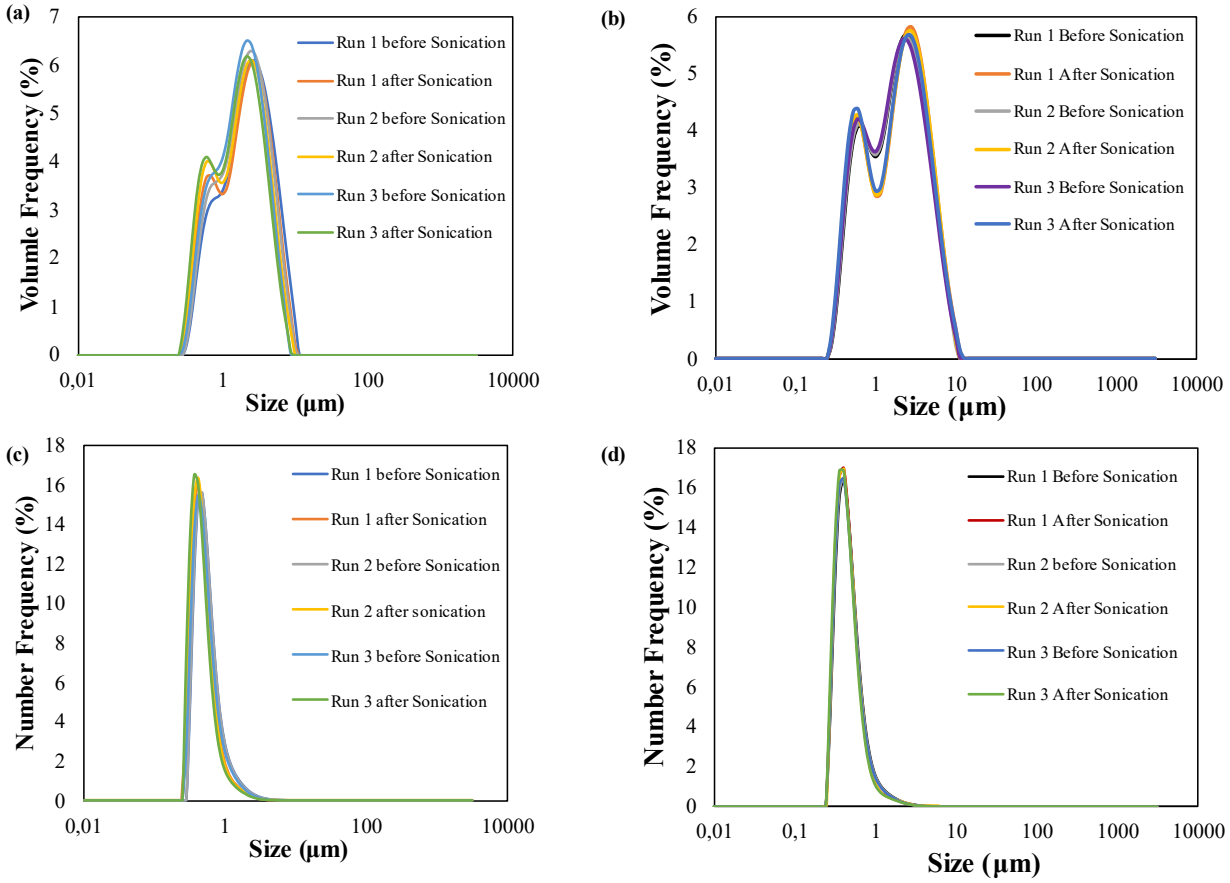

Figure 4.39 – Comparison of the PSDs of fresh and one-week-old kaolinite suspensions: a) fresh volume distribution, b) 1W old volume distribution, c) fresh number distribution, d) 1W old number distribution.

Sediment solids content varied from 47.7 ± 0.7 wt. % to 45.7 ± 0.7 wt. % with ageing, while the supernatant turbidity increased from 4.57 ± 0.05 NTU to 6.29 ± 0.03 NTU. There are multiple reasons for this decrease in performance. The pH decreases with ageing which affects:

- the rheology of the suspension [137] (and so the hydrodynamic conditions).
- the adsorption of the polymers [138] onto kaolin particles.

For instance, Nabzar et al. showed that the specific adsorption of a polyacrylamide ($M_W = 1.2\times10^6$) decreased from 23 mg/g to 18 mg/g for a concentration of 1.5 mg/ml at pH 10 because of one week of ageing [138]. Since aluminol sites are the main adsorption sites for the neutral polymers (typically for amide groups), the dissolution of these sites (kaolinite solubilization) affects the quantity of polymer that can be adsorbed onto kaolinite particles. Besides, this study

found that fine particles were more affected by the dissolution process than the coarse particles due to their lower degree of crystallinity [138], which confirms that the effect of ageing was not negligible on a full CCD design with 48 runs completed over a period of two weeks.

The same full CCD design as the one presented in Section 4.6.1 was carried out with one stock kaolinite suspension. All the regression models showed a bias when plotting the residuals as the suspension was continuously ageing over the course of the treatments (Appendix B11). Therefore, a fresh suspension was prepared for each run for the flocculations previously presented in Sections 4.6.2, 4.6.3 and 4.6.4, to ensure that this bias was not introduced in the results.

This discussion on kaolinite ageing is of great matter for the flocculation performance, it could have been interesting to compare the results with a purified kaolinite suspension [139] to see if impurities affected the experiments or if the changes in the suspension's property prevailed.

4.6.6 Proof of Image Processing Size Estimates with FBRM

Top-view pictures of the flocs were taken and processed using MATLAB (see Section 3.7) to study the evolution of their size throughout the runs of the CCD. The image processing efficiency (segmentation) was checked by comparing the processed results to already flocculated flocs measured with FBRM (averaged over ~ 5-10 measurements, Appendix B13). This verification was necessary since segmentation was likely to fail because of flocs overlapping.

Five flocculation runs leading to different floc sizes gave the results showed in Figure 4.40. This test is not rigorous because it compares a volume mean diameter (obtain from FBRM calibration) with a minimum Feret diameter, but the aim was to verify the order of magnitude of the flocs size given by image processing. Figure 4.40 confirms the close proportionality (slope ~ 0.9, R^2 = 0.99) between the volume mean diameter from FBRM and minimum Feret diameter obtained by image processing. Figure 4.40 also shows that this result has important limits. The first one is comparing a Feret diameter to a mean volume diameter, and the correlation covers a narrow range of floc sizes (375-525 µm). Flocs smaller than 375 µm cannot be separated effectively by the program, while larger flocs (> 600 µm) are broken down by shear during the FRBM (using an axial impeller at 300 rpm). Lastly, the calibration used to convert the chord length to a mean volume diameter is only applicable for flocs smaller than 500 µm [98].

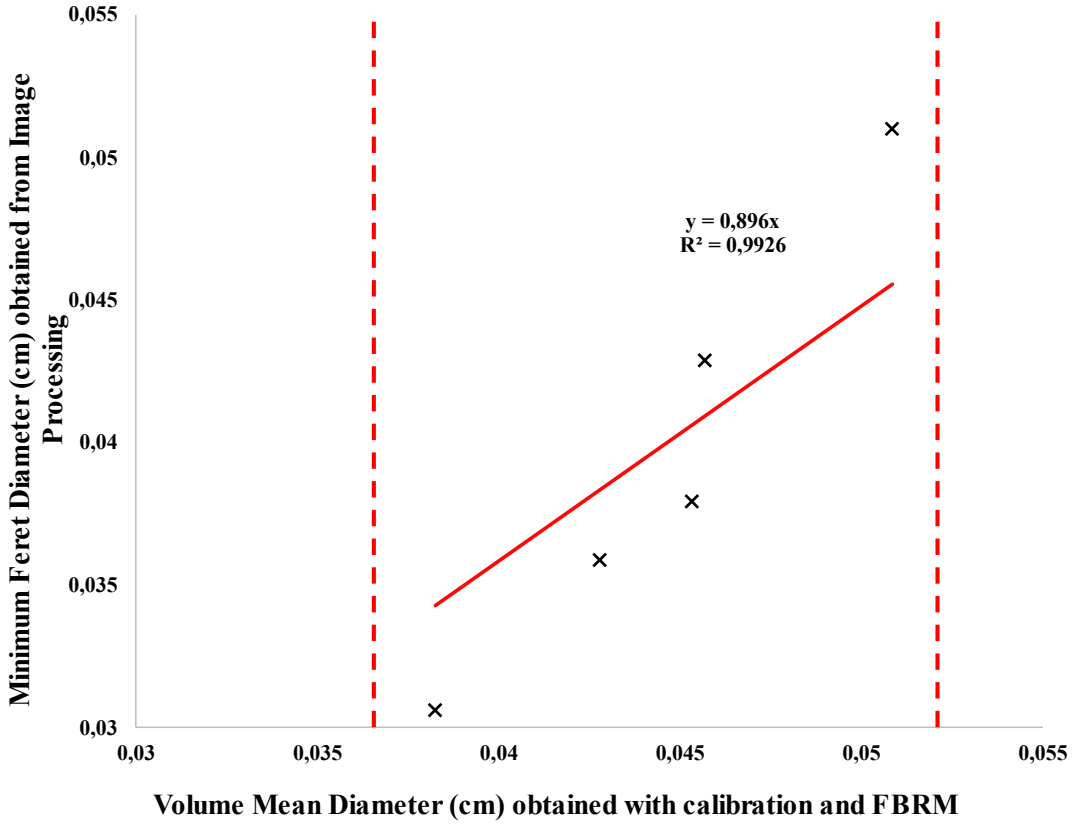

Figure 4.40 – Comparison between volume mean diameter from FBRM with minimum Feret diameter from image processing.

The first size estimation method relying on the marker-based watershed segmentation was discarded because the results were inconsistent. The marker and the background marking are key for the watershed to be efficient (Figure 4.41), but it highly relies on the chosen value of the H-maxima transform – morphological operation used to filter local maxima based on different local contrasts, acts as a threshold – in the function @imextendedmax used to find the markers (Figure 4.42.A) for the watershed (Figure 4.42.B). The "m" values displayed on Figure 4.42.B, correspond to the mean projected diameter of the particle size distribution obtained from the floc segmentation fitted with a log-normal distribution. Different arbitrary choices of H lead to different segmentation results for a same run (Figure 4.42.B).

This method did not perform well with the overlaid flocs on the top-view pictures, as shows the segmentation result (orange lines) in Figure 4.41.C, the program was not able to isolate the flocs as well as the second method (Figure 4.43). All the photos that follow are pictures obtained from the first run of the CCD in order to compare the image processing method used.

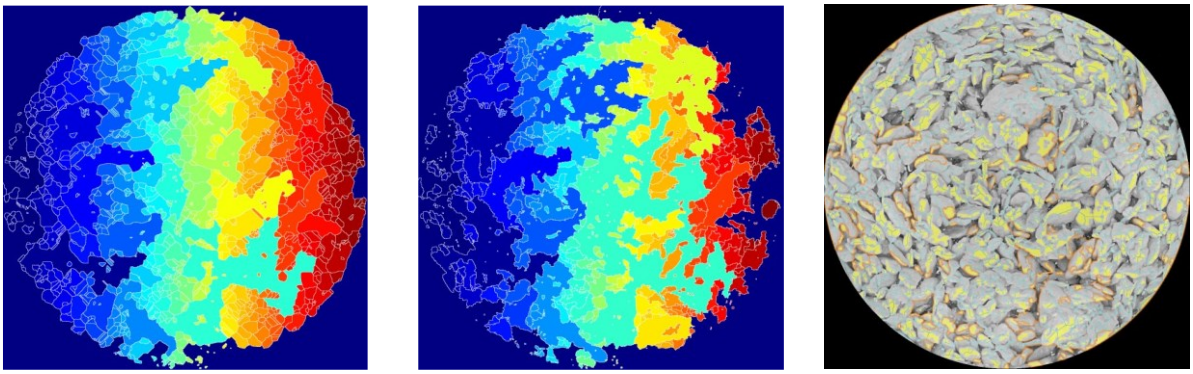

A B C

Figure 4.41 – Importance of the marker used for the segmentation result of a same run: A) over-segmentation due to improper marking, B) marker: local maxima, background: grey scale threshold, C) marker: local maxima (in yellow), background: gradient magnitude (segmentation = orange lines and blue lines are watershed ridge lines).

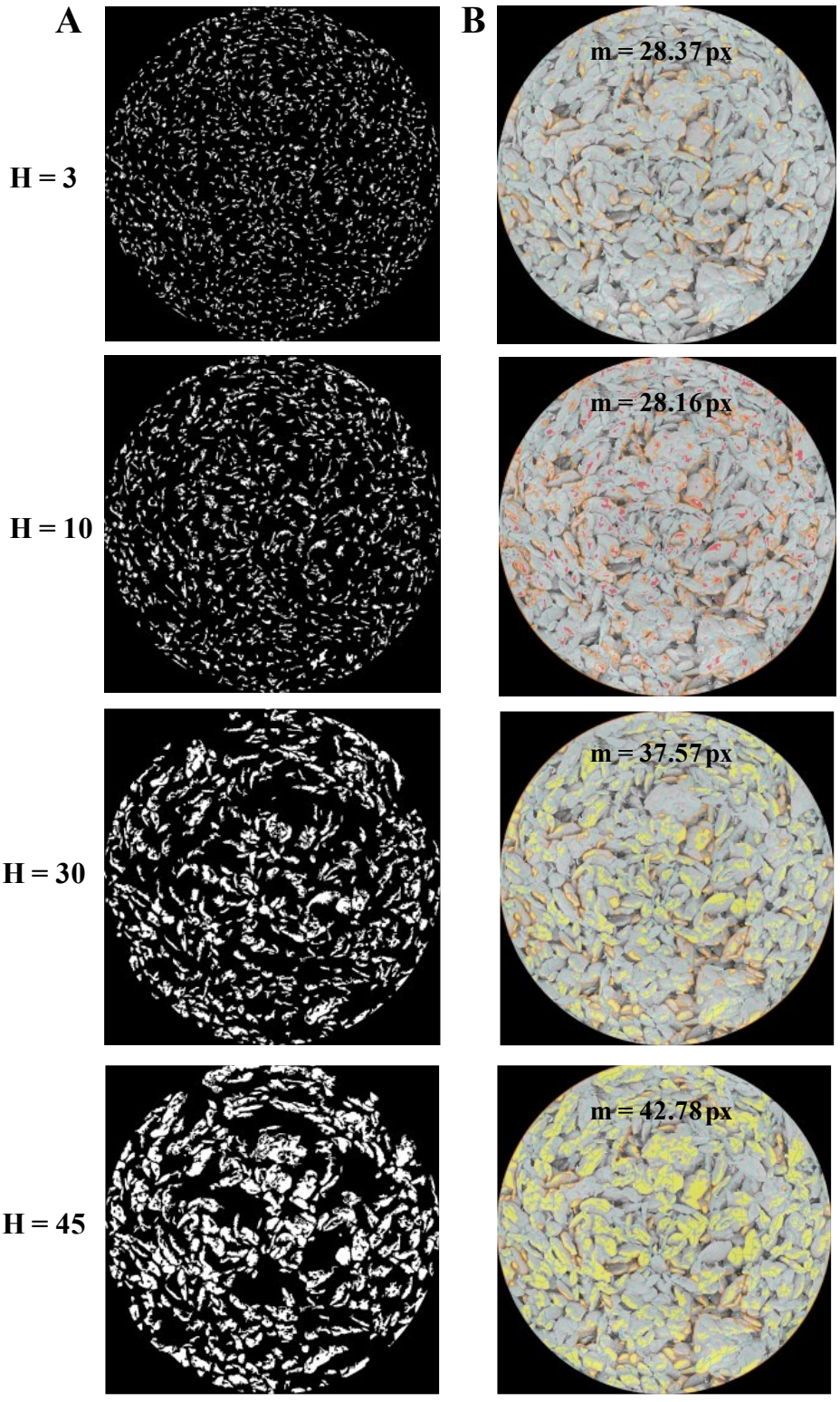

Figure 4.42 – A) Regional maxima of opening-closing by reconstruction image, B) Markers and object boundaries superimposed on original image for different H-transform values.

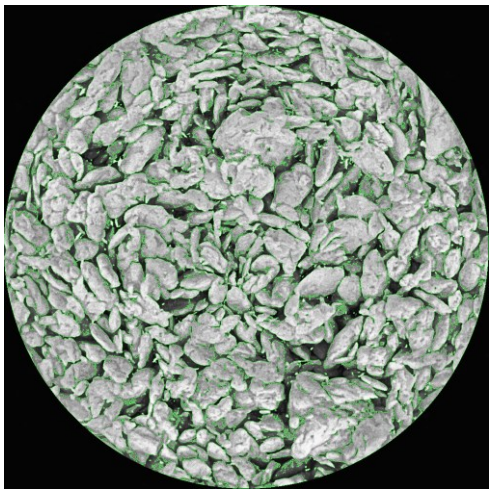

Figure 4.43 – Separation of the flocs using the binary perimeter function (perimeter superimposed to the original grayscale image).

The second method (Figure 4.43) is not a proper segmentation, but it showed better results. The binary perimeter function finds a pixel on the perimeter by assessing two conditions: the pixel has to be non-zero, and has to be linked to at least one pixel with a value 0. The mean of all the minimum Feret diameter found on the binary image (with perimeter), then allows to estimate flocs sizes in a consistent (Figure 4.40) and simpler way than with the marker-based watershed segmentation method (for this application). Surprisingly, the watershed struggled with flocs stacked on a picture despite the different treatments – which accurately estimated the topography of the picture (Figure 4.44.b) – applied to the image prior to run the watershed algorithm.

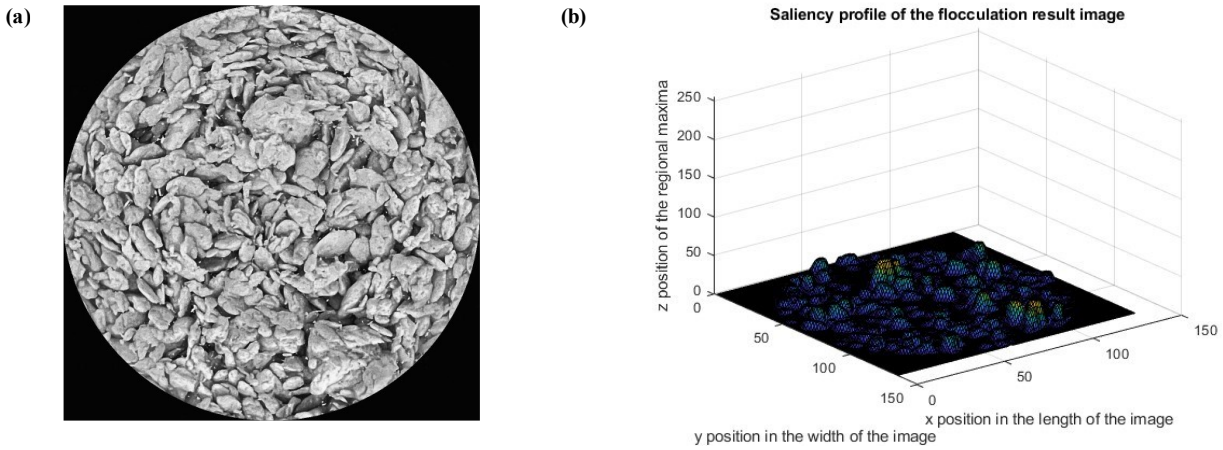

Figure 4.44 – a) Original grayscale image, b) Processed topography of the original image.

The mean minimum Feret diameters found by image processing, and the area-perimeter projected fractal dimension for each run of the CCD are presented in Table 4.14.

Table 4.14 – Image processing results.

RUN N°	*Mean Feret Diameter (cm)*	D_{pf}
1	0.045	1.97
2	0.023	1.88
3	0.026	1.95
4	0.035	1.97
5	0.027	1.93
6	0.025	1.82
7	0.032	1.99
8	0.033	1.81
9	0.040	1.98
10	0.026	1.65
11	0.028	1.92
12	0.031	1.94
13	0.025	1.56
14	0.030	1.81
15	0.024	1.80
16	0.027	1.69
17	0.031	1.85
18	0.034	2.05
19	2.63	2.03
20	0.117	1.99
21	0.031	1.94
22	0.036	2.03
23	0.028	1.88
24	0.027	1.89
25	0.115	1.92
26	0.029	1.96
27	0.034	1.91
28	0.031	1.96
29	0.150	2.00
30	0.031	1.69
31	0.059	2.02
32	0.038	1.87
33	0.028	1.93
34	0.027	1.70
35	0.043	1.83
36	0.046	1.98
37	0.036	1.92
38	0.033	1.89
39	0.029	1.91
40	0.041	1.84
41	0.052	1.99
42	0.027	1.82
43	0.029	1.82
44	0.031	1.85
45	0.099	1.90
46	0.039	1.94
47	0.032	1.96
48	0.032	1.94

Rows in red = Failed image processing
Runs in green = Double checked with FBRM

RUN 1

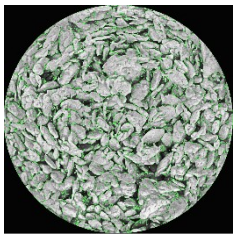

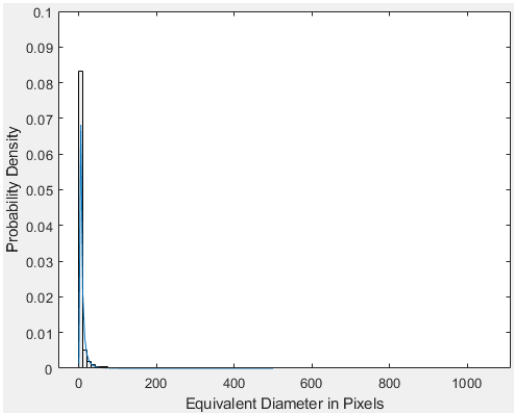

R2

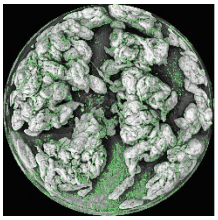

R3

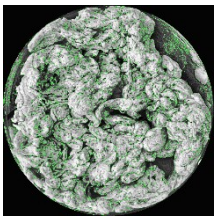

R4

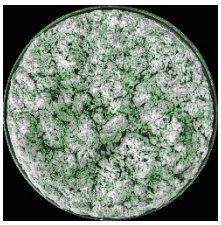

R5

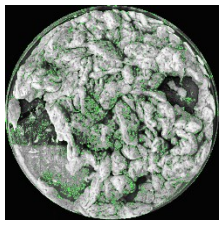

R6

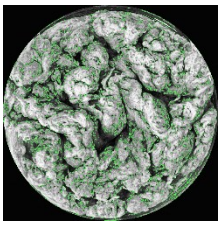

R7

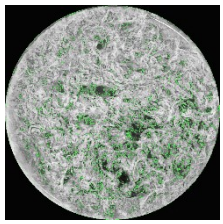

R8

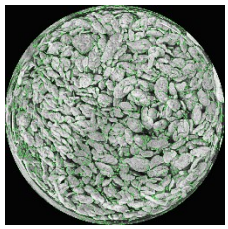

R9

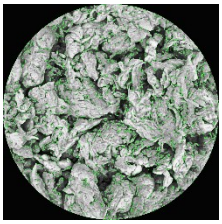

R10

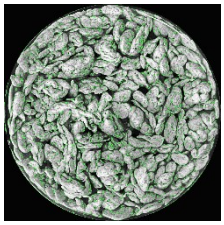

R11

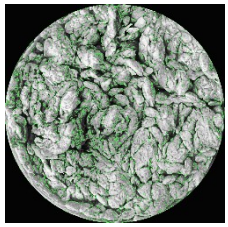

R12

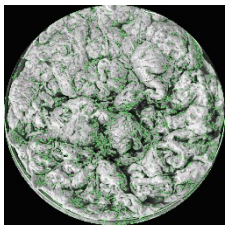

R13

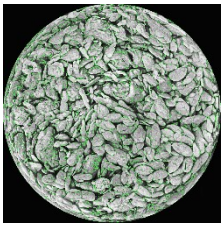

R14

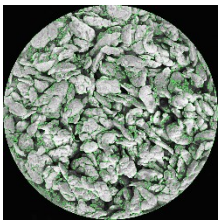

R15

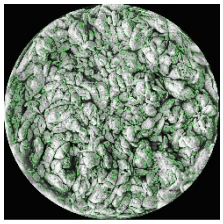

R16

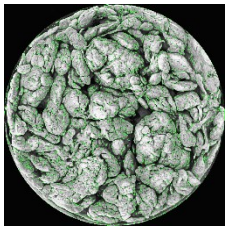

R17

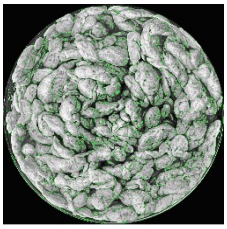

R18

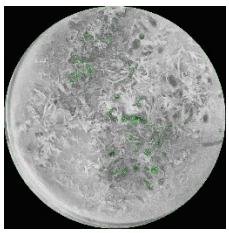

R19

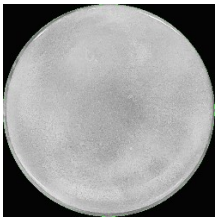

R20

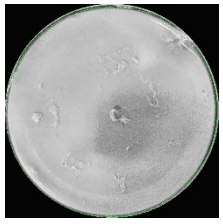

R21

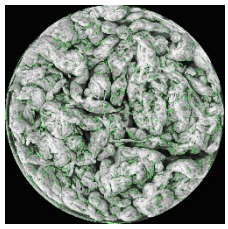

R22

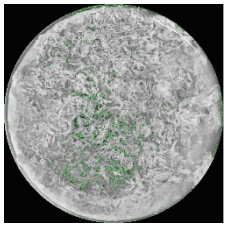

R23-24

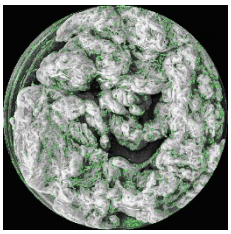

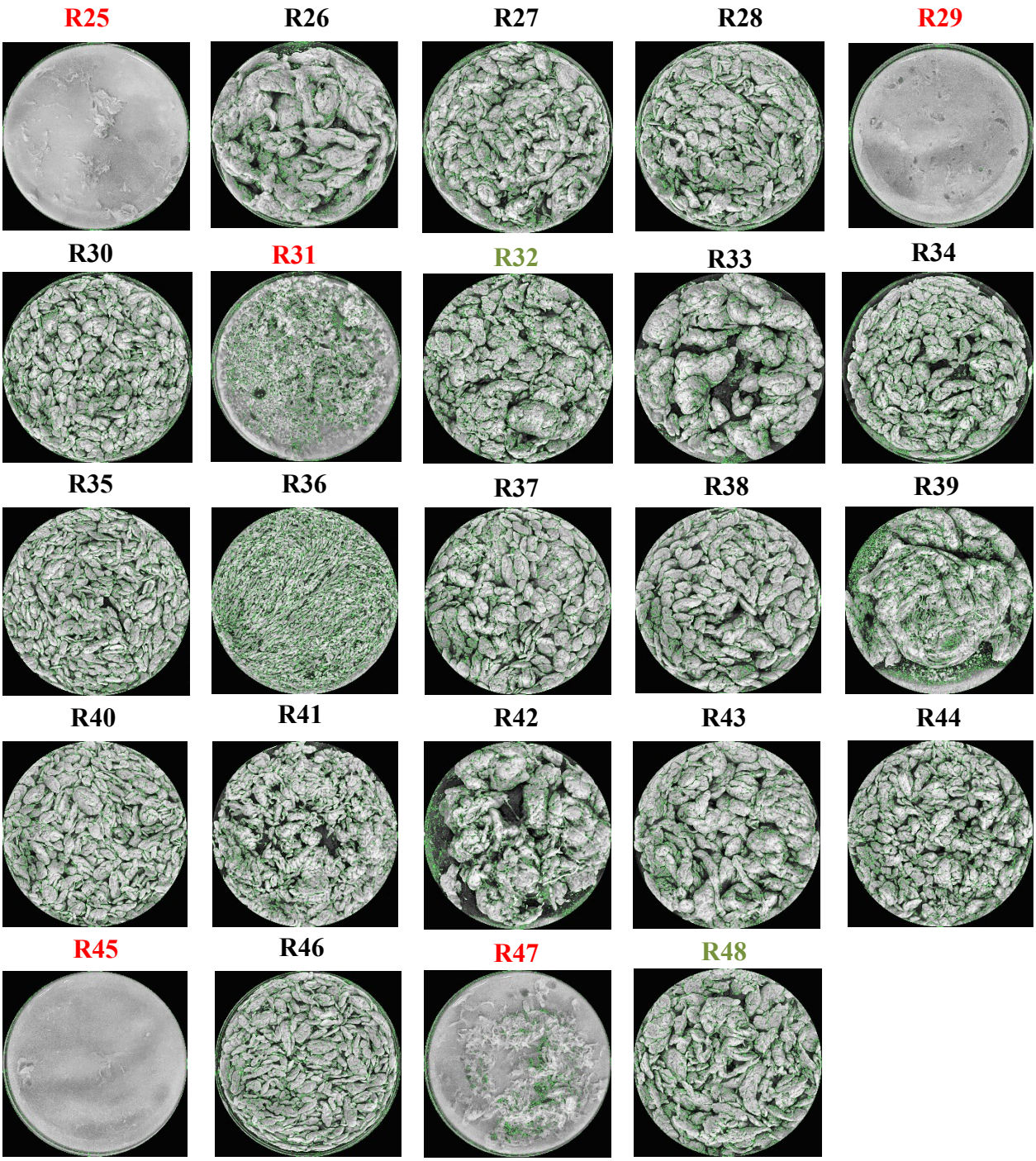

Figure 4.45 – Image processing results for the 48 runs of the CCD.

Unfortunately, 12 runs out of the total 48 runs of the CCD resulted in failed image processing because of undetectable small flocs or large flocs (blob shape) that were attached, so they could not be processed accurately (red labels in Figure 4.45). Pictures of the runs (Figure

4.45) show that adding a lower amount of the cationic polymer compared to the anionic, formed well separated and shear resistant flocs of medium size (runs: 1,10,13,35,46). Contrarily, adding 7k ppm of AP-*g*-PVBTMAC and 3k ppm MF1011 leads to small flocs (runs: 4,7,18,19,23,22,25,29,31,35,47) especially when the addition flowrate difference is high. The optimum is a faster addition of AP-*g*-PVBTMAC compared to MF1011 in the same proportions (runs: 14, 38 and 48) (Figure 4.45).

The estimated fractal dimensions range from 1.7 to 1.9, which indicates that the flocs are not spherical ($D_{pf} = 1$ for a perfect sphere). These values are high compared to the usual range of perimeter fractal dimensions for flocs (1.2 - 1.5) [140,141]. Since the calculation of the fractal dimension is based on the projected area and the perimeter, excessive D_{pf} values may be caused by the inaccurate estimation of the area because of flocs overlapping (as seen with the watershed segmentation).

Despite the inability to analyze some small floc sizes, these two results (mean floc size and D_{pf}) were added as response in the CCD treatment (with a fixed values for the runs with failed image processing). This attempt gave a model for both perimeter fractal dimension and mean floc size in function of the CCD predictors, but because of the inaccuracy of some estimations, they are not exploitable (presented in Appendix B12).

Processed top-view pictures taken for each run of the CCD presented in Figure 4.45 (along with the estimated PSD for the first run) confirm that polymers dosages and addition flowrates affect flocs sizes, even if they could not be quantified. The effort to develop a cheap and time saving method to estimate flocs sizes is still valuable, and should be improved to draw better conclusions from these results.

4.6.7 Dynamic Study of Kaolinite Suspension Dual Polymer Flocculation with FBRM

Multiple issues intrinsic to the FBRM apparatus were observed with the dual polymer system.

The first issue comes from the functioning of FBRM with large flocs. The incident laser beam hits one side of an aggregate which backscatters part of the incoming light, and converts it

into a signal, while the apparatus measures the time required for the beam to hit the other hand of the aggregate. This gives a chord length when this time is multiplied by the speed of the laser beam [142]. Therefore, the large flocs might screen smaller flocs behind them on the laser's path, or two flocs in close vicinity could be counted as one larger floc. This latter is increasingly important in concentrated suspensions, so we worked with 5 wt. % kaolin solids.

Secondly, because the flocs formed with MF1011 were sticky, they tended to cause fouling issues on the FBRM probe. This fouling was not observed when the flocs were already formed as for the verification (Figure 4.40) performed in Section 4.6.6 (Figure 4.46, raw results in Appendix B13), which indicates that poor dispersion of MF1011 and AP-g-PVBTMAC could cause this fouling issue. In the image processing validation tests, the only exception showing probe fouling was the run 9 (of the CCD), that formed larger flocs (Figure 4.45) which were starting to agglomerate on the probe after 2 min of mixing (large fake peaks in the > 100 µm region on the number chord length distribution, Figure 4.46).

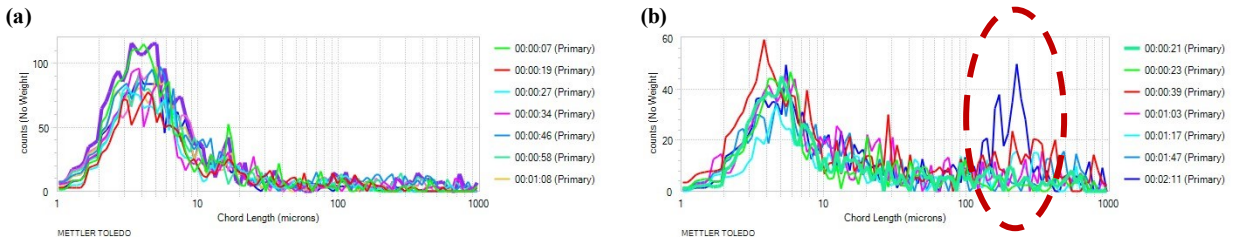

Figure 4.46 – Example of FBRM probe fouling issue on number chord length distribution: a) run 48 (CCD) with nominal distribution; b) run 9 (CCD) with marked fouling after 2 minutes.

Flocculations (see design in Table 3.5) monitored by FRBM are presented in Figure 4.47 (chord length distributions, mean squared weight evolution with flocculation time and tables B.14.1-14.18 are gathered in Appendix B14, including the two replicates for each run). Initially, we used 3k ppm dosage for both polymers but because of fouling issues, the dosage has been reduced to 1.5k ppm to reduce the viscosity of the medium. Figure B14.7 (in Appendix B14) shows that the trends are similar for both dosages with the example of the first run.

FBRM shows that the addition of polymers (at 25 s) generates an instantaneous steep decline in counts of particles smaller than 50 microns (red and light blue trends, Figure 4.47.a-c-e-f), indicating the efficient capture of the fines (Figure 4.48.a-c-e-f), in all the cases with a cationic polymer addition flowrate above 10 mL/min. This decrease in counts of fines is correlated to an

increase of newly formed flocs in the range of 150-300 and 300-1000-microns flocs (blue and green trends, Figure 4.47). The criteria on the cationic polymer addition flowrate required for effective fines capture may be partly explained by Gregory and Barany [143] modeling of polymer's adsorption rate onto clays:

$$t_{ads} = \frac{-\ln(1-\Psi)}{k \times N} \tag{4.5}$$

where Ψ is the fraction of total polymer needed for flocculation to happen, k is the collision rate coefficient between polymer and clay particles per unit time, and N is the initial number of particles in the suspension per unit volume.

For a same total dosage, changing the addition flowrate changes the instantaneous polymer dosage which is key for flocculation. Increasing the polymer dosage decreases the required fraction Ψ but also decreases the collision rate coefficient per unit time k when MF1011 is added fast, due to the change in viscosity of the medium (the addition of the cationic polymer effect on viscosity is negligible in front of MF1011's effect). So, it is necessary that AP-*g*-PVBTMAC addition flowrate (linked to its instantaneous dosage) overcomes the change in viscosity to keep a low characteristic adsorption time for the cationic polymer. In these conditions, the fines are efficiently captured.

After the peak corresponding to the formation of medium size flocs (150-300 microns), their number decreases from 2400 to 400, 20 seconds later, while the number of particles smaller than 10 microns increases, because of flocs breakage or restructuration – repeated aggregation / fragmentation leading to less porous and compact flocs – of the weaker flocs newly formed (Figure 4.47.a-e-f). This finding goes against some conclusions drawn for PVBTMAC only [98], but flocs are significantly larger in this case, which promotes aggregate breakage since hydrodynamic shear forces cannot be neglected (even at 300 rpm). FBRM also shows that the system reaches steady-state after only 1 min of flocculation, which is interesting from an industrial standpoint.

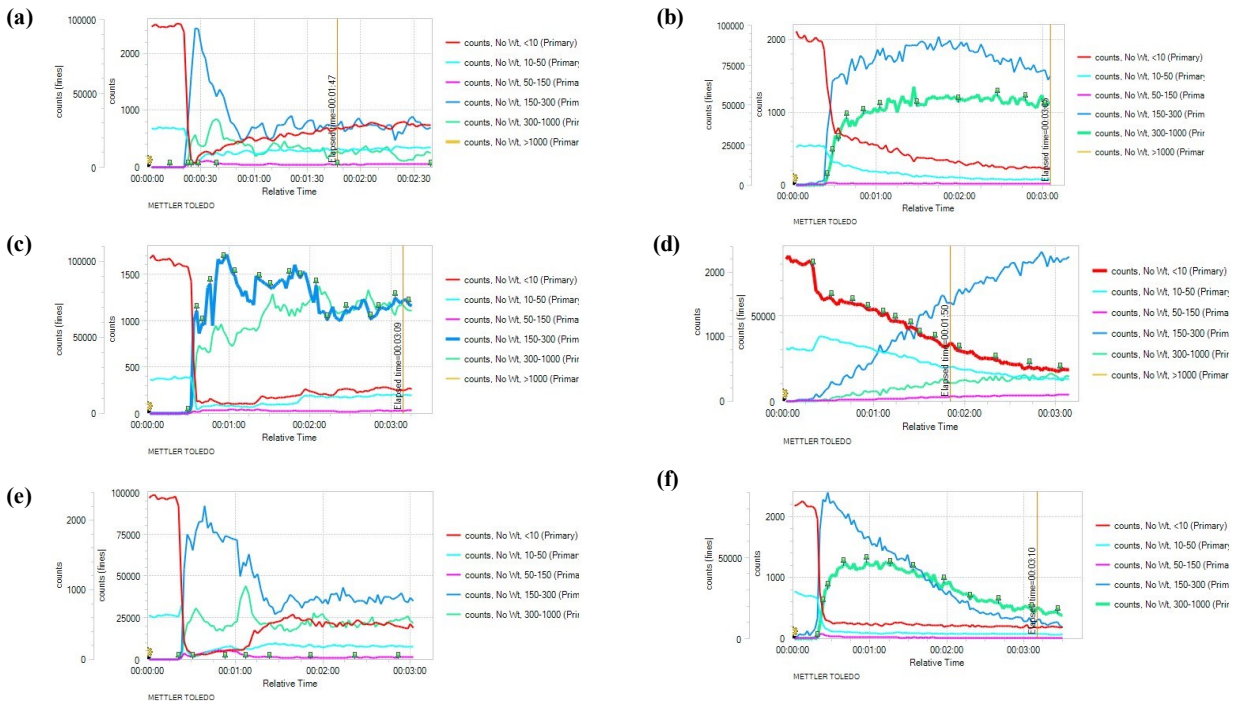

Figure 4.47 – Dynamic flocculation monitoring with different polymers dosages and addition flowrates: a) run 1 (80 / 10 mL/min cationic and anionic polymer flowrates respectively), b) run 2 (10 / 25 mL/min), c) run 3 (55 / 15 mL/min), d) run 4 (10 / 80 mL/min), e) run 5 (25 / 10 mL/min), and f) run 6 (15 / 55 mL/min) respectively (replicates confirming the trends in Appendix B14).

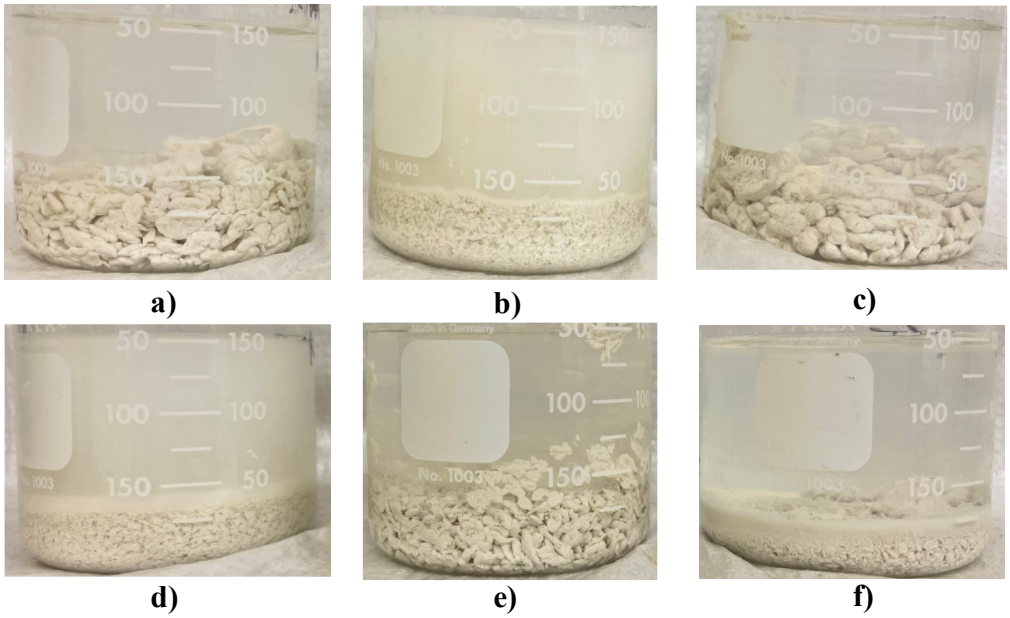

Figure 4.48 – Pictures of the flocculation results (1.5k ppm for both polymers) for the replicate 1: a) run 1, b) run 2, c) run 3, d) run 4, e) run 5, and f) run 6.

The 55 / 15 (cationic / anionic polymer) mL/min flowrates produce even larger flocs than in Run 1 (Figure 4.48.a) with clear supernatant (Figure 4.48.c). The relative increase in anionic polymer addition flowrate prevents flocs breakage with the additional shear strength MF1011 provides (no sharp decrease after the blue trend maximum in Figure 4.47.c compared to Figure 4.47.a). The small decrease in the number of 150-300 microns flocs is likely due to their conversion into larger 300-1000 microns flocs (see green trend continuous increase, Figure 4.47.c). The shear resistance that was previously attributed to MF1011 high molecular weight may also be related to a synergy between both cationic and anionic polymers, as the optimum is relatively close flowrates between the two polymers (55/15 mL/min addition flowrates) in FBRM and CCD tests. FBRM suggests that the anionic charges of MF1011 may develop attractive interactions with the cationic charges of AP-*g*-PVBTMAC, resulting in stronger flocs. So, the addition flowrate of MF1011 needs to be adjusted to be close to that of the cationic polymer (above the threshold for efficient fines capture) to reach optimum floc mechanical strength.

Finally, the dynamic study of flocculation gives information about the flocculation mechanism of this dual polymer system. The increase in floc size with faster addition of MF1011 (higher molecular weight) shows the combination between charge neutralization and bridging mechanism. AP-*g*-PVBTMAC flocculates with charge neutralization (and bridging) to destabilize the suspension and form the "primary" flocs, so its addition flowrate is the first criteria for efficient flocculation. Cationic polymer chains may then extend (loop and tails) in the solution to develop attractive interactions with negatively charged clay particles and the anionic charges of MF1011 that flocculates clays through bridging. It can also be speculated that attractive interactions between AP-*g*-PVBTMAC and MF1011 may produce some large-scale polyelectrolytes clusters [144] which can trap clay particles, resulting in larger and stronger flocs.

5. Conclusions and Future Work

Despite the work previously conducted on amylopectin graft copolymers, the use of amylopectin-graft-poly[(vinylbenzyl)trimethylammonium chloride] (AP-*g*-PVBTMAC) on MFT has not been published. Similarly, kaolinite is often chosen as a more controlled system to model MFT, but the addition flowrates of flocculants have not been monitored to deduce optimum operating conditions. Therefore, this work provides new results on dual polymer flocculation using a newly synthesized cationic polymer and a commercial anionic polymer with controlled addition flowrates.

MFT flocculation with AP-*g*-PVBTMAC revealed the interest of the modification of amylopectin backbones to improve sediment solids content and CST since it outperformed PVBTMAC homopolymer and the physical blend of AP-PVBTMAC with good reproducibility. Moreover, the use of this polymer eliminates the need for calcium ion addition and its subsequent recycling in the tailings management process.

The microstructure of AP-*g*-PVBTMAC (graft length and frequency) had a milder effect than the flocculant dosage on the flocculation metrics. This was attributed to charge neutralization mechanism being less sensitive to change in the polymer's structure than bridging. Limitations for the industrial use have also been identified. The solids content decreases as the polymer dosage increases, and the flocs formed by the cationic grafted polymer remain small which hinders their settling. However, the use of AP-*g*-PVBTMAC combined with the commercial anionic flocculant Magnafloc 1011® outperformed other existing flocculant systems (tested here).

The central composite design of experiments was used to see the effect of polymers addition flowrates on the flocculation of kaolinite suspensions with varying solids content. It showed that the effect of anionic addition flowrate was not significant for both initial CST and supernatant turbidity in the range of variables tested, but it had to be taken into account to describe the evolution of flocs solids content. Optimum conditions were found to be low anionic dosage (<2 kppm) (likely due MF1011 high molecular weight) and high cationic polymer dosage (~ 6 kppm), to allow for the best performance in terms of fines capture and floc dewaterability.

FBRM study confirmed that for a given dosage and suspension solids content, each polymer addition flowrates determine the structure of the flocs. Optimum addition flowrates were

found near 55 mL/min and 15 mL/min for the cationic and anionic polymers respectively, to maximize floc size and shear resistance. This result is in good agreement with the results from the CCD, even if CCD showed that addition flowrates had secondary effects (mostly interaction terms and quadratic term only for initial CST) compared to polymers dosages. The synergy between AP-*g*-PVBTMAC and MF1011, by developing attractive interactions between each polymers charged loops and tails, may explain the large and shear resistant flocs produced.

The focus of this work was to find optimum operating conditions for flocculation and reasonable synthesis conditions for AP-*g*-PVBTMAC and its large-scale use. This implies that the grafted AP-*g*-PVBTMAC and ungrafted material (PVBTMAC) have not been separated. Although, flocculation results showed that the grafted and homopolymer blend outperformed the homopolymer alone, more efforts should be put to purify the polymer by removing PVBTMAC, as the purification would help to control the grafting efficiency and the characterization of the polymer. Giving up on the scalability of the synthesis, it could be interesting to use living polymerization techniques such as atom transfer radical polymerization (ATRP) or nitroxide mediated polymerization (NMP) to control the graft length with the polymerization time, while making sure that the homopolymer PVBTMAC production is negligible. Unlike graft length, it can be speculated that increasing the graft frequency facilitates water expulsion from the flocs. The effective hydrophobicity is expected to be higher for high graft frequencies and short grafts, since the hydrophobicity provided by PVBMAC's benzene rings are closer to the amylopectin backbone in this case. This hypothesis could also be tested with living polymerization and controlled graft structures.

With a pure AP-*g*-PVBTMAC, one could conduct zeta potential measurements with the varying structures (graft length and frequency) of the grafted polymer to quantify the charge attraction/repulsion between the polymer and clay particles. Zeta potential measurements are necessary to gain a better understanding of the forces at stakes at the microscopic scale, which is needed to enlighten the reflection on some of the macroscopic results obtained in this project. One could also analyze the microscopic structure evolution of flocs with addition flowrates instead of their macroscopic size, to gain insights on the role of each polymer in the flocculation of a kaolinite suspension.

A concentration of 3 mg/mL was kept for both polymers solution in order to cover the widest range possible in the CCD. But, the viscosity of the MF1011 solution at this concentration impacted some measurements (supernatant turbidity, FBRM probe fouling), and it also affected the probability of effective collisions between polymers and clay particles by modifying the hydrodynamic conditions. Therefore, it could be interesting to reduce the polymer solution concentration to 0.5 mg/mL and carry out the CCD on actual MFT in complement of the kaolinite suspension, to test the performance of AP-g-PVBTMAC / MF1011 on a heterogeneous system containing bitumen.

The attempt of amylopectin co-grafting with VBTMAC and AM did not show satisfactory performance but additional future work could focus on co-grafting partially hydrolyzed anionic polymers such as hydrolyzed polymethyl acrylate (H-PMA) with PVBTMAC from the amylopectin backbone, to eliminate addition sequence considerations and confirm the synergy effect between anionic and cationic flocculants observed in this study.

Controlling the sequence of addition of polymers is only one aspect of the flocculation, but future studies should also focus on the influence of polymers dispersion, and suspension mixing to assess the best operating conditions for a complex heterogenous system such as MFT. Since polyelectrolytes solvation and hydration effects are key for polymer's conformation, stiffness and clusters in solution [144,145], it could be interesting to investigate the flocculation performance of multivalent ionic grafts, in comparison with the existing findings on monovalent grafts such as the quaternary ammonium studied here. Multivalent ionic grafts are expected to compress the electrical double layer while allowing for a more extended polymer conformation in solution due to increased repulsive forces among the polymer's chains. If these two effects were confirmed with experiments, less polymer dosage would be needed to have efficient flocculation, which is currently an obstacle to the use of grafted polymers in the industry.

Finally, instantaneous flocculation tests are convenient for large experiment designs but future works should also focus on long term consolidation and dewatering as this is the key property for flocculants environmental use and ultimately land reclamation.

References

[1] N. R. Canada, “Oil Resources”, [Online]. Available: [Accessed 02-Jul-2021].

[2] Alberta Government website, “Oil Sands Facts and Stastistics”, [Online]. Available: https://www.alberta.ca/oil-sands-facts-and-statistics.aspx [Accessed 02-Jul-2021].

[3] J. H. Masliyah, Z. Xu, and J. A. Czarnecki, “Chapter 1: Introduction to the Athabasca Oil Sands,” in Handbook on Theory and Practice of Bitumen Recovery from Athabasca Oil Sands, Vol. 1: Theoretical Basis, *Kingsley Knowledge Publishing*, pp. 1–39, 2011.

[4] “Alberta Canada Province PowerPoint Map Highways Waterways Cities”, [Online] Available: https://www.clipartmaps.com/product/alberta-canada-province-powerpoint-map-highways-waterways-cities/ [Accessed 02-Jul-2021].

[5] “Oil Sands Geology & The Properties of Bitumen”, 2016 [Online] Available: https://www.oilsandsmagazine.com/technical/properties [Accessed 02-Jul-2021].

[6] “Oil Sands 101: Process Overview.”, [Online] Available: https://www.oilsandsmagazine.com/technical/oilsands-101 [Accessed: 02-Jul-2021].

[7] “Energy resources: facts and stats - Open Government,” 2017. [Online]. Available: https://open.alberta.ca/dataset/energy-resources-facts-and-stats. [Accessed: 02-Jul-2021].

[8] “Steam Assisted Gravity Drainage Facts and Stats – Open Government”, 2017, [Online]. Available: https://open.alberta.ca/publications/steam-assisted-gravity-drainage-facts-and-stats [Accessed: 02-Jul-2021].

[9] “In-situ Recovery”, [Online]. Available: https://www.aer.ca/providing-information/by-topic/oil-sands/in-situ-recovery [Accessed: 02-Jul-2021].

[10] Peacock, M.J., “Athabasca oil sands: reservoir characterization and its impact on thermal and mining opportunities”, *Petroleum Geology Conference series*, vol. 7, pp. 1141-1150, 2010.

[11] Carrera-Hernández, J.J., Mendoza, C.A., Devito, K.J., Petrone, R.M., Smerdon, B.D., “Reclamation for aspen revegetation in the Athabasca oil sands: understanding soil water dynamics through unsaturated flow modeling”, *Can. J. Soil Sci*., 92, 103–116, 2012.

[12] “Surface Mining Techniques Used in the Oil Sands” [Online]. Available: https://www.oilsandsmagazine.com/technical/mining/surface-mining [Accessed: 02-Jul-2021].

[13] J. Masliyah, Z. J. Zhou, Z. Xu, J. Czarnecki, and H. Hamza, “Understanding Water-Based Bitumen Extraction from Athabasca Oil Sands”, *Can. J. Chem. Eng.*, vol. 82, no. 4, pp. 628–654, 2008.

[14] “In-Situ Bitumen Extraction”, [Online]. Available: https://www.oilsandsmagazine.com/technical/in-situ [Accessed: 02-Jul-2021].

[15] Canadian Association of Petroleum Producers, "The Facts on Oil Sands", in "Oil Sands: Water Management", 2014, [Online]. Available: https://www.nrcan.gc.ca/energy/publications/18750 [Accessed: 03-Jul-2021].

[16] Mahdavi E., Zebarjad F.S., "Screening Criteria of Enhanced Oil Recovery Methods", *Fundamentals of Enhanced Oil and Gas Recovery from Conventional and Unconventional Reservoirs* Book, Chap. 2, pp. 41-59, 2018.

[17] Petroleum Technology Alliance Canada (PTAC), "Needs Assessment for Partial and Field 105 Upgrading", 2015.

[18] T. R. B. and N. R. Council, TRB Special Report 311: Effects of Diluted Bitumen on Crude Oil Transmission Pipelines. Washington, D.C.: *National Academies Press*, 2013.

[19] E. W. Allen, "Process water treatment in Canada's oil sands industry: I. Target pollutants and treatment objectives", *J. Environ. Eng. Sci.*, vol. 7, no. 2, pp. 123–138, 2008.

[20] C. E. Willis, V. L. St. Louis, J. L. Kirk, K. A. St. Pierre, and C. Dodge, "Tailings ponds of the Athabasca Oil Sands Region, Alberta, Canada, are likely not significant sources of total mercury and methylmercury to nearby ground and surface waters," *Sci. Total Environ.*, vol. 647, pp. 1604–1610, 2019.

[21] L. Botha and J. B. P. Soares, "The Influence of Tailings Composition on Flocculation", *Can. J. Chem. Eng.*, vol. 93, no. 9, pp. 1514–1523, Sep. 2015.

[22] Small C.C., Cho S., Hashisho Z., Ulrich A.C., "Emissions from oil sands tailings ponds: Review of tailings pond parameters and emission estimates", *Journal of Petroleum Science and Engineering* 127, pp. 490-501, 2015.

[23] Elshorbagy, A., Jutla, A., Barbour, L. and Kells, J., "System dynamics approach to assess the sustainability of reclamation of disturbed watersheds", *Can. J. Civ. Eng.*, Vol. 32, pp. 144_158, 2005.

[24] "Directive 085: Fluid Tailings Management for Oil Sands Mining Projects", *Alberta Energy Regulator*, 2017.

[25] Johnson, E. A. and Miyanishi, K., "Creating new landscapes and ecosystems: the Alberta oil sands", *Ann N. Y. Acad.Sci*, Vol.1134, pp.120-145, 2008.

[26] D. R. L. Vedoy and J. B. P. Soares, "Water-soluble polymers for oil sands tailing treatment: A Review," *Can. J. Chem. Eng.*, vol. 93, no. 5, pp. 888–904, 2015.

[27] N. Beier, W. Wilson, A. Dunmola, and D. Sego, "Impact of flocculation-based dewatering on the shear strength of oil sands fine tailings," *Can. Geotech. J.*, vol. 50, no. 9, pp. 1001–1007, 2013.

[28] M. D. MacKinnon, J. G. Matthews, W. H. Shaw, and R. G. Cuddy, "Water Quality Issues Associated with Composite Tailings (CT) Technology for Managing Oil Sands Tailings", *Int. J. Surf. Mining*, Reclam. Environ., vol. 15, no. 4, pp. 235–256, 2001.

[29] Mikula R.J., Omotoso O.E., "High surface areas caused by smectitic interstratification of kaolinite and illite in Athabasca oil sands", *Applied Clay Science*, Vol. 25, pp. 37-47, 2004.

[30] "Coagulation-flocculation-general comments", [Online]. Available: https://www.suezwaterhandbook.com/water-and-generalities/fundamental-physical-chemical-engineering-processes-applicable-to-water-treatment/coagulation-floculation/general-comments [Accessed: 18-Nov-2020].

[31] P. Stocks, K. Parker, "Reagents", *Paste and thickened tailings: a guide*, 2nd edition, R. J. Jewell, A. B. Fourie, Eds., Australian Centre for Geomechanics, Nedlands, Australia, p. 90., 2006

[32] Faghihnejad, A.; Zeng, H., *Polymer Adhesion*, Friction, and Lubrification, 2013, chap.1.

[33] S. Park and M.-K. Seo, "Intermolecular Force," in *Interface science and composites*, vol. 18, S. Park and M.-K. Seo, Eds. Amsterdam: Academic Press, pp. 1–57, 2011.

[34] J. H. Masliyah and S. Bhattacharjee, "Electric Double Layer," in *Electrokinetic and colloid transport phenomena*, Hoboken, NJ, USA: John Wiley & Sons, Inc., pp. 105–178, 2005.

[35] Kaminsky, H., "Clays and DLVO" Pres., Tailings Flocculation and Thickening NAIT course, 03th Nov. 2020.

[36] R. Hogg, "Flocculation and dewatering," *Int. J. Miner. Process.*, vol. 58, no. 1, pp. 223–236, 2000.

[37] G. M. Moody, "Polymeric Flocculants," in *Handbook of Industrial Water-Soluble Polymers*, 1st ed., P. A. Willams, Ed. John Wiley and Sons, pp. 134–173, 2007.

[38] F.Vaezi G., R.S. Sanders, J.H. Masliyah, *Journal of Colloid and Interface Science*, 355, 96-105, 2011.

[39] A. Sworska, J. S. Laskowski, G. Cymerman, *International Journal Mineral Processing*, 60, 152, 2000.

[40] Fawell,P., "Flocculants and Flocculation" Pres., Tailings Flocculation and Thickening NAIT course, 05th Nov. 2020., partially based on Jeldres, Fawell and Florio., *Powder Technology*, 326, 190-207, 2008.

[41] Johnson, S.B.; Scales, P.J.; Boger, D.V.; Franks, G., *International Journal Mineral Processing*, 58, 267-304, 2000.

[42] L. Alagha, S. Wang, L. Yan, Z. Xu, J. Masliyah, *Langmuir*, 29, 3998, 2013.

[43] Y. Samoshina, A. Diaz, Y. Becker, T. Nylander, B. Lindman, *Colloids Surface A*, 231, 205, 2003.

[44] Ji,Y;Lu, Q.; Liu, Q.; Zeng, H., *Colloids and Surfaces A: Physicochem. Eng. Aspects*, 430, 29– 38, 2013.

[45] Quezada, G.; Jeldres, R.; Fawell, P.; Toledo, P., *Minerals Engineering*, 129, 102-105, 2018.

[46] Lu, Q.; Yan, B.; Xie, L.; Huang, J.; Liu, Y.; Zeng, H., *Science of the Total Environment*, 565, 369-375, 2016.

[47] P. Ekholm, E. Blomberg, P. Claesson, I. H. Auflem, J.Sjoblom, A. Kornfeld, *Journal Colloid Interface Science*, 247,350, 2002.

[48] G. Zhang, C. Wu, *Macromolecular Rapid Communications*, 30, 335, 2009.

[49] Long, J.; Li, H.; Xu, Z.; Masliyah, J.H., *AIChE J.*, vol. 52, n°1, 371-383, 2006.

[50] A. Sworska, J. S. Laskowski, G. Cymerman, *International Journal Mineral Processing*, 60, 161, 2000.

[51] Addai-Mensah J., Colloidal forces, rheology and implications. *BHR 19 Pre-Conference Workshop*, Golden Co.;1(1):1-3, 2014.

[52] Vietti, A., "Clay Mineralogy and Water Chemistry on Tailings Settling and Rheology", 2nd Conrad Clay Workshop, Edmonton, 2011.

[53] Israelachvili, J.N.; *Intermolecular and Surface Forces* (Third Edition), 16.6, 2011.

[54] Hripko, R.; Vajihinejad,V. ; Lopes Motta,F.; Soares, J.B.P; *Global Challenges*, Vol 2, 2018.

[55] Donaldson, E.C.; Alam, W., *Wettability*, 2, 2008.

[56] Fitzpatrick, C. S.; Gregory, J., *Handbook of Water and Wastewater Microbiology*, 38:633-655, 2003.

[57] J. Gregory and S. Barany, "Adsorption and flocculation by polymers and polymer mixtures", *Adv. Colloid Interface Sci.*, vol. 169, no. 1, pp. 1–12, 2011.

[58] Besra, L., Sengupta, D.K., Roy, S.K. and Ay, P., "Influence of polymer adsorption and conformation on flocculation and dewatering of kaolin suspension", *Separation and Purification Technology*, Vol. 37, pp. 231-246, 2004.

[59] X. S. Yuan, W. Shaw, *Can. Metall. Quart.*, 46, 272, 2007.

[60] Y. Xu, G. Cymerman, "Flocculation of fine oil sand tails," Proceedings of *3rd UBC McGill Bi-Annual Symposium on Fundamentals of Mineral Processing*, Quebec City, 22–26 August, 1999.

[61] Y. Zhu, X.Tan, Q. Liu, "Dual Polymer Flocculants For Mature Fine Tailings Dewatering", *Can. J. Chem. Eng.*, Vol. 95, pp. 3-10, 2017.

[62] Y. Zhu, "Cationic and Anionic Dual Polymer Pairs for Mature Fine Tailings Flocculation and Dewatering", MSc thesis, University of Alberta, Dpt. Chem. And Mat. Eng., 2015.

[63] R. Loerke, X. Tan, Q. Liu, "Dewatering of Oil Sands Mature Fine Tailings by Dual Polymer Flocculation and Pressure Plate Filtration", *Energy Fuels*, Vol. 31, pp. 6986-6995, 2017.

[64] H. Haroon, "Flocculation and dewatering of kaolinite suspensions and oil sands mature fine tailings using dual polymers", MSc thesis, University of Alberta, Dpt. Chem. And Mat. Eng., 2014.

[65] J. Zhou, H. Li, X. Zhang, "Synergy between Dual Polymers and Sand-to-Fines Ratio for Enhanced Flocculation of Oil Sand Mature Fine Tailings", *Energy Fuels*, Vol. 35, pp. 8884-8894, 2021.

[66] C. S. Lee, J. Robinson, and M. F. Chong, "A review on application of flocculants in wastewater treatment," *Process Saf. Environ. Prot.*, vol. 92, no. 6, pp. 489–508, 2014.

[67] S. Schwarz, W. Jaeger, B.R. Paulke, S. Bratskaya, N. Smolka and J. Bohrisch, "Cationic Flocculants Carrying Hydrophobic Functionalities: Applications for Solid/Liquid Separation", *J. Phys. Chem. B*, Vol. 111, pp. 8649-8654, 2007.

[68] V. Vajihinejad, J.B.P. Soares, "Monitoring polymer flocculation in oil sands tailings: A population balance model approach", *Chem. Eng. J.*, Vol. 346, pp. 447-457, 2018.

[69] V. Vajihinejad, S.P. Gumfekar, D.V. Dixon, M.A. Silva, J.B.P. Soares, "Enhanced dewatering of oil sands tailings by a novel water-soluble cationic polymer", *Separation and Purification Technology*, Vol. 260, 118183, 2021.

[70] W. Y. Yang, J. W. Qian, Z. Q. Shen, *J. Colloid Interface Sci.*, Vol.273, pp. 405, 2004.

[71] V. D. Athawale and S. C. Rathi, "Graft polymerization: starch as a model substrate," *J. Macromol. Sci. - Polym. Rev.*, vol. 39, no. 3, pp. 445–480, 1999.

[72] S. K. Rath and R. P. Singh, "Flocculation characteristics of grafted and ungrafted starch, amylose, and amylopectin," *J. Appl. Polym. Sci.*, vol. 66, no. 9, pp. 1721–1729, 1997.

[73] M. Tizzotti, A. Charlot, E. Fleury, M. Stenzel, and J. Bernard, "Modification of Polysaccharides Through Controlled/Living Radical Polymerization Grafting-Towards the Generation of High-Performance Hybrids," *Macromol. Rapid Commun.*, vol. 31, no. 20, pp.1751-1172, 2010.

[74] B. Bazoubandi, "Synthesis and Characterization of Amylopectin-grafted Polyacrylamide (AP-g-PAM) Flocculants for Dewatering of Oil Sands Mature Fine Tailings (MFT)," University of Alberta Libraries, 2018.

[75] C.K. Na, H.J. Park, "Photoinduced grafting of vinyl benzyl trimethyl ammonium chloride on polyester nonwoven fabric with surfactant coating and its anion-exchange properties", *J. Appl. Polym. Sci.*, p. 41674, 2015.

[76] V.J. Thakur, "Biopolymer Grafting Applications", 1st Edtion, Advances in Polymers and Fibers, Elsevier, *ISBN: 9780128104620*, 2017.

[77] S. Davey, J. B. P. Soares, "Amylopectin graft copolymers for oil sands tailings treatment", Can. J. Chem. Eng., 100(4), 731, 2022.

[78] R. P. Singh, "Advanced Turbulent Drag Reducing and Flocculating Materials Based on Polysaccharides," in *Polymers and Other Advanced Materials*, P. N. Prasad, J. E. Mark, and T. J. Fai, Eds. Boston, MA: Springer, Boston, MA, pp. 227–249, 1995.

[79] W. Brostow, S. Pal, and R. P. Singh, "A model of flocculation," *Mater. Lett.*, vol. 61, no. 22, pp. 4381–4384, 2007.

[80] M. Worzakowska and M. Grochowicz, "Effect of some parameters on the synthesis and the physico-chemical properties of new amphiphilic starch-g-copolymers," *Carbohydr. Polym.*, vol. 130, pp. 344–352, 2015.

[81] O. Olatunji, “Classification of Natural Polymers,” in *Natural Polymers: Industry Techniques and Applications*, 1st ed. 20., O. Olatunji, Ed. Cham: Springer, pp. 1–17, 2015.

[82] Vilaplana, F.; Di Meng; Hasjim, J.; Gilbert, R. G. “Two-dimensional macromolecular distributions reveal detailed architectural features in high-amylose starches”, *Carbohydrate polymers 2014*, 113, 539–551. *DOI: 10.1016/j.carbpol.2014.07.050*. Published Online: Jul. 31, 2014.

[83] S. Davey, “Amylopectin-graft-hydrolyzed-poly(methyl acrylate) (AP-g-H-PMA) Flocculants for the Treatment of Oil Sands Tailings,” University of Alberta Libraries, 2020.

[84] A. K. Sarkar, N. R. Mandre, A. B. Panda, and S. Pal, “Amylopectin grafted with poly (acrylic acid): development and application of a high-performance flocculant,” *Carbohydr. Polym.*, vol. 95, no. 2, p. 753, 2013.

[85] R. P. Singh, S. Pal, V. K. Rana, and S. Ghorai, “Amphoteric amylopectin: A novel polymeric flocculant,” *Carbohydr. Polym.*, vol. 91, no. 1, pp. 294–299, 2013.

[86] K. Kumar, P. Adhikary, N. C. Karmakar, S. Gupta, R. P. Singh, and S. Krishnamoorthi, “Synthesis, characterization and application of novel cationic and amphoteric flocculants based on amylopectin,” *Carbohydr. Polym.*, vol. 127, pp. 275–281, 2015.

[87] Y. Chen, S. Liu, G. Wang, “A kinetic investigation of cationic starch adsorption and flocculation in kaolin suspension”, *Chem. Eng. J.*, Vol. 133, pp. 325-333, 2007.

[88] B. Bazoubandi, J.B.P. Soares, “Amylopectin-*graft*-polyacrylamide for the flocculation of oil sands tailings”, *Miner. Eng.*, Vol. 148, 106196, 2020.

[89] L. Botha, S. Davey, B. Nguyen, A. K. Swarnakar, E. Rivard, and J. B. P. Soares, “Flocculation of oil sands tailings by hyperbranched functionalized polyethylenes (HBfPE),” *Miner. Eng.*, vol. 108, pp. 71–82, 2017.

[90] Thermo Elemental ® Handout, “AAS, GFAAS, ICP or ICP-MS? Which technique should I use? – An elementary overview of elemental analysis”, 2001.

[91] E.S. Dipietro, M.M. Bashor, P.E. Stroud, B.J. Burgess, W.E. Turner and J.W. Neese, “Comparison of an an inductively coupled plasma-atomic emission spectrometry method for the determination of calcium, magnesium, sodium, potassium, copper and zinc with atomic absorption spectroscopy and flame photometry methods”, *The Science of the Total Environment*, Vol. 74, pp. 249-262, 1988.

[92] M. Worzakowska and M. Grochowicz, “Effect of some parameters on the synthesis and the physico-chemical properties of new amphiphilic starch-g-copolymers,” *Carbohydr. Polym.*, vol. 130, pp. 344–352, 2015.

[93] Rudin A.; Choi P., Eds. *The Elements of Polymer Science & Engineering 3rd Edition*, 3rd ed.; Academic Press, 2012.

[94] Netopilík, M.; Podešva, J.; Lokaj, J.; Kratochvíl, P., “Number-average molecular weight of branched polymers from SEC with viscosity detection and universal calibration”, *Polym. Int.*, Vol. 57, 2008.

[95] Dawkins, J. V.; Dawkins, J. V., Eds, "Developments in Polymer Characterisation-4", *Springer International Publishing*, 1983. DOI: 10.1007/978-94-009-6628-4.

[96] Hamielec A., "Characterization of Complex Polymer Systems by Size Exclusion Chromatography", *Pure & Appl. Chem,* Vol.54 (2), pp.293-207, 1982.

[97] X. Qiu, D. Japikse, M. Anderson, "A meanline model for impeller flow recirculation", *Proceedings of ASME Turbo Expo 2008*, 2008.

[98] V. Vajihinejad, "Polymer Treatment of Oil Sands Tailings: Experimental and Modeling Investigations", University of Alberta Libraries, 2020.

[99] G.E.P. Box, K.B. Wilson, "On the Experimental Attainment of Optimum Conditions", *J. R. Stat. Soc. Ser. B*, vol. 13, no. 1, pp. 1–38, 1951.

[100] S. Bhattacharya, "Central Composite Design for Response Surface Methodology and Its Application in Pharmacy", *IntechOpen ,* [Online]: http://dx.doi.org/10.5772/intechopen.95835 [Accessed June – 2021].

[101] J.J. Borkowski, "Spherical Prediction-Variance Properties of Central Composite and Box-Behnken Designs", *Technometrics*, Vol. 37, No. 4, pp. 399-410, 1995.

[102] B.A. Oyejola, J.C. Nwanya, "Selecting the Right Central Composite Design", *Internat. J. of Stat. and App.*, Vol. 5 (1), pp. 21-30, 2015.

[103] M. A. Bezerra, R. E. Santelli, E. P. Oliveira, L. S. Villar, and L. A. Escaleira, "Response surface methodology (RSM) as a tool for optimization in analytical chemistry," *Talanta*, vol. 76, no. 5, pp. 965–977, Sep. 2008.

[104] "How to crop circle from an image?", MATLAB Central Answers forum [Online]: https://www.mathworks.com/matlabcentral/answers/567441-how-to-crop-circle-from-an-image [Accessed: 05-May-2022].

[105] "Cell segmentation", Steve Eddins' post on Image Processing with MATLAB [Online]: https://blogs.mathworks.com/steve/2006/06/02/cell-segmentation/ [Accessed: 05-May-2022].

[106] "Marker-Controlled Watershed Segmentation", MATLAB Documentation [Online]: https://www.mathworks.com/help/images/marker-controlled-watershed-segmentation.html [Accessed: 06-May-2022].

[107] Huang, Yu-Len, Dar-Ren, "Watershed segmentation for breast tumor in 2-D sonography", *Ultrasound in medicine & biology*, vol. 30, n°5, p.625-362, 2004.

[108] "Particle size distribution using image processing in MATLAB", MATLAB Central Answers forum [Online]: https://www.mathworks.com/matlabcentral/answers/65623-particle-size-distribution-using-image-processing-in-matlab [Accessed: 05-May-2022].

[109] Dhodapkar S., Trottier R., "A Guide to Characterizing Particle Size and Shape", CEP, *AIChE*, July 2014.

[110] Chunwoo Lee and Timothy A Kramer. “Prediction of three-dimensional fractal dimensions using the two-dimensional properties of fractal aggregates”, *Advances in colloid and interface science*, 112.1, pp. 49–57, 2004.

[111] D. Dudasova, S. Simon, P. V. Hemmingsen, J. Sjöblom, *Colloid Surface A.*, pp. 317,1, 2008.

[112] D. Dudasova, G. R. Flåten, J. Sjöblom, G. Øye, *Colloid Surface A.*, pp. 335, 62, 2009.

[113] Connolly J.R., “Introduction Quantitative X-Ray Diffraction Methods”, EP400-002, Introduction to X-Ray Powder Diffraction, 2003.

[114] Hubbard C.R., Snyder R.L., “RIR-Measurement and Use in Quantitative XRD”, *Powder Diffraction*, Vol. 3, No. 2, 1988.

[115] “Properties”, DIFFRAC.SUITE user manual, page 104, 2011.

[116] M. A. Mohamed, J. Jaafar, A. F. Ismail, M. H. D. Othman, and M. A. Rahman, “Fourier Transform Infrared (FTIR) Spectroscopy”, *Membrane Characterization*, N. Hilal, A. F. Ismail, T. Matsuura, and D. Oatley-Radcliffe, *Eds. Elsevier*, pp. 3–29, 2017.

[117] L. Xia, G. Wenyuan, J. Qianqian, H. Luqi, and L. Changxiao, “Study on the morphology, crystalline structure, and thermal properties of Fritillaria ussuriensis Maxim. starch acetates with different degrees of substitution,” *Starch - Stärke*, vol. 63, no. 1, pp. 24–31, 2011.

[118] M. Braglia, I.V. Ferrari, L. Pasquini, T. Djenizian, M. Sette, M.L. Di Vona, P. Knauth, “Electrochemical synthesis of thin, dense, and conformal anion exchange membranes with quaternary ammonium groups”, *Electrochimica Acta*, Vol. 265, p.78-88, 2018.

[119] P. Wang, Y-N. Zhou, J-S. Luo, Z-H. Luo, “Poly (ionic liquid) s-based nanocomposite polyelectrolytes with tunable ionic conductivity prepared via Si-ATRP”, *Polym. Chem.*, Vol.5, pp. 882-891, 2014.

[120] T. Zhang, I. Zhitomirsky, “Strategies for electrosynthesis of poly((vinylbenzyl)trimethylammonium chloride) and composite films”, *Materials and Manufacturing Processes*, Vol. 32:4, pp. 404-408, 2017.

[121] Q. Liu, J.R. de Wijn, K. de Groot, C.A. van Blitterswijk, “Surface modification of nano-apatite by grafting organic polymer”, *Biomaterials*, Vol. 19, pp. 1067-1072, 1998.

[122] C.M. Kok, A. Rudin, “Relationship between the hydrodynamic radius and the radius of gyration of a polymer in solution”. *Makromol. Chem. Rapid. Commun.,* Vol. 2(11), pp. 655–659, 1981.

[123] M. Schmidt, D. Nerger, W. Burchard, “Quasi-elastic light scattering from branched polymers: 1. Polyvinylacetate and polyvinylacetate—microgels prepared by emulsion polymerization”, *Polymer,* Vol. 20(5), pp. 582–588, 1979.

[124] X. Wang, H. Xin, Y. Zhu, W. Chen, E. Tang, J. Zhang and Y. Tan, “Synthesis and characterization of modified xanthan gum using poly(maleic anhydride/1-octadecene)”, *Colloid Polym. Sci.*, Vol. 294, pp. 1333-1341, 2016.

[125] G. Del Monte, D. Truzzolilo, F. Camerin, A. Ninarello, E. Chauveau, L. Tavagnacco, N. Gnan, L. Rovigatti, S. Sennato and E. Zaccarelli, "Two-step deswelling in the Volume Phase Transition of thermoresponsive microgels", *PNAS*, Vol. 118 (37), 2021.

[126] L. Wang, W. Dong, and Y. Xu, "Synthesis and characterization of hydroxypropyl methylcellulose and ethyl acrylate graft copolymers", *Carbohydr. Polym.*, vol. 68, no. 4, pp. 626–636, 2007.

[127] Z.R. Najafabadi, J.B.P. Soares, "Flocculation and dewatering of oil sands tailings with a novel functionalized polyolefin flocculant", *Separation and Purification Technology*, Vol. 274-119018, 2021.

[128] C. Costa, V.H.S. Santos, P.H.H. Araujo, C. Sayer, A.F. Santos, M. Fortuny, "Microwave-assisted rapid decomposition of persulfate", *European Polymer Journal*, Vol. 45, pp. 2011-2016, 2009.

[129] S-C. Hsu, T-M. Don, W-Y. Chiu, "Free radical degradation of chitosan with potassium persulfate", *Polymer Degradation and Stability*, Vol.75, pp. 73-83, 2002.

[130] V. Vajihinejad et al., "Water Soluble Polymer Flocculants: Synthesis, Characterization, and Performance Assessment", *Macromolecular Materials and Engineering* p. 1800526, 2018.

[131] S. Balemans, S.E. Vlaeminck, E. Torfs, L. Hartog, L. Zaharova, U. Rehman, I. Nopens, "The Impact of Local Hydrodynamics on High-Rate Activated Sludge Flocculation in Laboratory and Full-Scale Reactors", *Processes*, 8, 131, 2020.

[132] R.V. Lenth, "Response-Surface Methods in R, Using rsm", *The University of Iowa*, version 2.10.2, 2020.

[133] R. DeLoach, N. Ulbrich, "A Comparison of Two Balance Calibration Model Building Methods", *American Institute of Aeronautics and Astronautics*, 45th AIAA Aerospace Sciences Meeting and Exhibit, 2007.

[134] J. Neter, W. Wasserman, and M. H. Kutner, "Applied linear statistical models: regression, analysis of variance, and experimental designs", *Irwin*, Boston ,1990.

[135] J. Zhang, X. Shen, Q. Zhang, J.P.-Y. Maa, G. Qiao, "Bimodal particle size distributions of fine-grained cohesive sediments in a settling column with oscillating grids", *Continental Shelf Research*, Vol.174, pp.85-94, 2019.

[136] L. Besra, D.K. Sengupta, S.K. Roy, "Particle characteristics and their influence on dewatering of kaolin, calcite and quartz suspensions", *Int. J. Miner. Process*., Vol. 59, pp. 89-112, 2000.

[137] B. Derakhshandeh, "Kaolinite suspension as a model fluid for fluid dynamics studies of fluid fine tailings", *Rheol Acta*, Vol. 55, pp. 749-758, 2016.

[138] L. Nabzar, E. Pefferkorn, "An Experimental Study of Kaolinite Crystal Edge-Polyacrylamide Interactions in Dilute Suspensions", *J. of Colloid and Int. Sci.*, Vol.108, No.1, pp.243-248, 1985.

[139] Greenhill et al., "Method of Treating an Aqueous Suspension of Kaolin", *US Patent 6615987 B1*, 2003.

[140] A. Vahedi, B. Gorczyca, “Application of fractal dimensions to study the structure of flocs formed in lime softening process”, *Water research*, Vol. 45, pp. 545-556, 2011.

[141] D. H. de Boer, M. Stope, L. M. J. Lévesque, “Fractal dimensions of individual flocs and floc populations in streams”, Hydrol. Process., Vol. 14, pp. 653-667, 2000.

[142] J. Worlitschek, M. Mazzotti, “Choice of the focal point position using Lasentec FBRM”, *Particle & Particle Systems Characterization*, Vol. 20.1, pp. 12-17, 2003.

[143] J. Gregory, S. Barany, “Adsorption and flocculation by polymers and polymer mixtures”, *Advances in Colloid and Interface Science,* Vol. 169.1, pp. 1-12, 2011.

[144] A. Chremos, J. F. Douglas, “Competitive Solvation Effects in Polyelectrolyte Solutions”, *ACS Symposium Series*, Vol. 1296, Chap. 2, pp. 15-32, 2018.

[145] C. Forrey, J.F. Douglas, M. K. Gilson, “The fundamental role of flexibility on the strength of molecular binding”, *Soft Matter*, Vol. 8, 6385-6392, 2012.

Appendix A1

Calibration between nominal and small vial, used for supernatant turbidity measurements

Table A1 – Vial Calibration for Supernatant Turbidity Measurement.

Turbidity (NTU)	Pt 1	Pt 2	Pt 3	Pt 4	Pt 5	Pt 6	Pt 7	Pt 8	Pt 9	Pt 10	Pt 11	Pt 12	Pt 13
Nominal Vial 50mL	0.566	2.84	10.9	41.6	67.2	92.7	156	163	408	878	1310	1894	3240
	0.571	2.86	11.0	41.6	67.2	93.1	153	165	406	878	1309	1887	3242
	0.570	2.85	11.0	41.4	67.4	92.9	154	165	404	882	1305	1883	3239
Small Vial 15mL	1.58	2.08	6.47	19.2	35.8	40.9	75.1	76.2	219	650	734	1074	2067
	1.56	2.09	6.43	19.1	35.5	40.9	75.2	75.9	220	652	735	1074	2066
	1.57	2.09	6.44	18.8	35.7	50.0	74.9	76.1	221	650	734	1072	2064
Average													
Nominal Vial 50mL	0.570	2.85	10.9	41.5	51.5	68.4	154	164	406	879	1020	1480	3240
Small Vial 15mL	1.57	2.09	6.45	19.0	35.7	43.9	75.1	76.1	220	651	734	1070	2070
Std Error													
Nominal Vial 50mL	0.001	0.005	0.03	0.05	0.05	0.09	0.72	0.54	0.94	1.09	1.25	2.62	0.72
Small Vial 15mL	0.005	0.003	0.01	0.1	0.07	2.48	0.07	0.07	0.47	0.54	0.27	0.54	0.72

Appendix A2

Half-Factorial design used for screening tests prior to full central composite design

Table A2 – Half-factorial design.

Run	C* dosage (kppm)	A** dosage (kppm)	C* addition flowrate (mL/min)	A** addition flowrate (mL/min)	Solids content (wt.%)
1	0.5	8	85	5	31.3
2	8	0.5	5	25	31.3
3	0.5	0.5	85	5	5
4	0.5	0.5	5	25	5
5	0.5	8	85	25	5
6	8	0.5	5	5	5
7	0.5	8	5	25	31.3
8	8	8	85	5	5
9	8	0.5	85	5	31.3
10	0.5	8	5	5	5
11	8	0.5	85	25	5
12	8	8	5	25	5
13	8	8	85	25	31.3
14	8	8	5	5	31.3
15	0.5	0.5	85	25	31.3
16	0.5	0.5	5	5	31.3

*C refers to the cationic polymer specie, here AP-g-PVBTMAC F_4L_2
**A refers to the anionic polymer specie, here MF 1011

Appendix A3

Code portions used for flocs sizes estimation with image processing

```
% Get image.
originalImage=imread('D:\Documents\UofA\ALBERTA\CLASSES\RESEARCH\Image treatment\RUNS PICS\RUN1.jpg');
[rows, columns, numberOfColorChannels] = size(originalImage)
subplot(2, 2, 1);
imshow(originalImage);
axis('on', 'image');
title('Original Image', 'FontSize', fontSize);
% Maximize the window to make it easier to draw.
g = gcf;
g.WindowState = 'maximized'
% Ask user to draw a circle:
%uiwait(helpdlg('Please click and drag out a circle.'));
h.Radius = 0;
while h.Radius == 0
        h = drawcircle('Color','k','FaceAlpha',0.4)
        if h.Radius == 0
                uiwait(helpdlg('You double-clicked.  You need to single click, then drag, then single
click again.'));
        end
end
% Get coordinates of the circle.
angles = linspace(0, 2*pi, 10000);
x = cos(angles) * h.Radius + h.Center(1);
y = sin(angles) * h.Radius + h.Center(2);
% Show circle over image.
subplot(2, 2, 2);
imshow(originalImage);
axis('on', 'image');
hold on;
plot(x, y, 'r-', 'LineWidth', 2);
title('Original image with circle mask overlaid', 'FontSize', fontSize);
% Get a mask of the circle
mask = poly2mask(x, y, rows, columns);
subplot(2, 2, 3);
imshow(mask);
axis('on', 'image');
title('Circle Mask', 'FontSize', fontSize);
% Mask the image with the circle.
if numberOfColorChannels == 1
        maskedImage = originalImage; % Initialize with the entire image.
        maskedImage(~mask) = 0; % Zero image outside the circle mask.
else
        % Mask the image.
        maskedImage = bsxfun(@times, originalImage, cast(mask, class(originalImage)));
end
% Crop the image to the bounding box.
props = regionprops(mask, 'BoundingBox');
maskedImage = imcrop(maskedImage, props.BoundingBox);
% Display it in the lower right plot.
subplot(2, 2, 4);
imshow(maskedImage, []);
```

Figure A3.1 – Code used to circle crop an image.

```
%%%%%%%%%%%%%%%%%%%%%%%%%%%%%%%%%%%%%%%%%%%%%%%%%%%%%%%%%%%%%%%%%%%%%%
%%
%SEGMENTATION
%WATERSHED WITH GRADIENT
%Gradient
%Manually
%hy = fspecial('sobel');
%hx = hy';
%Iy = imfilter(double(I_eq), hy, 'replicate');
%Ix = imfilter(double(I_eq), hx, 'replicate');
%gradmag = sqrt(Ix.^2 + Iy.^2);
%With MATLAB Function
gradmag= imgradient(I_eq);
figure, imshow(gradmag,[])
%MARK THE FOREGROUND OBJECTS
%OPENING
se = strel('disk',2);
Io = imopen(I_eq, se);
figure, imshow(Io), %title('Opening (Io)')
%OPENING-BY-RECONSTRUCTION
Ie = imerode(I_eq, se);
Iobr = imreconstruct(Ie, I_eq);
figure, imshow(Iobr), title('Opening-by-reconstruction (Iobr)')
%OPENING-CLOSING BY RECONSTRUCTION
Iobrd = imdilate(Iobr, se);
Iobrcbr = imreconstruct(imcomplement(Iobrd), imcomplement(Iobr));
Iobrcbr = imcomplement(Iobrcbr);
figure, imshow(Iobrcbr), title('Opening-closing by reconstruction
(Iobrcbr)')
%DEFINING FOREGROUND MARKERS
fgm = imextendedmax(Iobrcbr,30);
%%%%%%%%%%%%%%%%%%%%%%%%%%%%%%%%%%%%%%%%%%%%%%%%%%%%%%%%%%%%%%%%%%%%%%
%%%%%%%%%%%%%%%%%%
figure, imshow(fgm), title('Regional maxima of opening-closing by
reconstruction (fgm)')
I2 = I_eq;
I2(fgm) = 255;
figure, imshow(I2), title('Regional maxima superimposed on original
image (I2)')
se2 = strel(ones(5,5));
fgm2 = imclose(fgm, se2);
fgm3 = imerode(fgm2, se2);
fgm4 = bwareaopen(fgm3, 20);
I3 = I_eq;
I3(fgm4) = 255;
figure, imshow(I3)
title('Modified regional maxima superimposed on original image
(fgm4)')
%BACKGROUND MARKERS
bw2 = im2bw(Iobrcbr, graythresh(Iobrcbr));
D=bwdist(~bw2);
%WATERSHED
DL = watershed(D);
bgm = DL == 0;
imshow(bgm)
title('Watershed Ridge Lines')
gmag2 = imimposemin(gradmag, bgm | fgm4);
L1 = watershed(gmag2);
figure, imshow(label2rgb(L1))
%SEGMENTATION RESULT
labels = imdilate(L1==0,ones(3,3)) + 2*bgm + 3*fgm4;
I4 = labeloverlay(I,labels);
figure,imshow(I4)
title('Markers and Object Boundaries Superimposed on Original Image')
%PLOT SALIENCY PROFILE
background = imopen(D,strel('disk',15));
figure, surf(double(background(1:8:end,1:8:end))),zlim([0 255])
title('Saliency profile of the flocculation result image')
xlabel('x position in the length of the image')
ylabel('y position in the width of the image')
zlabel('z position of the regional maxima')
set(gca,'ydir','reverse');
```

```
%%%%%%%%%%%%%%%%%%%MARKER2%%%%%%%%%%%%%%%%%%%%%%%%%
%%%%%%%%%%%%%%%%%%%%%%
%MARKER-BASED WATERSHED SEGMENTATION WITH REGIONAL
MAXIMA
mask_em = imextendedmax(I_eq, 30);
figure, imshow(mask_em)
%Cleaning and Overlaying
mask_em = imclose(mask_em, ones(5,5));
mask_em = imfill(mask_em, 'holes');
mask_em = bwareaopen(mask_em, 40);
bw4_perim = bwperim(bw);
overlay2 = imoverlay(I_eq, bw4_perim | mask_em, [.3
1 .3]);
figure, imshow(overlay2)
%Need for the peaks to become valley since
watershed transform identifies
%low points not high points
I_eq_c = imcomplement(I_eq);
I_mod = imimposemin(I_eq_c, ~bw | mask_em);
L = watershed(I_mod);
figure, imshow(label2rgb(L))
%%%%%%%%%%%%%%%%%%%METHOD2%%%%%%%%%%%%%%%%%%%%%%%%%
%%%%%%%%%%%%%%%%%%%%%%%
%Cleaning not necessary here / superposing with
perimeter
bw2 = imfill(bw,'holes');
se = strel('disk',3);
bw3 = imopen(bw2, se);
bw4 = bwareaopen(bw3, 10);
bw4_perim = bwperim(bw);
overlay1 = imoverlay(I_eq, bw4_perim, [.3 1 .3]);
figure, imshow(overlay1)
```

Figure A3.2 – Code used for the marker-based watershed segmentation method (adapted from [107]) with two different markers and the second method with perimeter.

```
% PARTICLE SIZE ANALYSIS
% Ask user for one integer number to define the
number of classes of the
% PSD
defaultValue = 50;
titleBar = 'Enter an integer value';
userPrompt = 'Enter the integer';
dialogBoxWidth = 100;
fontSize=15;
caUserInput = inputdlg(userPrompt, titleBar,
[1, dialogBoxWidth], {num2str(defaultValue)});
if isempty(caUserInput),return,end % Bail out
if they clicked Cancel.
% Round to nearest integer in case they
entered a floating point number.
numberOfBins =
round(str2double(cell2mat(caUserInput)));
% Check for a valid integer.
if isnan(numberOfBins)
        % They didn't enter a number.
        % They clicked Cancel, or entered a
character, symbols, or something else not
allowed.
        numberOfBins = defaultValue;
        message = sprintf('I said it had to
be an integer.\nTry replacing the user.\nI
will use %d and continue.', numberOfBins);
        uiwait(warndlg(message));
end
```

Figure A3.3 – User interaction for number of classes in the PSD.

```
%ANALYSIS
%WITH PERIMETER METHOD
binaryImage = bw4_perim;
labeledImage = bwlabel(binaryImage);
fprintf('Measuring particles.\n');
[out1,LM1]=bwferet(bw4_perim,'MinFeretProperties');
[out2,LM2]=bwferet(bw4_perim,'MaxFeretProperties');
minFeret= mean(out1.MinDiameter(:,:));
maxFeret= mean(out2.MaxDiameter(:,:));
figure,histObject = histogram(out1.MinDiameter,
numberOfBins)
diamDistribution = histObject.Values;
binWidth = histObject.BinEdges(2) -
histObject.BinEdges(1);
% Get a number that is the center value of the bin
instead of the left edge.
binDiameters = histObject.BinEdges(1:end-1) +
binWidth/2;
bar(binDiameters, diamDistribution, 'BarWidth', 1.0);
% Put labels atop the bars
for k = 1 : length(diamDistribution)
        x = binDiameters(k);
        y = diamDistribution(k) + 2;
        if diamDistribution(k) > 0
                caption = sprintf('%d particles\nECD =
%.2f', y, x);
                text(x, y, caption, 'FontWeight',
'bold', 'FontSize', 7, 'Color', 'r',
'HorizontalAlignment', 'center');
                % Report how many particles are in
this bin
                fprintf('The bin at %6.2f has %5d
particles in it.\n', x, diamDistribution(k));
        end
end
title('Histogram of min Feret Equivalent Diameters in
Pixels', 'FontSize', fontSize);
xlabel('min Feret Diameter in Pixels', 'FontSize',
fontSize);
ylabel('Count (# of particles)', 'FontSize', fontSize);
%Fitting the data with distrib
x= out1.MinDiameter;
pd=fitdist(x,'Lognormal');
%MEAN EQUIVALENT DIAMETER
m=mean(pd);
%PARTICULE SIZE DISTRIBUTION
lastVal =ceil(max(x));
binEdges=0:binWidth:lastVal+1;
figure, h =
histogram(x,binEdges,'Normalization','pdf','FaceC
olor',[.9 .9 .9]);
xlabel('Equivalent Diameter in Pixels');
ylabel('Probability Density');
ylim([0 0.1]);
xgrid = linspace(0,500,100)';
pdfEst = pdf(pd,xgrid);
line(xgrid,pdfEst)
binaryImage2 = bw4_perim;
labeledImage2 = bwlabel(binaryImage2);
fprintf('Measuring particles1.\n');
measurements2 = regionprops(labeledImage2,
'EquivDiameter','Area','Perimeter');
numParticles2 = length(measurements2);
allDiameters2 = [measurements2.EquivDiameter];
Area2 = [measurements2.Area];
Perim2 = [measurements2.Perimeter];
md=mean(Area2);
mp=mean(Perim2);
%PERIMETER FRACTAL DIMENSION FROM LEE AND KRAMER
CORRELATION
dpf= 2*log(mp)/log(md);
dpf3D= -1.63*dpf+4.6;
```

Figure A3.4 – Code portion used for the analysis of the mean floc size with the perimeter method and the estimation of the fractal dimension.

Appendix B1

PSD results details for MFT and kaolinite suspensions

The narrow span in the PSD of the sample (Figure 4.1, Figure 4.2) is a first indicator of the accuracy of the measurements. The weighted residual (Table 4.3) is another indicator. The calculated data fitted well the data since the residuals are less than 1% for all runs. To ensure measurements were relevant, the trend chart (obtained with 10 consecutive measures) was monitored to check its stability. The variations of D_{90} with sonication highlights the usefulness of this technique since these aggregates originally present in the MFT sample would bias the particle size distribution to higher sizes or lead to unstable measurements of particle sizes. The PSD of the kaolinite suspension is bimodal (uncharacteristic secondary mode near 0.7 µm), which is likely due to a poor fit in comparison with the fit obtained for the MFT (see higher values for the weighted residuals Table B1.2 versus Table B1.1).

Table B1.1 – PSD results in volume basis for the MFT sample.

VOLUME		D[3,2] (µm)	D[4,3] (µm)	D_{10} (µm)	D_{50} (µm)	D_{90} (µm)	Weighted Residual* (%)	Specific Surface Area (m^2/kg)
RUN 1	Pre-Sonication	3.82	21.0	1.44	10.3	51.9	0.28	1571
	Post-Sonication	3.73	19.5	1.40	9.99	48.0	0.29	1610
RUN 2	Pre-Sonication	3.77	19.7	1.42	10.0	48.0	0.31	1593
	Post-Sonication	3.62	18.6	1.36	9.46	45.2	0.32	1656
RUN 3	Pre-Sonication	3.70	18.6	1.40	9.66	44.9	0.29	1621
	Post-Sonication	3.62	17.5	1.36	9.38	43.3	0.31	1659
MEANS	Pre-Sonication	3.76	19.8	1.42	10.0	48.3	0.30	1595
	Post-Sonication	3.66	18.5	1.37	9.61	45.5	0.31	1642
GLOBAL MEANS		3.71	19.2	1.40	9.80	46.9	0.30	1618

* Weighted residual is calculated by the Mastersizer 3000 software based on the data fit.

Table B1.2 – PSD results in volume basis for the kaolinite suspension.

VOLUME		D[3,2] (µm)	D[4,3] (µm)	D_{10} (µm)	D_{50} (µm)	D_{90} (µm)	Weighted Residual* (%)	Specific Surface Area (m^2/kg)
RUN 1	Pre-Sonication	1.58	2.90	0.685	2.33	6.01	0.85	3789
	Post-Sonication	1.39	2.63	0.592	2.14	5.46	0.95	4313
RUN 2	Pre-Sonication	1.48	2.61	0.654	2.13	5.30	0.80	4059
	Post-Sonication	1.28	2.37	0.557	1.93	4.91	0.91	4680
RUN 3	Pre-Sonication	1.35	2.30	0.611	1.91	4.60	0.93	4445
	Post-Sonication	1.18	2.14	0.520	1.74	4.40	1.04	5081
MEANS	Pre-Sonication	1.47	2.60	0.65	2.12	5.30	0.86	4098
	Post-Sonication	1.28	2.38	0.56	1.94	4.92	0.97	4691
GLOBAL MEANS		1.38	2.49	0.60	2.03	5.11	0.91	4395

* Weighted residual is calculated by the Mastersizer 3000 software based on the data fit.

Table B1.3 – Calculated results of number PSD for the MFT sample.

NUMBER		D_{10} (µm)	D_{50} (µm)	D_{90} (µm)
RUN 1	Pre-sonication	0.366	0.514	0.964
	Post-sonication	0.366	0.513	0.961
RUN 2	Pre-sonication	0.367	0.515	0.966
	Post-sonication	0.366	0.516	0.960
RUN 3	Pre-sonication	0.367	0.516	0.967
	Post-sonication	0.366	0.514	0.962
MEANS	Pre-sonication	0.367	0.516	0.966
	Post-sonication	0.366	0.514	0.961
OVERALL MEANS		**0.366**	**0.515**	**0.963**

Table B1.4 – Calculated results of number PSD for the kaolinite suspension.

NUMBER		D_{10} (µm)	D_{50} (µm)	D_{90} (µm)
RUN 1	Pre-sonication	0.375	0.534	1.010
	Post-sonication	0.346	0.489	0.860
RUN 2	Pre-sonication	0.373	0.529	0.988
	Post-sonication	0.335	0.472	0.829
RUN 3	Pre-sonication	0.349	0.500	0.942
	Post-sonication	0.321	0.447	0.784
MEANS	Pre-sonication	0.366	0.521	0.980
	Post-sonication	0.334	0.469	0.824
OVERALL MEANS		**0.350**	**0.500**	**0.900**

Appendix B2

Molecular Weight Distributions obtained with GPC:

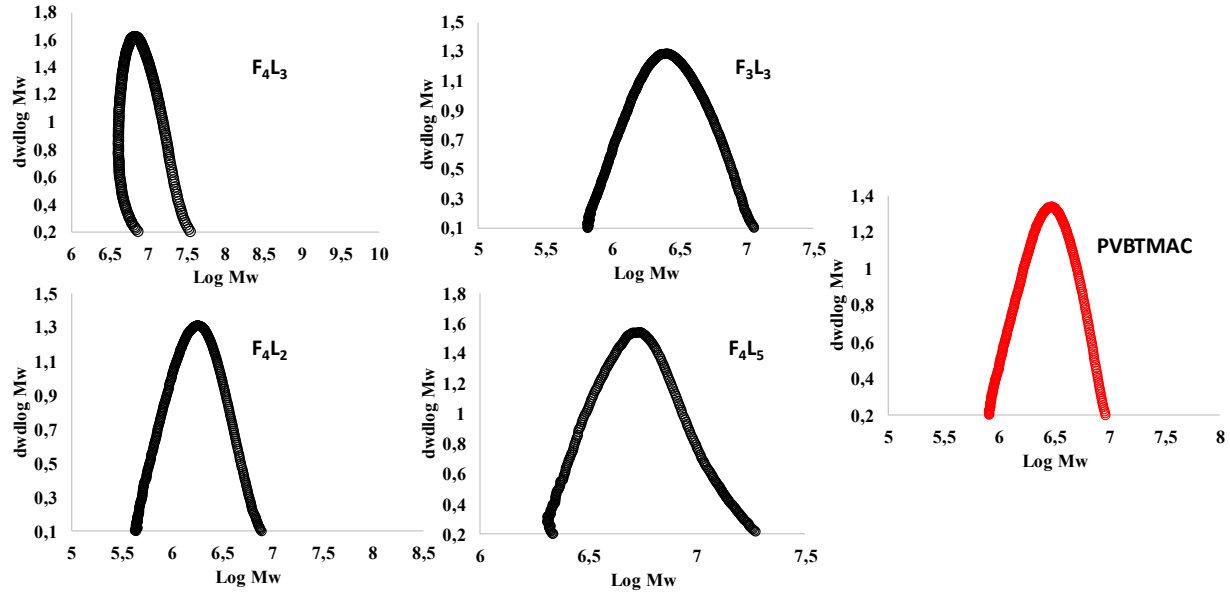

Figure B2.1 – Molecular weight distributions for polymer synthesized at 50 °C.

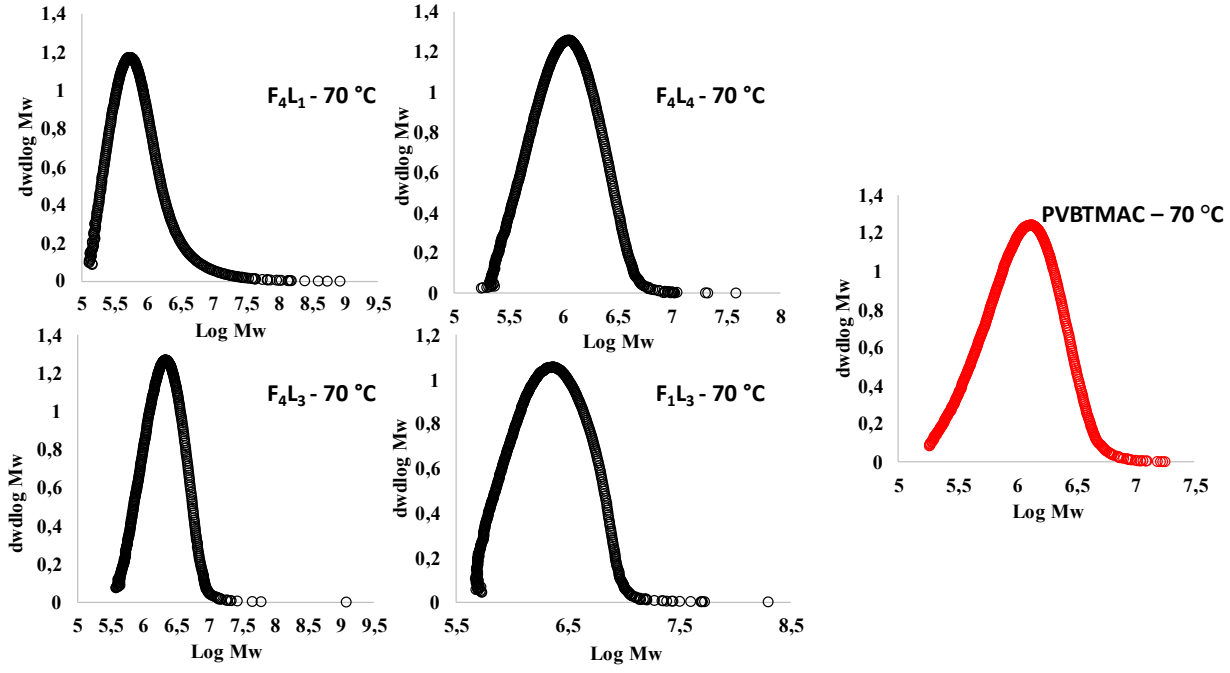

Figure B2.2 – Molecular weight distributions for polymer synthesized at 70 °C.

Appendix B3

Flocculation results with polymer synthesized at 70 °C

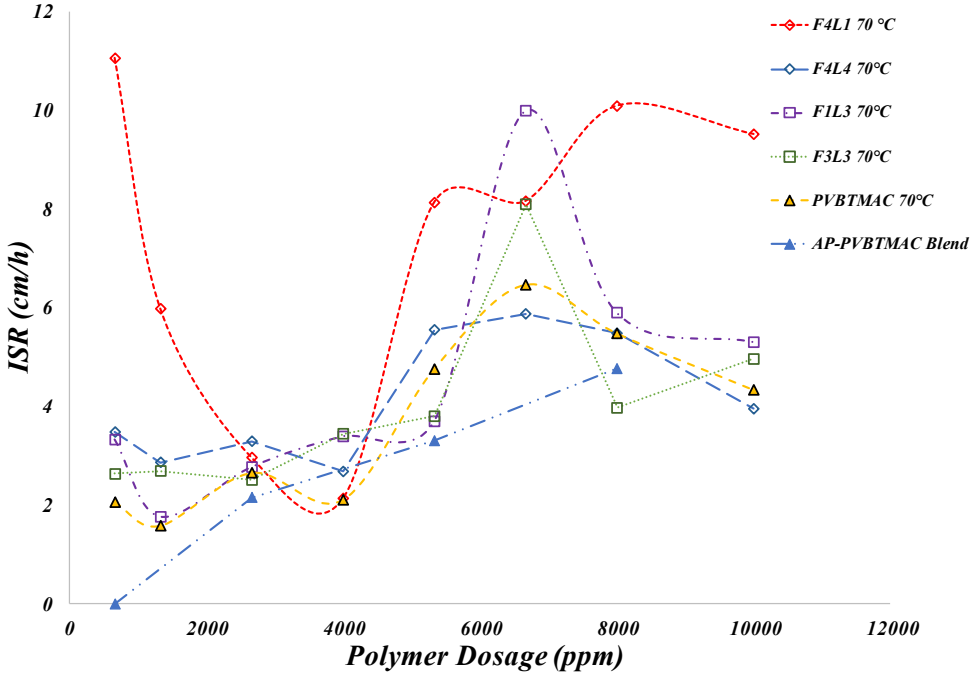

Figure B3.1 – Effect of polymer dosage on ISR.

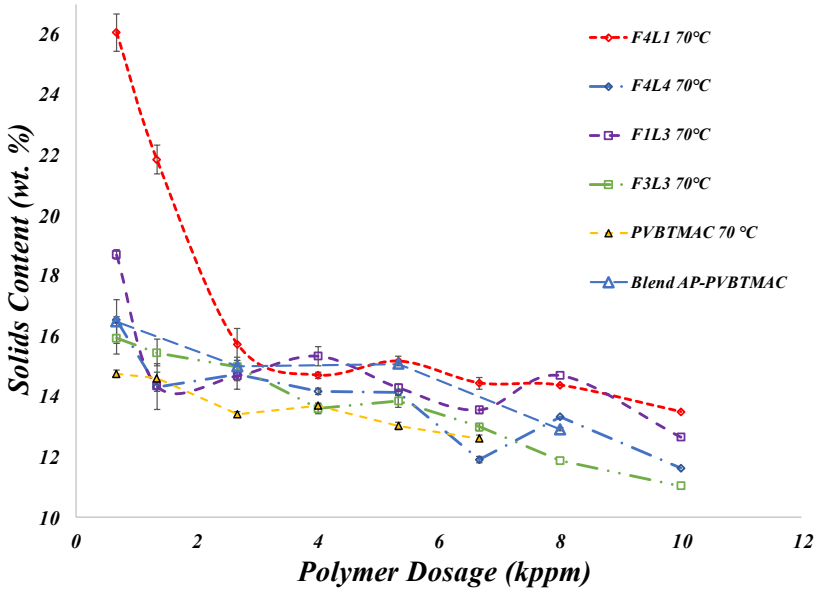

Figure B3.2 – Effect of polymer dosage on solids content.

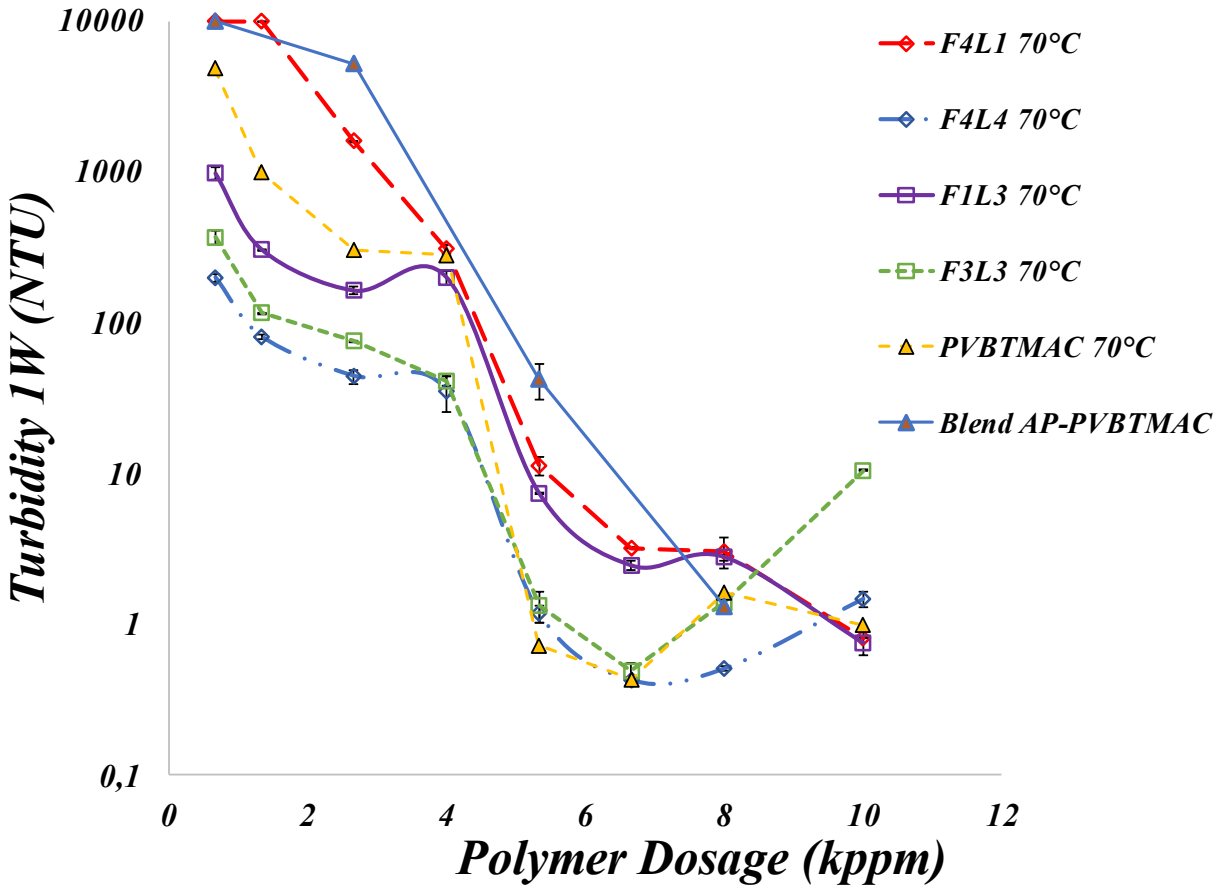

Figure B3.3 – Effect of polymer dosage on supernatant turbidity after one week.

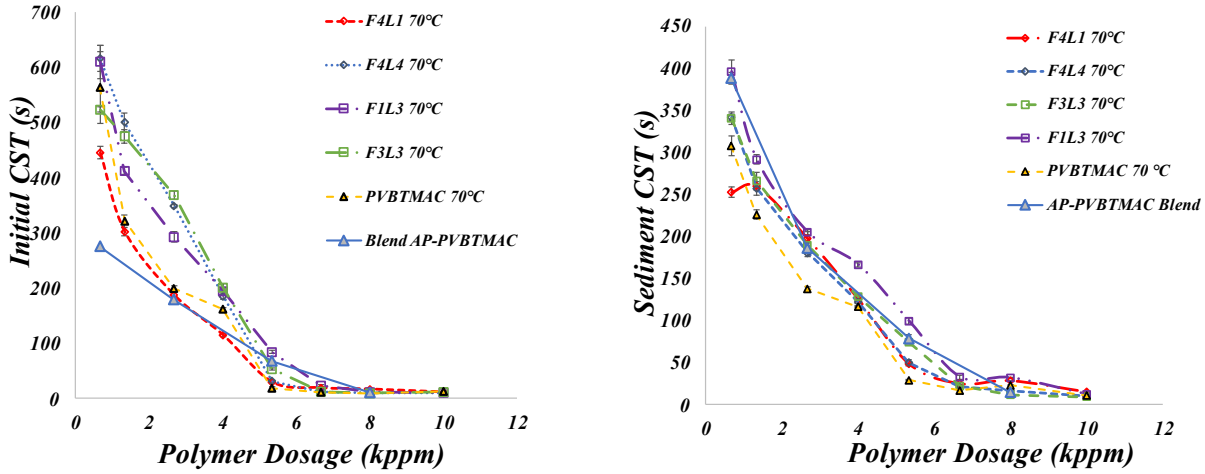

Figure B3.4 – Effect of polymer dosage on initial (a) and sediment (b) CSTs.

Flocculation results for a same polymer structure synthesized at 50 or 70°C

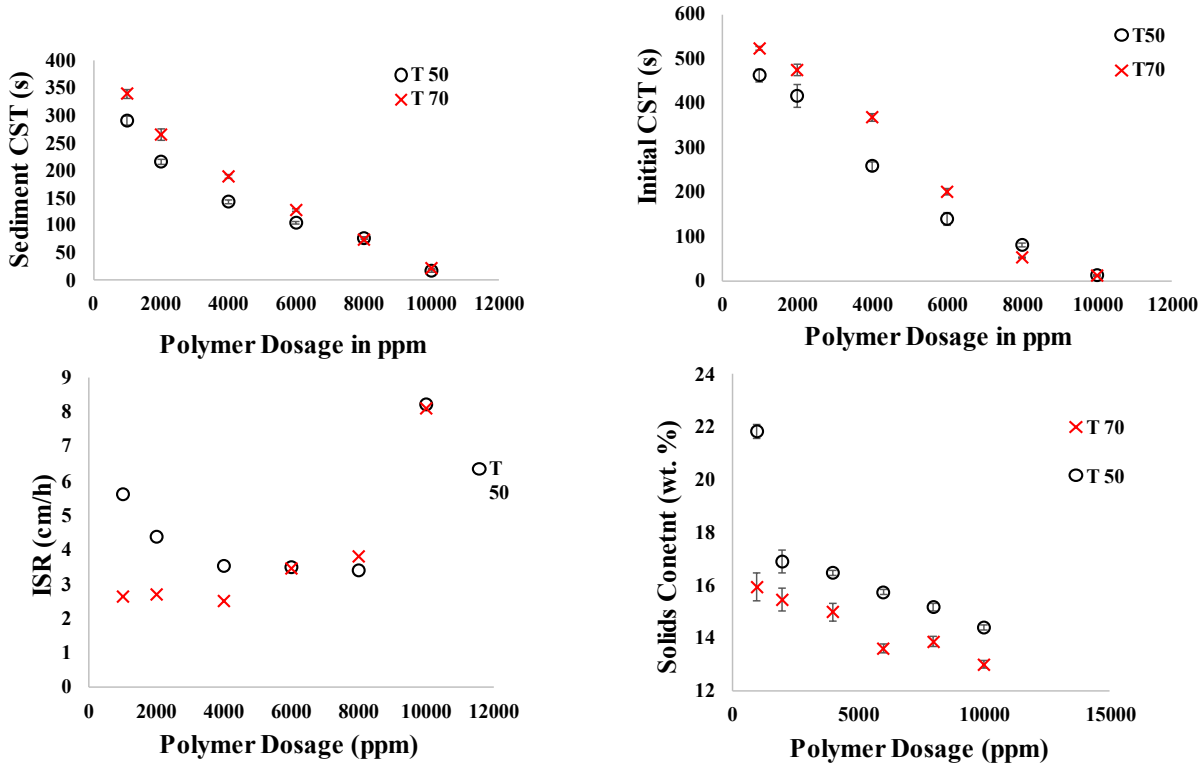

Figure B3.5 – Comparison of flocculation performance for two different polymerization temperatures 50 and 70 °C for P7.

Appendix B4

Effect of graft length on flocculation performance for polymers synthesized at 70°C

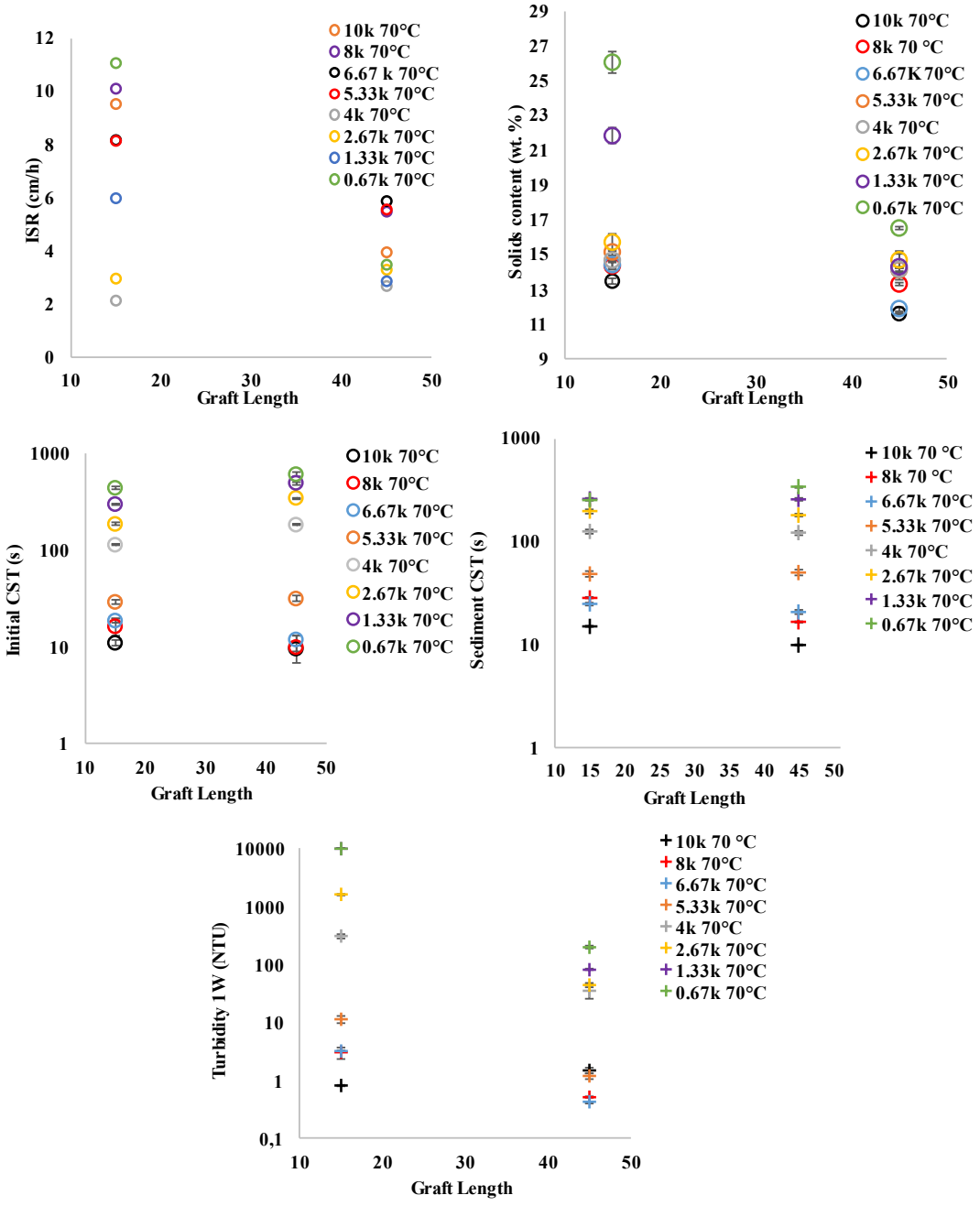

Figure B4 – Effect of graft length on flocculation performance for polymers synthesized at 70 °C.

Appendix B5

Effect of graft frequency on flocculation performance for polymers synthesized at 70°C

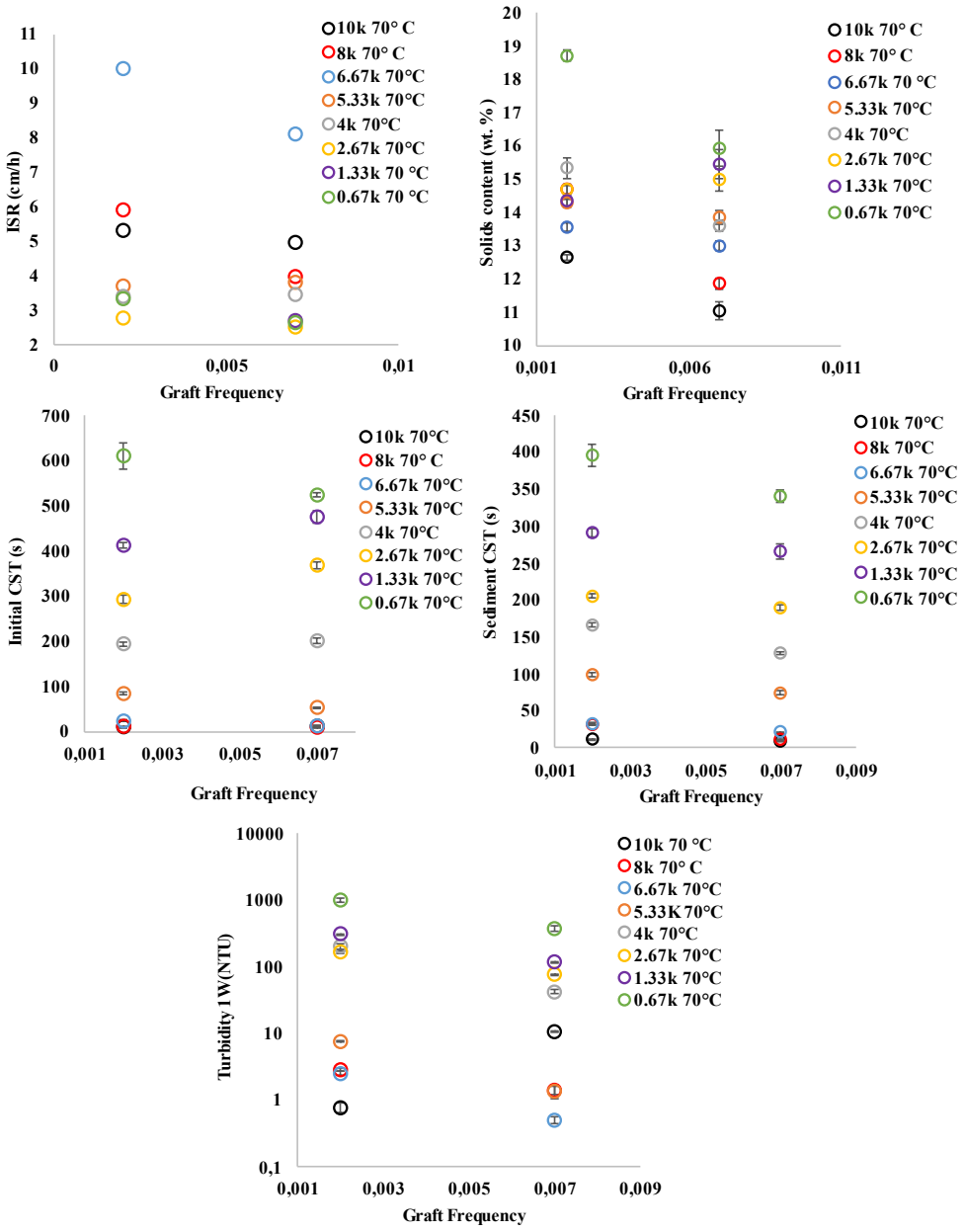

Figure B5 – Effect of graft frequency on flocculation performance for polymers synthesized at 70 °C.

Appendix B6

AP-g-PVBTMAC flocculation results with molecular weight for 50 and 70 °C synthesis temperature

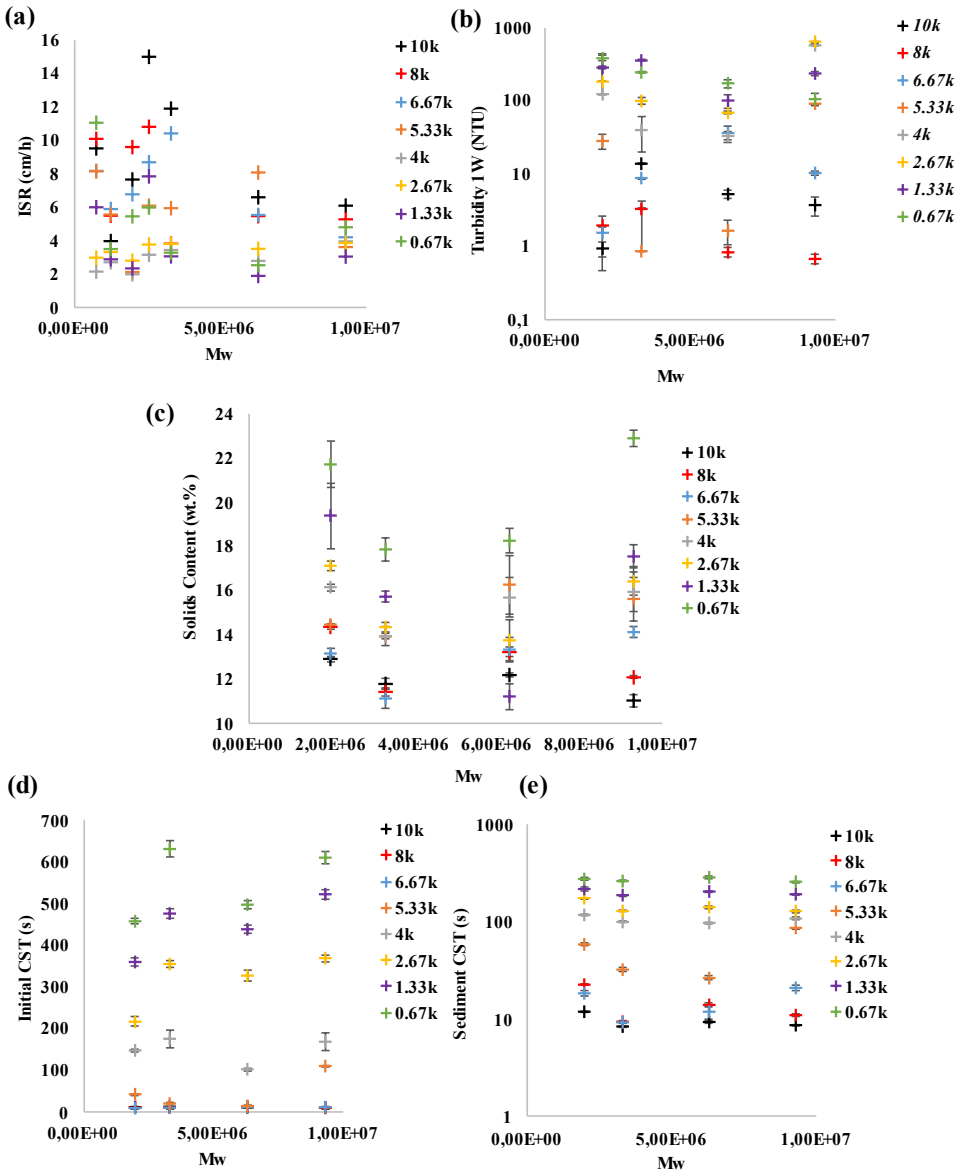

Figure B6.1 – Effect of Weight Average Molecular Weight on flocculation: a) ISR, b) Supernatant turbidity after one week, c) Sediment solids content, d) Initial CST and e) Sediment CST for different dosages in ppm.

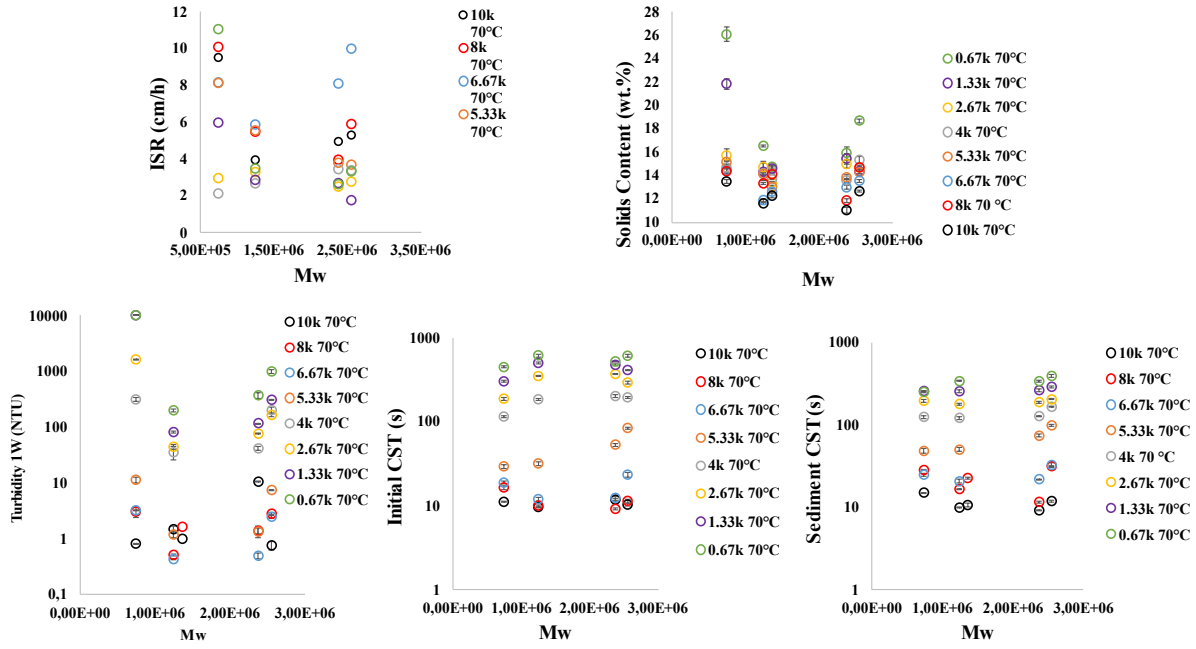

Figure B6.2 – Same as Figure B3.1 for 70°C polymer synthesis.

Appendix B7

Impact of different mixer type on flocculation results

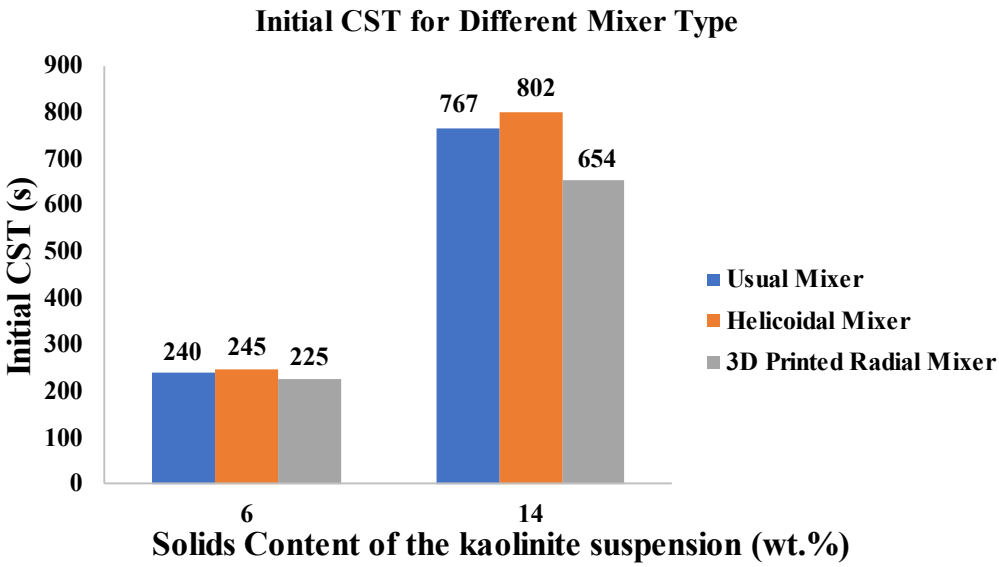

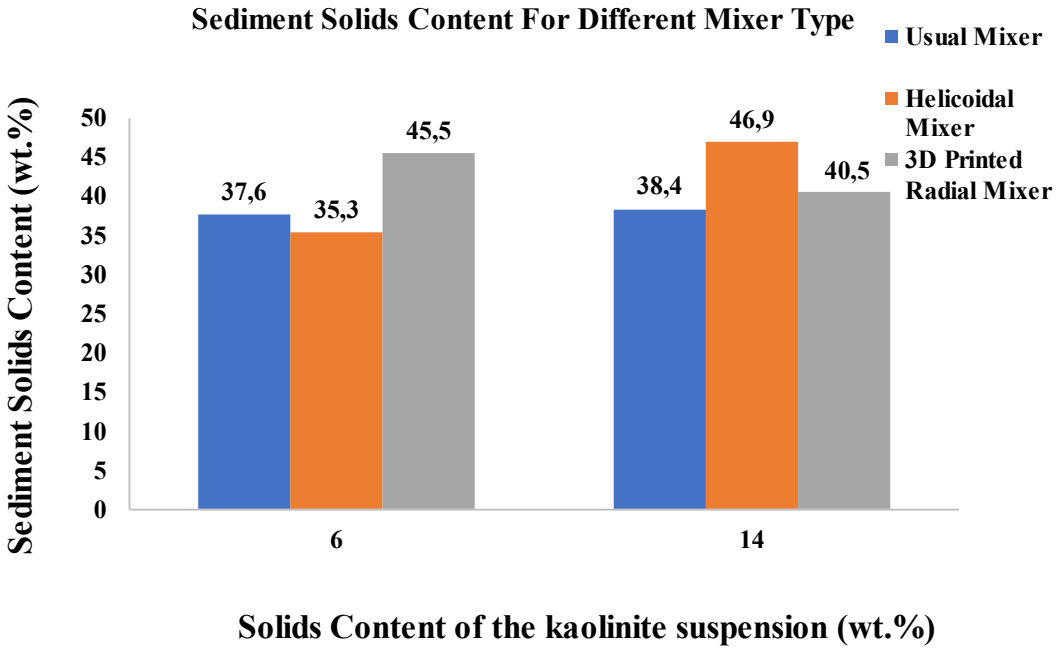

Note: Only two runs (one replicate) have been conducted for this study therefore no standard error is provided (only the averaged values).

Figure B7 – Impeller type impact on flocculation metrics: a) sediment solids content, b) initial CST.

Appendix B8

Results of the Half-factorial Design used as screening tests prior to the full CCD

Table B8 – Overview of the results and screening half-factorial design with randomized runs.

	Cat_d	Ani_d	Flow_cat	Flow_ani	SC	CST	Turbidity	SSolidsc
1	500	8000	85	5	31,3	2150	2517	55,2
2	8000	500	5	25	31,3	21,5	2,66	47,1
3	500	500	85	5	5	82,6	3104	64,4
4	500	500	5	25	5	30,3	169	63,1
5	500	8000	85	25	5	961	10000	51,2
6	8000	500	5	5	5	12,9	158	61,1
7	500	8000	5	25	31,3	1416	529	54,9
8	8000	8000	85	5	5	156	13,5	40,2
9	8000	500	85	5	31,3	23	12,6	46,9
10	500	8000	5	5	5	485	3825	59,3
11	8000	500	85	25	5	12,4	8,18	51,9
12	8000	8000	5	25	5	1211	4640	53,8
13	8000	8000	85	25	31,3	175	48	43,3
14	8000	8000	5	5	31,3	134	14,6	46,4
15	500	500	85	25	31,3	250	3364	50,1
16	500	500	5	5	31,3	235	2507	51,1

Clear Supernatant + Large flocs

Small flocs + large water volume

No instantaneous settling

Dense paste with large flocs

Dense paste with small flocs

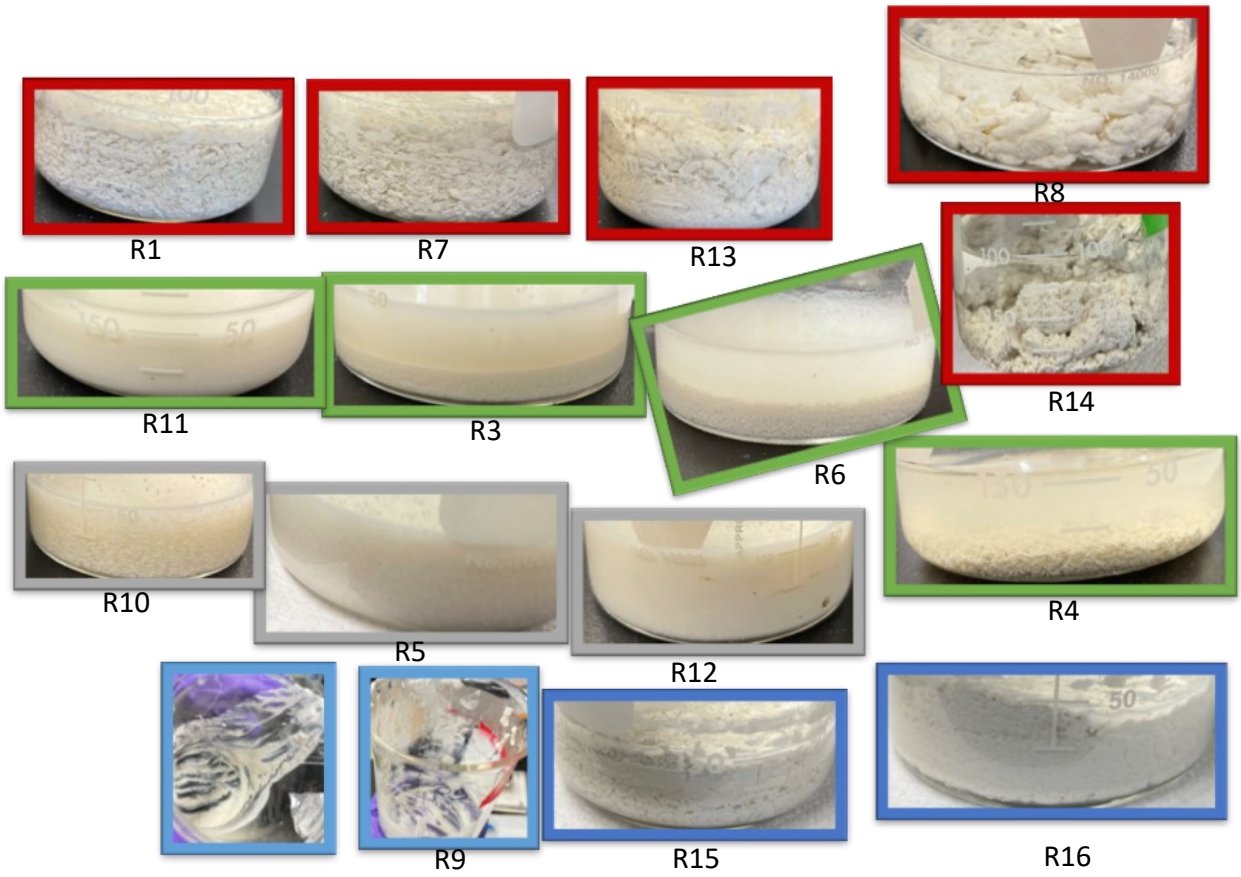

Figure B8. 1 – Picture of the flocculation results with the run number associated to the conditions.

a)

```
                                Df  Sum Sq Mean Sq F value  Pr(>F)
Factor_catd                      1  932981  932981   7.246 0.03101 *
Factor_anid                      1 2264565 2264565  17.587 0.00407 **
Factor_floa                      1   39909   39909   0.310 0.59506
Factor_sc                        1  132040  132040   1.025 0.34495
Factor_catd:Factor_anid          1  492180  492180   3.822 0.09148 .
Factor_catd:Factor_sc            1  779495  779495   6.054 0.04344 *
Factor_catd:Factor_anid:Factor_sc 2  526517  263259   2.044 0.19986
Residuals                        7  901365  128766
---
Signif. codes:  0 '***' 0.001 '**' 0.01 '*' 0.05 '.' 0.1 ' ' 1
> |
```

b)

```
Call:
lm(formula = CST ~ A + B + E + A:B + A:E + A:B:E, data = Screeningdual)

Residuals:
    Min      1Q  Median      3Q     Max
-569.31  -44.33   18.43   63.89  485.62

Coefficients:
            Estimate Std. Error t value Pr(>|t|)
(Intercept)   459.75      82.04   5.604 0.000333 ***
A            -241.48      82.04  -2.943 0.016399 *
B             376.21      82.04   4.585 0.001317 **
E              90.84      82.04   1.107 0.296898
A:B          -175.39      82.04  -2.138 0.061245 .
A:E          -220.72      82.04  -2.690 0.024784 *
A:B:E        -176.51      82.04  -2.151 0.059898 .
---
Signif. codes:  0 '***' 0.001 '**' 0.01 '*' 0.05 '.' 0.1 ' ' 1

Residual standard error: 328.2 on 9 degrees of freedom
Multiple R-squared:  0.8403,    Adjusted R-squared:  0.7338
F-statistic: 7.892 on 6 and 9 DF,  p-value: 0.003515
```

Figure B8.2 – Statistical results for the initial CST: a) ANOVA, b) Regression model with coded variables.

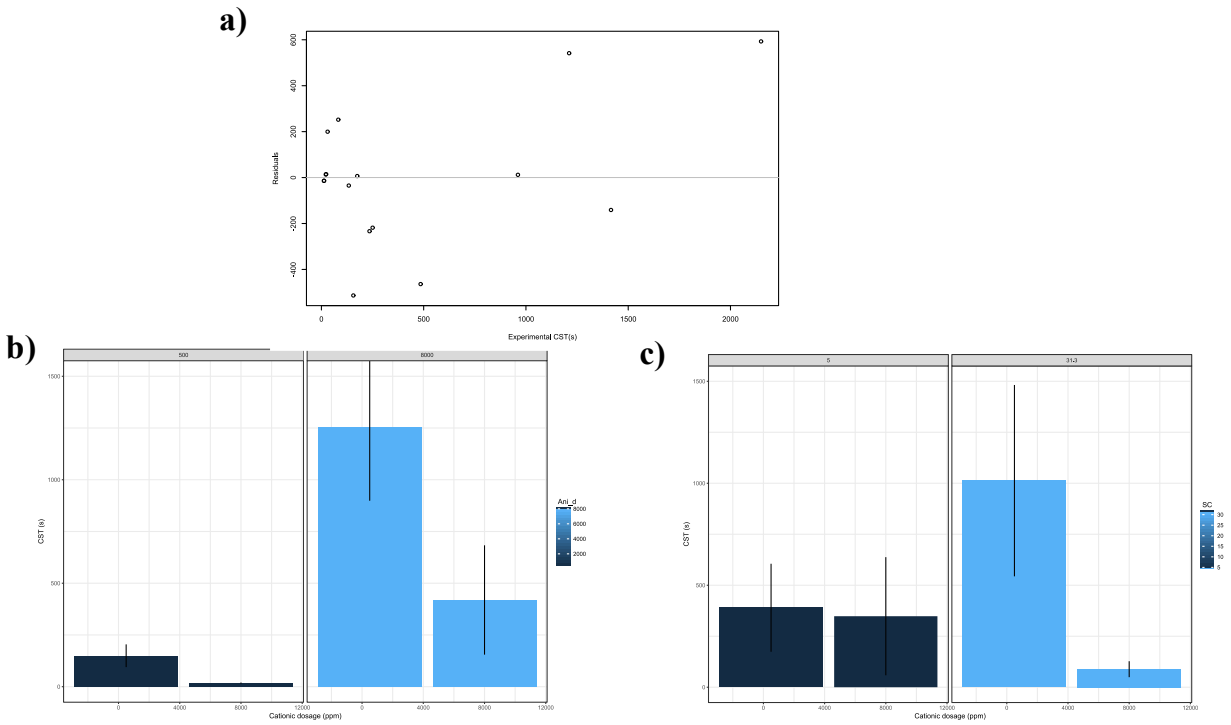

Figure B8.3 – CST model output: a) Residual plots, b) CST in function of cationic and anionic dosage, c) CST in function of suspension solids content and cationic dosage.

a)

	Df	Sum Sq	Mean Sq	F value	Pr(>F)	
Factor_catd	1	27873534	27873534	16.644	0.00469	**
Factor_anid	1	9394772	9394772	5.610	0.04971	*
Factor_floa	1	2729580	2729580	1.630	0.24243	
Factor_floc	1	3261019	3261019	1.947	0.20555	
SC	1	10436319	10436319	6.232	0.04121	*
Factor_catd:Factor_floc	1	17411182	17411182	10.397	0.01456	*
Factor_anid:Factor_floa	1	7679397	7679397	4.586	0.06949	.
Factor_anid:Factor_sc	1	19840083	19840083	11.847	0.01081	*
Residuals	7	11722486	1674641			

Signif. codes: 0 ‘***’ 0.001 ‘**’ 0.01 ‘*’ 0.05 ‘.’ 0.1 ‘ ’ 1

b)

```
Call:
lm(formula = Turbidity ~ A + B + C + D + E + A:C + B:D + B:E,
    data = Screeningdual)

Residuals:
    Min      1Q  Median      3Q     Max
-1588.7  -506.4  -102.4   596.8  1460.0

Coefficients:
            Estimate Std. Error t value Pr(>|t|)
(Intercept)   1932.2      323.5   5.972 0.000557 ***
A            -1319.9      323.5  -4.080 0.004691 **
B              766.3      323.5   2.369 0.049712 *
C              451.5      323.5   1.395 0.205548
D              413.0      323.5   1.277 0.242429
E             -807.6      323.5  -2.496 0.041209 *
A:C          -1043.2      323.5  -3.224 0.014564 *
B:D            692.8      323.5   2.141 0.069488 .
B:E          -1113.6      323.5  -3.442 0.010808 *
---
Signif. codes:  0 ‘***’ 0.001 ‘**’ 0.01 ‘*’ 0.05 ‘.’ 0.1 ‘ ’ 1

Residual standard error: 1294 on 7 degrees of freedom
Multiple R-squared:  0.8938,    Adjusted R-squared:  0.7724
F-statistic: 7.362 on 8 and 7 DF,  p-value: 0.008099
```

Figure B8.4 – Statistical results for the initial supernatant turbidity: a) ANOVA, b) Regression model with coded variables.

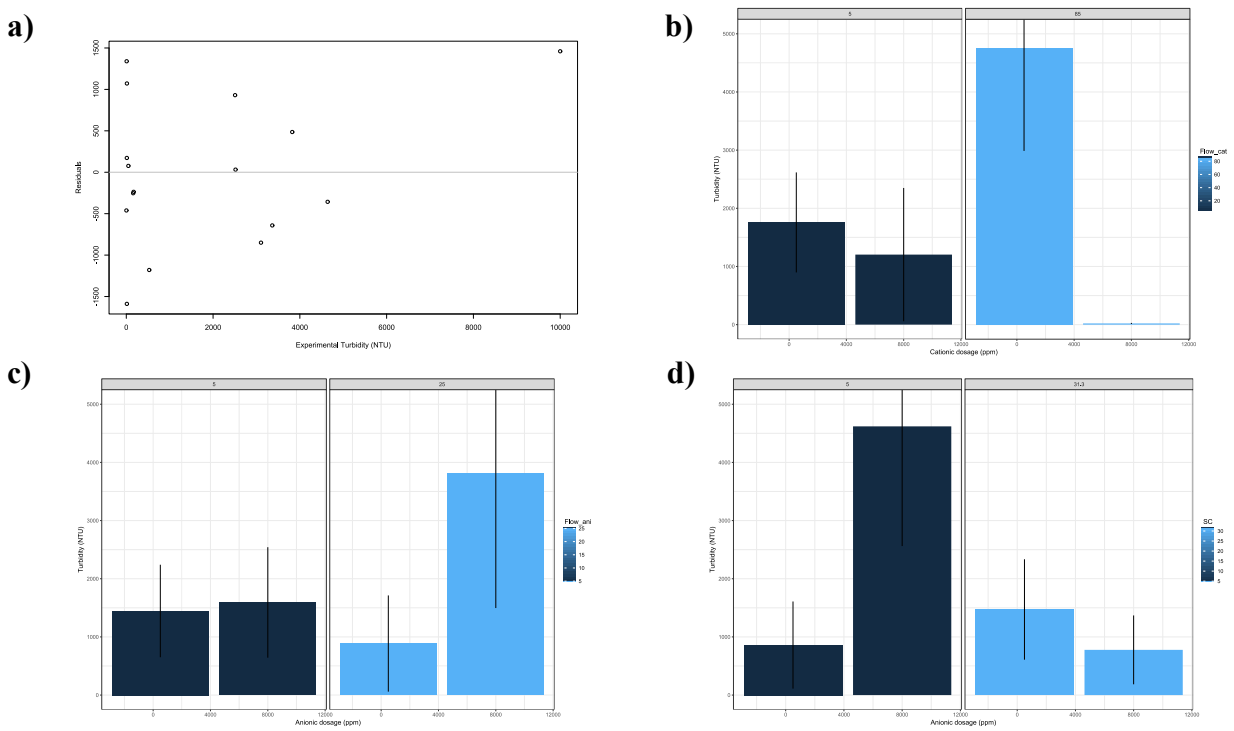

Figure B8.5 – Supernatant turbidity model output: a) Residual plots, b) Turbidity in function of cationic dosage and flowrate, c) Turbidity vs. anionic flowrate and dosage, d) Turbidity vs. suspension solids content and anionic dosage.

a)

	Df	Sum Sq	Mean Sq	F value	Pr(>F)	
Factor_catd	1	214.47	214.47	586.47	0.00170	**
Factor_anid	1	61.30	61.30	167.63	0.00591	**
Factor_floc	1	70.00	70.00	191.40	0.00518	**
Factor_floa	1	5.41	5.41	14.79	0.06146	.
Factor_sc	1	157.13	157.13	429.66	0.00232	**
Factor_catd:Factor_anid	1	14.20	14.20	38.82	0.02481	*
Factor_catd:Factor_floc	1	21.72	21.72	59.38	0.01643	*
Factor_anid:Factor_floc	1	14.19	14.19	38.81	0.02481	*
Factor_catd:Factor_floa	1	9.07	9.07	24.80	0.03803	*
Factor_anid:Factor_floa	1	11.38	11.38	31.13	0.03066	*
Factor_floc:Factor_floa	1	7.94	7.94	21.72	0.04309	*
Factor_anid:Factor_sc	1	103.20	103.20	282.20	0.00352	**
Factor_floc:Factor_sc	1	41.28	41.28	112.88	0.00874	**
Residuals	2	0.73	0.37			

Signif. codes: 0 ‘***’ 0.001 ‘**’ 0.01 ‘*’ 0.05 ‘.’ 0.1 ‘ ’ 1

b)

Coefficients:

	Estimate	Std. Error	t value	Pr(>|t|)	
(Intercept)	52.4945	0.1512	347.222	8.29e-06	***
A	-3.6612	0.1512	-24.217	0.00170	**
B	-1.9574	0.1512	-12.947	0.00591	**
C	-2.0916	0.1512	-13.835	0.00518	**
D	-0.5814	0.1512	-3.845	0.06146	.
E	-3.1338	0.1512	-20.728	0.00232	**
A:B	-0.9419	0.1512	-6.230	0.02481	*
A:C	-1.1650	0.1512	-7.706	0.01643	*
B:C	-0.9418	0.1512	-6.230	0.02481	*
A:D	0.7530	0.1512	4.980	0.03803	*
B:D	0.8435	0.1512	5.579	0.03066	*
C:D	-0.7045	0.1512	-4.660	0.04309	*
B:E	2.5397	0.1512	16.799	0.00352	**
C:E	1.6063	0.1512	10.625	0.00874	**

Signif. codes: 0 ‘***’ 0.001 ‘**’ 0.01 ‘*’ 0.05 ‘.’ 0.1 ‘ ’ 1

Residual standard error: 0.6047 on 2 degrees of freedom
Multiple R-squared: 0.999, Adjusted R-squared: 0.9925
F-statistic: 153.8 on 13 and 2 DF, p-value: 0.006477

Figure B8.6 – Statistical results for the sediment solids content: a) ANOVA, b) Regression model with coded variables.

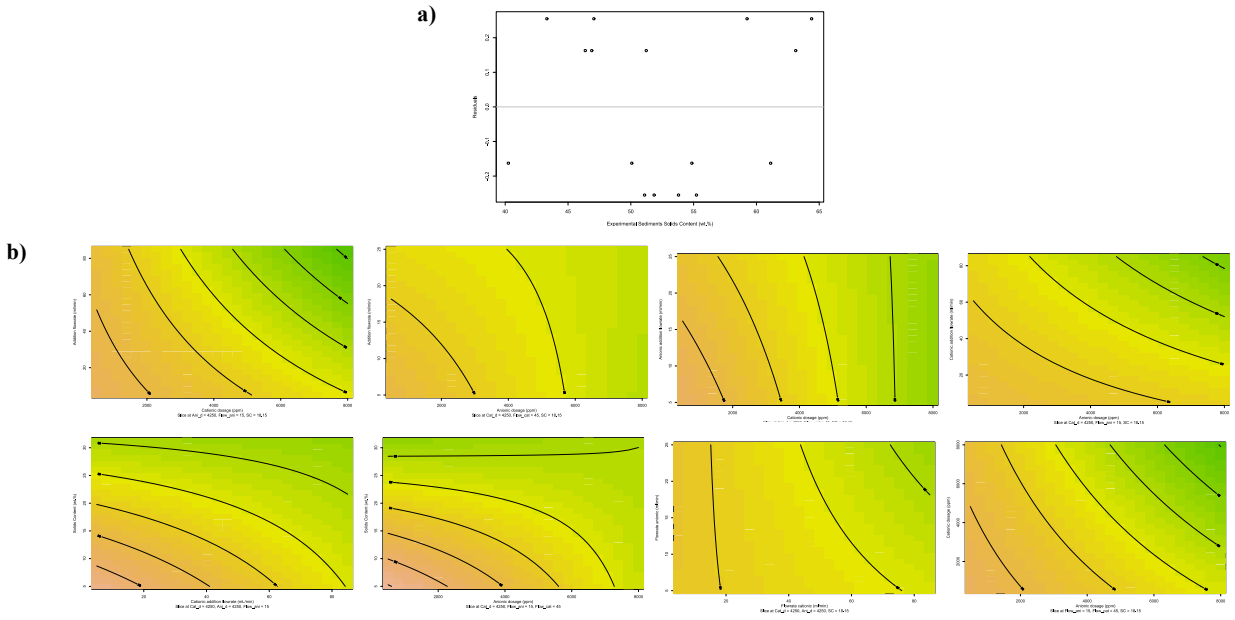

Figure B8.7 – Sediment solids content model output: a) Residual plots, b) and c) contour plots of the interaction terms.

These screening tests were used to determine the best conditions to carry out the full CCD while keeping the widest range possible for all the predictors. Since it was only a half-factorial design, the regression models are linear (using the *lm* package from R) and do not account for the internal error.

Appendix B9

Regression models results for CST, turbidity and solids content for the full CCD

a)

```
Call:
rsm(formula = sqcst2 ~ FO(A, B, C, E) + A:C + C:E + A:B + PQ(C),
    data = CCDr2)

            Estimate Std. Error  t value  Pr(>|t|)
(Intercept) 14.05623    0.52075  26.9922 < 2.2e-16 ***
A           -4.60039    0.41355 -11.1241 1.151e-13 ***
B            3.80595    0.41355   9.2031 2.546e-11 ***
C            0.11636    0.41355   0.2814 0.7799096
E            1.47301    0.41355   3.5619 0.0009893 ***
C^2          0.78073    0.39842   1.9595 0.0572235 .
A:C         -0.89113    0.47378  -1.8809 0.0674694 .
C:E          0.81213    0.47378   1.7141 0.0944398 .
A:B          1.87892    0.47378   3.9658 0.0003033 ***
---
Signif. codes:  0 '***' 0.001 '**' 0.01 '*' 0.05 '.' 0.1 ' ' 1

Multiple R-squared:  0.8638,    Adjusted R-squared:  0.8358
F-statistic: 30.91 on 8 and 39 DF,  p-value: 1.434e-14

Analysis of Variance Table

Response: sqcst2
              Df  Sum Sq Mean Sq F value    Pr(>F)
FO(A, B, C, E)  4 1588.95  397.24 55.3025 1.486e-15
PQ(C)           1   27.58   27.58  3.8398 0.0572235
A:C             1   25.41   25.41  3.5377 0.0674694
C:E             1   21.11   21.11  2.9383 0.0944398
A:B             1  112.97  112.97 15.7276 0.0003033
Residuals      39  280.14    7.18
Lack of fit    16  123.04    7.69  1.1259 0.3886718
Pure error     23  157.10    6.83

Stationary point of response surface:
          A           B           C           E
 0.00000000  0.00000000 -0.07452216  0.00000000
```

b)

```
Call:
rsm(formula = logT2 ~ FO(A, B, C, E) + TWI(A, B) + TWI(B, C) +
    TWI(A, C) + TWI(B, E) + PQ(A, B, E), data = CCDr2)

             Estimate Std. Error t value  Pr(>|t|)
(Intercept)  4.361451   0.171210 25.4742 < 2.2e-16 ***
A           -0.021656   0.090571 -0.2391 0.8123822
B           -0.174733   0.090571 -1.9292 0.0616118 .
C            0.037494   0.090571  0.4140 0.6813461
E            0.247483   0.090571  2.7325 0.0096801 **
A:B         -0.374457   0.103762 -3.6088 0.0009276 ***
B:C          0.262233   0.103762  2.5273 0.0160289 *
A:C         -0.228923   0.103762 -2.2062 0.0338339 *
B:E          0.136842   0.103762  1.3188 0.1955594
A^2          0.435832   0.088352  4.9329 1.844e-05 ***
B^2          0.097945   0.088352  1.1086 0.2749651
E^2          0.105199   0.088352  1.1907 0.2415694
---
Signif. codes:  0 '***' 0.001 '**' 0.01 '*' 0.05 '.' 0.1 ' ' 1

Multiple R-squared:  0.634,     Adjusted R-squared:  0.5222
F-statistic:  5.67 on 11 and 36 DF,  p-value: 3.287e-05

Analysis of Variance Table

Response: logT2
              Df  Sum Sq Mean Sq F value    Pr(>F)
FO(A, B, C, E)  4  3.9335  0.9834  2.8542 0.0374703
TWI(A, B)       1  4.4870  4.4870 13.0235 0.0009276
TWI(B, C)       1  2.2005  2.2005  6.3871 0.0160289
TWI(A, C)       1  1.6770  1.6770  4.8675 0.0338339
TWI(B, E)       1  0.5992  0.5992  1.7393 0.1955594
PQ(A, B, E)     3  8.5911  2.8637  8.3119 0.0002491
Residuals      36 12.4030  0.3445
Lack of fit    13  7.1566  0.5505  2.4134 0.0313590
Pure error     23  5.2464  0.2281

Stationary point of response surface:
          A           B           C           E
 0.9170554   0.6575857   2.3216129 -1.6039440

Stationary point in original units:
     Cat_d     Ani_d  Flow_cat        SC
 6.834111  6.315171 84.824194  3.584224
```

c)

```
Call:
rsm(formula = sqsc ~ FO(A, B, D, E) + TWI(A, B) + TWI(B, E) +
    PQ(A, B, D, E), data = CCDr2)

             Estimate Std. Error  t value  Pr(>|t|)
(Intercept)  6.754386   0.043819 154.1423 < 2.2e-16 ***
A           -0.068894   0.019549  -3.5241  0.001150 **
B           -0.130220   0.019549  -6.6611 8.051e-08 ***
D            0.075135   0.019549   3.8434  0.000461 ***
E           -0.141154   0.019549  -7.2204 1.444e-08 ***
A:B         -0.073981   0.022397  -3.3032  0.002127 **
B:E         -0.047201   0.022397  -2.1075  0.041911 *
A^2          0.123046   0.019241   6.3950 1.836e-07 ***
B^2          0.029969   0.019241   1.5576  0.127848
D^2         -0.033613   0.019241  -1.7469  0.088948 .
E^2          0.032602   0.019241   1.6944  0.098594 .
---
Signif. codes:  0 '***' 0.001 '**' 0.01 '*' 0.05 '.' 0.1 ' ' 1

Multiple R-squared:  0.8363,    Adjusted R-squared:  0.792
F-statistic:  18.9 on 10 and 37 DF,  p-value: 1.185e-11

Analysis of Variance Table

Response: sqsc
              Df  Sum Sq Mean Sq F value    Pr(>F)
FO(A, B, D, E)  4 1.98548 0.49637 30.9239 2.419e-11
TWI(A, B)       1 0.17514 0.17514 10.9113  0.002127
TWI(B, E)       1 0.07129 0.07129  4.4416  0.041911
PQ(A, B, D, E)  4 0.80181 0.20045 12.4882 1.587e-06
Residuals      37 0.59390 0.01605
Lack of fit    14 0.23361 0.01669  1.0652  0.432710
Pure error     23 0.36029 0.01566

Stationary point of response surface:
       A        B        D        E
21.835670 71.703933  1.117666 54.071075

Stationary point in original units:
    Cat_d     Ani_d  Flow_ani        SC
 48.67134 148.40787  20.58833 226.28430
```

Figure B9 – Statistical Results Summary of: a) Initial CST model, b) Supernatant turbidity model, c) Solids content model.

Appendix B10

Desirability Functions To Optimize the Solids Content and Initial CST

Desirability functions were defined on the basis of the following two conditions:

- Need a minimum sediment solids content of 53 wt.%
- Need a maximum CST of 20 s

A portion of the code used to achieve this work is presented in Figure B9.

```
#DESIRABILITY FUNCTIONS
### Functions for desirability
# (Derringer and Suich)
# y = response
# L = unacceptability boundary
# T = target acceptability boundary T
# U = upper unacceptability boundary
# r, r1, r2 = exponent 1 for L and U
# d = desirability function
# Maximum
maxD <- function(y, L, T, r) {
  if (y < L){d <- 0}
  else if (y > T){d <- 1}
  else{d <- ((y - L) / (T - L))^r}
  return(d) }
# Minimum
minD <- function(y, U, T, r) {
  if (y < T){d <- 1}
  else if (y > U){d <- 0}
  else{d <- ((U - y) / (U - T))^r}
  return(d) }
# Target
targetD <- function(y, L, T, U, r1, r2) {
  if (y < L){d <- 0}
  else if ( L<=y & y<=T ){
    d <- ((y - L) / (T - L))^r1}
  else if( T<=y & y<=U ){
    d <- ((U - y) / (U - T))^r2}
  else {
    d <- 0}
  return(d)}
# create a grid for the desirability determination
dataD <- expand.grid(seq(-2.23608, 2.23608, by=1), seq(-
2.23608, 2.23608, by=1), seq(-2.23608, 2.23608, by=1),
seq(-2.23608, 2.23608, by=1), seq(-2.23608, 2.23608, by=1))
colnames(dataD) <- c("A", "B", "C", "D","E")
View(dataD)
# add the natural variables
dataD$Cat_d <- dataD$A*2+5
dataD$Ani_d <- dataD$B*2+5
dataD$Flow_cat <- dataD$C*15+50
dataD$Flow_ani <- dataD$D*5+15
dataD$SC <- dataD$E*4+10
# add the predicted responses
dataD$CST <- predict(codedsqcst22.model, newdata = dataD)
#dataD$TurbidityT <- predict(codedturb22.model, newdata =
dataD)
dataD$SSC <- predict(codedsscsq2.model, newdata = dataD)
# For each data value, calculate desirability
for (i in 1:nrow(dataD)) {
  d1 <- minD(dataD$CST[i]
             , U = 4.5, T = 4, r = 1)
  #d2 <-  minD(dataD$Turbidity[i]
              #, U = 2.1761, T = 2.0, r = 1)
  d3 <- maxD(dataD$SSC[i]
             , L = 7.07, T = 7.28, r = 1)
  D <- (d1 * d3)^(1/2)
  dataD[i, c("d1", "d3","D")] <- c(d1, d3, D)
}
dataD2 <- expand.grid(seq(-2.23608, 2.23608, by=1), seq(-
2.23608, 2.23608, by=1), seq(-2.23608, 2.23608, by=1), seq(-
2.23608, 2.23608, by=1), seq(-2.23608, 2.23608, by=1))
colnames(dataD2) <- c("R1", "R2", "R3", "R4","R5")
View(dataD2)
for (i in 1:nrow(dataD)) {
  if (is.na(d1[i])==1.0 && is.na(d3[i])==1.0){dataD2$R1[i]<-
dataD$Cat_d[i]; dataD2$R2[i]<- dataD$Ani_d[i];dataD2$R3[i]<-
dataD$Flow_cat[i];dataD2$R4[i]<-
dataD$Flow_ani[i];dataD2$R5[i]<- dataD$SC[i]}
}
library(dplyr)
distinct(dataD2)
```

Figure B10 – Code section dedicated to define and use the desirability functions.

The regression model for supernatant turbidity has been discarded because of its inaccuracy. The desirability functions allow to maximize or minimize a value by defining a threshold value (minimum or maximum depending on the goal) and a target. If the goal is reached, the function takes a value 1. If the comparison with the unacceptable boundary is rejected, the function takes 0. Between these two cases, it assigns an intermediate value with a power ponderation. The desirability function has been applied to every run, in order to identify the runs where the objectives were met.

Appendix B11

Full CCD Results with continuously ageing kaolinite suspension

Initial CST:

a)

```
Call:
rsm(formula = sqcst ~ FO(A, B, C, E) + TWI(A, E) + TWI(A, C) +
    TWI(A, B) + PQ(A), data = CCDr)

            Estimate Std. Error t value  Pr(>|t|)
(Intercept) 13.56765    0.49467 27.4277 < 2.2e-16 ***
A           -2.95733    0.39284 -7.5281 4.081e-09 ***
B            4.07531    0.39284 10.3740 8.954e-13 ***
C            0.15638    0.39284  0.3981 0.6927370
E            1.60793    0.39284  4.0931 0.0002071 ***
A:E         -1.32201    0.45005 -2.9374 0.0055302 **
A:C          0.91941    0.45005  2.0429 0.0478634 *
A:B          0.77059    0.45005  1.7122 0.0947958 .
A^2          0.59475    0.37847  1.5715 0.1241526
---
Signif. codes:  0 ‘***’ 0.001 ‘**’ 0.01 ‘*’ 0.05 ‘.’ 0.1 ‘ ’ 1

Multiple R-squared:  0.8364,    Adjusted R-squared:  0.8029
F-statistic: 24.93 on 8 and 39 DF,  p-value: 4.634e-13

Analysis of Variance Table

Response: sqcst
                Df  Sum Sq Mean Sq F value    Pr(>F)
FO(A, B, C, E)  4 1174.48 293.621 45.3012 3.735e-14
TWI(A, E)       1   55.93  55.926  8.6286   0.00553
TWI(A, C)       1   27.05  27.050  4.1734   0.04786
TWI(A, B)       1   19.00  19.002  2.9317   0.09480
PQ(A)           1   16.01  16.006  2.4695   0.12415
Residuals      39  252.78   6.482
Lack of fit    16   95.32   5.957  0.8702   0.60605
Pure error     23  157.46   6.846

Stationary point of response surface:
         A          B          C          E
-0.3635267  0.8196633  0.9779517 -1.4061853

Stationary point in original units:
    Cat_d     Ani_d  Flow_cat        SC
 4.272947  6.639327 64.669275  4.375259
```

b)

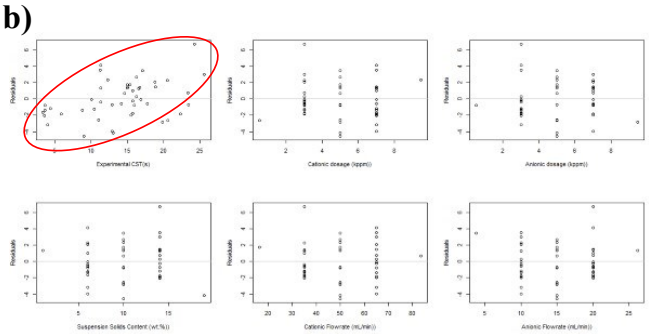

c)

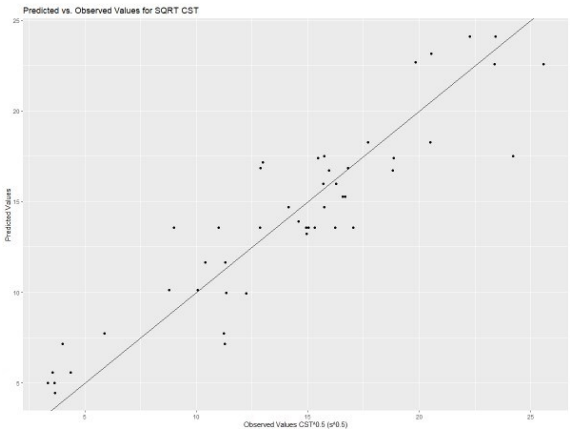

d)

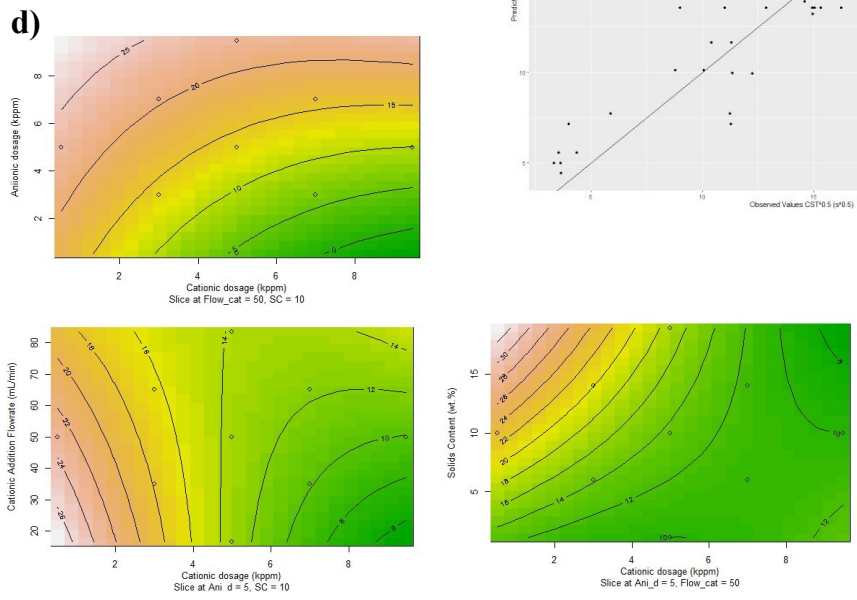

Figure B11.1 – CCD Results for the Initial CST: a) Regression Model, b) Residual plots, c) Predicted vs. observed values, d) Contour plots of the interaction terms.

Supernatant Turbidity:

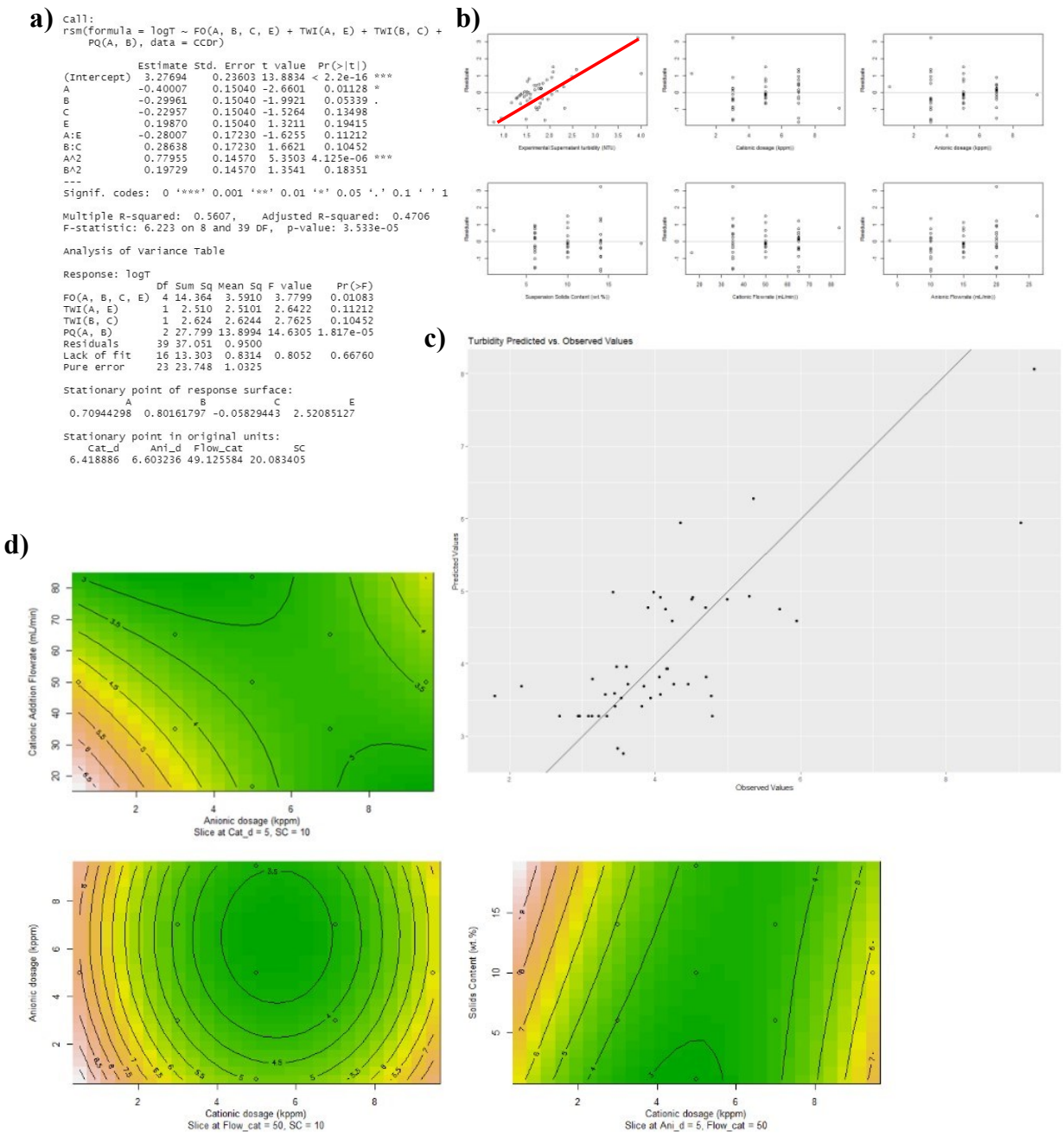

Figure B11.2 – CCD Results for the Supernatant Turbidity: a) Regression Model, b) Residual plots, c) Predicted vs. observed values, d) Contour plots of the interaction terms.

Flocs Solids Content

a)

```
Call:
rsm(formula = SSolidsc ~ FO(A, B, E, C, D) + TWI(A, B) + TWI(C,
    E) + TWI(B, C) + TWI(D, C) + PQ(A, E, B), data = CCDr)

             Estimate Std. Error t value  Pr(>|t|)
(Intercept) 44.72295    1.16839 38.2774 < 2.2e-16 ***
A            0.11740    0.61808  0.1899  0.850449
B           -2.05541    0.61808 -3.3255  0.002081 **
E           -0.72714    0.61808 -1.1765  0.247355
C           -0.91688    0.61808 -1.4834  0.146910
D            0.99536    0.61808  1.6104  0.116294
A:B         -1.34453    0.70810 -1.8988  0.065861 .
C:E         -1.03921    0.70810 -1.4676  0.151141
B:C          0.77569    0.70810  1.0955  0.280797
D:C         -0.67019    0.70810 -0.9465  0.350405
A^2         -1.42607    0.60294 -2.3652  0.023694 *
E^2          1.87232    0.60294  3.1053  0.003755 **
B^2          0.71782    0.60294  1.1905  0.241852
---
Signif. codes:  0 ‘***’ 0.001 ‘**’ 0.01 ‘*’ 0.05 ‘.’ 0.1 ‘ ’ 1

Multiple R-squared:  0.5547,    Adjusted R-squared:  0.402
F-statistic: 3.633 on 12 and 35 DF,  p-value: 0.001399

Analysis of Variance Table

Response: SSolidsc
                  Df Sum Sq Mean Sq F value  Pr(>F)
FO(A, B, E, C, D)  5 277.14  55.429  3.4546 0.01216
TWI(A, B)          1  57.85  57.849  3.6054 0.06586
TWI(C, E)          1  34.56  34.559  2.1539 0.15114
TWI(B, C)          1  19.25  19.254  1.2000 0.28080
TWI(D, C)          1  14.37  14.373  0.8958 0.35041
PQ(A, E, B)        3 296.29  98.763  6.1554 0.00179
Residuals         35 561.58  16.045
Lack of fit       30 486.95  16.232  1.0876 0.51806
Pure error         5  74.62  14.924

Stationary point of response surface:
         A          B          E          C          D
-0.1772233  0.4632583  0.6063540  1.4851942 -1.7721422

Stationary point in original units:
    Cat_d     Ani_d        SC  Flow_Cat  Flow_ani
 4.645553  5.926517 12.425416 72.277914  6.139289
```

b)

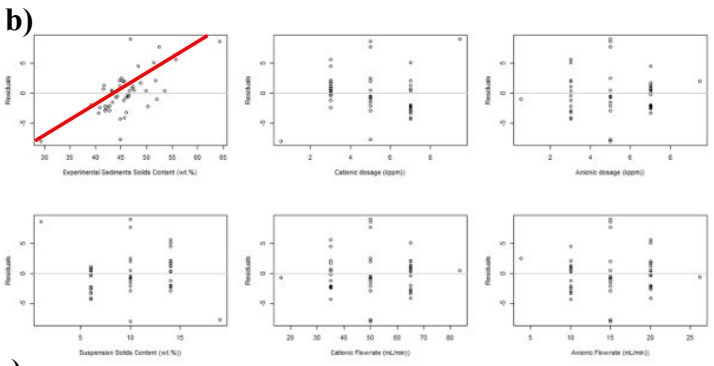

c)

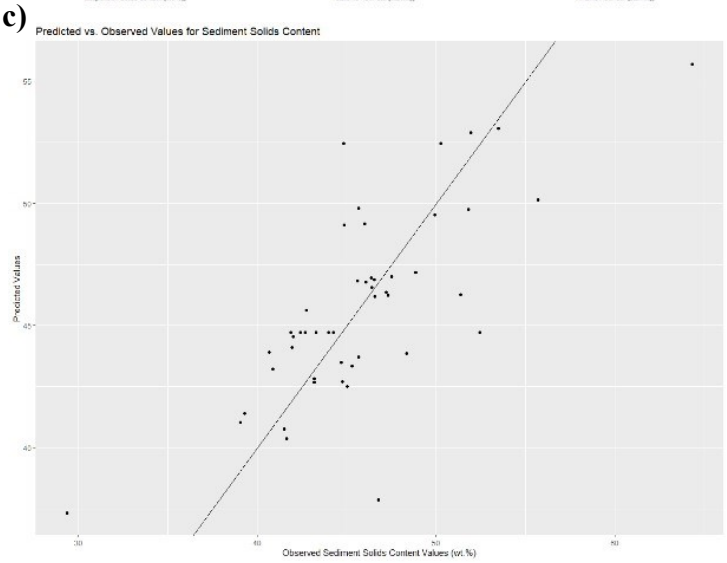

d)

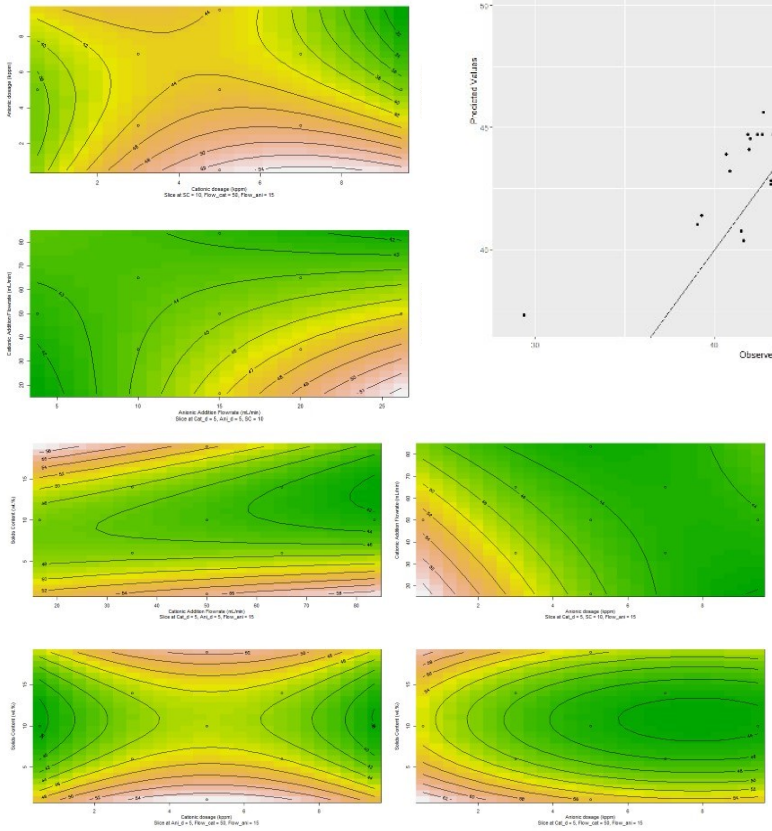

Figure B11.3 – CCD Results for the Flocs (Sediment) Solids Content: a) Regression Model, b) Residual plots, c) Predicted vs. observed values, d) Contour plots of the interaction terms.

Appendix B12

Statistical Prediction of floc sizes and perimeter fractal dimension

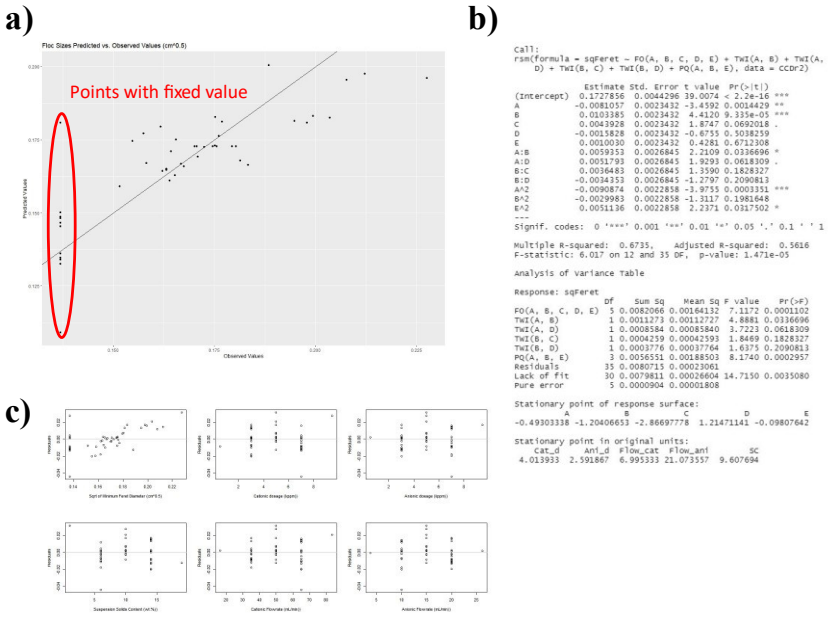

Figure B12.1 – CCD Results for (sqrt) mean floc size: a) Predicted vs. observed values, b) Regression Model, c) Residual plots.

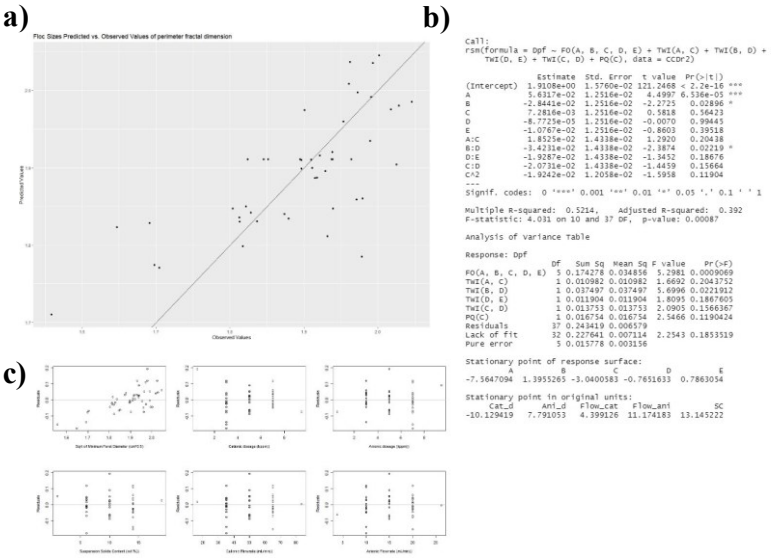

Figure B12.2 – CCD Results for perimeter fractal dimension: a) Predicted vs. observed values, b) Regression Model, c) Residual plots.

Appendix B13

FBRM Runs used to validate the image processing floc size estimation

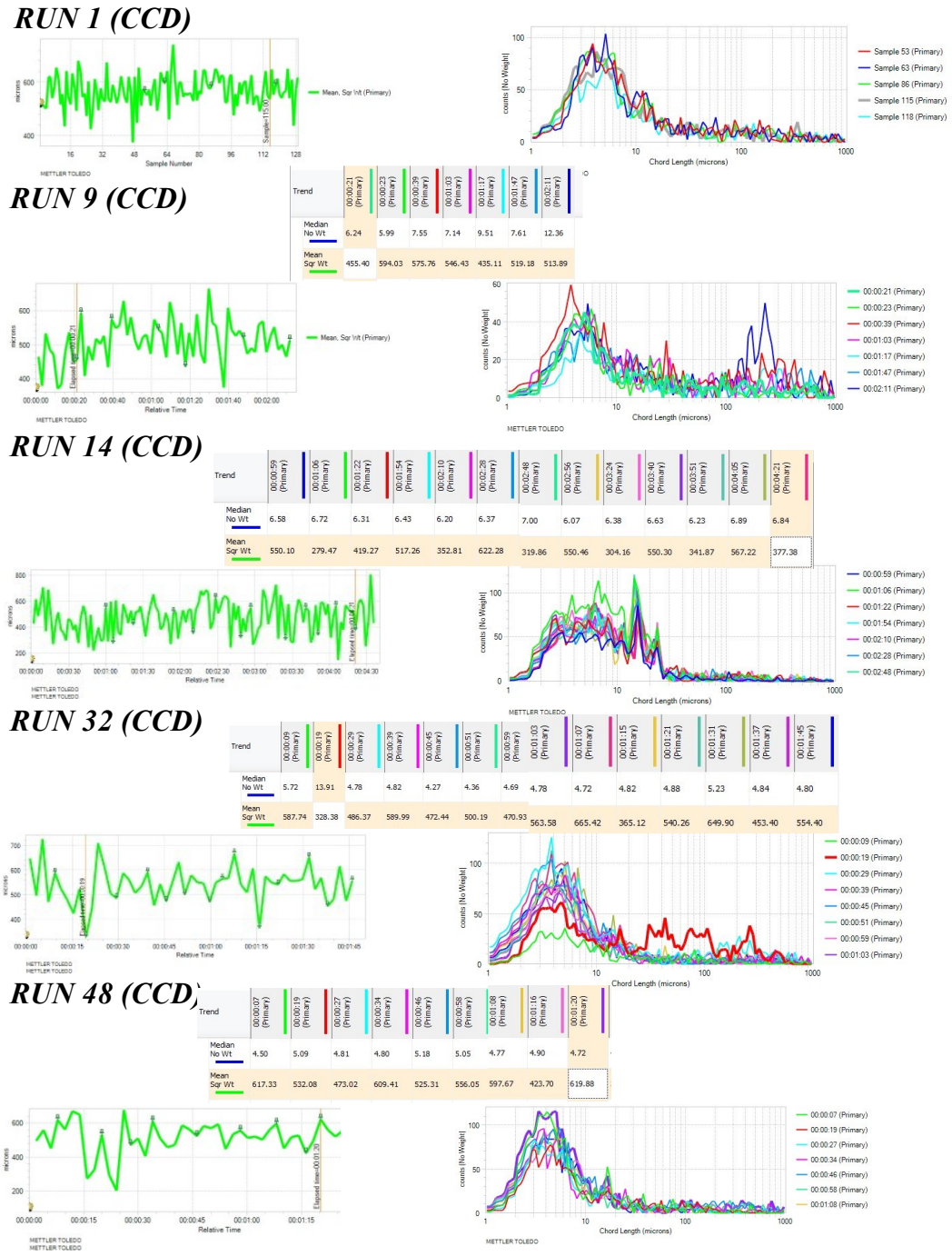

Figure B13 – FBRM Results of the runs tested to validate the image processing.

Appendix B14

Summary of the FBRM results with replicates to show reproducibility

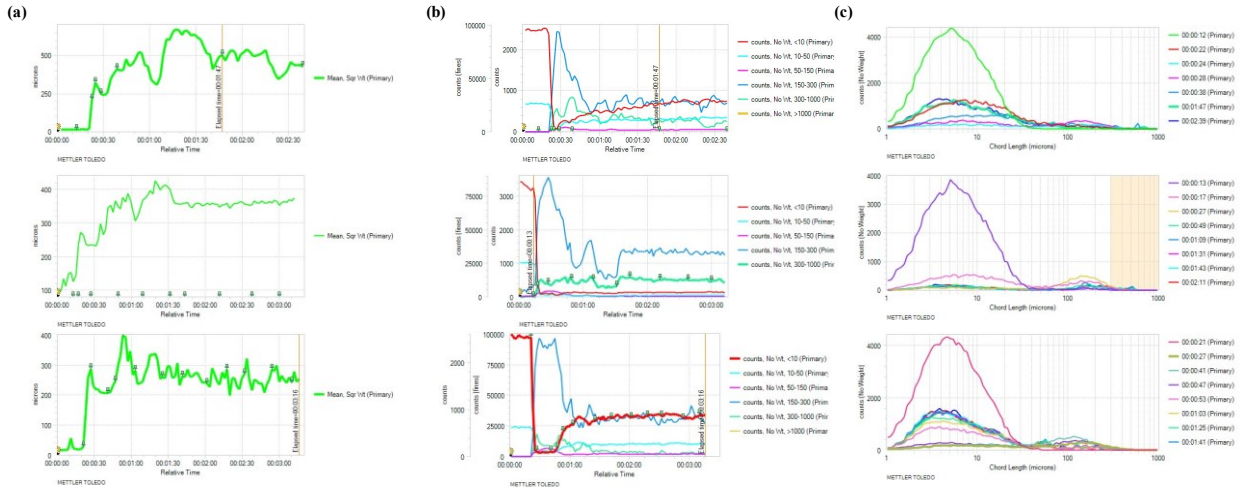

Figure B14.1 – FBRM Results of the three replicates for Run 1: a) Mean squared weight evolution, b) Counts evolution with flocculation time for each class, c) Chord length distribution.

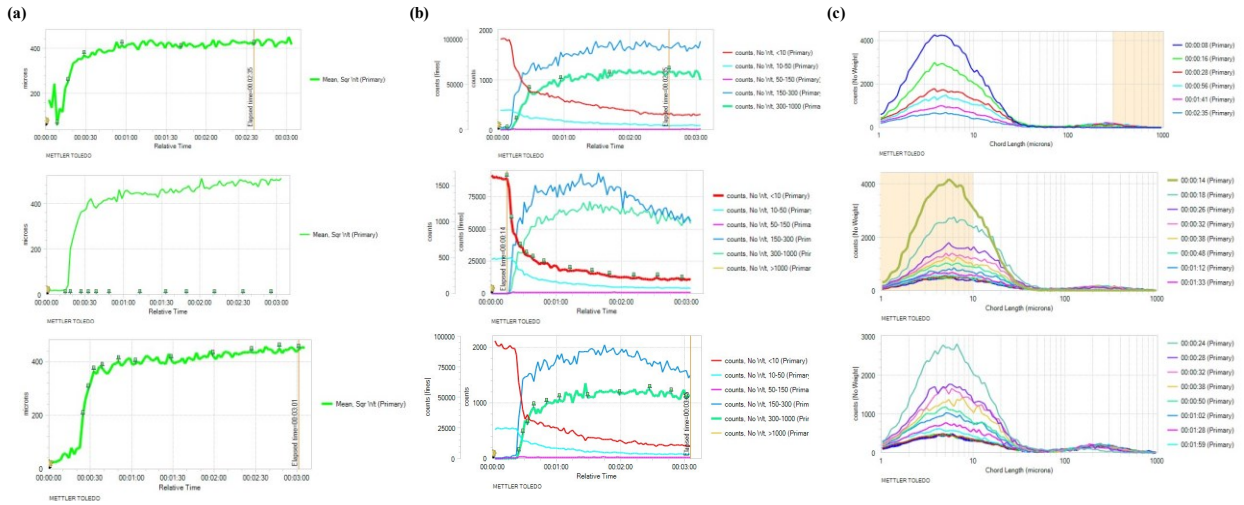

Figure B14.2 – FBRM Results of the three replicates for Run 2: a) Mean squared weight evolution, b) Counts evolution with flocculation time for each class, c) Chord length distribution.

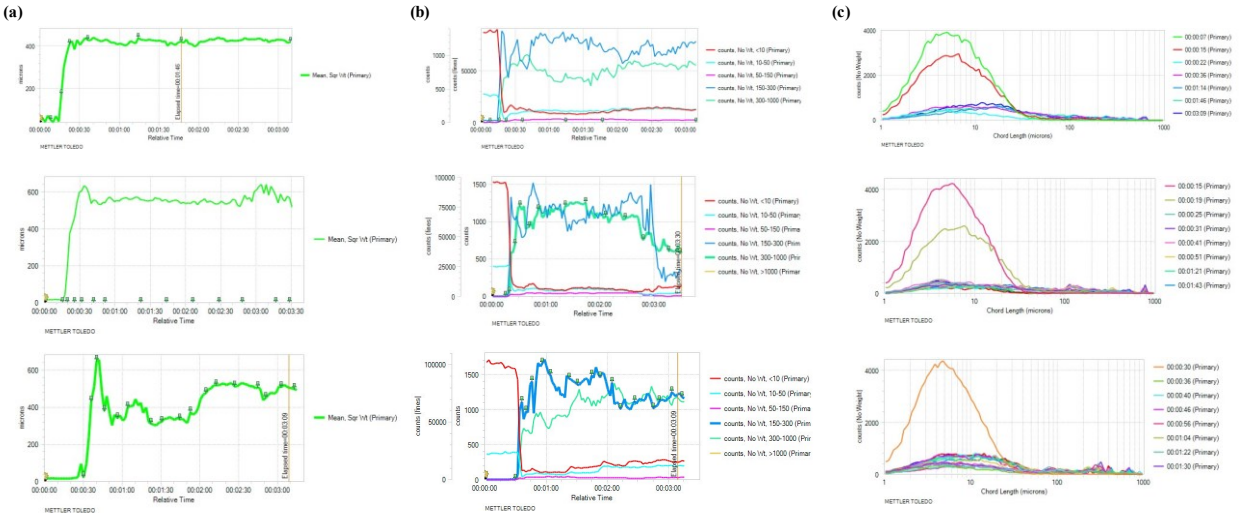

Figure B14.3 – FBRM Results of the three replicates for Run 3: a) Mean squared weight evolution, b) Counts evolution with flocculation time for each class, c) Chord length distribution.

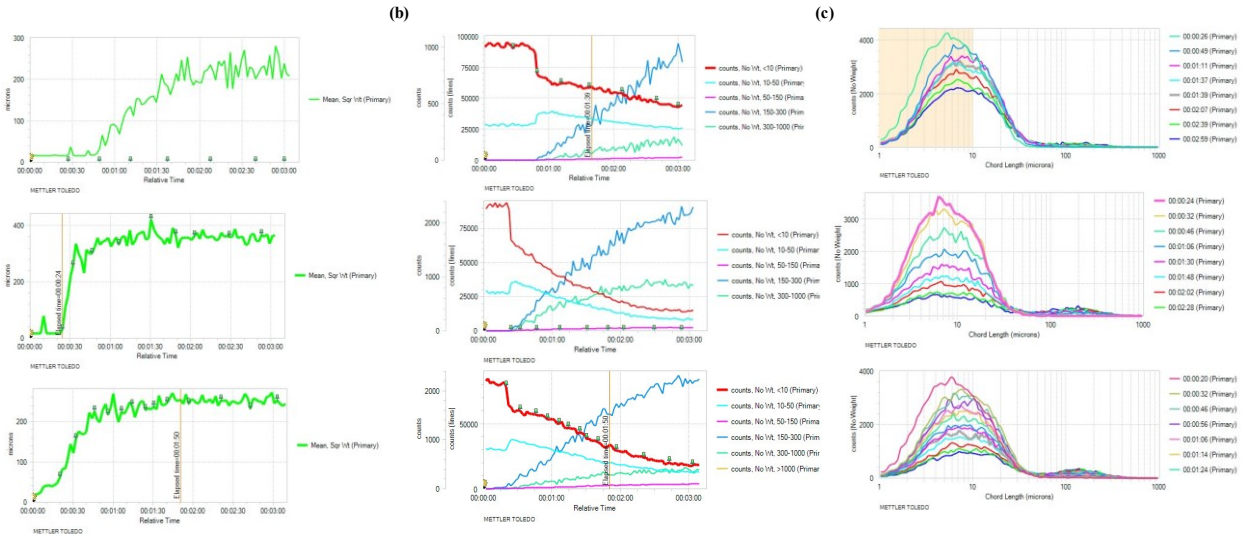

Figure B14.4 – FBRM Results of the three replicates for Run 4: a) Mean squared weight evolution, b) Counts evolution with flocculation time for each class, c) Chord length distribution.

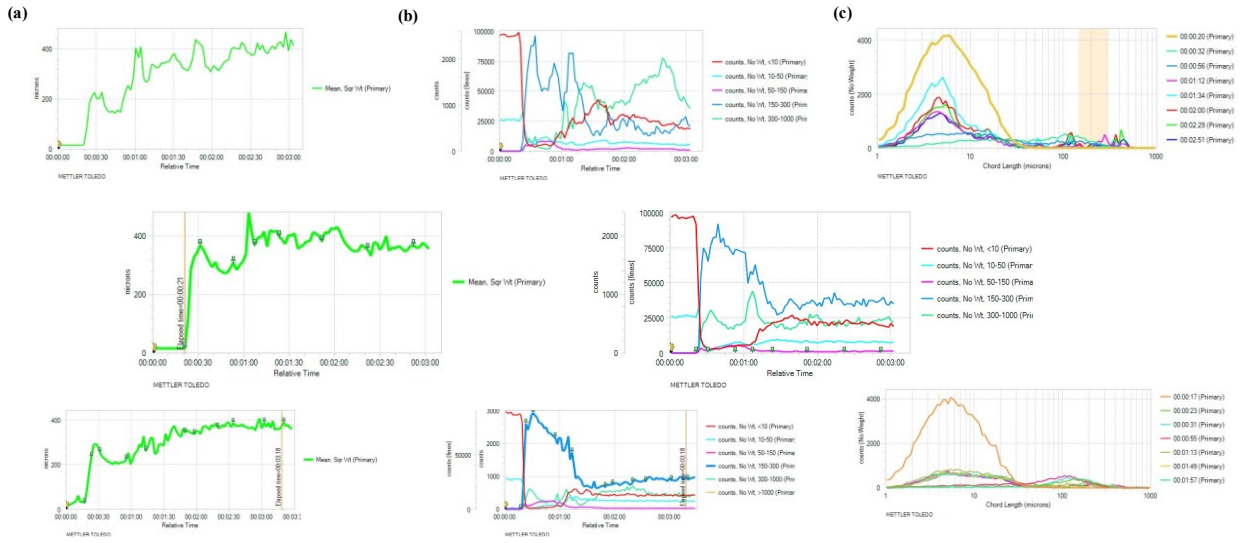

Figure B14.5 – FBRM Results of the three replicates for Run 5: a) Mean squared weight evolution, b) Counts evolution with flocculation time for each class, c) Chord length distribution.

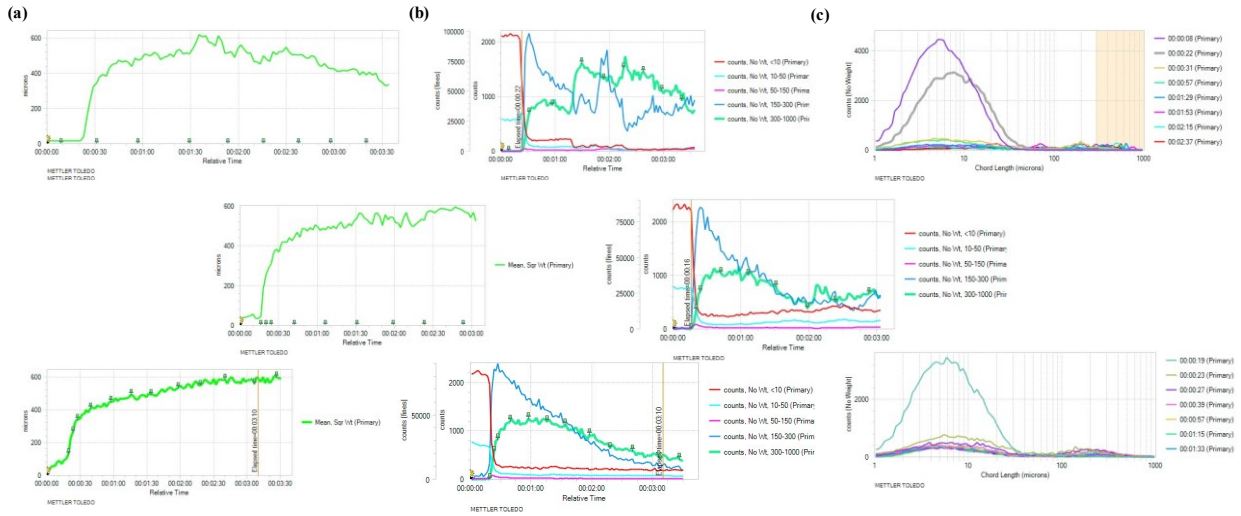

Figure B14.6 – FBRM Results of the three replicates for Run 6: a) Mean squared weight evolution, b) Counts evolution with flocculation time for each class, c) Chord length distribution.

Table B14.1 – FBRM Results for Run 1-1.

Trend (µm)	*00:12*	*00:22*	*00:24*	*00:28*	*00:38*	*01:47*	*02:39*
Median No. Wt	5.39	8.62	18.7	15.8	12.5	6.8	6.6
Mean Sqr Wt	16.4	214	324	248	415	504	428
Counts No Wt <10	95,598	26,041	4,433	7,426	11,787	26,733	28,324
Counts No Wt 10-50	26,607	17,282	3,099	4,560	10,225	12,690	13,240
Counts No Wt 50-150	18.68	2,700	2,335	3,785	3,098	1,955	2,110
Counts No Wt 150-300	0.00	810	1,610	2,436	1,249	731	695
Counts No Wt 300-1000	0.00	128	448	402	852	279	248

Table B14.2 – FBRM Results for Run 1-2.

Trend (µm)	*00:13*	*00:17*	*00:27*	*00:49*	*01:09*	*01:31*	*01:43*	*02:13*	*02:37*	*03:00*
Median No. Wt	5.61	10.9	113	16.7	14.7	8.75	11.18	10.26	11.51	9.42
Mean Sqr Wt	126	234	235	349	368	401	361	355	354	354
Counts No Wt <10	81,455	11,360	2,011	2,963	2,937	2,631	3,243	3,401	3,404	3,700
Counts No Wt 10-50	24,592	6,924	1,480	1,037	884	860	1,026	1,165	1,481	1,220
Counts No Wt 50-150	584	3,007	4,150	1,239	813	522	597	476	491	461
Counts No Wt 150-300	324	2,320	3,561	1,079	1,363	633	1,358	1,335	1,348	1,345
Counts No Wt 300-1000	0.00	298	418	524	507	325	589	503	508	486

Table B14.3 – FBRM Results for Run 1-3.

Trend (µm)	*00:21*	*00:27*	*00:41*	*00:47*	*00:53*	*01:03*	*01:25*	*02:01*	*02:31*	*02:53*	*03:10*
Median No. Wt	5.06	34.1	50.3	21.3	6.42	6.11	5.89	5.63	5.44	5.67	5.56
Mean Sqr Wt	29.0	289	209	246	397	283	262	239	272	286	243
Counts No Wt <10	97,503	4157	4107	6528	20,260	25,645	29,026	31,759	32,989	30,995	33,920
Counts No Wt 10-50	23,600	3,144	4,876	3,869	7,839	9,616	9,905	10,475	9,661	10,275	10,768
Counts No Wt 50-150	58.1	3,267	6,456	4,302	1,882	1,684	2,310	2,030	2,083	2,228	2,08
Counts No Wt 150-300	0.00	2,258	2,358	2,165	1,179	858	909	859	813	867	804
Counts No Wt 300-1000	3.34	481	216	319	337	213	128	108	137	88,1	59,7

Table B14.4 – FBRM Results for Run 2-1.

Trend (µm)	*00:08*	*00:16*	*00:28*	*00:56*	*01:41*	*02:35*
Median No. Wt	4.85	5.26	5.59	5.65	5.60	5.69
Mean Sqr Wt	61.3	251	369	413	399	414
Counts No Wt <10	98,038	66,321	41,735	34,211	23,568	16,885
Counts No Wt 10-50	22,092	18,633	13,016	10,674	6,307	4,299
Counts No Wt 50-150	319	869	778	692	758	842
Counts No Wt 150-300	53.7	739	1,191	1,556	1,759	1,646
Counts No Wt 300-1000	0.00	184	800	987	1,096	1,182

Table B14.5 – FBRM Results for Run 2-2.

Trend (µm)	*00:14*	*00:18*	*00:26*	*00:32*	*00:48*	*01:12*	*01:33*	*02:11*	*02:55*
Median No. Wt	5.60	6.83	7.25	7.25	6.98	7.34	6.98	7.38	7.34
Mean Sqr Wt	18.5	201	361	406	423	447	446	481	509
Counts No Wt <10	89,697	57,241	35,847	29,782	23,107	18,218	15,788	12,354	10,574
Counts No Wt 10-50	27,146	27,879	18,553	15,134	10,248	8,110	6,234	4,946	4,177
Counts No Wt 50-150	67.7	849	959	1,093	921	1,012	1,001	911	855
Counts No Wt 150-300	0.00	362	1,055	1,127	1,391	1,426	1,486	1,342	1,110
Counts No Wt 300-1000	0.00	72.6	567	786	1,008	1,155	1,164	1,122	943

Table B14.6 – FBRM Results for Run 2-3.

Trend (µm)	*00:24*	*00:28*	*00:32*	*00:38*	*00:50*	*01:02*	*01:28*	*01:59*	*02:27*	*02:47*	*03:01*
Median No. Wt	5.76	6.19	6.46	6.64	6.10	6.35	6.74	6.49	6.94	6.76	7.03
Mean Sqr Wt	199	299	364	377	403	393	408	424	437	450	445
Counts No Wt <10	61,862	39,917	35,935	30,729	26,505	23,389	17,703	14,972	11,541	11,833	10,856
Counts No Wt 10-50	20,193	14,643	14,399	12,282	8,918	8,252	6,300	4,603	3,647	3,745	3,773
Counts No Wt 50-150	1,234	1,225	1,064	998	974	1,033	1,157	1,146	943	984	935
Counts No Wt 150-300	729	1,425	1,476	1,386	1,738	1,784	1,922	1,907	1,718	1,599	1,587
Counts No Wt 300-1000	106	441	612	932	994	1,070	1,098	1,146	1,246	1,182	1,069

Table B14.7 – FBRM Results for Run 3-1.

Trend (µm)	*00:07*	*00:15*	*00:22*	*00:36*	*01:14*	*01:46*	*03:09*
Median No. Wt	5.42	5.84	6.60	10.7	16.0	13.7	12.4
Mean Sqr Wt	52.6	172	410	427	437	421	419
Counts No Wt <10	88,840	64,843	10,473	13,704	8,454	10,513	12,469
Counts No Wt 10-50	25,400	22,498	3,661	10,328	10,732	10,451	12,710
Counts No Wt 50-150	259	1,117	1,232	2,588	2,978	3,280	2,235
Counts No Wt 150-300	62.3	478	814	911	1,203	1,100	1,209
Counts No Wt 300-1000	0.00	47.0	680	926	737	808	860

Table B14.8 – FBRM Results for Run 3-2.

Trend (µm)	*00:15*	*00:19*	*00:25*	*00:31*	*00:51*	*01:21*	*01:43*	*02:06*	*02:28*	*02:48*	*03:16*
Median No. Wt	5.26	6.67	8.22	11.7	17.6	19.3	16.3	17.9	21.7	9.45	5.74
Mean Sqr Wt	16.4	186	460	605	540	557	558	548	539	552	582
Counts No Wt <10	95,575	55,383	8,913	7,537,62	6,401	4,848	6,871	6,180	5,153	4,849	7,696
Counts No Wt 10-50	25,299	25,410	4,152	5,042	5,959	4,732	6,201	5,326	4,550	1,866	2,356
Counts No Wt 50-150	23,1	1,053	1,205	1,646	2,942	2,438	2,770	2,950	2,974	980,8	232,5
Counts No Wt 150-300	0.00	433,61	1,026	913,6	1,291	1,059	978	1,167	1,277	931	284
Counts No Wt 300-1000	0.00	51.5	695	1,213	1,161	1,210	12,6	1,073	1,044	759	607

Table B14.9 – FBRM Results for Run 3-3.

Trend (µm)	*00:00:30*	*00:00:36*	*00:00:46*	*00:00:56*	*00:01:22*	*00:01:44*	*00:02:04*	*00:02:44*	*00:03:03*
Median No. Wt	5.07	7.31	8.74	15.5	11.6	9.35	10.8	9.82	10.3
Mean Sqr Wt	24.0	432	380	340	314	335	476	509	510
Counts No Wt <10	96,599	7,624	10,082	6,350	9,365	11,028	13,546	15,438	15,854
Counts No Wt 10-50	23,644	2,838	4,645	5,392	5,993	6,118	10,898	11,429	12,327
Counts No Wt 50-150	152	807	1,888	2,318	2,382	1,650	1,459	1,426	1,872
Counts No Wt 150-300	1,59	1,107	1,401	1,653	1,438	1,488	1,383	1,012	1,244
Counts No Wt 300-1000	0.00	650	661	883	943	1,051	1,231	1,253	1,061

Table B14.10 – FBRM Results for Run 4-1.

Trend (µm)	*00:26*	*00:49*	*01:11*	*01:37*	*01:39*	*02:07*	*02:39*	*02:59*
Median No. Wt	5.83	7.33	7.80	7.56	7.54	7.48	7.66	7.88
Mean Sqr Wt	16.7	30.7	135	185	163	237	202	238
Counts No Wt <10	89,956	69,612	61,680	58,505	59,850	54,604	47,568	42,774
Counts No Wt 10-50	30,053	36,443	37,232	33,407	33,890	30,069	26,631	25,062
Counts No Wt 50-150	24.7	160	527	1,092	866	1,273	1,869	1,954
Counts No Wt 150-300	0.00	11.8	122	319	303	507	805	1,038
Counts No Wt 300-1000	0.00	0.00	41.7	72.9	50.3	105	140	189

Table B14.11 – FBRM Results for Run 4-2.

Trend (µm)	*00:24*	*00:32*	*00:46*	*01:06*	*01:30*	*01:48*	*02:02*	*02:28*	*02:53*
Median No. Wt	7.23	7.51	7.69	7.92	8.20	8.47	8.83	9.72	9.76
Mean Sqr Wt	28.7	256	300	332	420	368	363	360	368
Counts No Wt <10	66,604	60,875	49,968	39,921	30,955	24,845	20,879	15,434	14,083
Counts No Wt 10-50	34,903	35,184	29,499	24,563	18,644	15,287	13,166	9,861	8,175
Counts No Wt 50-150	209	401	824	1,163	1,789	1,896	1,954	2,125	2,355
Counts No Wt 150-300	10.2	117	568	908	1,260	1,422	1,619	2,023	2,314
Counts No Wt 300-1000	0.00	70.2	292	550	585	705	841	895	844

Table B14.12 – FBRM Results for Run 4-3.

Trend (µm)	*00:20*	*00:32*	*00:46*	*00:56*	*01:06*	*01:30*	*01:56*	*02:42*	*03:03*
Median No. Wt	6.14	7.74	7.74	7.84	7.71	8.17	8.69	10.0	10.5
Mean Sqr Wt	62.2	157	225	216	224	238	243	232	252
Counts No Wt <10	78,345	60,046	57,037	53,136	49,835	38,160	29,514	20,272	17,989
Counts No Wt 10-50	29,774	35,671	33,268	31,338	28,201	22,934	18,878	14,258	13,150
Counts No Wt 50-150	401	584	819	1,178	1,455	2,185	2,641	3,591	3,771
Counts No Wt 150-300	43.5	305	370	578	758	1,348	1,746	2,174	2,150
Counts No Wt 300-1000	4.97	55.0	139	146	188	217	327	319	339

Table B14.13 – FBRM Results for Run 5-1.

Trend (µm)	*00:20*	*00:32*	*00:56*	*01:12*	*01:34*	*02:00*	*02:29*	*02:51*
Median No. Wt	5.57	35.9	10.3	5.37	5.01	5.70	5.59	5.66
Mean Sqr Wt	18.6	205	236	339	350	335	385	422
Counts No Wt <10	89,127	4,371	12,929	23,180	42,916	29,137	24,905	20,997
Counts No Wt 10-50	26,312	6,743	8,177	5,415	8,455	7,870	6,086	5,352
Counts No Wt 50-150	34.9	6,080	3,202	962	1,819	2,445	1,939	1,252
Counts No Wt 150-300	2.50	2,285	1,605	1,518	431	623	372	569
Counts No Wt 300-1000	0.00	209	305	935	905	999	1,662	1,292

Table B14.14 – FBRM Results for Run 5-2.

Trend (µm)	*00:21*	*00:31*	*00:53*	*01:07*	*01:23*	*01:51*	*02:21*	*02:51*	*03:02*
Median No. Wt	5.52	33.3	28.4	14.9	6.57	6.51	6.30	6.83	6.69
Mean Sqr Wt	15.9	368	309	367	397	383	355	369	356
Counts No Wt <10	91,801	3,014	5,203	7,621	21,643	24,375	22,215	19,880	19,129
Counts No Wt 10-50	25,410	1,882	7,499	6,716	9,394	9,095	7,863	7,935	7,656
Counts No Wt 50-150	13.5	1,958	5,247	2,668	1,366	1,102	1,288	1,281	1,360
Counts No Wt 150-300	0.00	1,571	1,770	1,345	778	863	815	913	837
Counts No Wt 300-1000	0.00	644	474	1,056	519	473	497	559	521

Table B14.15 – FBRM Results for Run 5-3.

Trend (µm)	*00:17*	*00:31*	*00:55*	*01:13*	*01:49*	*01:57*	*02:33*	*03:02*
Median No. Wt	5.65	115	68.9	8.80	8.64	8.93	8.58	8.21
Mean Sqr Wt	27.9	256	222	259	342	336	385	388
Counts No Wt <10	86,875	807	2,415	16,634	12,670	12,508	12,759	13,014
Counts No Wt 10-50	27,387	1,236	3,830	10,019	8,083	8,424	7,846	7,459
Counts No Wt 50-150	241	4,599	6,704	1,913	1,046	1,014	1,090	1,101
Counts No Wt 150-300	4.22	2,937	2,195	1,732	678	764	846	883
Counts No Wt 300-1000	0	520	242	271	529	539	539	444

Table B14.16 – FBRM Results for Run 6-1.

Trend (µm)	*00:08*	*00:22*	*00:31*	*00:57*	*01:29*	*01:53*	*02:15*	*02:37*	*02:57*
Median No. Wt	5.39	7.38	9.26	7.25	12.9	24.2	13.9	65.5	43.7
Mean Sqr Wt	15.6	41.3	345	476	509	518	499	503	427
Counts No Wt <10	96,512	59,670	10,355	9,538	4,813	3,588	3,580	1,128	1,583
Counts No Wt 10-50	26,154	32,727	5,378	3,364	2,876	3,657	1,245	1,399	1,475
Counts No Wt 50-150	11.6	345	1,294	763	739	1,792	1,063	1,120	1,070
Counts No Wt 150-300	0.00	39.3	2,156	1,369	1,053	1,575	572	623	724
Counts No Wt 300-1000	0.00	0.00	700	849	1,616	1,326	1,524	1,463	1,111

Table B14.17 – FBRM Results for Run 6-2.

Trend (µm)	*00:16*	*00:20*	*00:24*	*00:42*	*01:06*	*01:30*	*01:58*	*02:22*	*02:53*
Median No. Wt	5.88	10.3	9.84	7.42	7.00	7.17	6.76	6.24	6.65
Mean Sqr Wt	46.0	257	310	442	480	540	544	529	577
Counts No Wt <10	82,679	18,634	10983	9,348	10,234	11,253	12,442	15,925	13,226
Counts No Wt 10-50	28,777	13,655	5,515	3,247	3,394	4,494	5,516	5,699	5,170
Counts No Wt 50-150	394	3,532	2,306	905	1,018	1,100	916	866	1,103
Counts No Wt 150-300	21.3	1,735	2,279	1,451	1,188	661	444	706	583
Counts No Wt 300-1000	0.00	348	705	1,048	1,016	800	383	515	668

Table B14.18 – FBRM Results Summary for Run 6-3.

Trend (µm)	*00:20*	*00:32*	*00:46*	*00:56*	*01:06*	*01:14*	*01:24*	*01:40*	*01:50*	*02:20*	*02:42*	*03:03*
Median No. Wt	6.14	7.74	7.74	7.84	7.71	7.93	7.94	8.35	8.09	9.31	10.0	10.5
Mean Sqr Wt	62.2	157	225	216	224	242	229	247	254	252	232	252
Counts No Wt <10	78345	60046	57037	53136	49835	47023	43373	35692	33706	23896	20272	17989
Counts No Wt 10-50	29774	35671	33268	31338	28201	27787	25534	21787	19803	15870	14258	13150
Counts No Wt 50-150	400.6	585	819	1178	1455	1495	1952	2373	2725	3218	3591	3771
Counts No Wt 150-300	43.5	308	370	578	759	935	1095	1488	1533	1857	2174	2150
Counts No Wt 300-1000	4.97	55.0	139	146	188	204	200	312	281	395	319	339

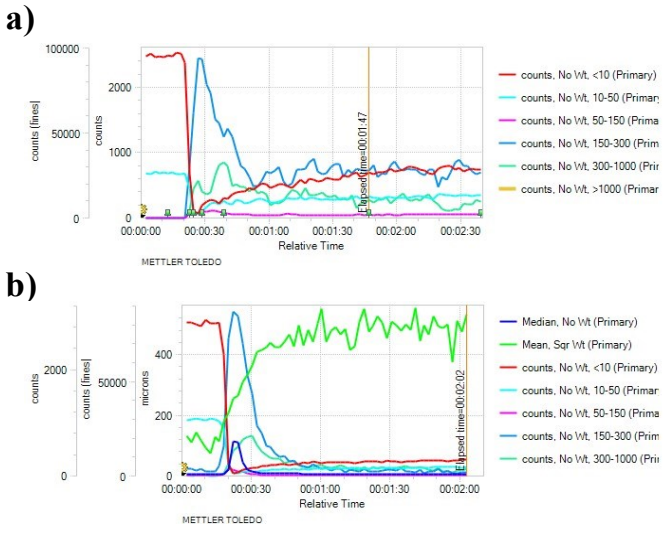

Figure B14.7 – Comparison of FBRM Results for a) 1.5k ppm dosage and b) 3k ppm.